NOVEL FINE PITCH INTERCONNECTION METHODS USING METALLISED POLYMER SPHERES

By

Junlei Tao

A Doctoral Thesis

Submitted in Partial Fulfilment of the Requirements

For the Award of

Doctor of Philosophy of Loughborough University

April 2016

CERTIFICATE OF ORIGINALITY

This is to certify that I am responsible for the work submitted in this thesis, that the original work is my own except as specified in acknowledgments or in footnotes, and that neither the thesis nor the original work contained therein has been submitted to this or any other institution for a degree.

…… (Signed)

…… (Date)

Certificate of Originality

Thesis Access Conditions and Deposit Agreement

Students should consult the guidance notes on the electronic thesis deposit and the access conditions in the University's Code of Practice on Research Degree Programmes

Author Junlei Tao

Title Novel Fine Pitch Interconnection Methods Using Metallised Polymer Spheres

I [Junlei Tao, Wolfson School, Loughborough University, Epinal Way, Loughborough, LE11 3TU], "the Depositor",
would like to deposit [Please insert title of dissertation], hereafter referred to as the "Work", once it has successfully been examined in Loughborough University Institutional Repository
.
Status of access OPEN ~~/ RESTRICTED / CONFIDENTIAL~~

Moratorium Period……..……years, ending……..……

Status of access approved by (CAPITALS):……

Supervisor (Signature)……...……...……

School of……...……

Author's Declaration *I confirm the following :*

CERTIFICATE OF ORIGINALITY

This is to certify that I am responsible for the work submitted in this thesis, that the original work is my own except as specified in acknowledgements or in footnotes, and that neither the thesis nor the original work therein has been submitted to this or any other institution for a degree

NON-EXCLUSIVE RIGHTS

The licence rights granted to Loughborough University Institutional Repository through this agreement are entirely non-exclusive and royalty free. I am free to publish the Work in its present version or future versions elsewhere. I agree that Loughborough University Institutional Repository administrators or any third party with whom Loughborough University Institutional Repository has an agreement to do so may, without changing content, convert the Work to any medium or format for the purpose of future preservation and accessibility.

DEPOSIT IN LOUGHBOROUGH UNIVERSITY INSTITUTIONAL REPOSITORY

I understand that open access work deposited in Loughborough University Institutional Repository will be accessible to a wide variety of people and institutions - including automated agents - via the World Wide Web. An electronic copy of my thesis may also be included in the British Library Electronic Theses On-line System (EThOS).

I understand that once the Work is deposited, a citation to the Work will always remain visible. Removal of the Work can be made after discussion with Loughborough University Institutional Repository, who shall make best efforts to ensure removal of the Work from any third party with whom Loughborough University Institutional Repository has an agreement. Restricted or Confidential access material will not be available on the World Wide Web until the moratorium period has expired.

- That I am the author of the Work and have the authority to make this agreement and to hereby give Loughborough University Institutional Repository administrators the right to make available the Work in the way described above.
- That I have exercised reasonable care to ensure that the Work is original, and does not to the best of my knowledge break any UK law or infringe any third party's copyright or other Intellectual Property Right. I have read the University's guidance on third party copyright material in theses.
- The administrators of Loughborough University Institutional Repository do not hold any obligation to take legal action on behalf of the Depositor, or other rights holders, in the event of breach of Intellectual Property Rights, or any other right, in the material deposited.

*The statement below shall apply to **ALL** copies:*

This copy has been supplied on the understanding that it is copyright material and that no quotation from the thesis may be published without proper acknowledgement.

Restricted/confidential work: All access and any copying shall be strictly subject to written permission from the University Dean of School and any external sponsor, if any.

Author's signature……..Date……...…

user's declaration: for signature during any Moratorium period (Not Open work): ***I undertake to uphold the above conditions:***			
Date	Name (CAPITALS)	Signature	Address

献给我的母亲

Abstract

There is an ongoing demand for electronics devices with more functionality while reducing size and cost, for example smart phones and tablet personal computers. This requirement has led to significantly higher integrated circuit input/output densities and therefore the need for off-chip interconnection pitch reduction. Flip-chip processes utilising anisotropic conductive adhesives anisotropic conductive films (ACAs/ACFs) have been successfully applied in liquid crystal display (LCD) interconnection for more than two decades. However the conflict between the need for a high particle density, to ensure sufficient the conductivity, without increasing the probability of short circuits has remained an issue since the initial utilization of ACAs/ACFs for interconnection. But this issue has become even more severe with the challenge of ultra-fine pitch interconnection.

This thesis advances a potential solution to this challenge where the conductive particles typically used in ACAs are selectively deposited onto the connections ensuring conductivity without bridging. The research presented in this thesis work has been undertaken to advance the fundamental understanding of the mechanical characteristics of micro-sized metal coated polymer particles (MCPs) and their application in fine or ultra-fine pitch interconnections. This included use of a new technique based on an in-situ nanomechanical system within SEM which was utilised to study MCP fracture and failure when undergoing deformation. Different loading conditions were applied to both uncoated polymer particles and MCPs, and the in-situ system enables their observation throughout compression. The results showed that both the polymer particles and MCP display viscoelastic characteristics with clear strain-rate hardening behaviour, and that the rate of compression therefore influences the initiation of cracks and their propagation direction.

Selective particle deposition using electrophoretic deposition (EPD) and magnetic deposition (MD) of Ni/Au-MCPs have been evaluated and a fine or ultra-fine pitch deposition has been demonstrated, followed by a subsequent assembly process. The MCPs were successfully positively charged using metal cations and this charging mechanism was analysed. A new theory has been proposed to explain the assembly mechanism of EPD of Ni/Au coated particles using this metal cation based charging method. The magnetic deposition experiments showed that sufficient magnetostatic interaction force between the magnetized particles and pads enables a highly selective dense deposition of particles. Successful bonding to form conductive interconnections with pre-deposited particles have been demonstrated using a thermocompression flip-chip bonder, which illustrates the applicable capability of EPD of MCPs for fine or ultra-fine pitch interconnection.

Acknowledgements

This research is financially supported by the Loughborough University and UK Engineering and Physical Sciences Research Council (EPSRC) through the Innovative Electronics Manufacturing Research Centre (IeMRC).

I would like to express my sincerest gratitude and appreciation to my supervisors, Mr. David C. Whalley and Prof. Changqing Liu, for their constant support and enduring guidance during this research. I would like to sincerely thank Mr. David C. Whalley for his constructive feedback, numerical suggestions and proofreading, which has been of great significance for the success of my PhD study. I would also like to extend my deep thanks to Prof. Changqing Liu for valuable suggestions and strong support from the Marie Curie project entitled "Micro-Multi-Material Manufacture to Enable Multifunctional Miniaturised Devices (M6)". Their remarkable patience and academic skills are greatly appreciated. This thesis would not have been accomplished without their professional inputs along with the strength of a team work.

I would also like to thank Conpart AS. Norway especially Dr. Helge Kristiansen for supplying the Ni/Au-MCPs for this research project. I would also like to thank Dr. Jianying He from Norwegian University of Science and Technology for her shared results in developing FEA models, and Miss Giang Nghiem from Buskerud and Vestfold University College for her great assistance for the assembly trials. Their inputs and fruitful discussions have been very important for the work presented in this thesis.

I would like to acknowledge Prof. Fengshun Wu from Huazhong University Science and Technology (HUST) for his patient guidance and useful suggestions during my exchange study at HUST. Prof. Jianjun Lai, Prof. Yuandi Zhao, Miss Mengyao Qin, Dr. Shuai Huang from HUST have also been very helpful in the silicon chip fabricating process and relevant experiments. I would also like to thank Prof. Zhiwei Shan and Mr. Zhanming Zhang at Center for Advancing Materials Performance from the Nanoscale in Xi'an Jiaotong University. Their positive cooperation and strong support have been am immense help for the individual particles compression tests.

I would also like to extend my gratitude to Dr. David Hutt for his valuable discussions and all the technical staff in Wolfson School who helped me during my research, in particular to Mr. Andy Sandaver for his assistance in the sample preparation. I would also like to than Dr. Keith Yendall and Mr. Scott Doak, in Materials Department for their training and assistance during sample characterisation using SEM and FIB.

At last but not least, I would like to thank my father and brother for their love, support and encouragement. Without their understanding and faith I would not have achieved this research. I would like to thank my friends who have accompanied and helped me along the PhD journey.

Loughborough, Leicestershire Junlei Tao

June, 2016

Contents

List of Tables

List of Figures

List of Abbreviations

ACA	-	Anisotropic Conductive Adhesive
Ag	-	Silver
Al	-	Aluminum
ASIC	-	Application-specified Integrated Circuit
at.%	-	Percentage of atoms
Au	-	Gold
BGA	-	Ball Grid Array
C4	-	Controlled-collapse Chip Connection
CTE	-	Coefficient of Thermal Expansion
Cu	-	Copper
DI	-	Deionised Water
DMA	-	Dynamic Mechanical Analysis
DNA	-	Deoxyribose Nucleic Acid
ECA	-	Electrical Conductive Adhesive
EDX	-	Energy Dispersive X-ray
EPD	-	Electrophoretic Deposition
ESC	-	Encapsulant Solder Connection
FC	-	Flip Chip
FEA	-	Finite Element Analysis
FEGSEM	-	Field Emission Gun-scanning Electron Microscope
FIB	-	Focus Ion Beam
GGI	-	Gold to Gold Interconnection
HCl	-	Hydrochloric Acid
IC	-	Integrated Circuit
ICA	-	Isotropic Conductive Adhesive
ICPCVD	-	Inductively Coupled Plasma Chemical Vapour Deposition

IEP	-	Isoelectric Point
IMCs	-	Intermetallic compounds
I/O	-	Inputs/outputs
LCD	-	Liquid Crystal Display
LED	-	Light-emitting Diode
IPA	-	Isopropyl Alcohol
mm	-	Millimetre
MCP	-	Metal Coated Polymer Particle
MRI	-	Magnetic Resonance Imaging
MPa	-	Mega Pascal
nA	-	Nano- ampere
NCF	-	Non Conductive Film
NCP	-	Non Conductive Paste
Ni	-	Nickel
nm	-	Nanometer
PCB	-	Printed Circuit Board
PH	-	Potential Of Hydrogen
RFID	-	Radio Frequency Identification
SA	-	Self-assembly
Sn	-	Tin
TAB	-	Tape-automated Bonding
T_B	-	The bonding Temperature
t_d	-	Dwell Time
TEM	-	Transmission Electron Microscopy
Ti	-	Titanium
TLP	-	Transient liquid phase
T_M	-	The melting Point Temperature
TSV	-	Through Silicon Via
UBM	-	Under Bump Metallurgy/Metallisation

UV	-	Ultraviolet
VSM	-	Vibrating Sample Magnetometer
WB	-	Wire Bonding
WLCSP	-	Wafer Level Chip Scale Package
wt.%	-	Percentage of Weight

Chapter 1

Introduction

This chapter first identifies the background to the research undertake and general problems facing nowadays. Based on these identified problems, proposed solutions (the research aims and objectives) are introduced, followed by the discussion of the thesis structure and its main achievements.

1.1 Background

Electronic devices have penetrated into every aspect of human life, and will continue to change the way of life in the future. Electronic packaging, provides the physical structures bridging between individual functional components such as integrated circuits (ICs) also known as semiconductor chips and electronic systems, and plays an import role during the manufacturing of electronic products. Traditionally it is divided into three different levels for the electronic packaging including the first IC assembly level, second board assembly level, and the third system packaging level [1]. Nowadays, the increasing development of electronic packaging technologies, as shown in Figure1, has resulted in the large integration at different levels and has blurred the boundaries. This has also dominated major factor driving the significantly decreasing dimensions of components and complete electronics systems [2].

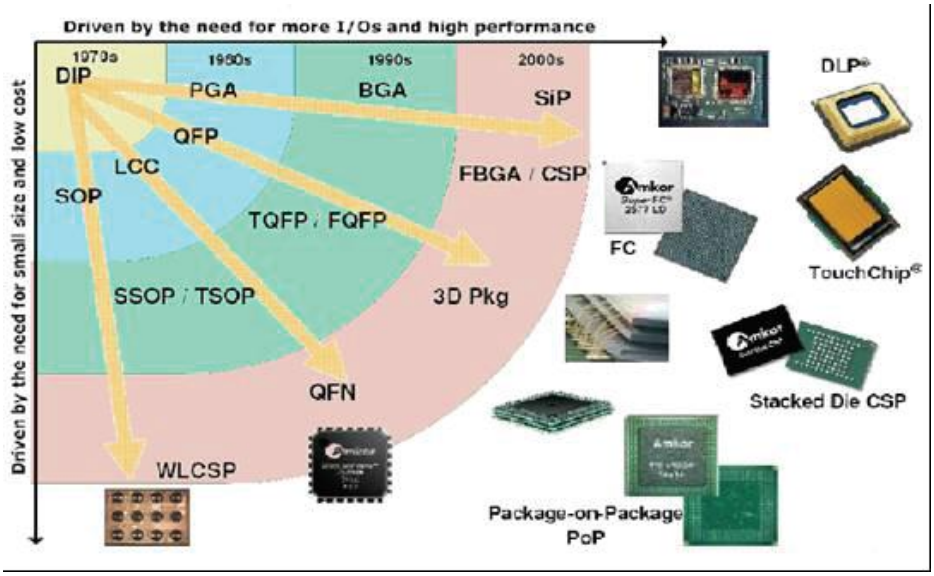

Figure 1.1 Development of the packages driven by the need for small size, low cost, more I/Os and high performance [2].

Higher interconnection densities are still demanded by the electronics industry with the aim of avoiding increased packaging size as well as increasing performance [3]. New materials, processes and configurations are needed to be utilized to achieve higher integration in modern electronics technologies. Meanwhile packaging technologies also have to incorporate with a wide range of aspects such as the employment of small interconnections to build high density circuits, achieving competitive cost, electrical (high signal processing) and physical (better heat transfer and cooling) issues, and mechanical reliability. As shown in Figure 1.2, compared with the conventional wire bonding and tape-automated bonding (TAB), flip-chip technology has the potential for use within a much wider range of applications in the packaging of electronic devices because of its advantages of shorter and higher density interconnections, with better electrical performance, lower inductance, higher frequency, better noise control [4].

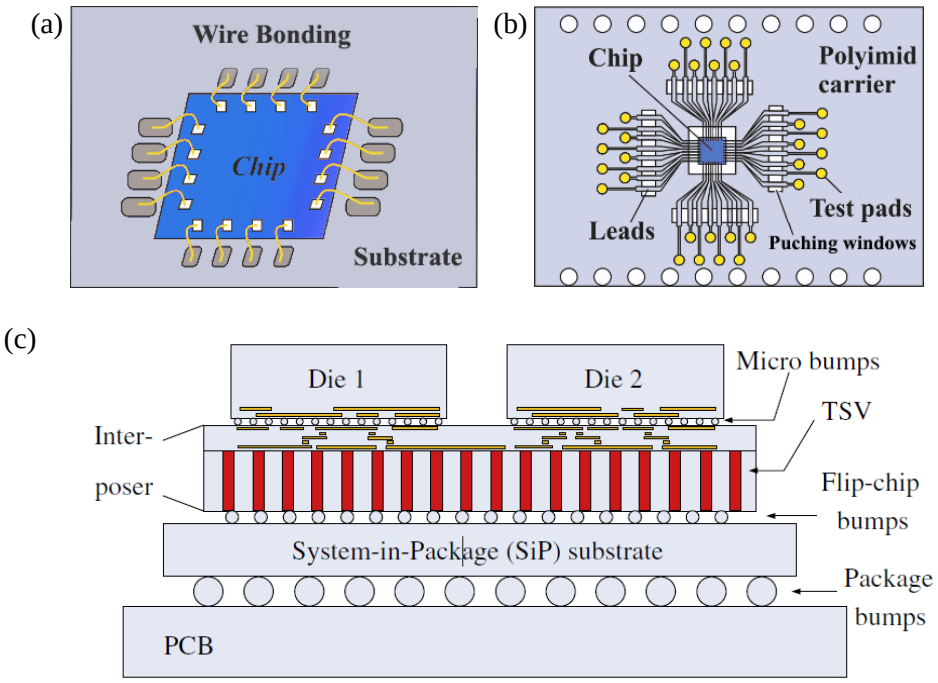

Figure 1.2 Schematic images of (a) wire bonding, (b) tape-automated bonding (TAB), and (c) flip-chip bonding in the application of 3D packaging [5].

Solder based flip-chip were firstly designed and fabricated by IBM using the controlled collapse chip connection (C4) technology [6], which has been developed into a variety of updated approaches to meet the increasing demand of higher I/O density and decreasing pitch bumps, e.g. micro-controlled collapse chip connection (μ-C4) [7] and copper pillar bump technology [4]. Flip-chip packaging also includes contacting interconnection methods such as Anisotropic Conductive Adhesives (ACAs), Isotropic Conductive Adhesives (ICA), and Non-

conductive Adhesives (NCA) [8]. Anisotropic Conductive Adhesives (ACAs) consist of a polymer adhesive matrix containing a relative low loading level of micronised conductive particles. A typical packaging using ACAs is shown in Figure 1.3. As one of the most important technologies for flip-chip interconnections, ACAs have been successfully utilised in flat panel display modules [9] and smart cards [10-12] for approximately two decades. The conductive particles are trapped between the pads of the two parts being connected e.g. an IC and substrate forming the electrical interconnection between them. The anisotropic conductivity makes them very suitable for the fine pitch interconnections, for example for Liquid Crystal Displays (LCD) with less than 100 μm pitch. Bonding using a combination of heat and pressure is usually employed to achieve the ACAs interconnection instead of the conventional reflow processes used for solders. However processing lower temperature is required which allows use with produces which cannot survive the high temperature solder reflow process.

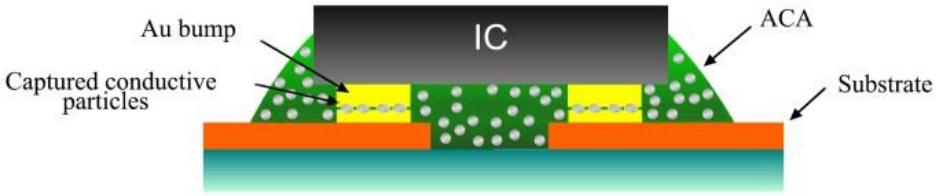

Figure 1.3 Schematic image showing the cross section of a typical ACAs package.

Traditional solder bumps are unable to meet the challenge for fine-pitch or ultrafine-pitch and high-count integration due to the increasing probability of short circuits which can occur during reflow [13]. Consequently, a number of novel processes such as μ -C4 and copper pillar bump technology have been developed because of their ultra-fine pitch capability and electrical performance advantages [14, 15]. However the multiple-reflow processes are required to achieve multiple layers of interconnection through the vertical direction in 3D stacking package, and the high bonding temperature is an inevitable potential threat to the reliability [16, 17]. These processes are particularly unsuitable for the growing flexible wearable electronics sector [18].

1.2 Proposed Solution

Research work will be presented on novel interconnection methods using selectively deposited metal coated polymer core microparticles (MCPs). Two different deposition processes, i.e. electrophoretic deposition (EPD) and magnetic deposition (MD), are established to precisely control deposition of particles onto the targeted pad instead of them being randomly dispersed

as shown in Figure 1.4. These novel methods maintain the advantages of traditional ACAs as well as being applicable to ultra-fine pitch interconnection without increasing the risk of short or open circuits connect issues. Furthermore, the low bonding temperature of these novel approaches reduces the potential damage for sensitive components and thus provides promising solutions for the applications which are sensitive to temperature, for instance the wearable electronics and smart textiles [18]. In particular, the ultra-fine pitch capability of the novel processes help to meet the challenges of the continuous demand for higher density interconnections.

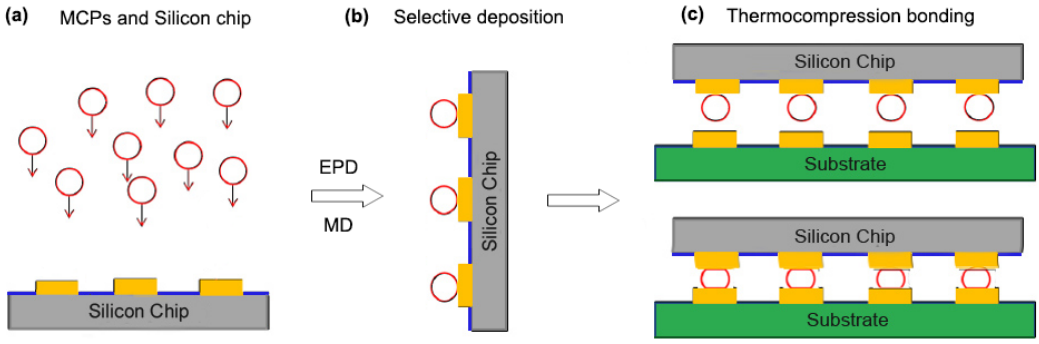

Figure 1.4 Schematic image of the selective deposition principle using MCPs to achieve ultra-fine pitch flip-chip interconnections.

Commonly used particles in ACAs are comprised of Ni/Au coatings on a polymer core. The polymer core enables the particles to withstand large deformations, while the metal coatings provide the electric conductive path. The characteristics of the particles are critical for the reliability and electrical performance of the final interconnection. However due to the extremely small size of a single particle (typically 3μm to 10 μm) and the limitations of available test equipment, only limited studies have been conducted on the characteristics of individual particles. The research in this thesis therefore includes a systematic study on the viscoelastic behaviour of the Ni/Au coated polymer particles as well as their fracture modes using a combination of an in-situ nanomechanical testing system within SEM and finite element analysis (FEA). The FEA analysis using COMSOL Multiphysics, helps to provide an understanding of the stress distribution within the particle during its deformation process, and has led to a credible explanation for the observed crack propagation within the particle. Furthermore the particles will endure a temperature increasing process during the thermocompression bonding, at which the properties of the particles will be significantly different because of the high co-efficient of thermal expansion (CTE) mismatch between the polymer core and the metal coating layer. The results also contribute to the fundamental

understanding of ACA technology and establish the failure model, thereby providing significant reference value to the parameters optimization process in industry.

1.3 Research Aims and Objectives

Given the need for higher I/O density flip-chip interconnections identified in section 1.1, the research presented in this thesis has been dedicated to the exploration of the novel processes to achieve ultra-fine pitch interconnections using metal coated polymer core particles and investigation of viscoelastic characteristics and fracture of the individual particles. The methodology employed to undertake this research is a combination of novel systematic experiments and numerical modelling. Based on the identified problems the overall aims of this research are defined as being:

- To investigate the characteristics of individual conductive particles under different loading conditions by combining finite element analysis with a series of novel experiments, to obtain a better understanding of the viscoelastic properties of the particles, and their fracture mechanism.
- To explore novel processes to achieve fine or ultra-fine pitch flip-chip interconnection using Ni/Au coated polymer particles. To understand the assembly mechanism behind the electrophoretic deposition of Ni/Au coated particles, and the effect of each parameter during the EPD process, to determine the factors affecting electrophoretic deposition of the metal coated polymer particles. To establish a novel magnetic assembly process for the Ni/Au coated particles.

To achieve these aims the following objectives were established:

- To determine the efficacy of using ACA as an interconnecting material in flip-chip packaging and identify the various advantages and limitations of ACA interconnection, the potential approaches to achieve fine or ultra-fine pitch interconnection and the fundamental mechanism of electrophoretic deposition through a critical review.
- To develop a theoretical model to gain an understanding of the viscoelastic characterization of the polymer core and the Ni/Au coated polymer core particles by compressing the individual polymer core particle at different strain rates, and the dynamic mechanical analysis (DMA).

- To gain an understanding of the deformation of individual particle so that to analyse

the stress and strain during the deformation process and the crack propagation and fracture mechanism of the metal coated particle under different loading conditions by the in situ nanomechanical experiment system and COMSOL Multiphysics analysis.

- To evaluate the merits and demerits of electrophoretic deposition of mono-sized metal coated polymer particles as a new method of flip-chip technology, and gain an understanding of the effect of different factors such as hydrochloric acid immersion, electric field intensity, and most importantly explore the fundamental assembly mechanism of the electrophoretic deposition
- To establish the magnetic assembly process using metal coated polymer particle combined and systematically study the magnetic properties of both the Ti/Ni/Au pad chip and Ni/Au coated particles thus to gain a better utilization of the magnetic field and the various force analysis during the assembly process.
- To study the properties of the final interconnection achieved through electrophoretic deposition and magnetic assembly after thermocompression bonding, such as the electrical conductivity and the effect of underfill on the reliability of metal coated polymer particles deposition interconnection, therefore, find the most efficient and reliable method to accomplish the underfill process.

1.4 Structure of the Thesis

There are seven chapters in this thesis in total, and Figure 1.5 shows the thesis structure Chapter 1 presents an introduction to this thesis, where the background, research aims and the objectives, and original findings are included. This includes the problems which are identified in the interconnection with anisotropic conductive adhesives (ACA). The research objectives proposes the possible solutions to these problems and established the promising novel processes.

In Chapter 2, a literature review of the history and recent research related to ACA assembly is presented. Flip-chip history and ACA technologies, ACA assembly processes, ACA interconnections, and the reliability of ACA assembly are all discussed in this chapter. Meanwhile, technologies related to the potential processes to achieve the ultra-fine pitch interconnections are analysed especially electrophoretic deposition and magnetic assembly and their fundamental mechanisms.

Chapter 3 details the experiment set up and results for the mechanical characterisation of individual metal coated polymer particles, and the chemical and magnetic properties of the

Ni/Au coated particles. The viscoelastic characteristics of the polymer core and Ni/Au coated particles for different loading conditions are analysed. In this chapter, the in -situ nanomechanical experiment system used enables observation during the individual particle compression test, allowing the crack propagation and fracture mechanism to be studied. Finite elements models are used to help the better understanding of the stress distribution of the individual particle during the deformation process therefore enables the analysis and discussion of the crack propagation and fracture mechanism of the particles.

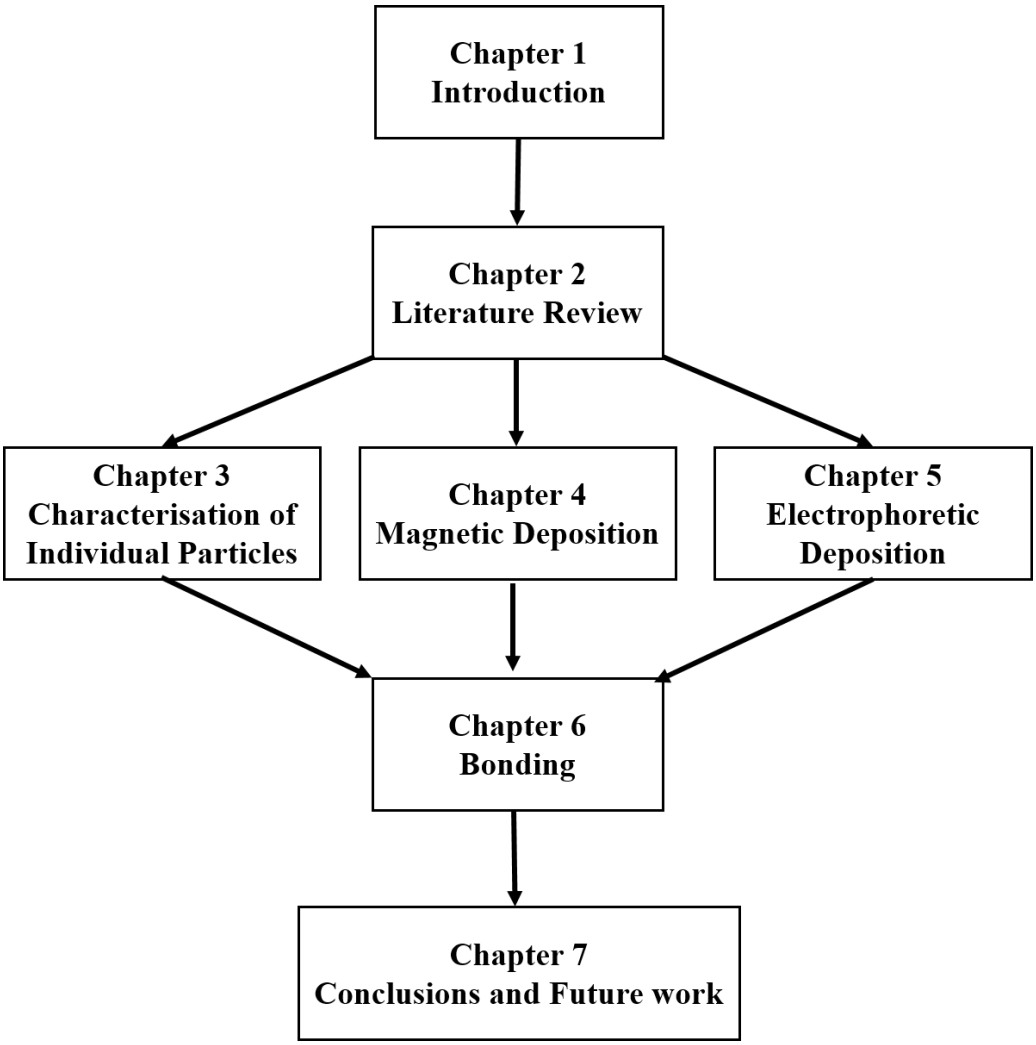

Figure 1.5 An overview of the thesis structure.

Chapter 4 presents the electrophoretic deposition of metal coated polymer particles. First the required charging process is discussed, including charging mechanisms and alternative charging methods. Then research into the assembly mechanism for the electrophoretic deposition of the metal coated particles is presented. Chapter 5 presents a novel magnetic assembly process which utilises the magnetic properties of the nickel within component pads

and particle coating. The magnetic characteristics of both the pads and particles are studied and two different variations magnetic assembly processes i.e. with and without the implement of an external magnetic field are presented as well as an analysis of forces on the particles during the assembly process and the potential risks.

Chapter 6, benefiting from the research in Chapter 3 and using chips deposited with particles as described in Chapter 4 and 5, describes how the final bonding process is conducted and the electrical conductivity tested. The results of these studies are presented and discussed in this chapter.

Chapter 7 concludes the thesis with a summary of the achievements and a discussion of potential future work.

1.5 Concluding Remarks

Various problems related to the related to the traditional electronic packaging methods have been presented in this chapter, e.g. their increasing difficulty to meet the demand of higher interconnection densities. For the identified problems, a solution is proposed, and based on this proposed solution the thesis are identified. The main aim of this research is to further study the mechanical characteristics of MCPs and then utilise them to achieve an ultra-fine pitch flip-chip interconnections. Based on the identified research aims, the objectives of this research have been presented in this chapter.

1.6 Publications Arising from the Thesis Work

So far, this research has resulted in five international conference papers, and some journal papers are in preparation.

Journal Papers in Preparation:

1. J. Tao, D.C. Whalley, C. Liu, F. Shun, and H. Kristiansen, “Magnetically tunable self-assembled monolayer of Ni/Au coated microspheres on silicon chip”

2. J. Tao, D.C. Whalley, C. Liu, and H. Kristiansen, “Self-assembly of Ni/Au coated polymer particles on silicon chip using a combination of electrophoretic and electroplating process”

3. J. Tao, D.C. Whalley, C. Liu, Z. Shan, Z. Zhang, and H. Kristiansen, “In Situ Study of Fracture Mechanism in Individual Ni/Au Coated Polymer Particle”

4. J. Tao, D.C. Whalley, C. Liu, Z. Shan, Z. Zhang, and H. Kristiansen, "Viscoelastic Characterisation of Individual ACA Conductive Spheres"

Conference Papers:

1. M. Suden, J. Tao, C. Liu, D. Hutt, D.C. Whalley, N. Lietaer, "Characterisation of Thermocompression Bonds of Metal Coated Polymer Core Particles for Fine Pitch Flip-Chip Interconnects", in Proc. IEEE Electronics System-Integration Technology Conference (ESTC), Grenoble, France, September 13-16, 2016, Accepted.

2. J. Tao, D.C. Whalley, C. Liu, "Electrophoretic Deposition of Ni/Au Coated Particles for Ultra-fine Pitch Interconnection", in Proc. IEEE 66th Electronic Components and Technology Conference (ECTC), Las Vegas, Nevada, USA, May 31 – June 4, 2016.

3. J. Tao, D.C. Whalley, C. Liu, F. Wu, and H. Kristiansen, "Novel Processes to Enable Deposition of Metal Coated Polymer Micro-Spheres for Flip-chip Interconnections", in Proc. IEEE 65th Electronic Components and Technology Conference (ECTC), San Diego, California, USA, May 26-29, 2015, pp. 1154-1159.

4. J. Tao, D. C. Whalley, C. Liu, and J. He, "Process and Performance Modelling for Individual ACA conductor Particles", in Proc. IEEE 5th Electronics System-Integration Technology Conference (ESTC), Helsinki, Finland, December 16-18, 2014, pp. 1-6.

5. J. Tao, D. C. Whalley, and C. Liu, "Magnetic Deposition of Ni/Au Coated Polymer Core Particles for Flip-chip Interconnection", in Proc. IEEE 15th Electronic Packaging Technology (ICEPT), Chengdu, China, August 12-15, 2014, pp. 409-413.

Chapter 2

Literature Review

2.1 Introduction

The purpose of this literature review is to present the background of ACA materials, identify the current challenges and future prospects for this technology. An overview of electronic packaging technologies using ACA materials was introduced, which includes material and its characterisations, assembly process, interconnections and reliability of ACA assemblies. The chapter presents the review of self-assembly technologies and discussed their potential application in flip-chip packaging area. Emphasis was particularly placed on the introduction of fundamental theories for electrophoretic deposition and magnetic assembly.

2.2 Flip-chip Packaging Review

With the growing demand for high density and low packaging profile interconnections, flip-chip packaging has become increasingly used in the electronics industry. Compared with traditional wire bonding and tape-automated bonding (TAB), flip-chip technology is a face-down process, thereby providing shorter interconnections, lower inductance, higher frequencies, better noise control, higher density, greater number of inputs/outputs (I/O) and allowing future miniaturization of electronic devices [11, 19]. Figure 2.1 shows the size comparison for the same device when employing the flip-chip technology.

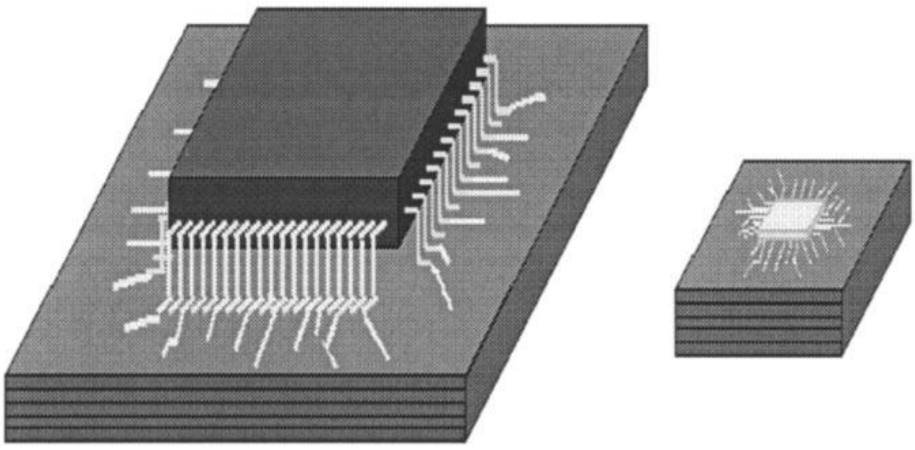

Figure 2.1 Comparison of required package area for an ASIC chip in a QFP160 package for surface mounting and the same ASIC chip for flip-chip ACF assembly [20].

There are various methods of flip-chip interconnections which can be distinguished into two different kinds: metal joint and contacting interconnections [21]. Traditional Controlled Collapse Chip Connection (C4), Encapsulant Solder Connection (ESC), and Gold to Gold Interconnection (GGI) belong to the metal joint group where eutectic interconnection is formed during bonding process. While contacting interconnections is normally comprised of Anisotropic Conductive Film/Adhesives (ACF/ACAs), Isotropic Conductive Adhesives (ICA), and Non Conductive Film/Paste (NCF/NCP) as shown in Figure 2.2.

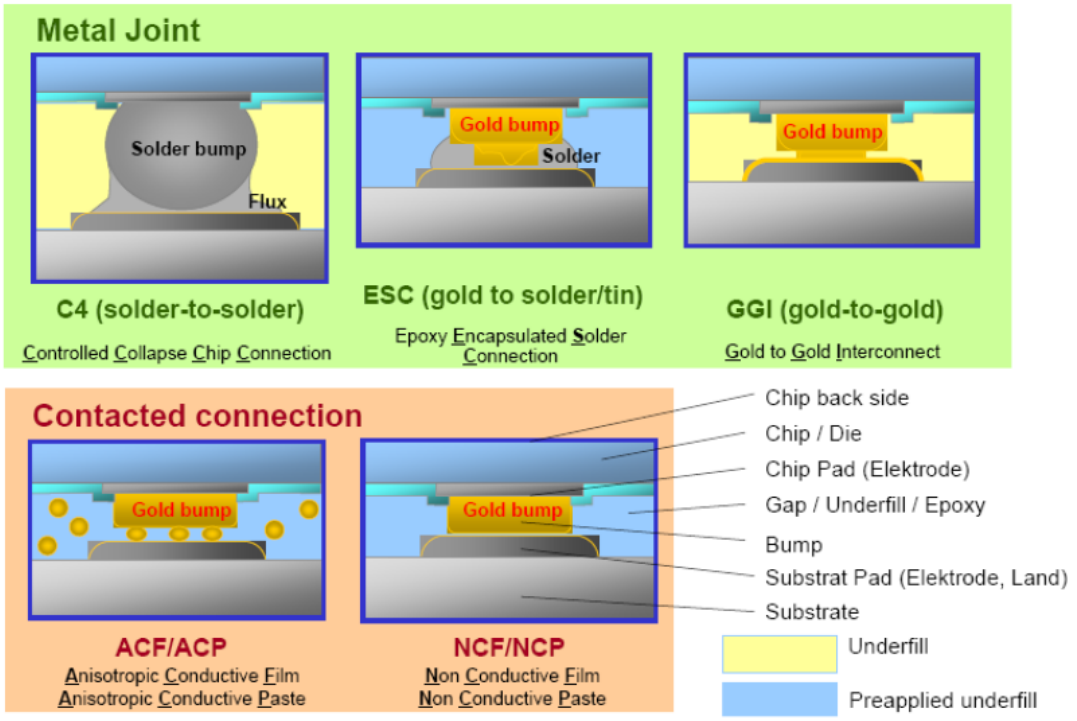

Figure 2.2 Various flip-chip assembly technologies [21].

Nowadays, there is an ongoing demand for electronics devices with more functionality while reducing size and weight, for example smart phones and tablet personal computers. Thus fine-pitch or ultrafine-pitch flip-chip packaging are becoming increasingly indispensable. However traditional FC uses a Controlled Collapse Chip Connection (C4) solder reflow process, which despite its many advantages (including self-alignment, and accommodation of noncoplanarities and warpage), has approached its pitch limitation at 150 μm in high-volume manufacturing because of the difficulty in ensuring short circuits do not occur during reflow [22, 23]. As a consequence, several new interconnection methods are established, which provide a semiconductor package that meets the electrical, thermal, and dimensional requirements of the application [4, 24, 25]. Micro C4 bump was developed by electroplating solder materials instead of conventional stencil method, thus forming solder bumps with finer pitch [4, 7]. Copper pillar bump is also one of the most promising choices for next generation

flip-chip technologly which, because of its limited solder volume on top of the copper pillar and high standoff, provides a more limited collapse of fine-pitch bumps thereby significantly reducing the probability of short circuits during reflow, while still providing the compliance required to achieve satisfactory thermo-mechanical reliability along with higher electro-migration resistance and higher thermal performance [4, 26, 27]. Another interesting novel approach is the insertion flip-chip technique i.e. metallic tubes are inserted in solder lands to perform ultra-fine pitch interconnections. The advantages are that this process is really flux less, low pressure, and room temperature joining process and enables the ultra-fine pitch (≤10μm) three-dimensional (3D) applications [28, 29]. There is also a promising approach, which is the use of metal coated polymer microparticles, similar to those already widely used in anisotropic conductive adhesives, but selectively deposited into the required locations.

2.3 Anisotropic Conductive Adhesives (ACAs)

The purpose of consecutive development of electronic packaging techniques is to increase the packaging density and improve electrical performance, while still maintaining a lower cost and better reliability of the electronic devices. Flip chip microelectronic assembly is a direct electrical connection by facing electronic components down to substrates, circuit boards, or carriers, via conductive bumps on the chip bond pads. ACA is particularly applicable to flip-chip packaging, considering that it consists of electrically conducting particles or metal coated polymer spheres dispersing in adhesive matrix. The advantages of ACA include ease of processing, low curing temperatures, and elimination of flux clean process after bonding, therefore ACA has been widely applied in the electronics industry especially flat panel display assembly and smart cards [8].

With regard to conductive filler loading level, electrical conductive adhesives (ECA) can be categorized into anisotropic conductive adhesives (ACAs), anisotropic conductive film (ACF), and isotropic conductive adhesives (ICA) [8, 30]. As is shown in Figure 2.3, ACA and ACF consist of similar compositions. The difference is that one is in paste form which can be applied by either printing or dispensed, while the film materials are typically supplied in a reel form. There are two kinds adhesive matrix available: thermoplastic and thermosetting. Thermoplastic adhesive has the advantage of reworking ability, which means they are thermally reversible and will melt if re-heated. As a comparison, thermosetting adhesives will permanently become cured once being applied with heat or UV radiation. Due to the stronger chemical interconnection at elevated temperature [31], thermosetting adhesives are more commonly used in electronics packaging nowadays.

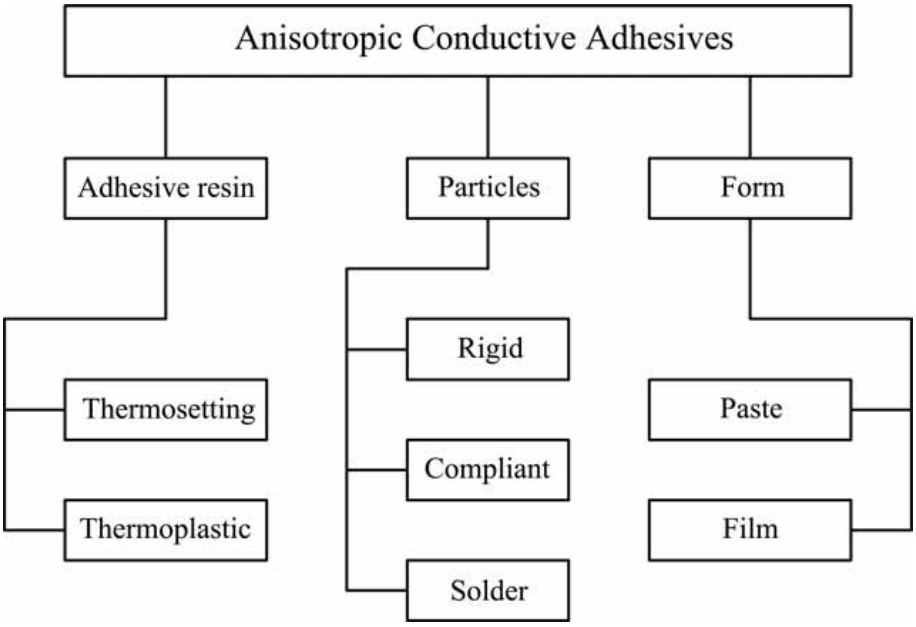

Figure 2.3 ACA types and their typical compositions [32].

There are three types of particles used in electrical conductive adhesives (ECA): rigid particles, compliant particles, and solder particles [30]. The schematics of the joint of single particle system are shown in Figure 2.4 (a) and (b) respectively. The rigid particles also remain the initial shape during assembly due to their relatively high hardness. Silver particles offer low chemical reactivity, moderate cost, and high electrical conductivity [33]. Nickel particles with its lower cost than silver and better thermal stability than copper, becomes one of the most suitable particles for ECA, which also offers the advantage of breaking the oxide layer on the electrodes and suitable for interconnecting easily oxidized metal [34]. Recent applications of solder particles as ACA fillers were reported in [35, 36], where metallurgical joints can be formed connecting the substrate and component through a reflow process. Compliant metal-coated polymer particles is able to provide high interconnection reliability because of the large deformation ability enabling a large contact surface between the particles and substrate during bonding, therefore they are the most widely used conductive fillers. Compliant particles are typically composed of gold and nickel plated polymer spheres, which are the main interest of our project.

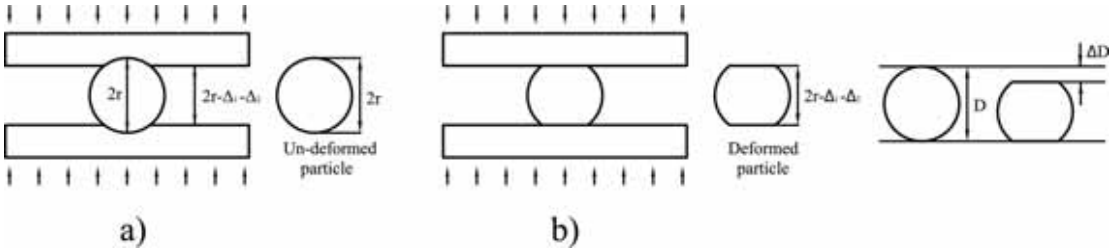

Figure 2.4 Schematics of (a) a rigid particle system; and (b) a compliant particle system [37].

2.4 Assembly Process of ACA

In the ACA assembly process, there are several essential steps identifiable:

• Pre-assembly (dispensing o printing of pastes or placement and tack bonding of film materials);

• Component placement;

• Heating;

• Assembly pressure application;

• Resin flow and particle compression;

• Resin cure;

• Assembly pressure release;

• Cooling

The sequence can be changed as needed, and the steps are also not always discrete. For example heating must take place before pressure release for thermoplastic cooling and is unnecessary for radiation resins [38].

ACA flip-chip packaging process has many advantages [30]:

- Fine-pitch capability, especially when using ACAs for flip-chip;
- The process is extremely simple, flexible, environmental friendly, and low cost with low contraposition accuracy;
- The hot-pressing temperature is low, and the time is short;
- Nonexistence of underfilling requirements;
- High production speed and meet various scale Requirements.

The product approach of roll-to-roll is the most common used method in the flip-chip packaging process of RFID inlay, and Figure 2.5 illustrates an application example of ACA in industry. The process is comprised of material feeding, dispensing, patching, hot-pressing and solidification, testing, and coiling. This kind of roll-to-roll techniques is very suitable for mass production, and the packaged RFID tags will be cut into pieces for subsequently use.

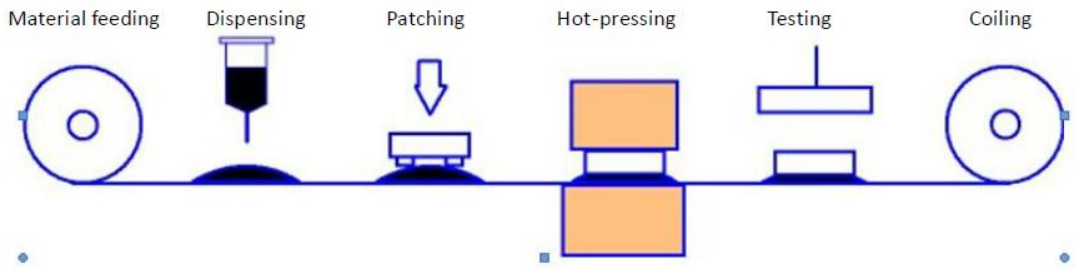

Figure 2.5 Manufacture of an RFID inlay with ACA using roll to roll flip-chip packaging method.

2.5 Reliability of ACA Assembly

Reliability of electronics packaging is a key issue, which needs to be fully considered and deserves much more research so as to achieve a reliable assembly quality. Compare with traditional solder joint, the assembly process with ACAs is much simple and cost-effective. However the reliability in ACA packaging has been a big challenge since the coefficient of thermal expansion (CTE) of joint with ACA is typically larger than that of solder joint. Generally, there are two possible reasons which can potentially increase the contact resistance of ACA interconnection: debonding at anisotropic conductive adhesives joint and corrosion of metallization. The reliability of an ACA joint is affected by various parameters such as bonding assembly process, materials, and environmental factors.

2.5.1 Effects of assembly process

A. Alignment

The assembly process of ACA interconnection includes alignment, bonding, and reflow process (if solder interconnections exist in the same board). Except for the utilisation of solder particles, conventional ACA interconnection lacks the benefits of self-alignment that would allow misplaced chips to be pulled into correct position by surface tension forces of molten solder [39]. Consequently, a stringent requirement on the alignment accuracy is needed during the ACA assembly process, especially for the fine-pitch assembly because the conducting pad size and conductor spacing are becoming increasingly small. Misalignment can be caused by placing effort, bump height variation and lace of flatness of the bump pads [40], uneven assembling pressure, and non-uniformity in thickness of ACA. It can impact the pressure distribution, decrease the contact area for electrical interconnection, increase the possibility of open connection or short-circuits.

B. Bonding Temperature

The bonding temperature and time significantly influence the curing degree of the adhesive which plays an essential role in the reliability of ACA joint [41]. Epoxy resin based ACA is thermosetting material, therefore their structure is highly dependent on the bonding temperature chosen. When temperature increased, the ACA will melt and transform into low viscosity liquid, and finally cross-linkage will performed to form the three dimensional crystallized networks which contributes to its stable physical properties. The cross-link density of ACA is relatively important in determining its reliability performance as reported by Chiu et al. [42]. The bonding temperature have an important effect on the contact resistance, adhesive strength, and thermal stability. It was found that the adhesive strengths increase with the bonding temperature increased; however too high temperature causes over-curing of ACA thus decreases the

adhesive strength [43, 44]

C. Bonding pressure

The bonding pressure is applied to force the conductive particles to contact the flip-chip bump and flexible/rigid substrate forming the conduct path. The deformation of particles plays the predominant effect on the contact resistance of the interconnection. In order to obtain a better electrical conductivity, larger contact area is needed; however, an excessive pressure might induce the fracture of the particle and high compressive stress and internal stress in the epoxy adhesive, thereby degrading the electrical performance [45]. Non-homogeneous bonding pressure can also cause the co-planarity issues, which increases the possibility of poor reliability especially for thin and flexible substrates [46]. Meanwhile, the distribution of particles, which significantly affects the contact performance of the ACA joint, is also determined by the bonding pressure to some extent. It was indicated that the number of conductive particles on bump was decreased along with a decreasing contact resistance when increasing the bonding pressure [47].

D. Curing conditions and reflow process

Theoretically, in order to improve the efficiency, the adhesive can be cured in a short time under high temperature. However high curing temperature usually induces many problems, such as the increased cross-link density and homogeneous heat resistance, shrinkage, cracks, and voids in adhesive materials, which will probably lead to a poor dielectric properties [43],. Some devices have another solder reflow process performed after the ACA bonding. The ability of ACA to withstand multiple solder reflows is a major milestone in its growing acceptance within the semiconductor packaging industry [48, 49]. Because of the higher coefficient of thermal expansion (CTE), the entrapped adhesives matrix tends to expand much more in *z*-direction than the tiny conductive particles during the reflow process. The induced thermal stress will try to lift the bump from the pad and decreased the contact area of the conductive path, leading to an increase of the contact resistance [50, 51]. Therefore, the peak temperature of reflow profile and the distance between the chip and substrate are the most important parameters.

2.5.2 Effects of the properties of components and materials

The height of bumps and pads determines the distance between the flip chip and substrate, which has a direct influence on the joint reliability. It was observed that the electrical resistance and reliability also depends on the distance between the pad and glass fibers in the substrate, and a long distance means a thick layer of soft epoxy, probably resulting in not enough deformation of the conductive particles [52]. The coefficient of thermal expansion between different materials greatly affects the fatigue life of ACA interconnection. Generally, the

interconnection material between chip and substrate should have close CTE value to reduce the thermally induced strain and stress. It was found that an ACA interconnection with lower CTE and high modulus can reduce thermally induced shear strain during the thermal cycling environment and thus increase the overall thermal cycling lifetime of ACA joints [53]. Therefore, optimized ACA properties can enhance ACA package reliability during thermal cycling regime.

2.5.3 Effects of environmental factors

It is well know that the polymer-based ACA interconnection is quite sensitive to moisture sorption, especially at elevated temperature, which is considered as the dominant factor in the ACA flip chip failures [54]. Water can be easily diffused into the adhesive layer, and also penetrated into the interfaces between the adhesive and the substrate/chip leading to a reduction of the adhesive strength and even the formation of micro-cracks [51, 55]. Due to the susceptibility of the resin polymer to hydrolysis and oxidation and the change in the effective average cross-link molecular weight, prolonged hydrothermal aging is very likely to result in irreversible degradation to the epoxy resin system. Meanwhile, most components lack the ability of absorbing the moisture. However the polymeric materials swell upon when absorbing moisture, hence easily leading to the thermal stress and the reduction of contact area. Increasing contact resistance and decreasing adhesion strength after harsh environmental tests were mainly due to the loss of contact by thermal stress effect and moisture absorption, and also partially due to the formation of metal oxide on the conductive particles [45, 50, 56, 57]

2.6 Self-assembly processes

Self-assembly (SA) refers to the process that distributes small discrete components into desired patterns due to direct specific interactions and/or indirectly through the environment, particularly in area of nanoscale manufacturing [58-60]. Benefiting the advantage of spontaneous building blocks into ordered structures, Self-assembly has been identified as one of the most efficient aspect of the bottom-up approaches within a wide areas by ultilising the template or applying external field, such as synthesis and crystallization, robotics and manufacturing, and nanoscience and technology [61]. As shown in Table 2.1, the applications of self-assembly process range at all scales from molecular (crystals) to the planetary (weather systems) scale by exploiting different kinds of interactions. For example N. V. Shestopalov et al. achieved the self-assembly of electrostatic binary monolayer through the temperature-pressure control under isothermal-isobaric conditions [62], and X.F. Ang et al. demonstrated a

method to reduce the Au-Au thermocompression bonding temperature by self-assembly a monolayer of dodecanethiol on the gold surface [63].

Table 2.1 Example of self-assembly (S-static, D-dynamic, T-temperature, B-biological) [61].

System	Type	Applications/importance
Atomic, ionic, and molecular crystals	S	Materials, optoelectronics
Phase-separated and ionic layered polymers	S	
Self-assembled monolayers (SAMs)	S, T	Microfabrication, sensors, nanoelectronics
Lipid bilayers and black lipid films	S	Biomembranes, emulsions
Liquid crystals	S	Displays
Colloidal crystals	S	Band gap materials, molecular sieves
Bubble rafts	S	Models of crack propagation
Macro- and mesoscopic structures (MESA)	S or D, T	Electronic circuits
Fluidic self-assembly	S, T	Microfabrication
"Light matter"	D, T	
Oscillating and reaction-diffusion reactions	D	Biological oscillations
Bacterial colonies	D, B	
Swarms (ants) and schools (fish)	D, B	New models for computation/optimization
Weather patterns	D	
Solar systems	D	
Galaxies	D	

Self-assembly reflects the basic characteristics of the individual components including shape, surface properties, charge, polarizability, magnetic dipole, mass etc., and then utilise these information to determine the interactions among them, design the system to final assemble the components to organized structures. The availability of the movement of the components is the first priority during SA process, and their steady-state positions balancing the attractions and repulsions enables the stability of the suspension, which together ensure the successful proceeding of self-assembly process. Besides there are also many other parameters which play important role, such as the adjustment availability of the assembly environment i.e. fluids phases or smooth surfaces and the equilibration control ability. If irreversible stick occurs between the components when they collide within the suspension, a glass structure will be formed instead of crystal or other regular structures. Self-assembly requires that the components either equilibrate between aggregated and non-aggregated states, or adjust their positions relative to one another once in an aggregate. Figure 2.6 illustrates an example of the successful self-assembly process in molecular system [60]. The DLVO theory [64] is shown in Figure 2.6 (a) describing the particle interaction from a dynamic aspect, which mainly describes the equilibrium relationship between electrostatic repulsion force and van der Waals attraction force. Figures 2.6 (B) and (C) illustrate the essential difference between irreversible aggregation and ordered self-assembly. Components (shown in blue) interact with one another irreversibly from disordered glasses (shown in green). Components can equilibrate, or adjust their positions once in contact, forming ordered crystals if the ordered form is the lowest-energy form (shown in red). Figure 2.11 (d) showed an example of the self-assembly of a protein, an asymmetric catalytically active nanostructure.

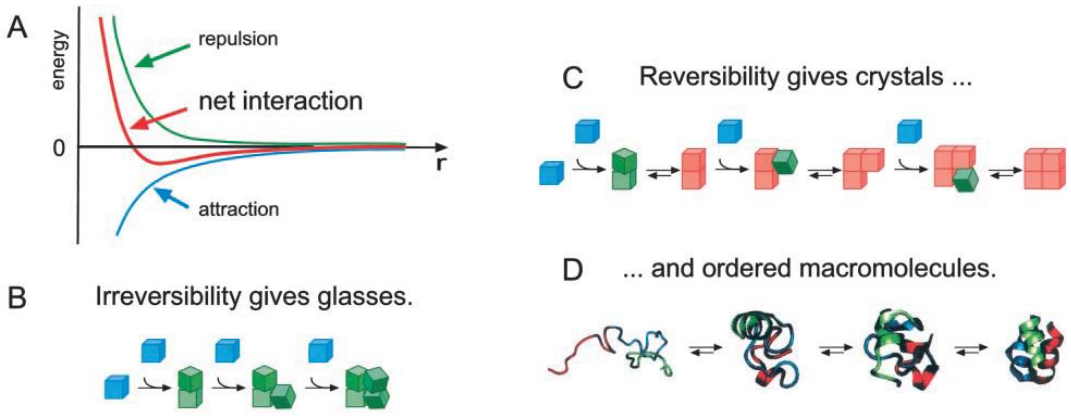

Figure 2.6 Schematic images showing the basic principle of self-assembly [60].

There are different classification standards for the self-assembly process. G. Whitesides et al. divided it into two groups: static self-assembly and dynamic self-assembly, where the difference is that if dissipating energy is the motivation to push the occur of self-assembly [61]. While A. Winkleman et al. classified it with templated self-assembly and non-templated self-assembly [59], and in this review, the same as the definition by M. Grzelczak et al. [58], it is defined into self-assembly by molecular interactions and external field influence.

Chemistry is one of the most commonly used method to create assemblies through the molecular interactions, where the non-covalent or weak covalent interactions are involved such as the van der Waals, electrostatic, and hydrophobic interactions, hydrogen and coordination bonds. As shown in Figure 2.7, there is a wide arrange of applications of self-assembly via molecular interactions including Self-assembly of gold nanoparticles on templates (macromolecules (e); carbon nanotubes (f); block-copolymers (g)) and template-free (particle clustering induced by temperature-sensitive DNA (a, b), two-dimensional superlattices (c), colloidal crystals induced by the light sensitive azobenzens via molecular dipole-dipole interactions (d), self-assembly of nanorods into low symmetry clusters (h), chainlike structures (i) or spherical objectives (j) induced by hydrophobic interactions, and assembly of highly anisotropic carbon nanotubes via H-bonding induced changes in the medium polarity [58]. Recently macromolecular self-assembly is attracting many interest right now, and it refers to the assembly of synthetic polymers, biomacromolecules and supermolecular polymers. The study of the macromolecules include the interaction between polymers and polymers, polymers and small molecules, polymers and molecular aggregates, and polymers and interfaces [65].

While the alternatives ways are developed by utilizing and maximizing the instinctive properties of the particles under external directing fields. In particular, the ratio between the surface area and particle volume decrease extensively when the particles size increase to micro scale level, thus the limited length scale of molecular forces cannot provide enough force and the application of the external field becomes more efficient to direct the assembly the

microscale particles. Electric and magnetic fields are the most common used candidates for the field-directed assembly as well as their combination, and in this chapter electrophoretic deposition and magnetic assembly will be detailed reviewed. Besides, the other fields i.e. flow field [66, 67] and assembly at liquid interfaces[68, 69] are also selected when suitable.

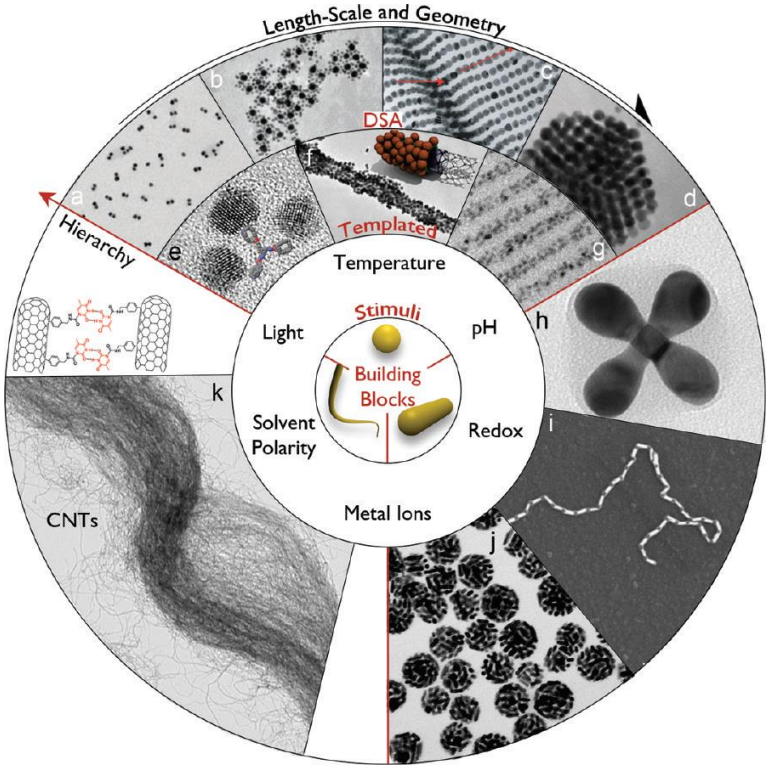

Figure 2.7 Some applications of directed self-assembly by molecular interactions which are classified in terms of aspect ratio (AR), ranging from AR=1 (isotropic, mostly spheres (a-g)) through 1<AR<15 (rod-like (j-h)) to AR>15 (wire (k)).

2.6.1 Electrophoretic deposition

The electrophoretic deposition (EPD) was first observed by the Russian scientist Ruess in 1808 when he found the induced movement of clay particles in water under the applied electronic field. However after more than one hundred years' later, the first successful application of this technique was established to deposit the thoria particles on a platinum cathode as an emitter in USA. Nowadays, the electrophoretic deposition techniques has been attracting increasing interest both in the academic and industrial sector , and also exploited in a wide range of fields, such as advanced ceramic materials and coatings [70], carbon nanotube film [71, 72], polymers [73], oxide nanorods [74], nitrides and glasses [75], continuously graded materials [76, 77] because of its advantages including high versatility and cost-effective process. Nevertheless, the mechanism of the electrophoretic deposition is still not completely clear and under debate right now, and further investigations are required to better understand this process.

In the electrophoretic deposition process, the charged particles suspended in a solution/suspension move towards the opposite charged electrode under the applied electric field, and finally deposit onto the electrode surface. Typically two kinds of electrophoretic deposition are defined depending on the different surface charge of the suspended particle: cathodic EPD refers to the movement of the positively charged particles towards the opposite cathode electrode, while the negatively charged particles will be attracted by the anode electrode, which is named anodic EPD. Various conductive surfaces can be used as the target electrode, such as the flat, cylindrical, membrane or any other conductive structure. Generally, relatively easy control of deposition quality, i.e. the thickness and morphology, can be achieved by simple adjustment of the deposition time and applied potential. Meanwhile, other parameters can also significantly impact the final deposition quality which include the zeta potential of the charged particles, particle size, conductivity and viscosity of the suspension, suspension stability etc. It is worth noticing that sometimes the deposit is just a close packed powder compact and a sintering process is compulsory in order to achieve a fully dense components [78].

2.6.1.1 Electrophoretic vs electroplating

Electrophoretic and electroplating deposition are two different processes, and the obvious difference is that the former is exploited to deposit particle, while the other refers to the ions. Table 2.2 shows the detailed comparison between these two deposition processes.

Table 2.2 Characteristics of electrodeposition techniques [79].

Property	Electroplating	Electrophoretic
Moving species	Ions	Solid particles
Charge transfer on deposition	Ion reduction	None
Required conductance of liquid medium	High	Low
Preferred liquid	Water	Organic

As shown in this table, there is no charge transfer on deposition during the electrophoretic deposition process according to the reference [79], which means that there should be no current flow in EPD. This is also satisfied with Sarkar and Nicholson's theory, where particle/electrode reactions are not involved in EPD [80]. While in Troelstra's experiment, the ceramic particles did not lose charge after being deposited and can be striped when reversing the applied electric field [81], which also provide strong evidence to support this theory. However, a current flow is existing between the electrodes during the electrophoretic deposition process in the latest review organized by Malika Ammam [82].

The current density follows the basic Ohm's law

$$J = kE \tag{2.1}$$

where J is the current density, E is the electric field strength in the suspension, and k is the conductivity of the suspension. A variety of parameters can generate the impact on the final current density, such as the cell constant, the solution conductivity, and interfacial electrochemical kinetics [82]. During the electrophoretic deposition, a current decrease phenomenon with time is observed by some authors as shown in Figure 2.8. The mechanism of the current decrease is not very clear and in debate at the moment.

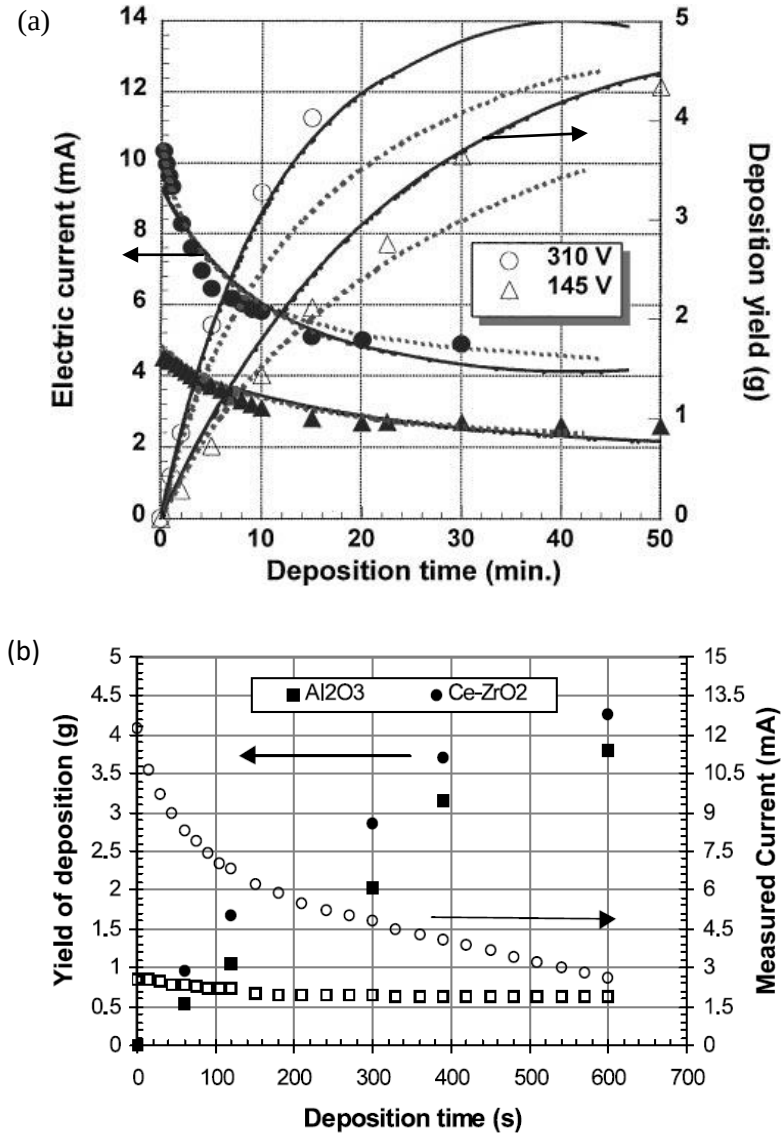

Figure 2.8 the current evolution and deposition yield during the electrophoretic deposition process of a) alumina particles from technical ethanol with 1 M acetic acid [75] and b) ceramic particles Ce-TZP and Al2O3 from an acetone/n-butylamine suspension [78].

2.6.1.2 Zeta potential

Zeta potential, usually ranges at millivolts level, describes the charge develops at the interface between the solid surface and the liquid medium. Four mechanisms of the charge potential have been identified: the dissociation of ionogenic groups of the particle surface, different adsorption of solution ions into the surface region from the liquid, adsorption or orientation of dipolar molecules at the particle surface, and electron transfer between the solid and liquid phase due to differences in work function.

A relatively high concentration of the counter ions are absorbed to the surface of the charged particles, and this layer is defined as stern layer. In the next diffuse layer, a balance between the electrostatic force and random thermal motion determines the ions distribution, and the potential decays gradually with the distance from the particle surface, until reaches to the bulk solution value which is conventionally taken to be zero. This electrical double layer is formed in the particle solid surface-liquid suspension interface as shown in Figure 2.9. In an electric field, each particle and its surrounding ions within the slipping layer move through the solution as a unit, and the potential at the shear surface between the unit and the surrounding medium is defined as the zeta potential.

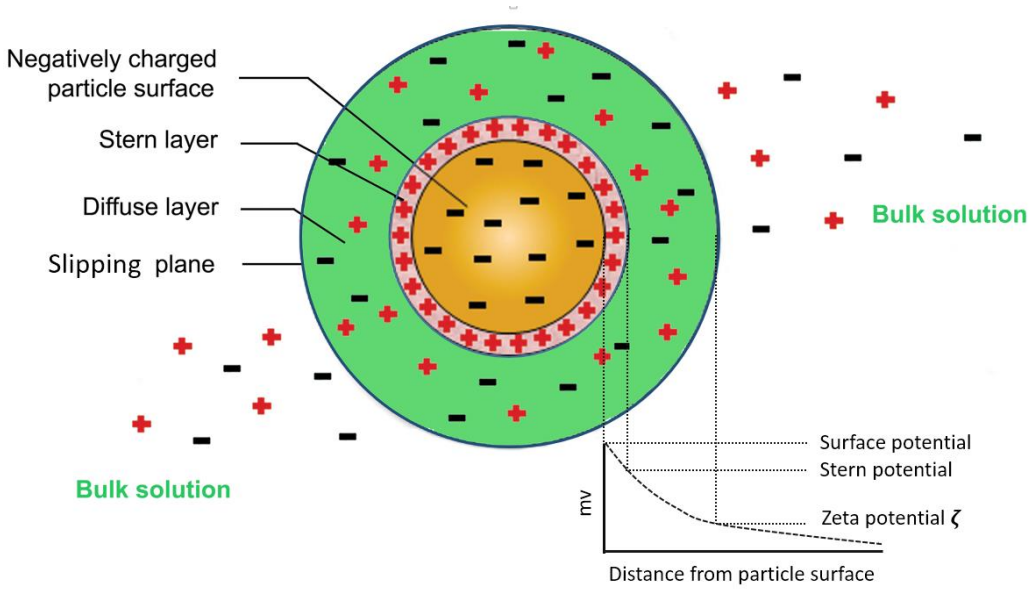

Figure 2.9 Schematic image showing the double layer and the ions distribution surrounding a charged particle and the evolution of the electric potential from the surface potential to zero far from the particle.

Zeta potential is the essential parameter during the electrophoretic deposition, which determines the stability as well as the direction and velocity of the particle migration in the suspension. The intensity of the repulsive and attractive interaction are mainly affected by the electrostatic and Van der Waals, and a high particle charge can create enough electrostatic

repulsion to maintain the stability of the suspension. On the contrary, low charge will lead to the agglomeration even for relative large inter-particle distances, resulting in poor deposition quality like porous or sponge-like structure. Under the applied electric field, the velocity of the particle in the suspension is not determined by the surface charge of the particle but by the net charge enclosed in the liquid medium, which is mainly the zeta potential at the shear surface. Theoretically, a particle with negative surface charge can get a positive zeta potential when the charge of specifically adsorbed ions is higher than the surface charge. Consequently, due to the dominating role of zeta potential during EPD, the particle will be driven to the cathode under applied electric field even with a negative surface charge. Thus it is very important to control the concentration of the solvents and additives in the suspension in order to achieve a proper zeta potential and the subsequent highest possible green deposit density.

The particle net charge or zeta potential can be effected by a variety of charging additives such as acids, bases, or specifically adsorbed ions or polyelectrolytes [83]. Different agents impact the charge magnitude and its polarity by different mechanisms. The pH adjustment of the suspension is one of the most direct and efficient methods to control the zeta potential. Generally, the particle will show no net charge at certain pH based on water suspension, which is called its isoelectric point (IEP) or point of zero charge [84].

2.6.1.3 Particle size

Particles with a wide range of sizes and configurations can be used for electrophoretic deposition, such as gold nanospheres [85], graphene [86], carbon nanotubes [72], and microscale colloidal particles [87]. In order to achieve a homogeneous and smooth deposition, a good dispersion and stability of the particles in the suspension is the first priority for thee electrophoretic deposition. The problem with large particle size is the increasing gravity leading to a tendency of sediment in vertical direction, which may result in a gradient deposit, i.e., thicker deposition on the bottom and thinner on top. Another consideration is the mobility of particle in the suspension. No literature studies the relationship between the particle size and zeta potential, however it is believed that large particle size will significantly decrease the ratio of surface to volume, thus impact the zeta potential. Consequently, the velocity of the particle in the suspension will be reduced because of the possible decreasing zeta potential as well as the increasing flow resistance.

2.6.1.4 Conductivity and viscosity of the suspension

The conductivity of the suspension has a close relationship with the particle mobility, and needs to be carefully controlled in electrophoretic deposition. It is found that the deposit is formed only when the conductivity ranges at a narrow band as proposed by Ferrari and Moreno [88], however this suitable region of conductivity is supposed to be different for different

deposit systems. The conductivity of the suspension depends on the coexisting ions (electrolyte). Under an applied voltage, it is the electrolyte that mainly carried out the electric field as well as the charged particles [89]. On the one hand the particle mobility is very low if the suspension is too conductive, because the thickness of the double layer surround the particle is compressed by the considerable amount of free ions leading to a lower zeta potential [90, 91]. While particle may lose charge and stability with a very low conductivity of the suspension [64].

Meanwhile, the conductivity is also close related to the dielectric constant of liquid. Powers reported that a good deposition rate and quality was achieved only when the dielectric constant was in the rage of 12-25 [92]. Too low dielectric constant results to the deposition failure because of the insufficient dissociation power, whilst a high dielectric constant enables a high ionic concentration in the liquid leading to the reduction of the double layer region size and consequently the electrophoretic mobility. Viscosity of the suspension also impact the deposition quality, and the result shows that lower viscosity provides an easier way to handle the suspension. The viscosity and relative dielectric constant of some solvents are shown in Table 2.3 [93].

Table 2.3 Physical properties of solvents [93].

Solvents	Viscosity(cP)=mPa s	Dielectric constant
Methanol	0.557	32.63
Ethanol	1.0885	24.55
n-Propanol	1.9365	20.33
Iso-propanol	2.0439	19.92
n-Butanol	2.5875	17.51
Ethylene glycol	16.265	37.7
Acetone	0.3087	20.7
Acetylacetone	1.09	25.7

2.6.2 Magnetic assembly

Magnetism is one of the intrinsic features of the nature just like light, water and so on. Due to the specific characterization of magnetism [94], which is invisible and difficult to control, the utilisation of magnetism is usually more complicated. Based on the magnetostatic interaction between the magnetic particles and their behavior under the magnetic field, magnetic field has already been successfully implemented in the biology area for many years, such as the labelling and separation of cells [95, 96], biomedicine[97], and the delivery magnetic therapeutic molecules [97-99] onto target tumour cell or lung cancer cells [98, 100].

Meanwhile magnetic resonance imaging (MRI) has also already been widely applied in the hospitals providing a patient specific and time dependent method for medical diagnosis without exposure to ionizing radiation [101, 102]. These successful applications significantly simplified lots of treatment methods, improved the medical level, and consequently benefit the public's health and life quality.

Some microspheres and nanoparticles display magnetic properties allowing them to be detected and controlled by magnetic fields, which enables the magnetism to be one of promising alternative in the self-assembly area. Magnetic field has already been proved that it can be served as an effective stimulus to precisely control the nanoscale objects [103-105], and the magnetic self-assembly has been successfully implemented in the deposition of colloidal particles [106]. Compared with the irreversible SA processes like electrostatic absorption [107] and electrophoretic deposition of charged particles [108], the magnetic self-assembly method has been regarded as a promising means because of its simple, tunable, and high efficiency advantages [103, 109, 110]. In addition, some applications are established by modulating the external magnetic field resulting in different organization of the magnetic particles, such as the structural collar printing[111], field-responsive color displays[112] as shown in Figure 2.10, and high-resolution magnetic printing [113].

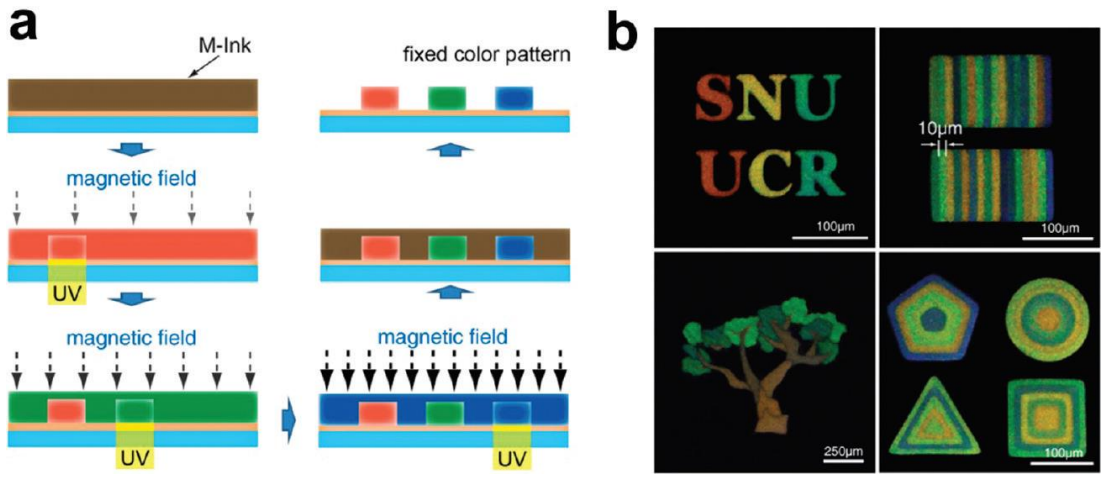

Figure 2.10 high-resolution patterning of multiple structural colors with a single magnetic ink [112]. (a) Schematic illustration of multicolor patterning with a single ink by the sequential steps of "tuning and fixing". (b) High-resolution multicolor patterns prod.

2.6.2.1 Mechanism of magnetic assembly

The external magnetic field is often exploited to precisely control the movement of the particles in the solvent, and it will induce the dipole moment in the particles along the direction of the external field. The essential part of the magnetic assembly is to systematically understand

and control the experienced forces of the particles in the solvent under the applied magnetic field. The two predominate kinds of magnetic induced forces are the dipole-dipole interaction between the particles and the dipole-field interaction between the particles and the external magnetic field.

Under an applied magnetic field of strength $\boldsymbol{H}$, the magnetic induction of the magnetic material is:

$$\boldsymbol{B} = \mu_0(\boldsymbol{H} + \boldsymbol{M}) \tag{2.2}$$

where μ_0 is the permeability of the free space, and $\boldsymbol{M}$ is the magnetization of the material.

Depending on the atomic structure and temperature, most materials shows some magnetic properties to some extent. The volumetric magnetic susceptibility, χ, where

$$\boldsymbol{M} = \chi \boldsymbol{H} \tag{2.3}$$

describes the magnetization induced in a material by the external field $\boldsymbol{H}$. Using SI units, both the magnetization $\boldsymbol{M}$ and applied magnetic field $\boldsymbol{H}$ are expressed in Am^{-1}, and χ is dimensionless. The magnetic susceptibility is the key parameter to classify different magnetic materials. For paramagnets, the magnetic susceptibility is in the range 10^{-6} to 10^{-3}, and it ranges from -10^{-6} to -10^{-3} for the diamagnetic materials. However some materials exhibit ordered magnetic states and have positive susceptibility like paramagnets, and these materials can possess permanent magnetization even without a magnetic field applied, which are called ferromagnets, ferrimagnets, and antiferromagnets. In these materials, the susceptibility is also strongly impacted by the external magnetic field $\boldsymbol{H}$. As shown in Figure 2.16, the M-H curves clearly illustrate the relationship between the induced magnetization and magnetic field for paramagnetic, diamagnetic, ferromagnetic, and superparamagnetic materials.

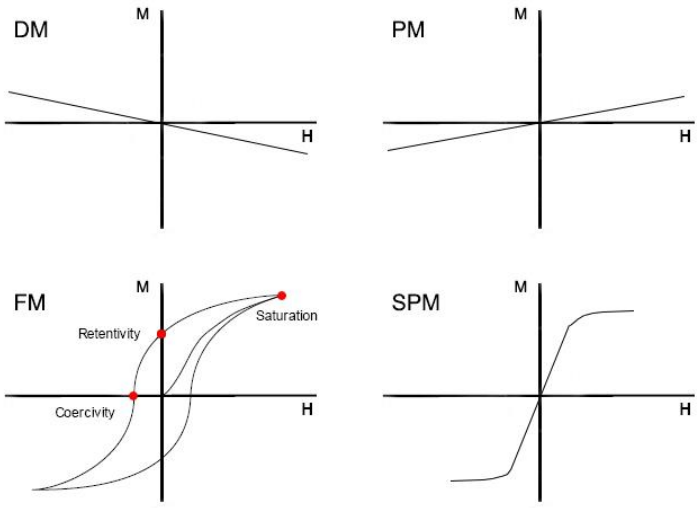

Figure 2.11 Schematic M-H curves of diamagnetic (DM), paramagnetic (PM), ferromagnetic (FM), and superparamagnetic (SPM) materials.

Hysteresis often occurs in the ferromagnetic and ferromagnetic materials, and there are only a few kinds of ferromagnets, and the common ones are iron, nickel, cobalt, and their alloys [94]. As shown in Figure 2.11 (c), this open ***M-H*** curve is called hysteresis loop. Lots of information can be achieved by studying the Hysteresis loop, including the saturation induction, retentivity, coercive force, permeability, and reluctance etc. The retentivity refers to the residue magnetization of the magnetic material, and it reveals the material's ability to retain the magnetic field when removed the external magnetic field after reaching to the saturation point. The difference between the residual magnetism and retentivity is that they are the same when the material has been magnetized to the saturation point, while the value of the residual magnetism may be lower than the retentivity when the external magnetic field did not reach the saturation level.

Nickel is a kind of commonly used material in the electronic packaging as a barrier layer of pad materials, and it is also one of the few ferromagnetic materials. Some research has been conducted to study the magnetic properties of thin nickel film, and this thin nickel film is deposited on glass substrates, which is similar to the structure of Ni/Au particles. The results presented the effect of thickness, ranging from 70 to 300 nm, to the magnetic Hysteresis loops as shown in Figure 2.12.

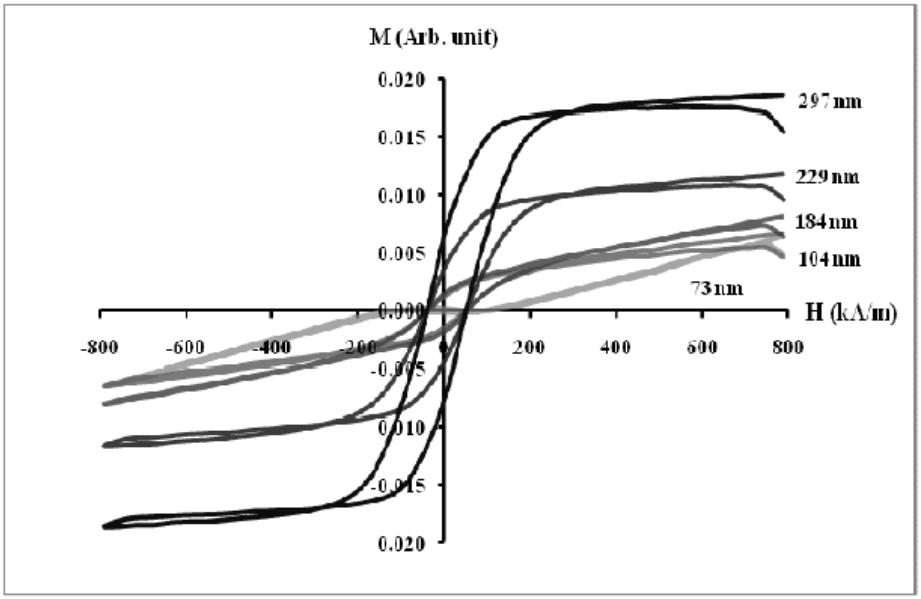

Figure 2.12 Hysteresis loops of nickel films with different thicknesses when applied in the magnetic field in the parallel direction to the film plane [114].

Curie temperature (T_c), sometimes called Curie point, refers to the temperature at which certain materials lose their permanent magnetic properties. The Curie temperature (T_c) of Nickel is 631K, and the relationship between saturation magnetisation and temperature is shown in Figure 2.13. With regard to ferromagnetic materials, increasing the external magnetic

field increases the parallel alignment of atomic magnetic moments, thus the magnetization of

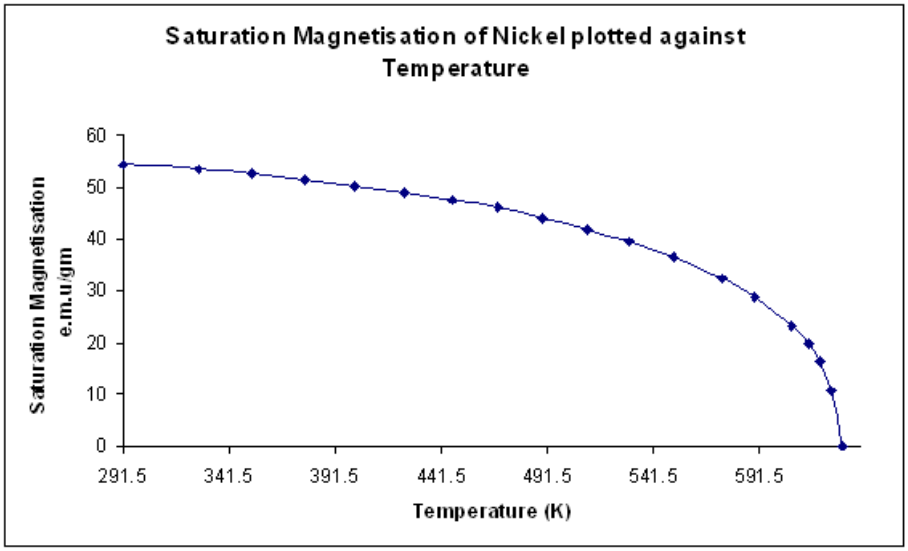

Figure 2.13 Variation of saturation magnetisation with temperature for Nickel [115].

the material increases. While the temperature of the material increases, the alignment is distributed by thermal motion, which results in a decreasing magnetization of the material. When the temperature is higher than its Curie temperature, the spin-spin forces lose its ability to maintain the alignment of magnetic moents and the materials lose its magnetic properties. When temperature reaches T_c, the ordered intrinsic magnetic moments change and become disordered, and this property provides the possible method of demagnetisation of the nickel after the magnetic self-assembly process to ovoid the potential influence of the magnetism to the electronic devices.

2.6.2.2 Magnetic dipole-dipole interaction force

Regarding to the magnetic particles under applied magnetic field, the induced magnetic dipole moment in a superparamagnetic particle is **m** along the direction of external magnetic field, and it can be described as:

$$\boldsymbol{m} = \boldsymbol{M}V \tag{2.4}$$

where V is the volume of the particle .

The interaction energy of two magnetic dipoles with dipole moments $\boldsymbol{m}_1$ and $\boldsymbol{m}_2$, often called Keesom Energy, can be derived as:

$$E_{\boldsymbol{m}_1\boldsymbol{m}_2} = \frac{1}{4\pi\mu}\left[\frac{\boldsymbol{m}_1\boldsymbol{m}_2 - 3(\boldsymbol{m}_1\cdot\boldsymbol{e}_r)(\boldsymbol{m}_2\cdot\boldsymbol{e}_r)}{l^3}\right] \tag{2.5}$$

where μ is the medium permeability, l is the distance between two magnetic dipoles, and $\boldsymbol{e}_r$ is

the unit vector of the centre line of the two magnetic dipoles. When the magnetic moments of two magnetic dipoles are the same ($\boldsymbol{m}_1 = \boldsymbol{m}_2$), the energy can be simplified as:

$$E_{mm} = \frac{|\boldsymbol{m}|^2 (1 - 3\cos^2\theta)}{4\pi\mu l^3} \tag{2.6}$$

where $\boldsymbol{m}$ is the magnetic dipole moment, θ is the angel between the direction of external magnetic field and the particles connection line of two magnetic dipoles, which ranges from 0 º to 90 º. The dipole force acted on one particle induced by the other one can be expressed as:

$$F_{dd} = \nabla E_{mm} = \frac{3\left(1 - 3\cos^2\alpha\right)\mu^2}{4\pi l^3} \tag{2.7}$$

From this equation, it is clear to see that the dipole-dipole interaction force depends much on the angle α, and it is attractive when $0 \le \theta < 54.09°$ and repulsive when $54.09° < \theta \le 90°$ derived from the force calculation. Therefore, the dipole-dipole interaction force between two particles is attractive along the external magnetic field and repulsive in the direction perpendicular to the magnetic field. Under modulated external magnetic field, the dipole-dipole attraction force can drive the particles self-assembled into the one-dimensional chain-like structures when it is strong enough to overcome the thermal fluctuation. The interparticle attraction can be balanced by the long-range repulsion, such as the electrostatic force, leading to a dynamic force equilibrium. Le He et al. conducted a simulation to analysis the configuration of magnetic particles under external magnetic field, and as shown in Figure 2.14 the results clearly illustrate the magnetic dipole-dipole forces between the particles which supports the fundamental theory study [111]. The theory and equations about the magnetic dipole-dipole interactions will be used to explain the movement behaviours of Ni/Au-MCPs under external magnetic field, i.e. the Ni/Au-MCPs particle chains.

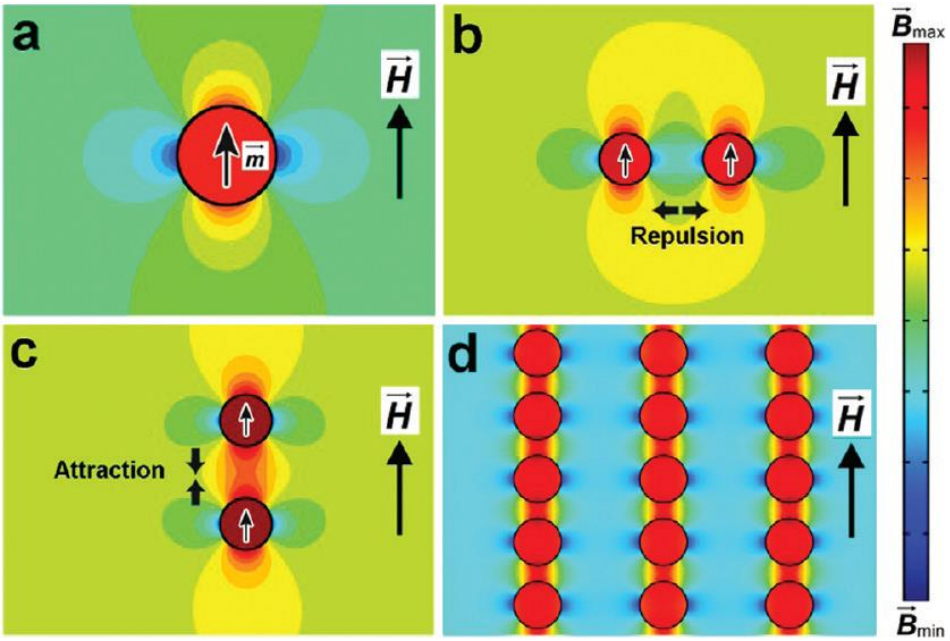

Figure 2.14 Interactions within the particles under external magnetic field (a) the magnetic dipole moment of the superparamagnetic particle in the external magnetic field distribution. Different angle α generating to different dipole-dipole interaction forces: (b) repulsive, and (c) attractive dipole-dipole force. (d) particle structure under the applied magnetic field [111].

2.6.2.3 The dipole-field parking force

Dipole-field force describes the interaction between the particle and external magnetic field, which is also called parking force. The interaction energy of a magnetic dipole $\boldsymbol{\mu}$ in an external magnetic field $\boldsymbol{H}$ can be expressed as

$$E_{df} = -\boldsymbol{\mu} \cdot \boldsymbol{H} \tag{2.8}$$

So the parking force induced by the gradient of the magnetic field can be calculated as

$$F_{df} = \nabla(\boldsymbol{\mu} \cdot \boldsymbol{H}) \tag{2.9}$$

This force causes drives the particles toward the regions with the maximum magnetic field strength and forms a particle concentration gradient or crystallization.

2.6.2.4 Magnetic assembly of nonmagnetic particles

There are only several kinds of ferromagnetic materials. Similarly, the magnetic particles belong to the minority part, and large percentage of particles are nonmagnetic ones. Therefore, the application areas will be significantly expanded if the efficient magnetic assembly strategy can be carried out using nonmagnetic particles. Some literatures have already shown the some successful applications of the magnetic assembly with nonmagnetic particles [105, 106, 111]. Figure 2.15 illustrates an example of magnetic assembly process using nonmagnetic particles and nonmagnetic pad. The energy “holes” is successfully created within the pad areas benefiting the medium ferrofluid under the controlled external magnetic field, and the

nonmagnetic particles were parked on the pad surface after the evaporation of the ferrofluid. Most materials in the electronic packaging area are non-magnetic, and this kind of application has a strong potential in the area of fine or ultra-fine pitch flip-chip interconnection.

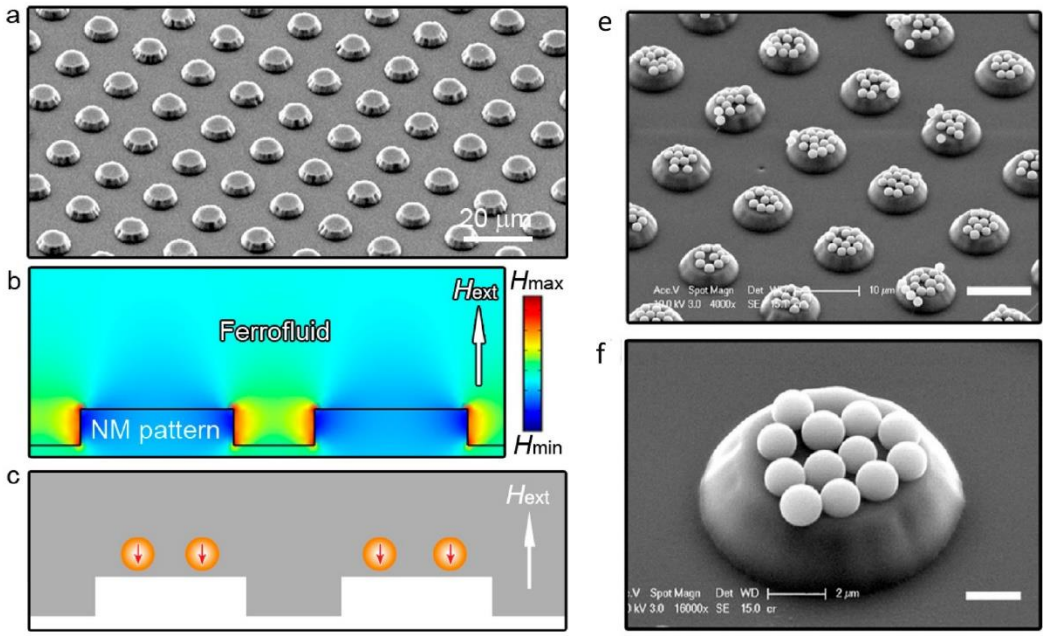

Figure 2.15 Magnetic assembly and patterning of nanoscale nonmagnetic particles [106]. (a) SEM image of a typical cone frustum type polyurethane pattern. (b) Stimulated cross-sectional magnetic field distribution around the nonmagnetic pattern immersed in a magnetized ferrofluid. Scheme (c) and SEM image (e)(f) of the assembly morphology of nonmagnetic particles on the nonmagnetic patterned surface.

The essential part is to employ the ferrofluids as media to disperse the nonmagnetic particles, where the nonmagnetic particles behaves as magnetic "holes" under external magnetic field. Ferrofluids were first developed as a method to control the fluids in space by Stephen Pappell at NASA in the 1960s, and then widely used in many areas such as electronic devices, mechanical and materials engineering, spacecraft propulsion, and medical areas. Ferrofluids are colloidal suspensions of nano-sized ferromagnetic particles in a magnetically inert liquid, which is composed with three parts: carrier, surfactant, and magnetic particles [116]. The magnetic moment of the nonmagnetic particle can be calculated as equal to the total moment of the displaced ferrofluid but in the opposite direction of the magnetic field, which is

$$\boldsymbol{\mu} = -V_{\chi eff}\,\boldsymbol{H} \tag{2.10}$$

where V is the volume of the nonmagnetic particle, χ_{eff} is the effective volume susceptibility of the ferrofluids, and $\boldsymbol{H}$ is the local magnetic field strength. The interaction

between the nonmagnetic particles equals to the dipole-dipole interaction between the magnetic holes, which has the same interaction force with the real moments and drives the nonmagnetic particles forming the chainlike structures under strong external magnetic field. However, the dipole-field parking force drives the nonmagnetic particles to the regions with the minimum magnetic field strength. This application extremely expand the area of the magnetic assembly, because most particles and pads are nonmagnetic material and only very limited are superparamagnetic or ferromagnetic materials.

2.7 Current Challenges and Thesis Tasks

Flip-chip processes utilising anisotropic conductive adhesives (ACAs)/anisotropic conductive films (ACFs) have been successfully applied in liquid crystal display (LCD) interconnection for more than two decades. However no significant improvement has been developed in these year. The conflict between the need for a high particle density, to improve the conductivity, without increasing the probability of short circuits has remained an issue since the initial utilisation of ACAs/ACFs for interconnection. Especially there is an ongoing demand for electronics devices with more functionality while reducing size and weight, for example smart phones and tablet personal computer. This conflict issue is becoming even more severe and needs to be solved to overcome the challenge of ultra-fine pitch interconnection.

Several processes have already been developed to better the benefits of ACAs by increasing its fine-pitch capability while decreasing the percentage of short circuits. For example, Lee et al. reported a novel ACF incorporating the conductive particles into a nano-fibre matrix as shown in Figure 2.16 [117]. Ultra-fine pitch chip-on-glass (COG) interconnection was achieved using these nanofiber ACFs, because the nano-fibres limited the mobility of the conductive particles preventing them from flowing out from the pad areas during the assembly process. However, although the particle capture ratio increased significantly as compared with conventional ACFs, around 40% of the particles were still not captured by the pads and were dispersed between adjacent pads after bonding, and the issue of short circuits therefore still exists.

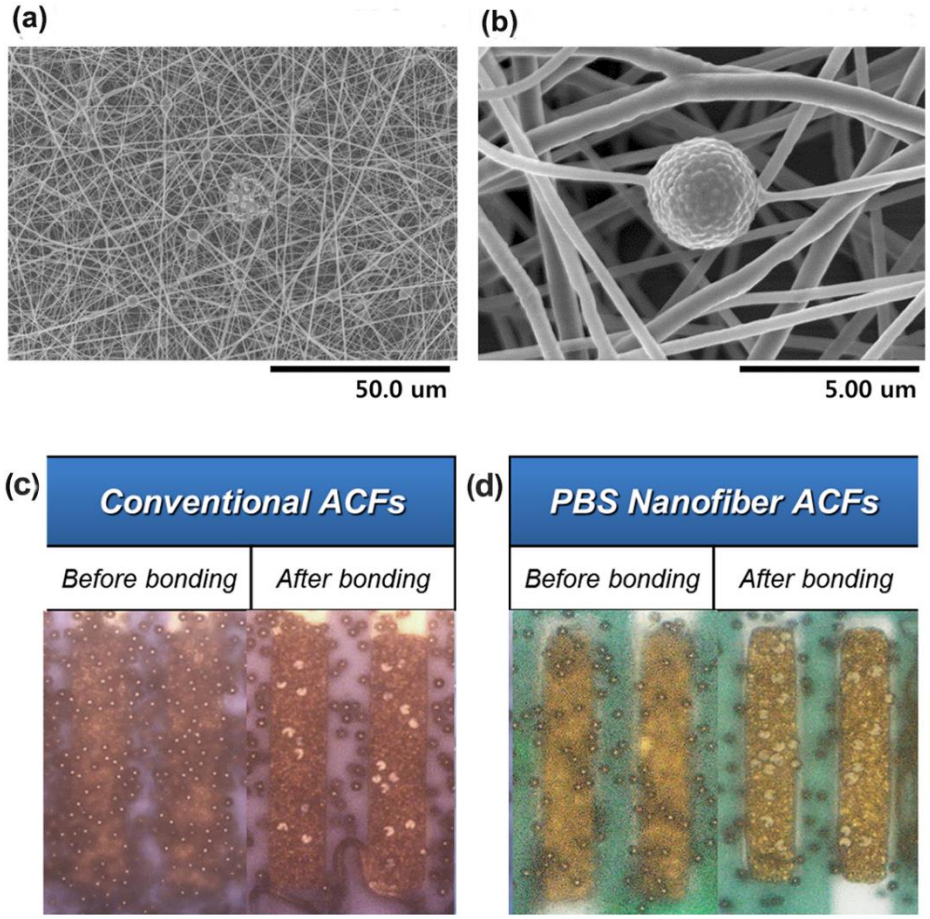

Figure 2.16 SEM images showing different magnification of nanofiber incorporated conductive particles (a) and (b), and the bonding results comparison between conventional ACFs and PBS Nanofiber ACFs [117].

As shown in Figure 2.17, Jia et al. developed a particle on bump (POB) technique [118]. In this process, the bumps have deposited onto them a thin layer of tin. Au coated polymer core particles are then deposited onto the top surfaces of the tin coated bumps and then fixed in place on the bump by a reflow soldering process. A typical result is shown in Figure 2.24. Finally thermocompression bonding onto the substrate completes the interconnection. This method enables selective deposition of the particles and a good conductivity due to the resulting Au-Sn intermetallic interconnection between the particle and pad surface. However the problem is that a reflow process at a minimum of 220°C is needed to form Au-Sn intermetallic compounds between the gold surface of the particles and tin bump. This temperature through the reflow process may damage the particle core or the organic substrate and also increases the complexity of this new method. Meanwhile the particle deposition system is very complicated and only achieves a limited density of the particles on the bump surface.

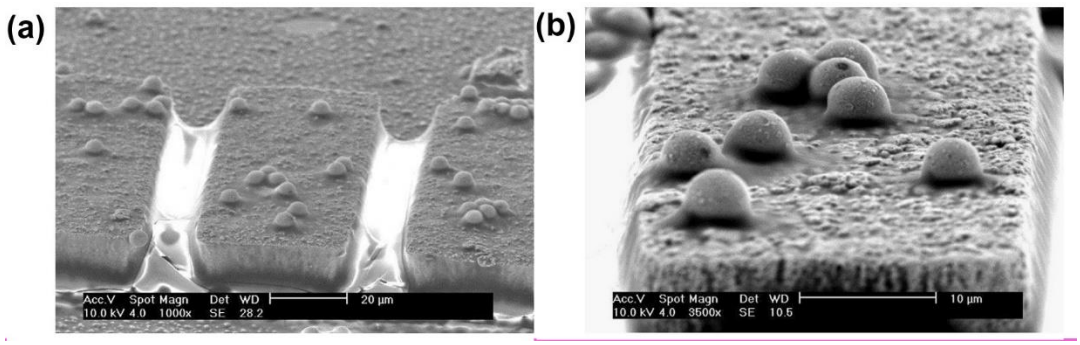

Figure 2.17 Particle on bump structure after the reflow process showing the intermetallic connection between conductive particles and bumps at different magnifications [118].

Therefore novel approaches are still needed to overcome the conflict issue which the traditional packaging using ACAs/ACFs faces. Self-assembly methods are attracting increasing interest nowadays because of its advantage of spontaneous building blocks into ordered structures. In particular, electrophoretic deposition and magnetic assembly have already been employed in various areas using micro-scale particles, but very limited literatures are found in the application of self-assembly in the area of electronic packaging.

The vast application of mono-sized polymer particles and Ni/Au coated particles, such as electronic packaging technologies and solar cell assemblies has made it indispensable to investigate the mechanical properties of such particles. However due to the extremely small size of ACA particles (<10 μm), it is very difficult to systematically study the deformation behaviours of the particles, and many mechanical characterisations of individual ACA particles are still unknown and not clear, such as its viscoelasticity of polymer core, the crack propagation and fracture patterns, and the mechanisms underneath. These have therefore been identified as the main topics for my Ph.D research presented in this thesis. Experiments on the mechanical characterisations of individual polymer particles and Ni/Au coated polymer core particles needed to be performed in this research project. Whilst, experiments were also demanded to study the possibility of self-assembly process i.e. employ electrophoretic deposition and magnetic assembly in the application of flip-chip packaging area using Ni/Au coated particles.

Chapter 3

Mechanical Characterisation of Individual Conductive Particles

3.1. Introduction

As discussed in the previous chapter, conductive microparticles have been utilised industrially for more than two decades. However the assembly process parameters in application such as ACAs are still heavily based on experience instead of scientific analysis. Although some previous research has been conducted to study the properties of individual particles, systematic study of the fundamental viscoelastic characteristics of the polymer core have not been reported and their fracture behaviour is not clear. This chapter describes the materials, equipment and experimental procedures used for the study of mechanical characteristics of both individual pure uncoated polymer particles and Ni/Au-MCPs. The polymer core of the particle plays has the primary role in determining the mechanical deformation process of the Ni/Au-MCPs, Tests were therefore carried out to investigate the properties of the pure polymer particles without the influence of the metal coating layer. The test included individual pure polymer particle compression experiments at different loading rates and strain rates. The metal coating layer on the particles determines their conductivity. Studies of the crack pattern and fracture morphology were also performed and presented in this chapter. In-situ compression experiment where the particles are compressed while being observed in an SEM for the first time enables the direct observation of crack propagation, and the results provides meaningful practical value for the industrial world. Finally finite element analysis (FEA) was performed to better understand the deformation behaviour of the particles under compression by analysing the viscoelastic behaviour of the polymer core and the stress distribution within the metal coating layer.

3.2. Materials

3.2.1. Particles

The particles used in the experiment were supplied by Conpart AS. The Ugelstad method is employed during the particle fabrication process, and this two-step activated swelling process creates the possibility to tightly control the size and size distribution of micro-sized polymer particles [119]. The coefficient of diameter variation of the particles fabricated using this

method is at very low, so that the particles are ideal to meet the planarity requirement for fine and ultra-fine pitch flip-chip applications. These polymer core particles consist of a highly cross-linked copolymer of acrylate and diacrylate, and its viscoelastic properties enables the particle to withstand large deformations. The metal coating layer provides the electrical conducting medium within the interconnection. Schematic images of the particls are shown in Figure 3.1. All kinds of particles used in this project are illustrated in Table 3.1: Type I and Type II are small particles with a polymer core diameter of 4.66 μm and 4.78 μm, and Type III has a 9.8 μm diameter core. These polymer cores are coated with layers of electroless nickel and immersion gold of different thicknesses.

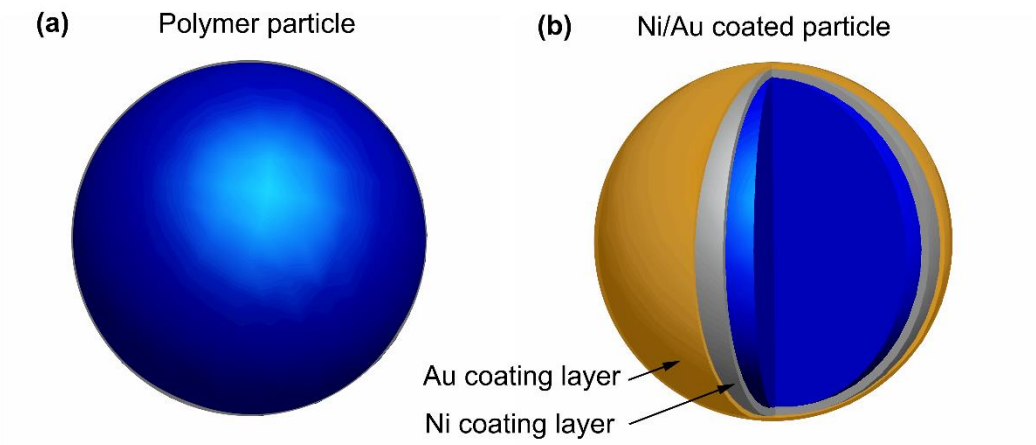

Figure 3.1 Schematic image of (a) a polymer core particle and (b) a typical metal coated polymer core particle.

Table 3.1 Table showing the constitution of the two types of particles used in this work.

	Polymer core diameter (μm)	*Percent in Volume/ Mass*	*Electroless nickel coating thickness (nn)*	*Percent in Volume/ Mass*	*Immersion gold coating thickness (nm)*	*Percent In Volume/ Mass*	*Density (g/cm^3)*
Type I	4.66	90.93% 51.16%	100	5.98% 23.03%	50	3.09% 25.81%	1.79
Type II	4.78	95.14% 66.47%	50	3.02% 14.42%	30	1.08% 19.11%	1.86
Type III	9.8	95.55% 69.20%	100	2.95% 14.65%	50	1.50% 16.15%	2.31

3.3 Experimental Methodology

3.3.1 Flat Punch Methodology

Due to the small size of the particles (5 μm -10 μm), universal testing machine is beyond its limitations to conduct the stress-strain tests for the particles. Flat punch methodology has been therefore developed to study the mechanical characteristics of individual particles utilising the nanoindentation system. Instead of the commonly used pyramidal geometry tip for the hardness test, the diamond tip was cut into a flat-end surface, enabling the investigation for individual micro-sized particles. The diamond material of tip is very hard, and also able to maintain a flat surface with low static friction coefficient so as to minimise the influence on the measurement. The experiment setup is shown in Figure 3.2 (a). Before experiments both diamond tip and silicon substrate were carefully cleaned by acetone to remove any residues e.g. dust or external impurities. The particles were dispersed into isopropyl alcohol (IPA) solution first, then placed on the silicon substrate. The quick evaporation of IPA left individual particles alone on the silicon substrate for subsequent test. As shown in Figure 3.2 (b), a three-step load or displacement function was applied including the linear loading, unloading, and peak holding stage.

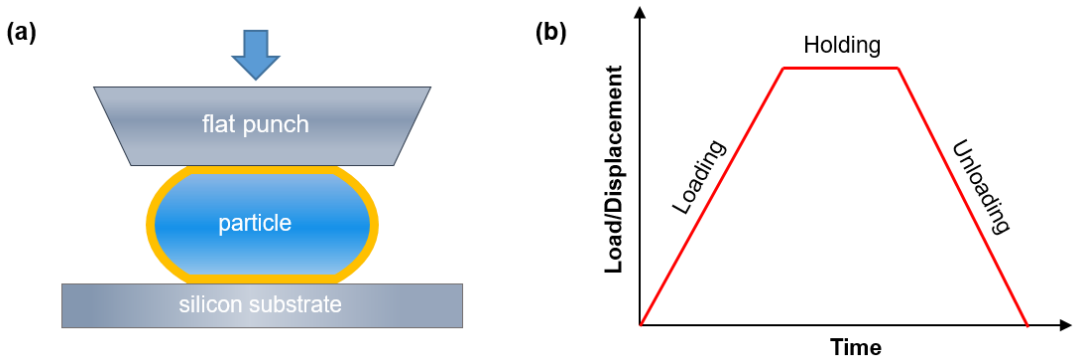

Figure 3.2 : Flat punch methodology (a) schematic image of the individual particle compression test, and (b) the applied load/displacement function.

3.3.2 Loading Rate Controlled Nano-mechanical Tests

The loading rates experiment was conducted by Dr. Jianying He at Norwegian University of Science and Technology, and the results were shared with this research project. The apparatus used was the Hysitron TI 950, which is illustrated in section 3.3.5. There are two kinds of particles used in this experiment, which are 3.0 μm acrylic copolymer particles and 3.8 μm Ni/Au coated on acrylic polymer core particles. The polymer in both kinds of particles is 40% acrylic strongly crosslinked with 60% diacrylic, and the coating thickness of nickel and gold is

50 nm and 30 nm respectively. Different loading rates 0.02, 0.2, and 2 mN/s were applied to test the mechanical characterisation of both kinds of particles. The nanoindentation recorded the contact load displacement curve during the compression test. Due to specific manufacturing process, the particles have a homogeneous materials microstructure and uniform size, and, several replicated tests on each of the different types of particles were also conducted. As a consequence, the results are reliable and indicate the properties of the particles correctly.

3.3.3 Strain Rates Controlled Nano-mechanical Tests

During the loading rates experiment, the force control mode used ensured that the Nanoindentation tip in keeps a relative good following effect by continuously touching the particles surface during deformation. However displacement control mode for strain rates experiments have been more commonly used in studies the properties of viscoelastic materials, and most constitutional equations are based on the strain rate experiments. The strain rate effect experiments were therefore carried out in the Center for Advancing Materials Performance from the Nanoscale (CAMP NANO) in Xi'an Jiaotong University, using the TI 950 TriboIndenter. The particles used for strain rates effect experiments are 4.66 um polymer core particles and Ni/Au coated particles with the coating thickness of 100 and 50 nm, respectively. Four different strain rates were applied for both kinds of particle and all at room temperature ranging over several orders of magnitude (0.004 μm/s, 0.04 μm/s, 0.4 μm/s, to 4 μm/s). The resulted force-displacement data were analysed to identify the viscoelastic characterisations of the polymer core and Ni/Au coated particles.

3.3.4 In-situ Nanomechanical Controlled Nano-mechanical Tests

The recovery ability of the polymer core determines that of Ni/Au coated polymer particles, and the later significantly impacts the contact area of the particle when in an assembly and therefore the final electrical conductivity. However the appearance of cracks or failure dramatically reduces the recovery ability of the particles. The in-situ nanomechanical system, combining the PI 87 SEM PicoIndenter with the electron scanning microscope beam within FIB, is perfect to examine the crack propagation and fracture mechanism of the particles under compression, which is illustrated in section 3.3.5. The maximum load force for the PI 87 is around 25 mN, which is supposed to be higher enough to crush the particles. While the scanning electron microscope (SEM) in FIB enables the in-situ observation and video recording so that detailed analysis can be performed subsequently. Compared with the compression test using TI 950 TriboIndenter with parallel silicon substrate and diamond tip surface, the silicon substrate was tilted at a small angel (3 °) so that the target particle can be easily found and not be covered by surrounding particles during the video recording process by the electron scanning

microscope beam. Both the polymer particles and Ni/Au coated particles were tested using this in-situ nanomechanical system. Four different strain rates as with the tests by Nanoindentation were applied, so as to get a better understanding of the mechanical properties of the particles under compression, especially the crack propagation and fracture mechanism.

3.3.5 Apparatus

3.3.5.1 Hysitron TI 950 TriboIndenter

In this chapter the experimental research was accomplished by using TI 950 TriboIndenter fabricated by Hysitron as shown in Figure 3.3. This system is developed as an automated, high throughput instrument to support the numerous nanomechanical characterization techniques. TI 950 provides both load and displacement control, allowing the operator to perform nanoscale creep and stress relaxation studies with superior control over tip-sample contact conditions.

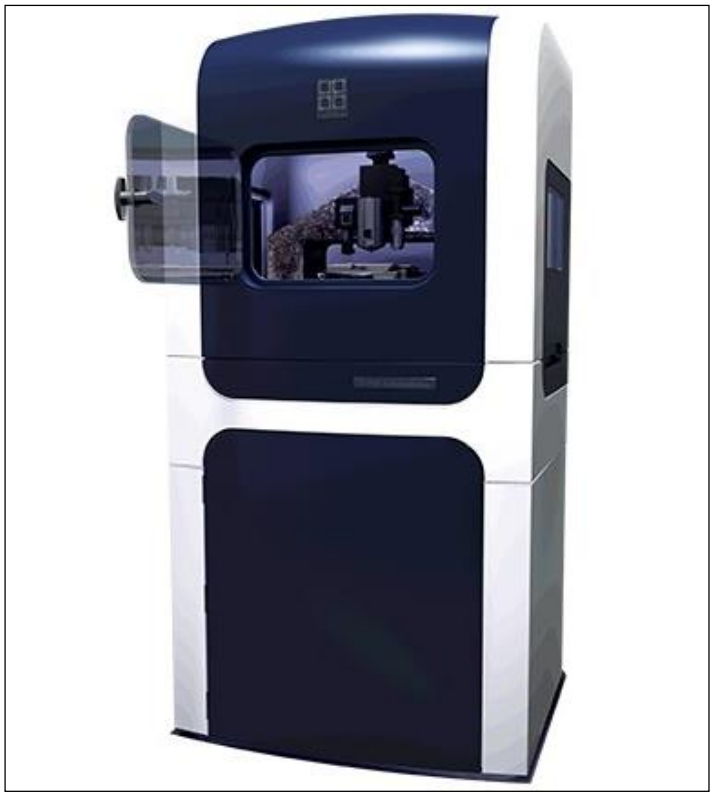

Figure 3.3 Hysitron's TI 950 TriboIndenter (https://www.hysitron.com/products-services/standalone-instruments/ti-950-triboindenter).

The sample stage is horizontal and the indenter tip is perpendicular to the sample stage as shown in Figure 3.4. The sample stage can travel in the *x* and *y* directions with an encoder resolution of 500 nm. The resolution in Load mode and Displacement mode is <1 nN and <0.02 nm, respectively, while the noise-floor performance is at unprecedented levels of < 30 nN in Load and <0.2 nm in Displacement.

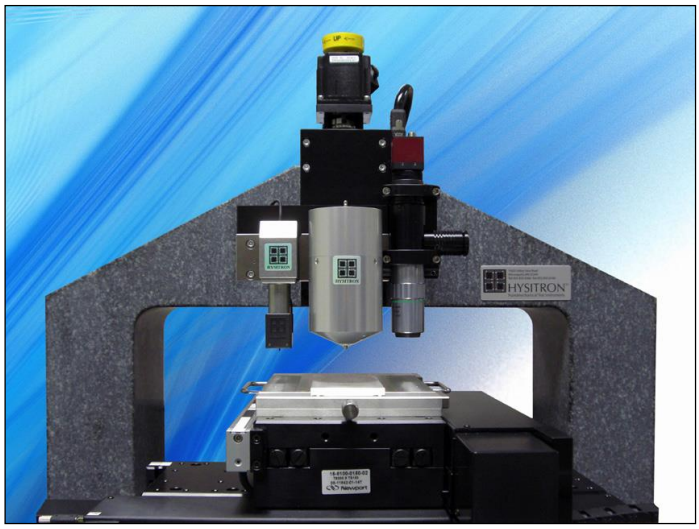

Figure 3.4 Main working station of TI 950 TriboIndenter.

3.3.5.2 Hysitron PI 87 SEM PicoIndenter

The Hysitron TI 950 TriboIndenter offers extremely high resolution load and displacement control. However the samples can only be observed and compared before and after the text, and the behaviour within the compression process cannot be seen. The Hysitron PI 87 SEM PicoIndenter, as shown in Figure 3.5, is a depth-sensing mechanical test instrument which can be incorporated within a Scanning Electron Microscope (SEM) or Focused Ion Beam (FIB) system. This system performs quantitative nanomechanical testing while simultaneously observing the results by SEM.

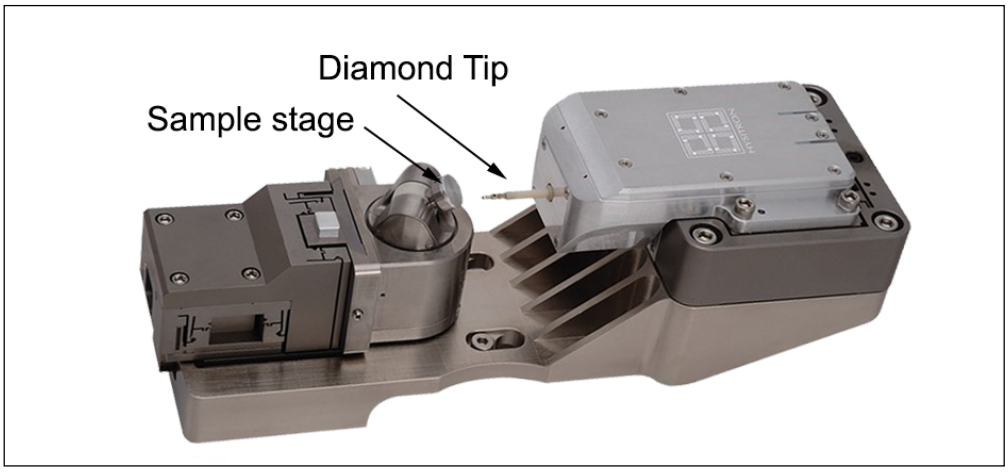

Figure 3.5 Hysitron PI 87 SEM PicoIndenter with five degrees of freedom sample stage (https://www.hysitron.com/products-services/instruments-for-microscopes/pi-8x-sem-picoindenter).

The Hysitron TI 950 is very suitable for studying the mechanical properties of samples e.g. the viscoelastic characteristics. While the PI 87 enables the in-situ observation so that it is ideal for characterizing fracture onset and crack propagation and delamination. The nanomechanical testing with SEM provides unique insights into material behaviour mechanisms. More importantly, the stage can provide five degrees of freedom (X, Y, Z, rotation, and tilt), which ensures that additional detectors (EBSD,EDS, WDS, etc.) are accessible for advanced analysis before, during, or after the mechanical test as shown in Figure 3.6. For example, through a simple 90 ° tilt, the sample can be directly aimed at the e-beam for top-down imaging. Furthermore, all the analysis can be accomplished without taking the samples out and exposing them to atmosphere, so as to avoid potential oxidation of certain materials. This in-situ system saves valuable time on the microscope and reduces analysis time as compared to conventional means. Compared with the TI 950, the PI 87 is a compact design which can be easily mounted onto a SEM/FIB stage. However, the force noise floor performance is significantly worse at <400 nN for force and < 1 nm for displacement. And the achievable noise floor can also be impacted by the SEM environment.

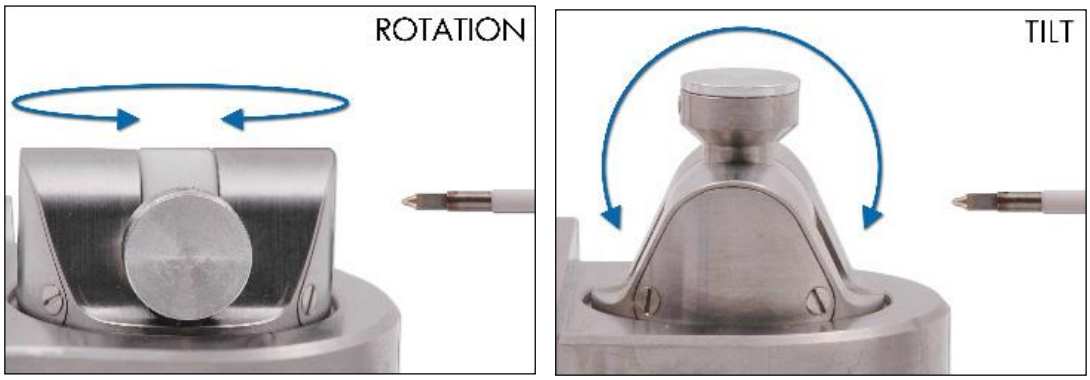

Figure 3.6 : Rotation and tilt of the stage to access an ion beam or various detectors (EBDS, EDS, WDS, etc.).

3.4 Experimental Results

3.4.1 Results and Analysis for Loading Rate Controlled Nano-mechanical Tests

The results were shared by Dr. Jianying He for this research. The force-displacement relationship for 3.0 μm acrylic particles is shown in Figure 3.7 [120]. It can be seen that the fracture load, where the displacement increases suddenly, is sensitive to the loading rate. The analysis of these results to determine the stress-strain relationship, fracture stress and strain, loading rates hardening, and fracture energy are discussed in this section.

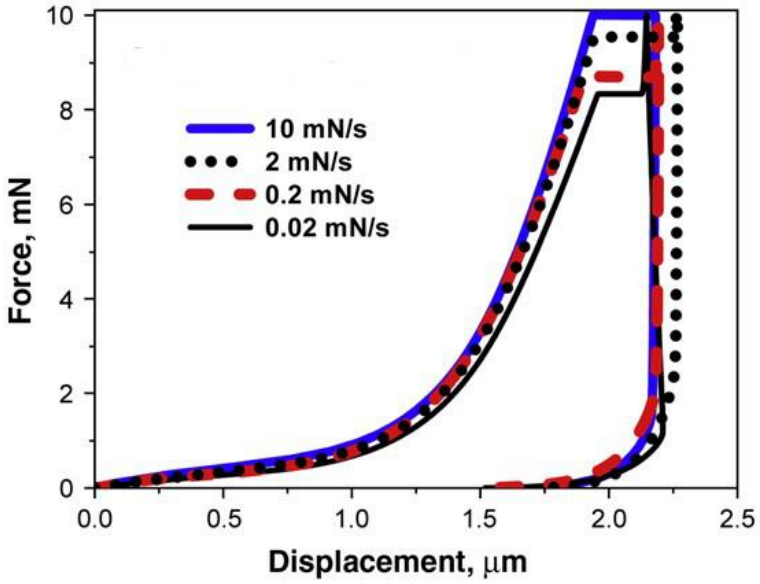

Figure 3.7 Force versus displacement for the 3.0 μm uncoated particles for different loading rates [120].

There are different kinds of stress and strain describing different kinds of situations, for example true stress and strain, engineering stress and strain. Analysis of the deformation of a sphere of material under compression is complex compared with the uniaxial loading of e.g. cylinder. This is because the relationship between the displacement and the cross-sectional area of a cylinder can be calculated under deformation, while it is very difficult for a sphere. In order to simply the analysis and comparison of different sized particles, Zhang et al. [121] proposed a definition of normalized compression stress σ_c and nominal strain ε_c for spherical particles, where the stress σ_c is calculated by dividing the applied load by the maximum cross-sectional area of the particle and the strain ε_c is the displacement *D* divided by the initial diameter of the particle i.e.

$$\sigma_c = \frac{P}{\pi R^2} \tag{3.1}$$

$$\varepsilon_c = \frac{D}{2R} \tag{3.2}$$

where *R* is the radius of the particles. An example normalized stress-strain plot for the acrylic copolymer particles at a loading rate 0.02 mN/s is shown in Figure 3.9. The curve exhibits a bilinear behaviour, with linear regions between 0 and 25% nominal strain (referred to as E1 or the Initial Modulus) and between 55% and 65% nominal strain (E2 or High-strain Modulus). The apparent modulus within these two regions was determined as the slope of the best linear fit within the two linear areas. The initial modulus and high-strain modulus at different loading rates were calculated using this method, and Figures 3.10 and 3.11 illustrate the effect of loading rate on the apparent moduli of the 3.0 μm acrylic copolymer particles and 3.8 μm Ni/Au

coated particles. It should be noted that E1 and E2 are non-physical parameters and they are used here to describe the hardness of the spheres under compression. Further study should be conducted to explore the possible relationship between the Initial Modulus (E1) and Young's Modulus of the material itself, and the High-strain Modulus is believed to be one of the other important parameter related to the material because large deformation deform the sphere into a near-cylindrical shape. Figure 3.8 illustrated a typical stress-strain relationship for a uniaxial cylinder under compression [123]. Compared with Figure 3.9, it can be seen that the curvature is totally opposite for the compression of cylinder and sphere and the initial modulus E1 is more related to the sphere structure.

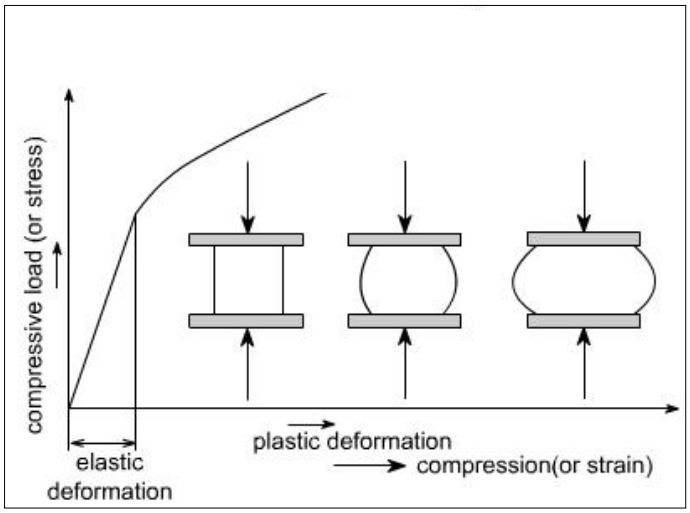

Figure 3.8 Typical stress strain relationship for a uniaxial cylinder structure under compression [123].

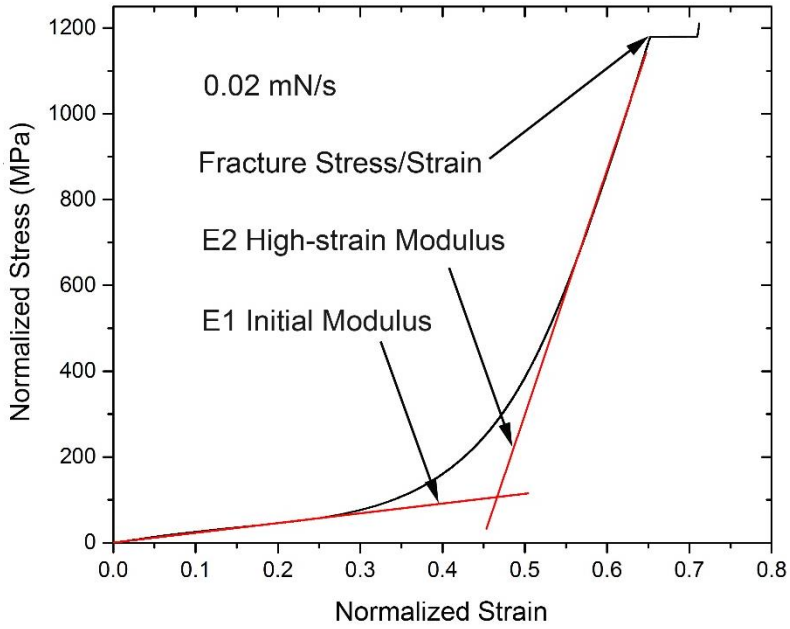

Figure 3.9 Normalized stress versus strain for a 3.0 μm uncoated particle at a loading rate of 0.02 mN/s.

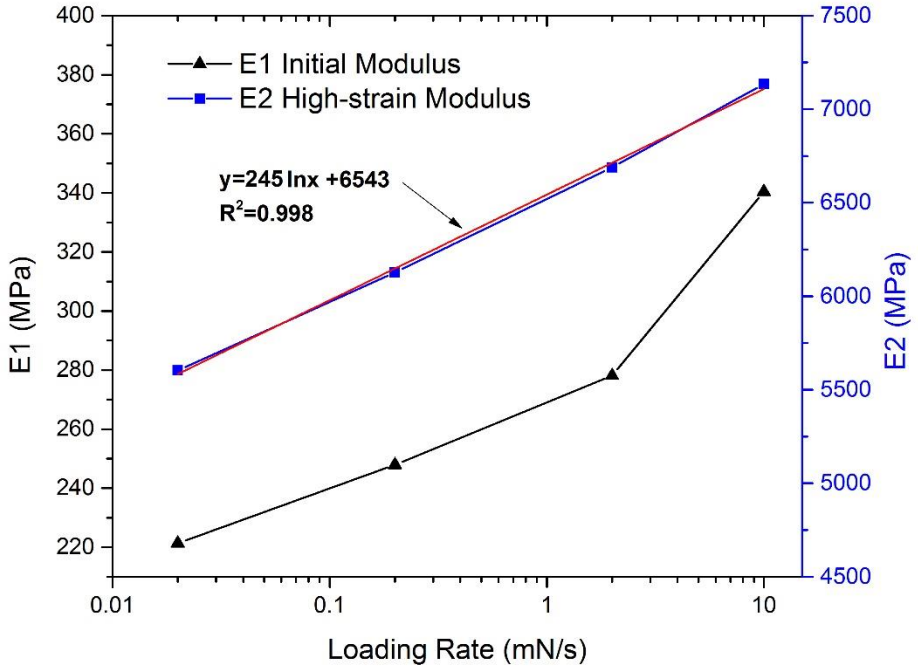

Figure 3.10 Apparent moduli calculated from compression tests on the 3.0 μm acrylic particles.

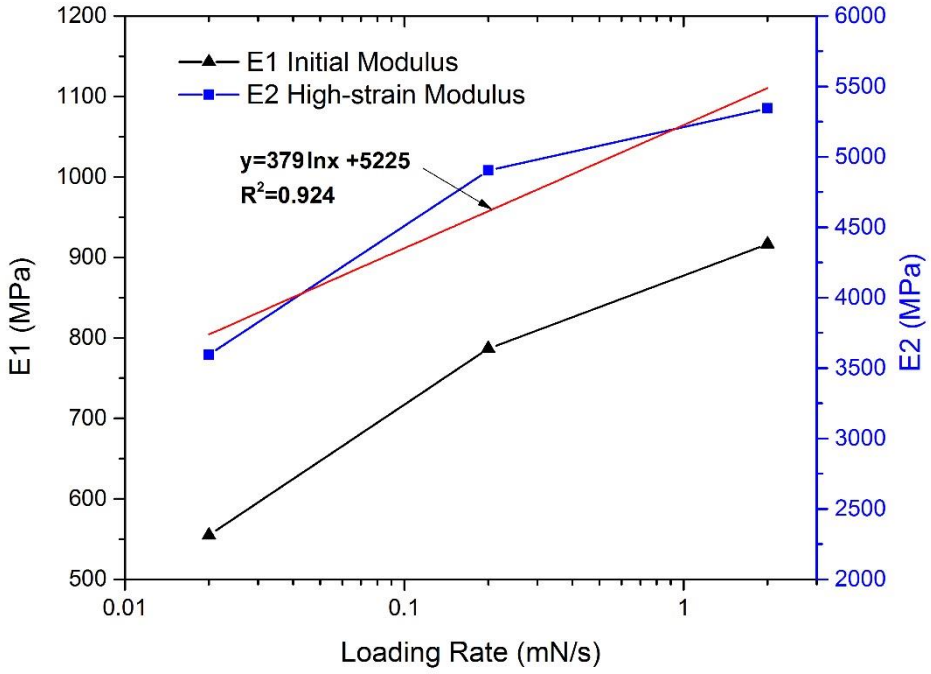

Figure 3.11 Apparent moduli calculated from compression tests on the 3.8μm Ni/Au coated particles

The fitted function has a very high standard error suggesting a very good fitting, and the fitted curve is a straight line in the logarithmic axes showing the clear relationship between the modulus E2 and loading rates. The results show that the mechanical behaviour of the particles is significantly impacted by the loading rate. The elastic Young's modulus is one of the most important parameters describing the mechanical deformation of linear elastic solid materials. Compared with metals and ceramics, the Young's modulus of polymers can be significantly affected by strain rate and temperature. Most semicrystalline polymers have a spherulitic molecular structures and deform in the following four steps. The first step is the elongation of amorphous tie chains, and then the lamellar chain folds start to tilt toward the tensile direction, followed by the separation of crystalline block segments. In the end the tie chains are oriented in the tensile direction [122]. In terms of the deformation of these highly crosslinked acrylic polymer particles, the situation is more complex due to their spherical shape. Meanwhile, the tensile Young's modulus is the same as the compressive Young's modulus for metals within the linear elastic deformation region. However the deformation of the polymeric material under tension and compression may differ, especially in the large strain regime [123]. In the first stage of the deformation, the strain remained at a relatively small level (below around 25% strain), and the initial modulus is relatively small ranging from 220 MPa to 340 MPa for the uncoated particles. This will lead to an initially high strain rate as any deformation at this this stage of the test will be mostly concentrated near to the contact areas due to the sphere structure of the particles. The relatively easier compression of the coiled molecules chains also contributes to the large deformation of the particles during this stage. At high strains the molecular chains are compressed from their initial "mushroom" structure to a "brush" structure and become overlapped with each other [124], thus making them more difficult to be compressed further. The fractional segments spread out in the radial direction under compression leading to a central lateral expansion with a larger diameter [125]. Therefore large strain areas become much stiffer [126].

The second linear stress-strain area begins at a strain of about 55%, and ends at fracture of the particle. A logarithmic function gives a very good fit to the *E2* versus loading rate data for both types of particles, showing a clear relationship between the loading rate and high-strain modulus. For the uncoated particles the fitted relationship between normalised loading rate $\dot{\sigma}$ and E2 is:

$$E2 = 245 \cdot \ln(\dot{\sigma}) + 6543 \tag{3.3}$$

which can be rearranged to:

$$exp(E2) = H'\dot{\sigma}^{m} \tag{3.4}$$

where $H' = 6543$ is here defined as the loading rate hardening coefficient and $m = 245$ is the loading-rate sensitivity factor. This function can be used to forecast the properties of the particle at different loading rates. During this deformation process before failure, inelastic deformation occurs and, after unloading, residual strains remain. Unlike the non-recoverable inelastic (i.e. plastic) deformation occurring in metals, the majority of the deformation in cross-lined polymers is reversible, and only a small part will permanently remain after unloading. Lee [18] proposed that there are two factors contributing to the deformation of the polymer. The first is that the polymer molecules stretch/compression in the direction of the applied stress, which is dominated by the storage modulus. The second is the viscous strain dominated by the loss modulus, which is due to the relative movements of the molecular chains, and is non-recoverable. As shown in Figure 3.11, the proposed loading rate equation is also a good fit for the coated particles, suggesting it can also be used to predict their behaviour.

3.4.2 Results of the Strain Rates Controlled Nano-mechanical Tests

3.4.2.1 Results for Uncoated Polymer Core Particles

The mechanical deformation of the viscoelastic materials is strongly affected by the strain rate. In order to better understand the effects of the strain rate on the deformation of the polymer core particles and Ni/Au coated particles strain rate controlled tests at i.e. four different strain rates, 0.004 μm/s (strain rate of around 8×10^{-4} s^{-1}), 0.04 μm/s (8×10^{-3} s^{-1}), 0.4 μm/s (8×10^{-2} s^{-1}), and 4 μm/s (8×10^{-1} s^{-1}), were performed for both kinds of particles. Figure 3.12 shows these compression results for the polymer particles at different strain rates. The normalized stress and strain of the compression test were calculated using Equations 3.1 and 3.2, and an example is plotted in Figure 3.13 for the polymer core particle at a strain rate of 8×10^{-4} s^{-1} (0.0004 μm/s). It can be seen that the deformation of the particle again exhibits a bilinear material curve. The first linear region is between 0 to 25% nominal strain, which is referred to as *E1* or the Initial Modulus. While *E2*, the High-strain Modulus is related to the second linear region for nominal strains from 45% to 55%. The apparent modulus within these two regions was determined by the best linear fit for the slope of two linear areas. The area of grey region is related with the absorbed energy during the deformation of the polymer core particles and of which most is dissipated as heat. The maximum load force in these tests, around 11 mN, was not enough to crush the particles. However it induced a deformation of 2.5 μm (a normalized strain around 0.5), which is believed to have reached the working region of the particle under compression in real application. During hold at the maximum force, the load force keeps the same while the displacement increased slightly due to viscoelastic creep of the material.

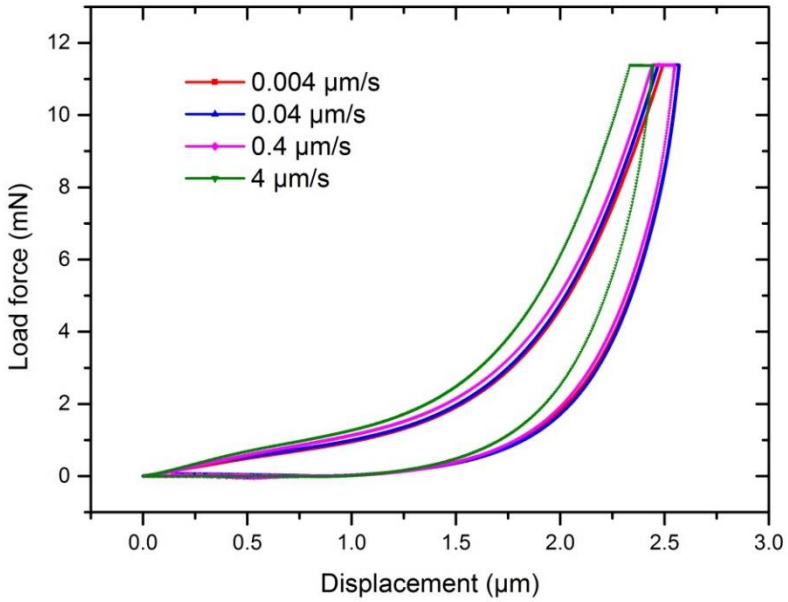

Figure 3.12 Load force vs displacement for the 4.66 μm polymer core particles at different strain rates.

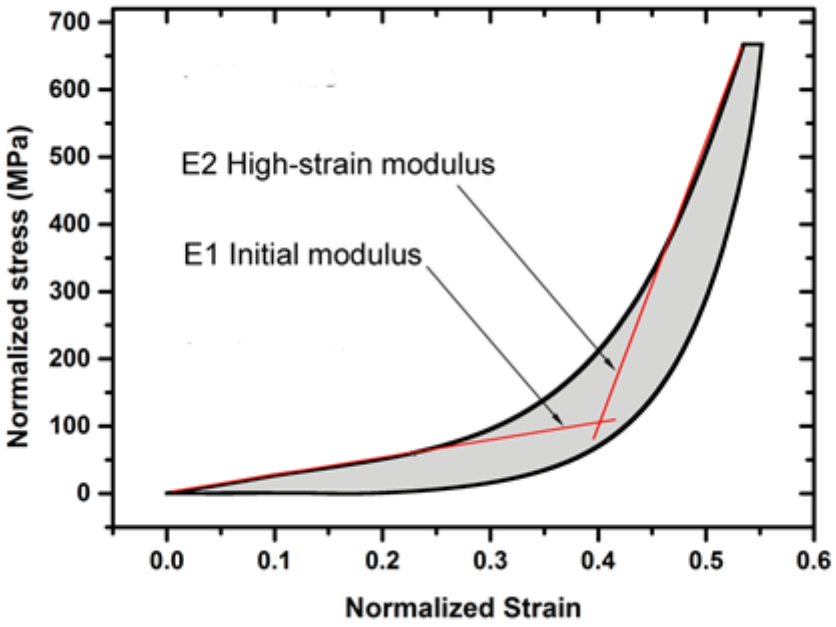

Figure 3.13 Normalized stress versus strain for a 4.66 μm polymer core particle at a strain rate around 8×10^{-4} s^{-1} (0.0004 μm/s).

Systematic study and theories have been well established to explain the strain hardening and strain rate hardening effect, and a power law of the strain rate hardening is:

$$\sigma = Q\dot{\varepsilon}^{m} \tag{3.5}$$

where σ is the flow stress, $\dot{\varepsilon}$ is the strain rate, Q is a constant of the material, and m is strain-rate sensitivity index [127-132]. The strain rate sensitivity exponent *m* is an important parameter, which describes the capacity of the material to resist necking and has been used as a criterion to evaluate the proposed mechanical deformation. The value of m is a function of the forming parameters i.e. the temperature and microstructural characteristic of the material. Usually the *m*-value lies around 0.01 and does not exceed 0.1 for most known materials at room temperature. However the value of m ranges from 0.3 to 0.9 and may even approximately 1 [128] for the materials in a superplastic state, for example the strain-rate sensitive values of superplastic aluminium alloy lie in the range of 0.4 to 0.8 [129]. According to the standard method, the value of m can be calculated by:

$$m\Big|_{\varepsilon=\varepsilon_0} = \frac{\ln(\sigma_1 / \sigma_2)}{\ln(\dot{\varepsilon}_1 / \dot{\varepsilon}_2)} \tag{3.6}$$

where σ_1 and σ_2 are the stresses correspond to the same strain, $\varepsilon = \varepsilon_0$, and the strain rate, $\dot{\varepsilon}_1$ and $\dot{\varepsilon}_2$, respectively. If there are more than two experimental strain rates, for example $\dot{\varepsilon}_i$ ($i = 1, 2, ..., \mathrm{N}$), the strain-rate sensitivity index m can be determined as the slope of the strain line in logarithmic coordinates, $\log\sigma - \log\dot{\varepsilon}$. Figure 3.14 shows the typical $\log\sigma - \log\dot{\varepsilon}$ curves for the polymer core at strains ranging from 0.1 to 0.5. The red linear lines fit very well with the curves, and the slope of the fitting curves represent the strain-rate sensitivity index at different strain level. The *m*-values of the polymer core particles lie in the range of 0.038 to 0.053, which are much higher for the common metals i.e. Cu (0.009) [130], Fe (0.006) [131] and Al (0.004) [132] at room temperature. Normally most studies on the strain-rate sensitivity index for metals are conducted at relatively high temperature, as a result the value of *m* will change significantly. For example, the strain-rate sensitivity (m) increased from 0.004 to 0.025 when increasing temperature from 25 ℃ to 250 ℃ for a conventional grain sized (CG) aluminium [132]. The mechanical behaviour of polymeric materials can be dramatically affected by temperature. However compression tests at different temperatures were not carried out in this work due to the limitations of the hot stage available in the Nanoindentation system. It is anticipated that the strain-rate sensitivity index will be much larger at high temperature for the polymer core particles.

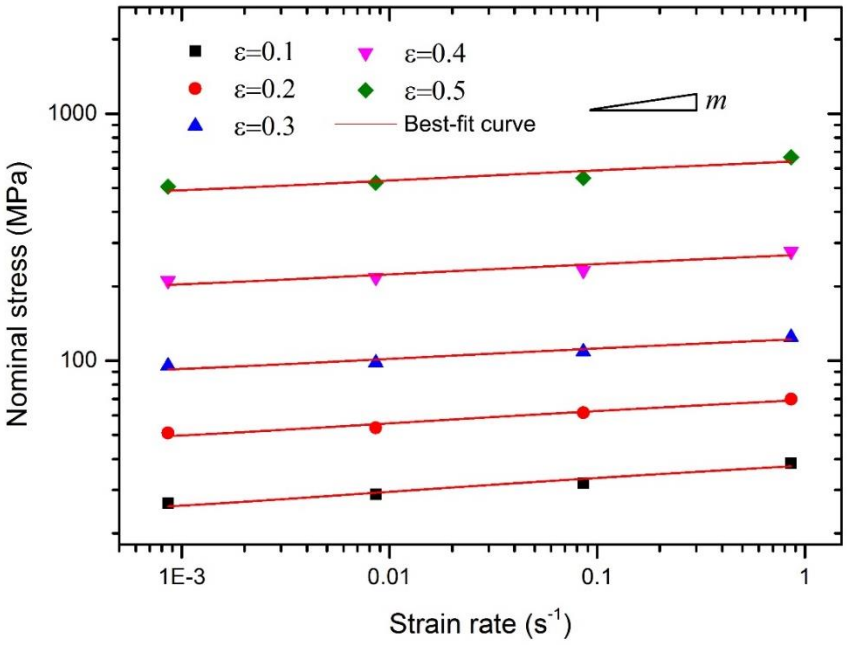

Figure 3.14 The log-log curves of the nominal stress at different strains as a function of the strain rate for the polymer core particles.

The influence of strain rate on most metals or ceramic materials is quite small [127] at room temperature, while the modulus of viscoelastic materials is dramatically impacted by the strain rate and temperature. The initial modulus *E1* and high-strain modulus *E2* of the polymer particles at different strain rates are shown in Table 3.2 and also plotted in Figure 3.15. The apparent initial modulus for the polymer particles ranges from 255 MPa to 328 MPa, while the high-strain modulus varies from approximate 4 GPa to 5GPa. It can be seen that the logarithmic regression shows a clear relationship between the strain rate and the modulus of the material, and both modulus increases significantly with the increasing strain rate. Very good fittings were provided using logarithmic functions, and the fitting function for high-strain modulus versus strain rate was illustrated in Figure 3.16 using the decimal coordinate system.

Table 3.2 Relationship between the apparent moduli and strain rate for 4.66 μm polymer particles.

Displacement rate μm/s	Nominal Strain rate s^{-1}	Initial Modulus MPa	High-strain Modulus MPa
0.004	0.00085	255	3957
0.04	0.0085	267	4160
0.4	0.085	315	4489
4	0.85	327	4983

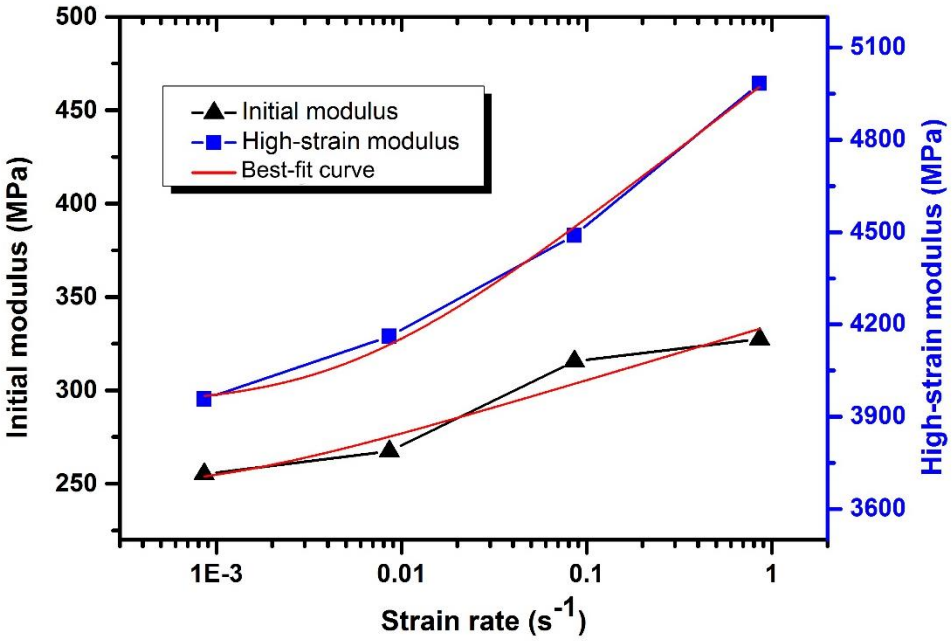

Figure 3.15 Apparent moduli calculated from compression tests on the 4.66 μm polymer core at different strains rates.

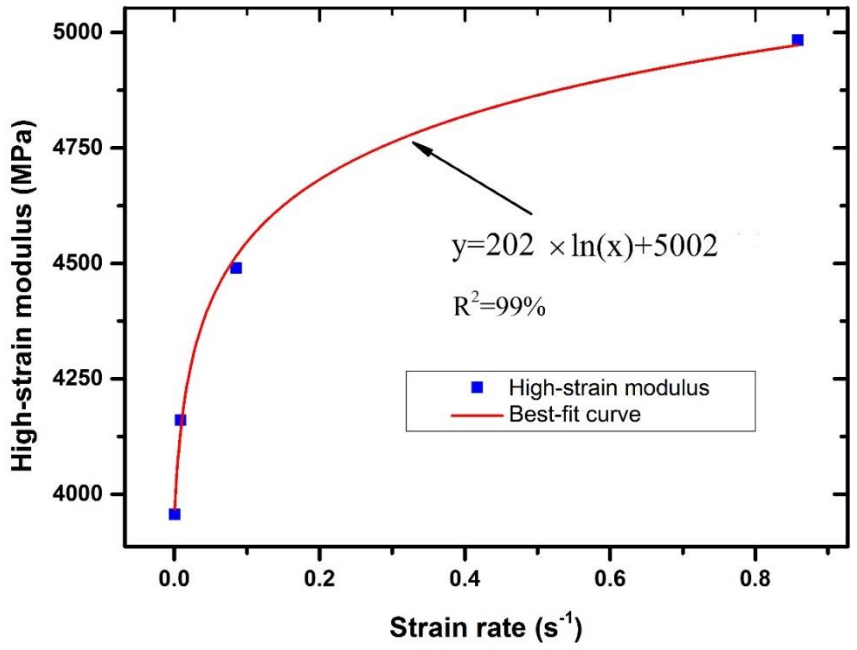

Figure 3.16 Logarithmic function fitted to the curve of high-strain modulus (E2) versus strain data plotted on linear axes.

The strain-rate sensitivity index (*m*) provides a measure of strain rate hardening on the material, while the exact hardness of the material under different loading conditions can provide a direct reference for the industrial application. For the uncoated polymer particles, the fitted relationship between normalized high-strain modulus *E2* and strain rate is:

$$E2 = 202\ln(\dot{\varepsilon}) + 5002 \tag{3.7}$$

which can be rearranged to:

$$e^{E2} = H'\dot{\varepsilon}^{n} \tag{3.8}$$

where H' and n are defined as the strain-rate coefficient and sensitivity for the high-strain modulus. The mechanical properties of the particles at different strain rates can be forecasted based on the analysis of the strain-rate sensitivity index (m), and the function describing the relationship between the high-strain modulus and strain rate.

3.4.2.2 Results for Ni/Au Coated Particles

The polymer core of the Ni/Au coated particles (Ni/Au-MCPs) is exactly the same as the pure polymer particles tested in the previous section, and it comprises the majority of the volume of the Ni/Au-MCPs. The study on the pure polymer core particles revealed their mechanical properties at different loading conditions, which also helps to better understand the mechanical characteristics of the Ni/Au-MCPs. The nickel and gold coating layer provides the electricity conductive path between the chip and substrate. The metal coating layer is very thin (150 nm) but is of a material much stiffer than the polymer core, which is supposed to impact on the mechanical properties of the whole particle. The Figure 3.17 illustrates the deformation results for Ni/Au-MCPs under different strain rates of approximately 8×10^{-4} s^{-1} (0.004 μm/s), 8×10^{-3} s^{-1} (0.04 μm/s), 8×10^{-2} s^{-1} (0.4 μm/s), and 0.8 s^{-1} (4 μm/s).

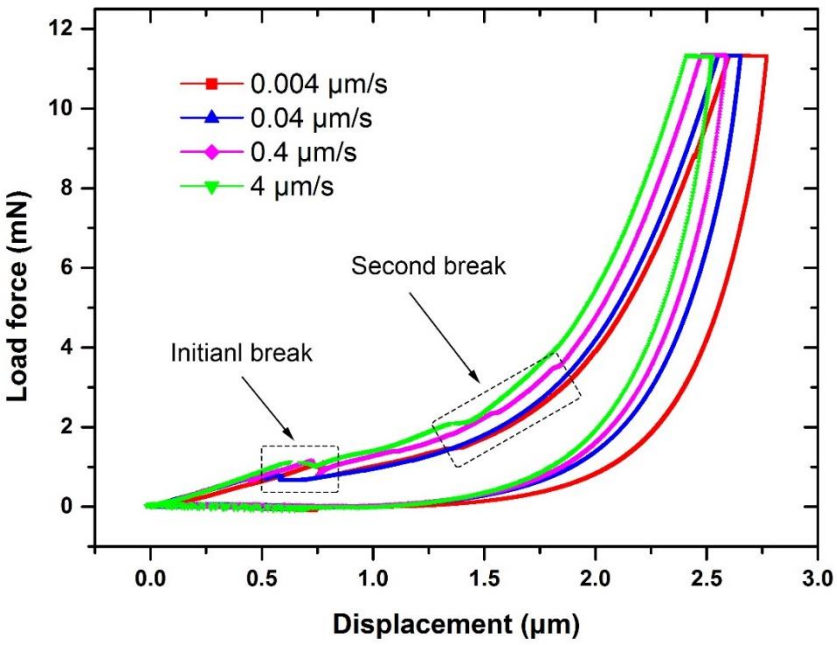

Figure 3.17 Load force vs displacement for the Ni/Au coated polymer particles at different strain rates.

As can be seen in Figure 3.17, the deformation of the Ni/Au-MCPs was also significantly impacted by the strain rate, which is similar to that for the pure polymer particles. The obvious difference is that the curve is not smooth and constant due to the crack of the metal layer. The first crack occurred when the displacement was around 0.75 μm (strain 15%), while the second obvious break happened around the displacement 1.5 μm (strain 31%). The detailed crack mechanism and its propagation will be studied in the following in-situ compression experiment section.

The nominal stress-strain relationship was calculated based on Equation (3.1 and 3.2), and the strain-rate sensitivity index (*m*) versus the strain rate is plotted in Figure 3.18. The value of *m* are varied from 0.047 to 0.058 for the strain from 0.1 to 0.5, which are larger than those for the pure polymer particles. The results illustrated that the Ni/Au coated particles are more likely to be affected by the strain rate. It is worth noticing that the equations fit better at higher strain level. The reason is that the crack of the metal coating layer has more effect on the initial deformation region, while the mechanical behaviour relies more on the properties of the polymer core at high strain levels. Further research on the relationship between the metal layer and polymer core will be presented in the following in-situ compression test section 3.4.3.

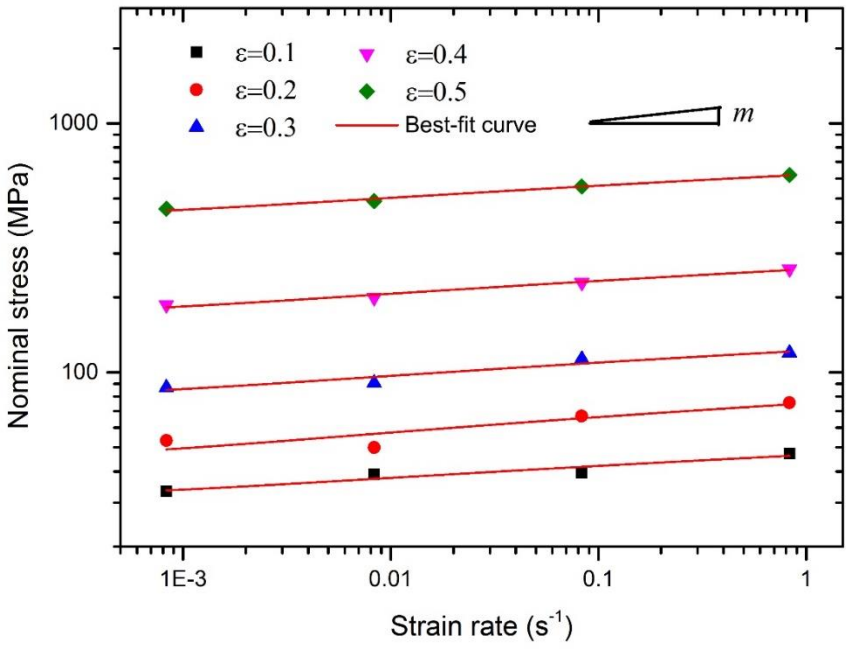

Figure 3.18 Log-log curves of nominal stress at different strain levels as a function of the strain rate for the Ni/Au coated polymer core particles

For the compression test at each strain rate, the nominal stress-strain curve was plotted and then a linear fit determined for the initial deformation and high-strain region moduli. *E1* and *E2.* The Ni/Au-MCPs for different strain rates are shown in Table 3.3 and also plotted in Figure 3.19. The apparent modulus was found to increase significantly with the increasing strain-rate, which means that the material stiffness appeared to be very sensitive to the strain rate. The apparent initial modulus *E1* for the Ni/Au-MCPs ranges from 389 MPa to 480 MPa, which is much higher than those for the polymer cores (255 MPa to 328 MPa). This is attributed to the significantly higher Young's moduli of nickel (154±50 GPa [133]) and gold (79 GPa [134]). However, compared with the high-strain moduli of the polymer cores, the high-strain moduli for Ni/Au-MCPs are lower, varying from approximatelyy 4 GPa to 5GPa. A possible explanation is that the cracking of the metal coating layer created damage to the polymer cores of the particles, which decreased their ostiffness. The experimental data fit very well to Logarithmic functions (R^2>95%), and the fitted function for high-strain modulus versus strain rate was also illustrated in Figure 3.20 using the linear axes.

Table 3.3 Relationship between the apparent moduli and strain rate for Ni/Au (100/50 nm) coated polymer core (4.66 μm) particles.

Displacement rate μm/s	Nominal Strain rate s^{-1}	Initial Modulus MPa	High-strain Modulus MPa
0.004	0.00083	388	3860
0.04	0.0083	421	4099
0.4	0.083	453	4348
4	0.83	479	4580

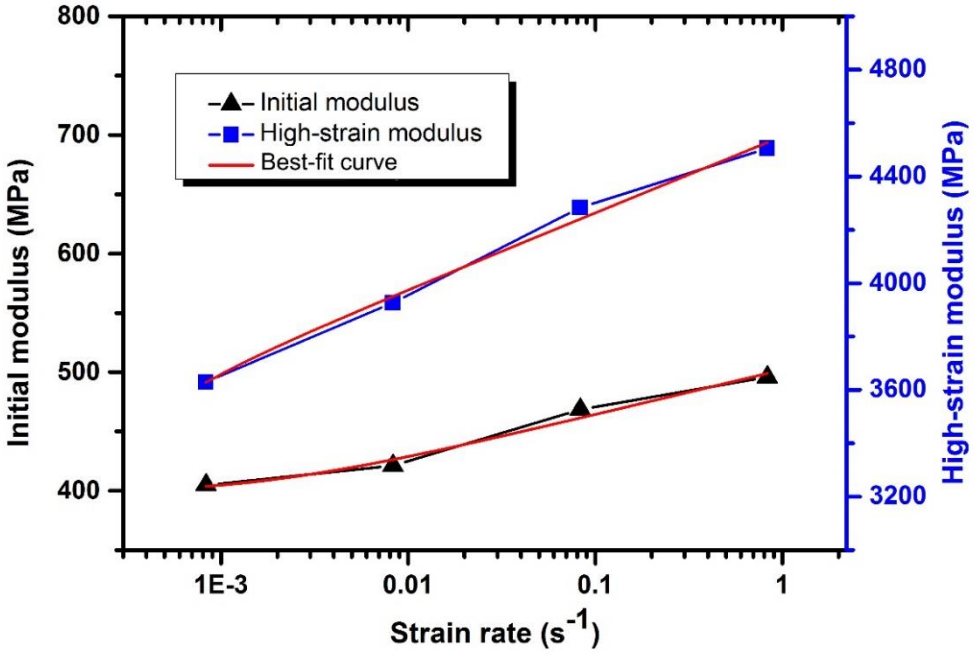

Figure 3.19 Apparent moduli calculated from compression tests on the 4.66 μm Ni/Au coated polymer core at different strain rates.

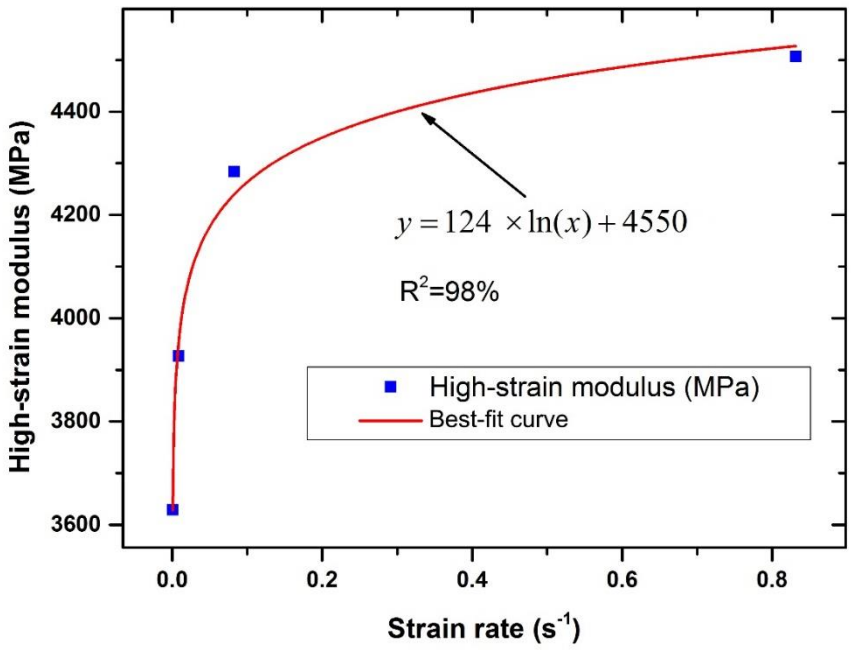

Figure 3.20 Logarithmic function fitting for the curve of high-strain modulus (E2) versus strain rate in linear axes.

The fitted Logarithmic equations shows a clear relationship between normalized high-strain modulus *E2* and strain rate for the Ni/Au coated particles:

$$E2 = 124\ln(\dot{\varepsilon}) + 4550 \tag{3.9}$$

which can also be rearranged to:

$$e^{E2} = H'\dot{\varepsilon}^{n} \tag{3.10}$$

where H' and n are defined as the strain-rate coefficient and sensitivity for the high-strain modulus. Both the polymer particles and Ni/Au coated particles showed strain-rate-dependent deformation behaviour. The material parameters including strain-rate sensitivity index (*m*), initial modulus (*E1*), and high-strain modulus (*E2*) were analysed. Correspondingly some constitutive models were established, which can be used to forecast the mechanical deformation behaviour of the particles. It should be noted that the Ni/Au coated particles are more rate-sensitive, and the high-strain modulus of metal coated particles is even much lower than that of pure polymer particles. It is believed that the crack of the coating layer created some damage to the polymer core. Furthermore, the data on the ultimate stress/strain is missing due to the force limitation of the nanoindentation.

3.4.3 Results of in-situ nanomechanical compression test

The in-situ nanomechanical system enables direct observation during an individual particle compression experiment, which helps to provide a better understand the crack propagation and failure of the particles. Figure 3.21 and Figure 3.22 were taken by the scanning electron microscope beam, and show the start of in-situ compression tests on a polymer particle and a Ni/Au-MCP. In order to obtain good quality SEM images of nonconductive materials, gold or carbon are usually pre-coated onto the sample surface to increase its conductivity. However no coating was applied to the polymer particles to avoid any potential influence on the crack and failure due to for example the possibility of an uneven coating thickness. As a consequence, as shown in Figure 3.21 the SEM image of the polymer particles are not very sharp because of the poor conductivity of the polymeric material that creates some image distortion around the middle part of the polymer particle forming the final “wormhole” like SEM image. However this does not impact on the subsequent data collection and analysis. The polymer particle was compressed by the diamond tip in the PicoIndenter, and all the data including the displacement, load force, time etc. were collected simultaneously. The load-displacement graphs using nanoindentation are very uniform, so that the viscoelastic behaviours (strain rate hardening effects) were studied using the data achieved by nanoindentation. As a comparison, the in-situ system focuses more on the crack and fracture studies. The load-displacement data received

from in-situ system was not accurate and uniform enough because of the less accuracy of the nanoindentation part in the system (much smaller size compared with the nanoindentation) and the slight rotate angle (about 3 °).

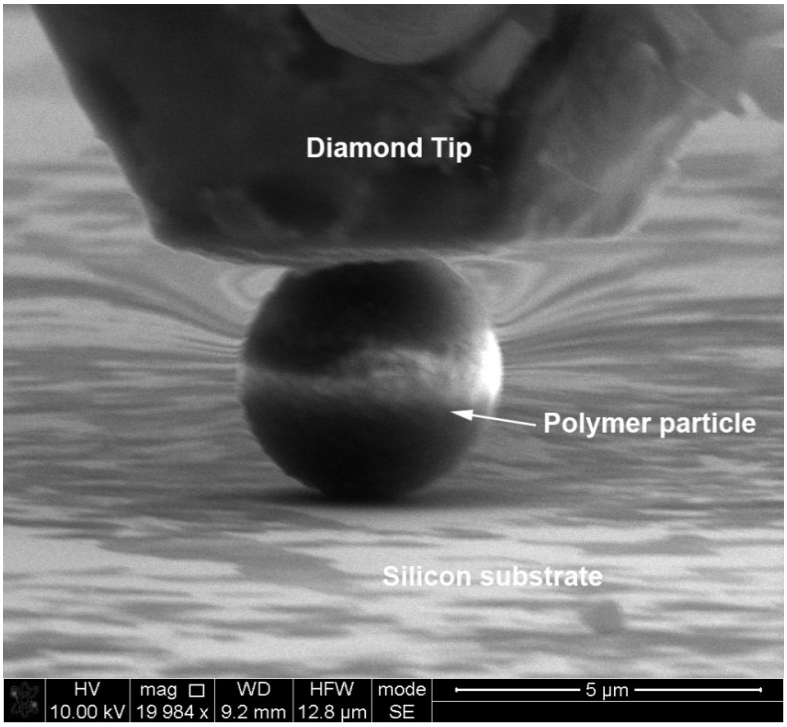

Figure 3.21 Scanning electron microscope (SEM) image of the in-situ compression test for an individual 4.66 µm polymer particle.

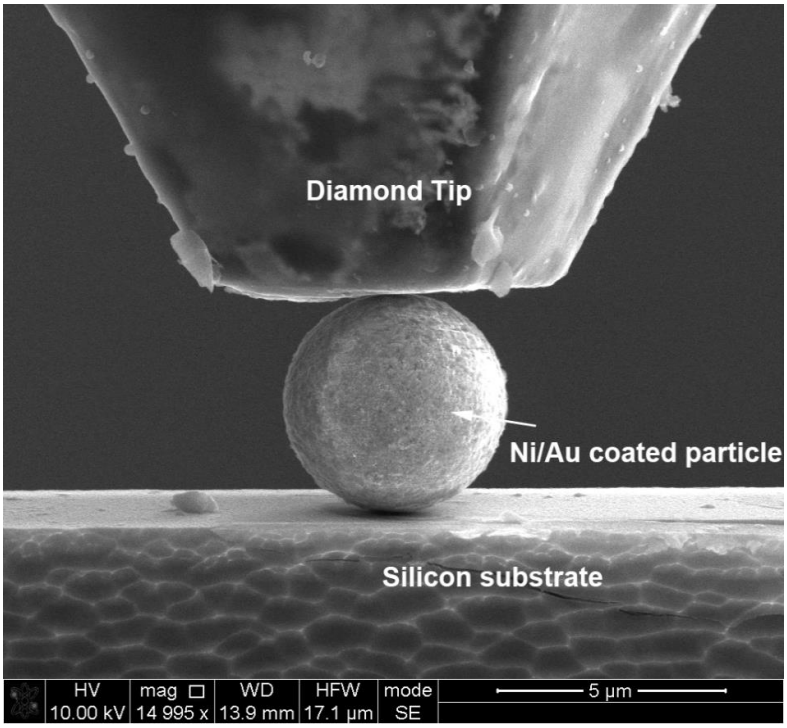

Figure 3.22 Scanning electron microscope (SEM) image of the in-situ compression test for an individual Ni/Au coated polymer core particle.

The individual particle compression experiment was fully recorded in the form of video with the quality of 100 frames per second, so that subsequent analysis could be performed by observing it frame by frame. Extra SEM images were then taken to clearly show crushed morphology of the fractured particles. Figure 3.23 illustrates the cracks propagation and failure process of the individual polymer particle in the in-situ compression experiment at the strain rate of approximately 0.0086 s^{-1}(40 nm/s). No obvious crack was observed until the nominal strain reached around 50% (Figure. 3. 23 (c)), which is consistent with the data acquired using PI 95 Nanoindenter. As can be seen in Figure 3.23 (c) and (d), two major cracks occurred when the displacement reached 2.44 μm (around 52.4% strain), and then propagated in the longitudinal direction. The two cracks shown in the Figure 3.23 (c) and (d) are believed to be two ends of one major crack through the middle part of the polymer particle, which was also indiciated by the final fracture morphology of the polymer particle shown in Figure 3.23 (f). Figure 3.23 (e) displays another crack which initiated in the region in contact with silicon substrate (contact corner) and propagated upwards in the longitudinal direction. It is worth noting that the propagation of the cracks occurred and then propagated very quickly to the other end within several frames and the fracture surface appears to be sharp and clear. This is attributed to the high crosslink density of the polymer. The crosslinking density is known to have a significant influence on the mechanical properties of polymeric materials [135], as it limits the mobility of molecular chains thus decreasing the freedom in rearranging the molecular chains and increasing the stiffness of the particle [136].

As discussed earlier, the polymer particles display viscoelastic behaviour and their behaviour is impacted significantly by the strain rate. The results of the compression test at 40nm/s indicate that these polymer particle with crosslinked molecular chains exhibit strongly brittle characteristics, where the crack occurs at a relatively large strain level then propagate rapidly leading to the particle failure. It was demonstrated earlier that higher strain rate result in a higher apparent hardness of the particle. The deformation behaviour of the polymer particles at 400 nm/s and 4000 nm/s was similar to that at 40 nm/s, and Figure 3.23 shows the compression process of a polymer particle at 4000 nm/s. The breaking force at nominal strain fracture did not show any obvious difference at strain rates of 40 nm/s, 400 nm/s, and 4000 nm/s. All the cracks are were observed initiate at the contact corner with the diamond tip or the silicon substrate and propagate in the longitudinal direction. After failure, the polymer particle appears to have broken into a group of crushed pieces.

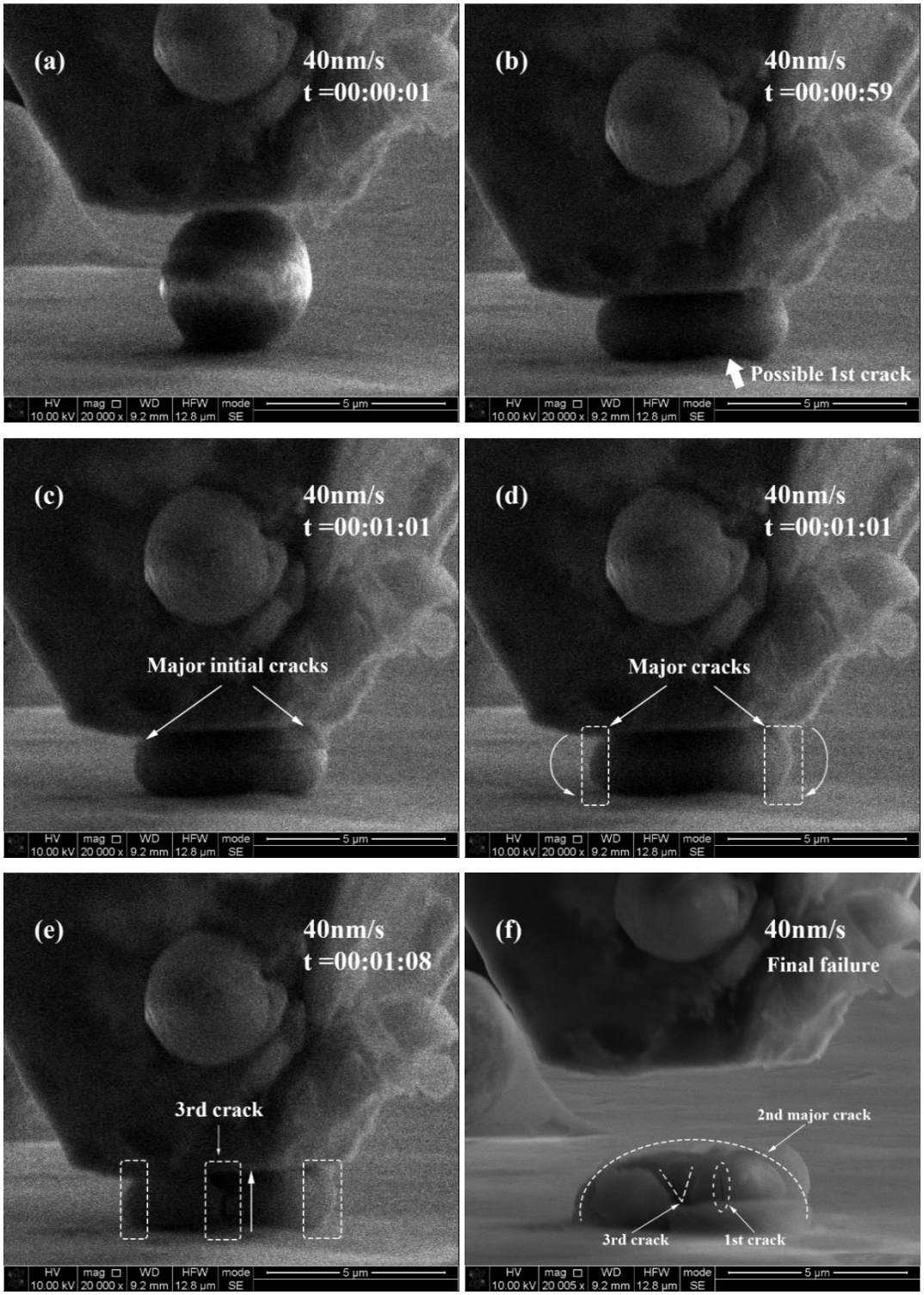

Figure 3.23 Screen capture images from the in-situ video record for the individual polymer particle compression experiment at 40 nm/s.

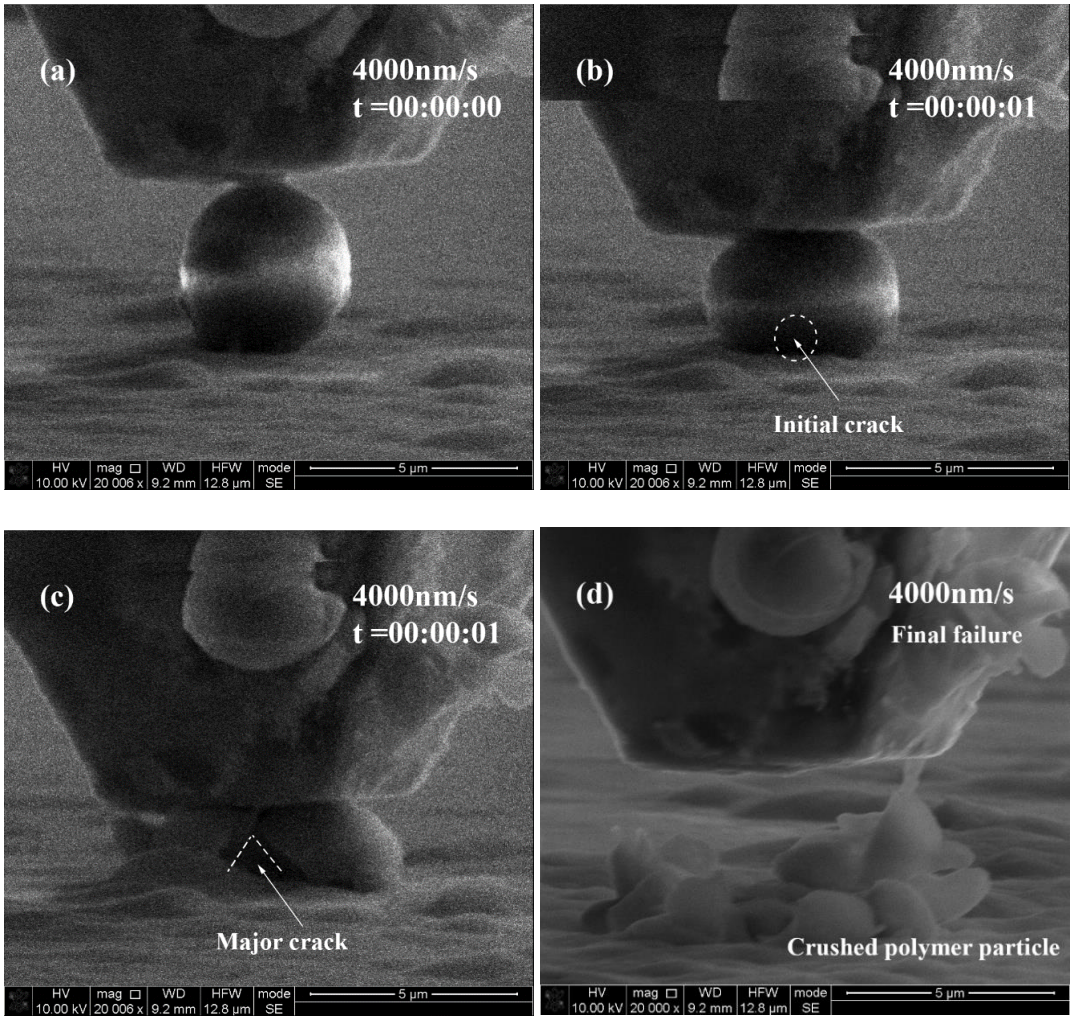

Figure 3.24 Individual frames from the in-situ video recording for a polymer particle compression test at 4000 nm/s.

In contrast, even though the load force reached the maximum for the instrument 24 mN, the polymer particle did not crush at the applied strain rate of 8.58×10^{-4} s^{-1}(4 nm/s) as shown in Figure 3.25, which suggests that the polymer particle displays greater viscous deformation capability at this very low strain rate. This is attributed to the slow compression process enabling enough time for relative movement between the molecular chains that dissipates most of the applied energy as heat. Conversely, the molecular chains have less relative movement at higher strain rate deformation. The applied energy is beyond the total capability of storage energy and viscous dissipating energy of the particle, and then released the excess energy to break the molecular chains, hence leading to the initial crack and its quick propagation. Meanwhile the stress within the polymer is becoming higher with the increasing strain rate even at the same strain level, which reaches the limitation the polymer can tolerate resulting in cracks. Highly crosslinked polymers show higher storage modulus, thus allowing them to have better recovery ability after deformation [136], but cracks and failure lead to poor recovery. The in-

situ compression tests suggest that the highly crosslinked particles are very brittle at high strain rates and a low strain rate reduces the probability of cracking and failure.

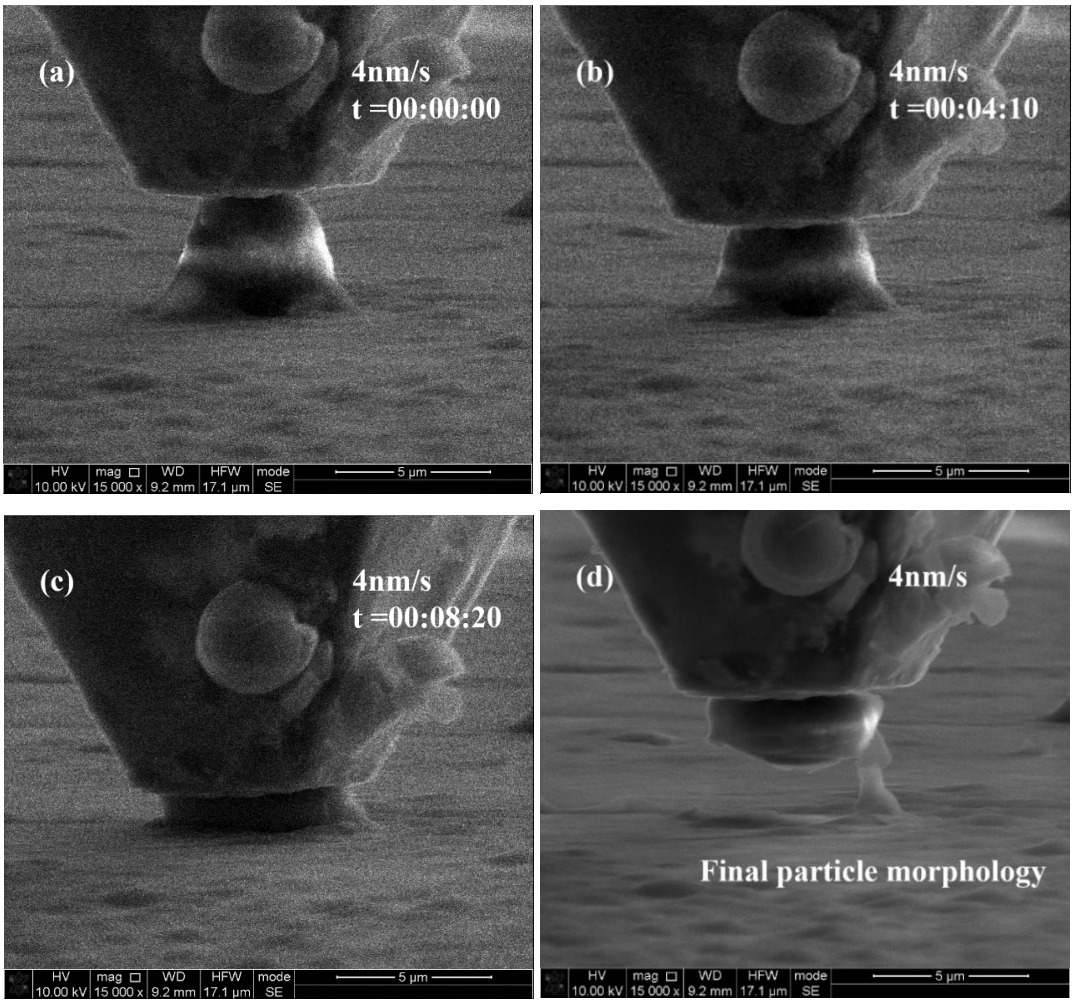

Figure 3.25 Individual frames from the in-situ video record for the individual polymer particle compression test at 4 nm/s.

The polymer core occupies more 90 percent of the volume of Ni/Au coated particles, and its mechanical properties plays an important role in determining the properties of the Ni/Au coated particles. The coated metal layer is the essential part of the particles which dominates the electrical resistance. The pattern of any crack propagation in the metal layer will directly affect the electrical conductivity of the particle in its application. Analysis of the individual particle compression results show several different crack patterns: cracks initiated either at the region in contact with silicon substrate/diamond tip (contact corner) or the midline (equator) of the particle, and cracks propagated either in longitudinal or latitudinal direction.

Figures 3.26 and 3.27 illustrate the compression process for Ni/Au-MCPs at applied strain rate of 40 nm/s and 400 nm/s respectively, where the cracks initiated at the contact corner and

propagated in the longitudinal direction. There are always some initial defects in the metal coating layer as shown in Figure 3.26 (a) and Figure 3.27 (a), and the areas around these initial defects are therefore the most vulnerable locations under compression because of their low capability to endure the stress concentration. It can be seen from Figure 3.26 (b) that the two cracks initiated at the contact corner between the particle and diamond tip under a very small compression deformation. One of the cracks was observed to rapidly propagate into the initial defects, and the propagation direction of this crack followed the direction of the initial defects as shown in Figure 3.26 (c) (d). It is found that the crack at the "edge" of the particle in Figure 3.26 (b) (c) (d) propagated in the longitudinal direction much quicker than the frontal crack. Similar "edge" shear cracks were also observed in most of other compression tests, as shown in Figures 3.27, 3.28, 3.29, and 3.30. This is believed to be due to the slight angle of the silicon substrate with respect to the indenter, which causes a shear effect at the edge circle leading to this quick crack propagation. The other possible reason is that there are larger initial defects in the area of the contact of the particle with the silicon substrate or diamond tip. As shown in Figure 3.27, two cracks also propagated in the longitudinal direction, where the first crack occurred around the initial defect area and the other cracks initiated at the contact corner between the particle and silicon substrate.

As discussed earlier, due to the much higher Young's modulus of the metal coating layer, the initial modulus of the Ni/Au coated particle is significantly higher than that of the pure polymer particles. However the high-strain modulus of the Ni/Au coated particles is lower than that of the polymer particles. As can be seen in Figures 3.26 (e) and (f) and 3.27 (e) and (f), severe delamination appeared followed by the propagation of the cracks. More importantly, it is clear to see that the cracks of the polymer core are parallel with the cracks in the metal coating. Therefore, the compression process of the Ni/Au coated particles can be concluded as occurring in three steps:

- The first deformation phase which both the polymer core and metal coating can tolerate without failure;
- The cracks initiate in the metal coating layer and propagate during the second deformation regime, where some corresponding initial defects are believed to be created in the polymer core;
- The fracture of the polymer core results in the total failure of the particle.

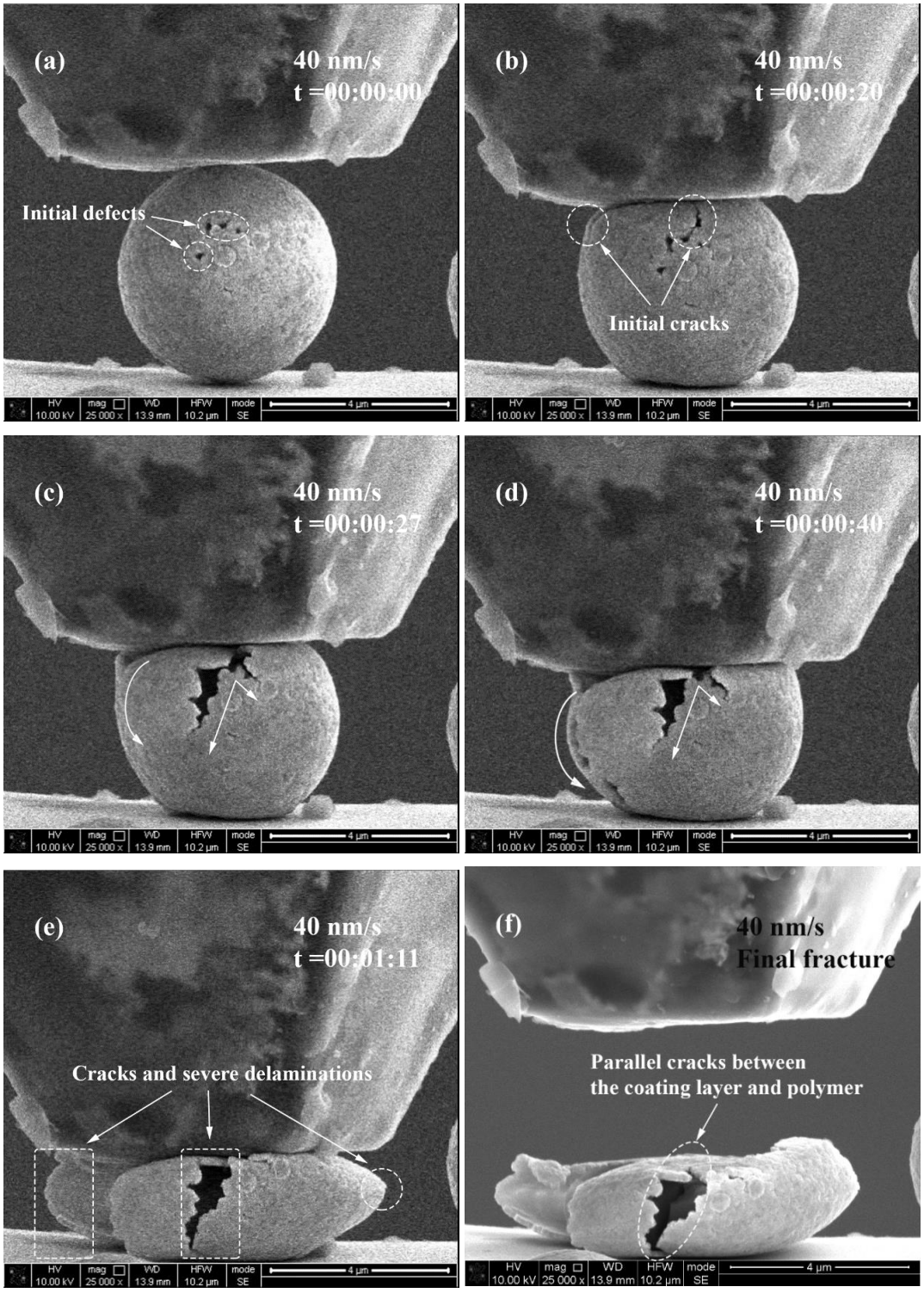

Figure 3.26 Individual frames from the in-situ video record for the individual Ni/Au-MCP compression test at 40 nm/s.:

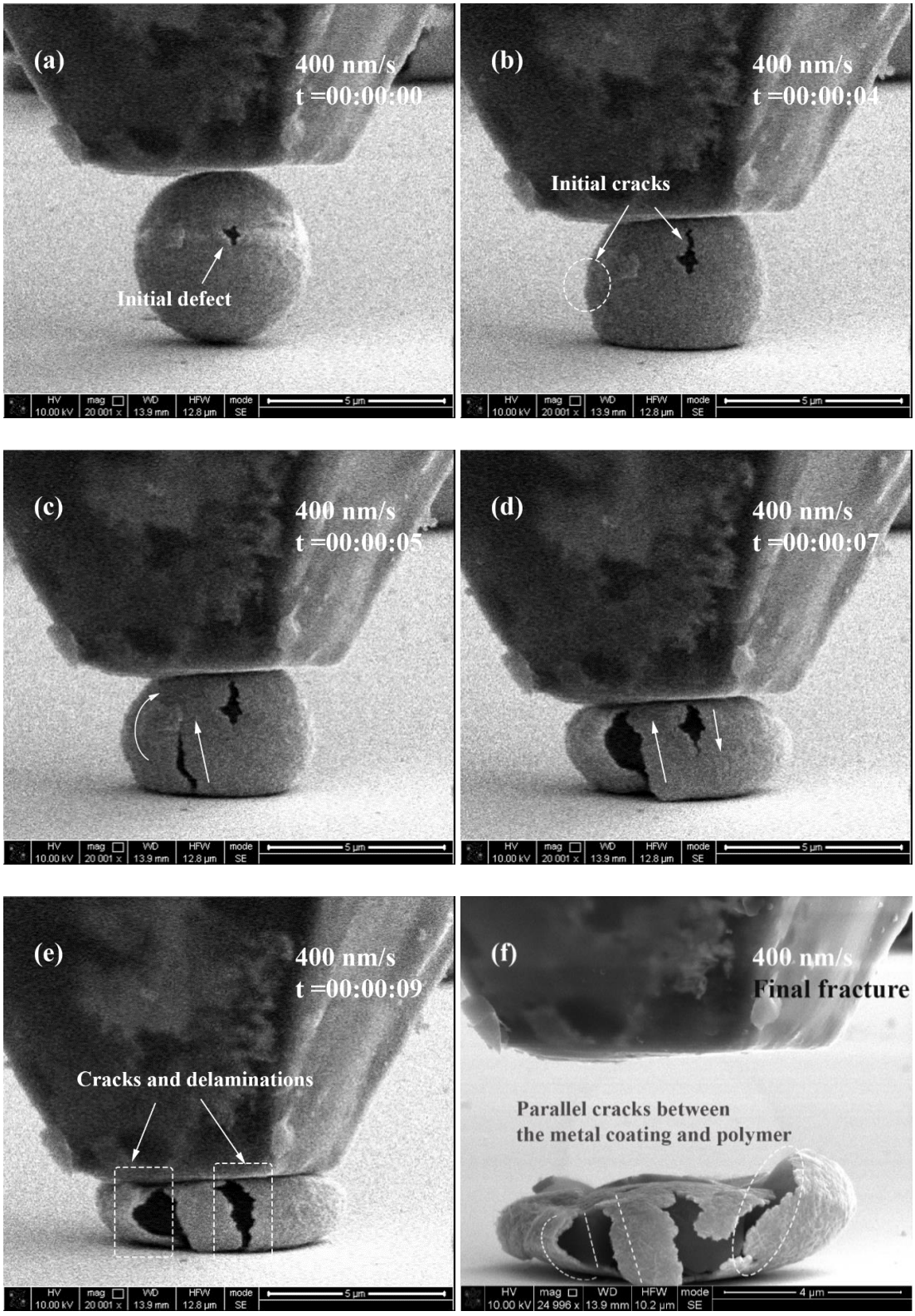

Figure 3.27 Individual frames from the in-situ video record for the individual Ni/Au-MCP compression test at 400 nm/s.

Cracks will strongly impact the conductivity of the Ni/Au coated particles. However they are inevitable under high levels of compression because of the spherical shape and difference

in Young's modulus between metal coating layer and polymer core. Cracks propagating in the longitudinal direction parallel to the current flow will have less effect. However cracks in the latitudinal direction will dramatically decrease the conductivity of particle and their occurrence should be avoided if possible. It is found that cracks which initiates near the middle equator of the particles are more likely to propagate in the latitudinal direction, as shown in Figure 3.28 and Figures 3.29 (a) and (b). As shown in Figure 3.28 (a) (b) (c), the crack at the "edge" of the particle (from the frontal view) initiated in the region in contact with the diamond tip, and this crack propagates quickly within tens of frames in the longitudinal direction. The other crack occurred in the middle of the particle and propagated longitudinally towards the two contact areas of the particle. However the crack split into two and started to propagate in the latitude direction after arriving at the contact area, finally forming a "Y" shaped crack, as shown in Figure 3.28 (d). This latitudinal propagation is attributed to the relatively fixed metal coating area contacted with the diamond tip surface. One possible reason is that extra energy is needed to overcome the friction between the metal coating and tip surface if the crack propagates in the contact area between the particle and diamond tip. The other kind of latitudinal crack can have a more severe effect on the conductivity of the particle, because it usually appears at the equator of the particle and propagates directly in the latitudinal direction as presented in Figure 3.29 (c), (e), and (f). This is believed to be attributed to that metal coating area changing from the sphere shape to plain board as a result of two severe longitudinal cracks on both sides. For a rectangular board fixed with two sides, the middle equator of the board is obvious to be the most vulnerable location under compression.

It should be noted that the latitudinal cracked occurs only during higher strain rate compression. No latitudinal cracks were observed among all the 15 particles at the compression strain rate of 0.00083 s^{-1} (4 nm/s) and 0.0083 s^{-1} (40 nm/s). On the contrary, nearly half of the particles (3/7) at 400 nm/s and all the four particles at 4000 nm/s displayed the latitudinal cracks. Furthermore, failure of the metal coating is closely related to the crushing of the polymer core. As discussed earlier, the fracture of the Ni/Au coated particle is separated into three steps, and the final failure of the polymer core results in the crushing of the Ni/Au coated particle. At higher stain rates, less time is left for the viscoelastic polymer core to absorb and dissipate the energy as heat, thus leading to severe cracks and large burst fracture displacement. Meanwhile the stiffness of nickel is also increased with the increasing strain rate [137]. Therefore, assembly processes leading to compression at a high strain rate should be avoided. The compression results at very strain rate of 0.00083 s^{-1} (4 nm/s) are analysed later. However production efficiency must also be considered in the industrial world.

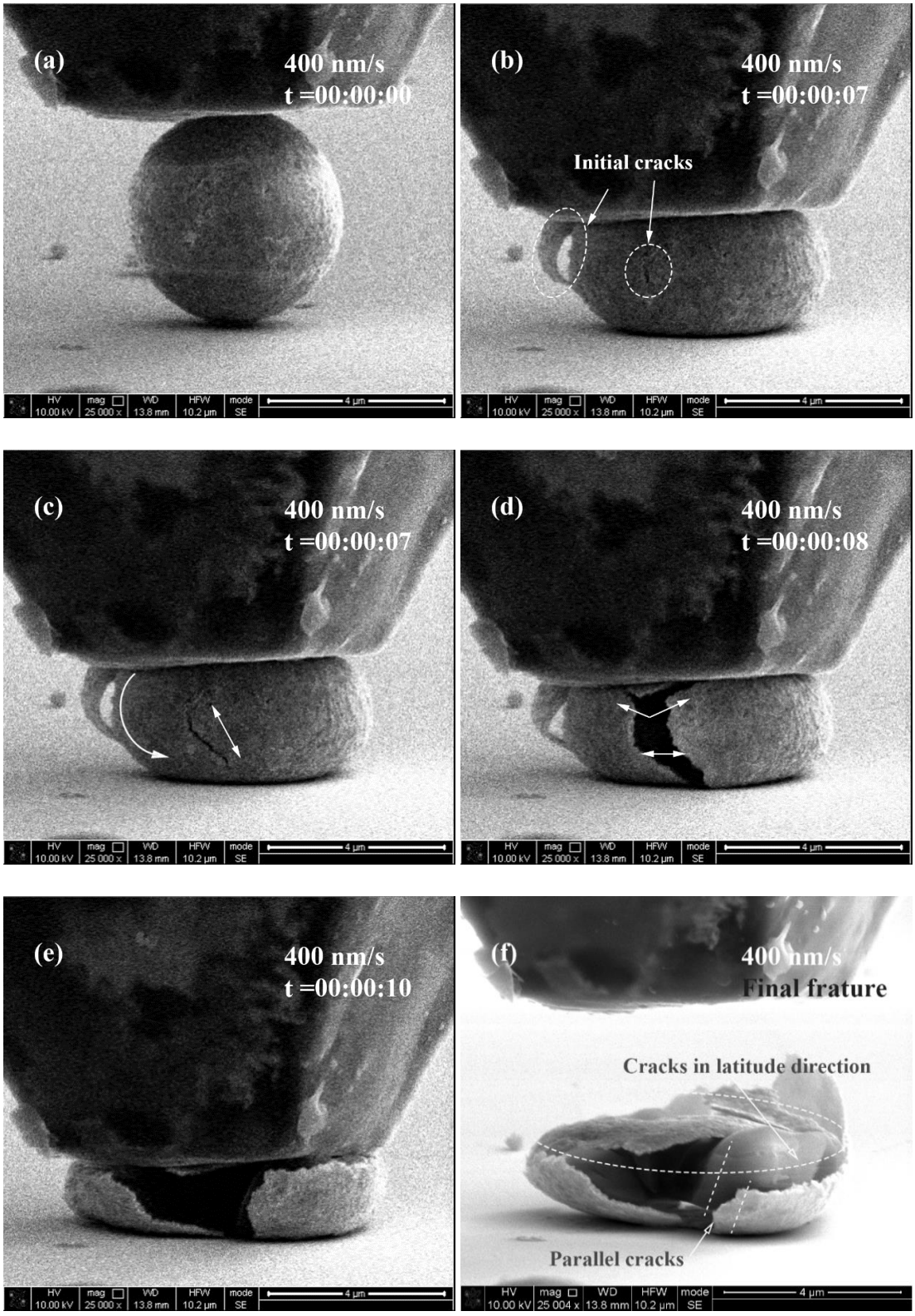

Figure 3.28 Individual frames from the in-situ video record for the individual Ni/Au coated polymer core particle compression test at 400 nm/s.

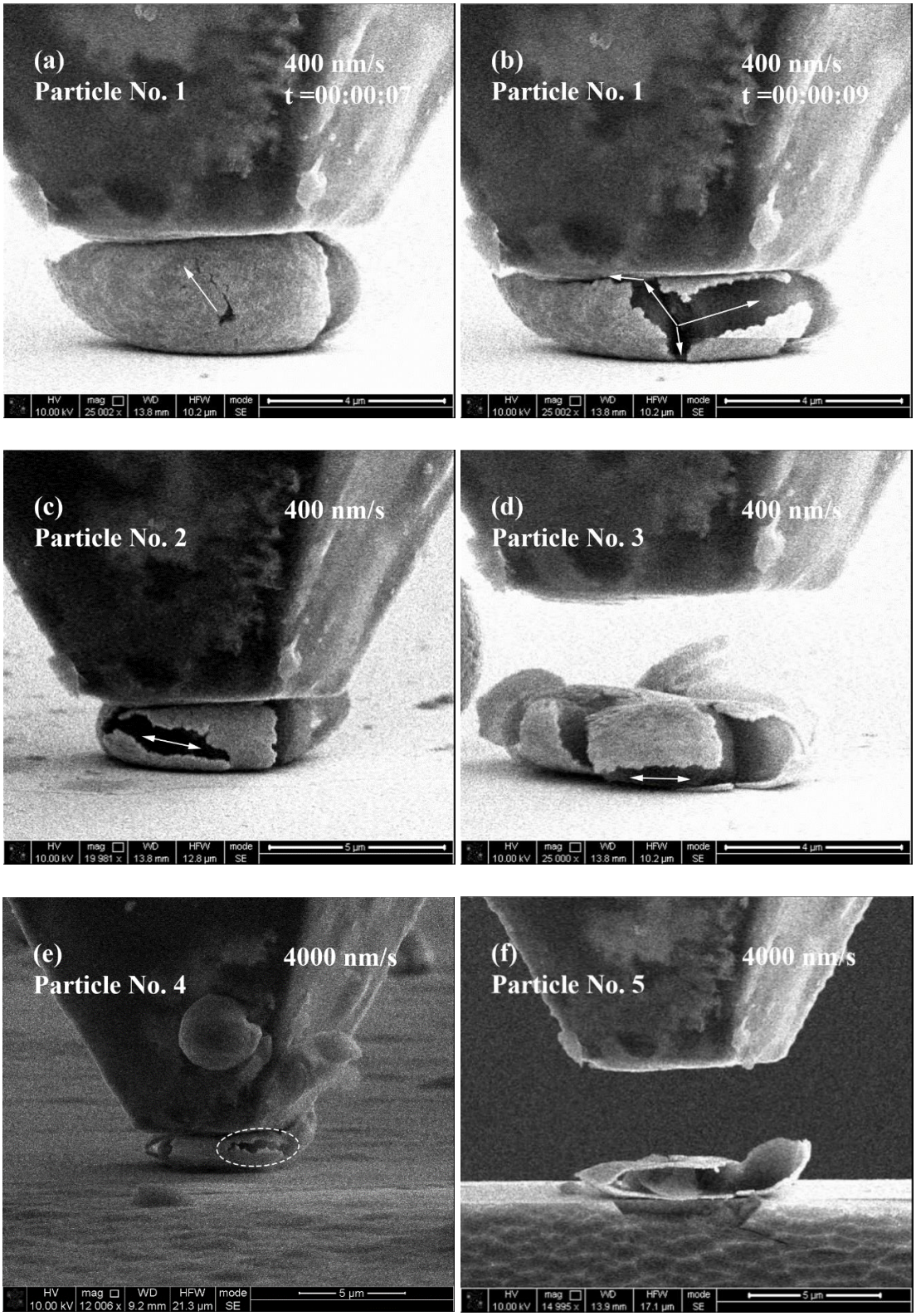

Figure 3.29 Individual frames from the in-situ video record for the individual Ni/Au coated polymer core particle compression test at 400 nm/s and 4000 nm.

Compared with the results at high strain rates, the compression results at the extremely low strain rate of 0.00083 s^{-1} (4 nm/s) revealed different mechanical deformation behaviour, as

shown in Figures 3.30, 3.31, and 3.32 (a). One of the typical tests of the particle at 4 nm/s is illustrated in Figure 3.30. The first crack commenced at an initial defect location, and then propagated upwards gradually within several minutes under compression as shown in Figure 3.30 (a), (b), and (c). The difference is that the slow compression process enables the metal layer to deform plastically instead of sudden fracture as depicted in Figure 3.30 (d). This is believed to due to the viscoelastic behaviour of the polymer core at slow loading rate reducing the stress concentration of nickel layer. The propagation directions of other cracks were observed to be longitudinal, and no latitudinal cracks were found for the Ni/Au coated particles at the strain rate of 0.00083 s^{-1} (4 nm/s). More importantly, at the applied deformation rate of 4 nm/s, the polymer core of the metal coated particles did not show any severe cracks and remained intact after compression, which is consistent with the results for pure polymer particles. Even though some severe cracks and delamination exist, most of the metal coating layer remains in good contact with the polymer core, as shown in Figures 3.30 (f), 3.31, and 3.32 (a). Consequently, the conductivity of the particle at 4 nm/s is believed to be less effected than at higher strain rates. In contrast, as can be seen in Figure 3.31 (b), (c), and (d), bursting of the polymer core produced a pushing effect, which aggravated the latitudinal cracks of the metal coating layer. It should be noted that cracks in some parts of the polymer core occurred in all tests except for the extreme low deformation rate of 4 nm/s, and its influence is much lower than the crushed parts as shown in Figure 3.32, which needs to be avoided.

In conclusion, the cracks occur in the metal layer first, while some corresponding initial defects are created as a result of the metal cracks. The polymer core starts to crack and those propagate quickly until the particle reaches a relatively large deformation level, when the fracture of the polymer core leads to the final crushing of the Ni/Au-MCP. It is worth noting that the strain rate dramatically impacts on the deformation behaviour of the Ni/Au coated polymer particles. The first aspect is that the cracks initiation position and its propagating direction are significantly affected by the strain rate. The probability of latitudinal cracks increases substantially from 0% to 100 % as a results of the increasing strain rate from 4 nm/s to 4000 nm/s. At the same time, the increasing strain rate contributes to a more severe fracture morphology due to its viscoelastic characterisation of the polymer core, which intensifies the latitudinal cracks hence affecting the conductivity of the Ni/Au coated particle under compression. A lower deformation rate is therefore recommended based on the comprehensive analysis of the compression results. Whilst deformation rates are preferred for the industrial world considering the work efficiency. Further experiments, including t electrical conductivity tests and high temperature tests are necessary to establish the optimized loading conditions.

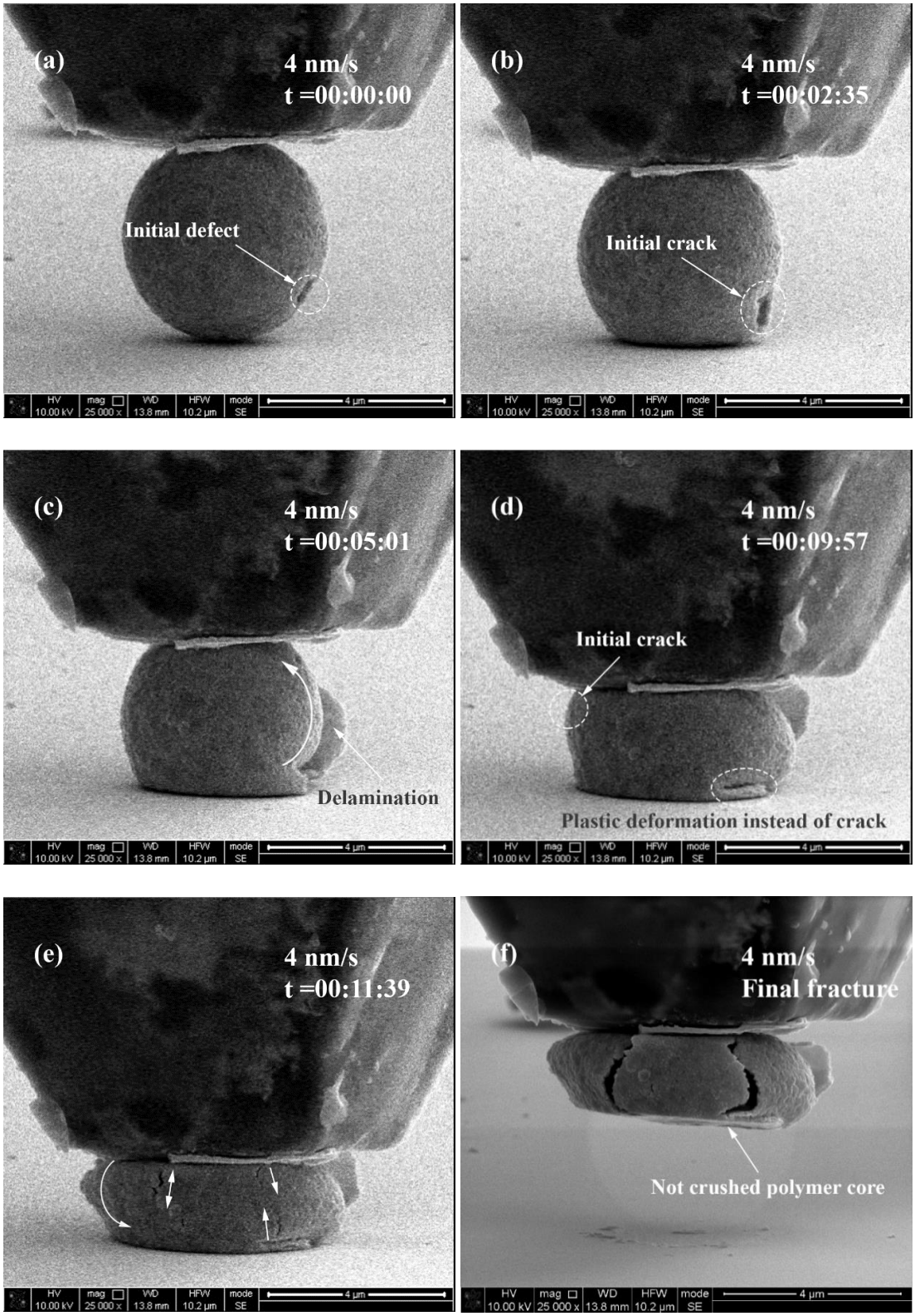

Figure 3.30 Individual frames from the in-situ video record for the individual Ni/Au coated polymer core particle compression test at 4 nm/s.

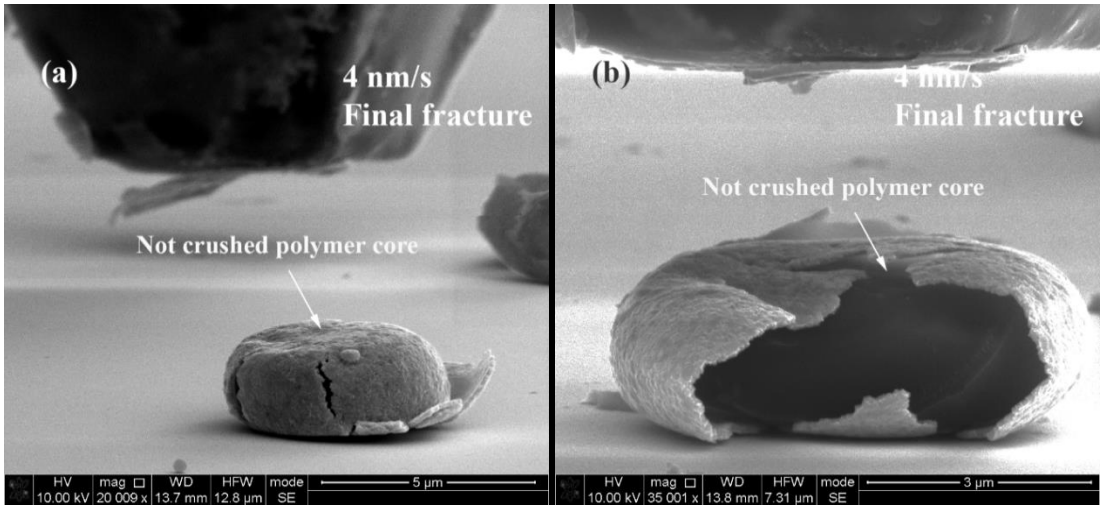

Figure 3.31 SEM images showing the morphology of Ni/Au coated polymer core particles after the compression test at 4 nm/s.

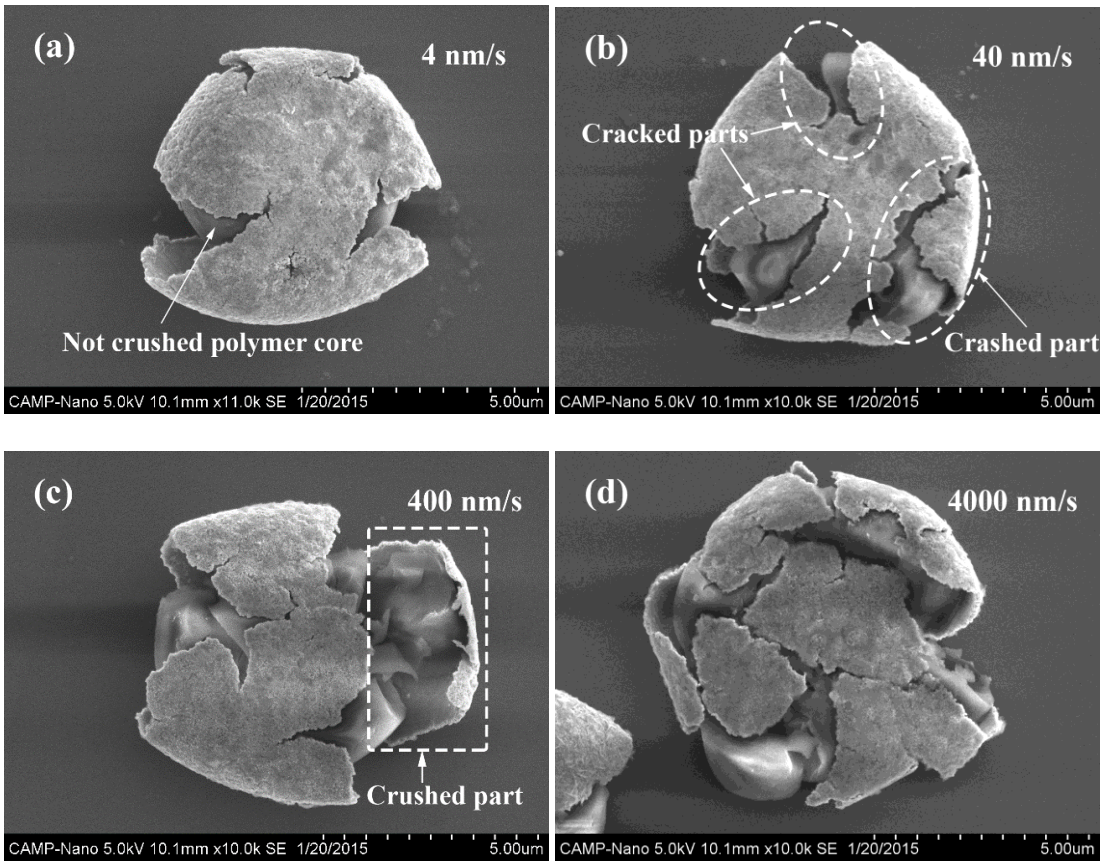

Figure 3.32 SEM images from the top view showing the fracture morphology of the Ni/Au coated polymer core particles after the compression test at (a) 4 nm/s, (b) 40 nm/s, (c) 400 nm/s, and (d) 4000 nm/s.

3.5 Finite Element Analysis

Given the small size of particles, the in-situ nanomechanical system in SEM has enabled the experiment setup for individual particles tests with direct observation during compression, and the achieved results were significant helpful to study the viscoelastic behaviour of the particles. The direct observations have revealed several different crack and failure modes. However the stress distributions within the polymer core and metal coating layer have not been revealed, and the analysis of the crack initial locations and propagate patterns is limited to suppositions without strong support. Finite element analysis (FEA) provides an efficient way to study the complicated material (Ni/Au coated polymer core) and geometrical (sphere) effects. Lots of FEA models can be built to study the significance of viscoelasticity of the polymer core, stress distributions within each material, effects of loading conditions, cracks propagation, temperature effect etc. In this research, the FEA analysis using COMSOL Multiphysics is still at the initial stage. The models were built based on the results shared by Dr. Jianying He in NTNU, and only limited work has been established. Further FEA analysis will be carried out using the in-situ nanomechanical test, and more work will be established to better understand the experimental results.

3.5.1 Material property extraction from compression experiments

A Maxwell-Wiechert model was adopted for simulation of the particle compression process. where the overall material response is a combination of linear elastic and viscoelastic components which can be represented schematically as a linear spring together with "dashpot" and spring pairs, as shown in Figure 3.33 [138]. In this model there can be as many spring-dashpot branches as are required to approximate the observed material behaviour satisfactorily.

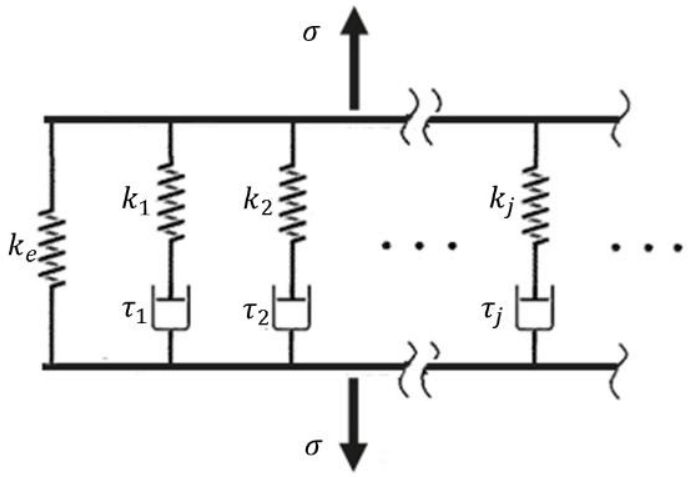

Figure 3.33 Schematic representation of the Maxwell-Weichaert model [138].

The total stress, σ, in the model is the stress in the linear elastic spring, $\sigma_e = k_e\varepsilon$, plus the viscous stresses, σ_v , resulting from the sum of each Maxwell spring-dashpot arm stress σ_i , i.e:

$$\sigma = \sigma_e + \sigma_v = \sigma_e + \sum_{i=1}^{j}\sigma_i \qquad (3.11)$$

The individual dashpot stresses are proportional to the internal strain rate i.e. $\sigma_d = \eta\dot{\varepsilon}_d$ where σ_d is the individual dashpot stress, η is the viscosity of dashpot, and ε_d is the strain. The relaxation time, τ_i, of each Maxwell arm is $\tau_i = \eta_i/k_i$, where η_i is the coefficient of viscosity of the dashpot, and k_i is the elastic modulus of the spring in this branch, and ε is the total strain. By applying a Laplace transformation the stress in each Maxwell arm can be calculated as [138]:

$$\overline{\sigma_i} = \frac{k_i s}{\left(s + \frac{1}{\tau_i}\right)}\bar{\varepsilon} \qquad (3.12)$$

Then the overall stress-strain relationship is given by

$$\bar{\sigma} = \overline{\sigma_e} + \sum_{i=1}^{j}\overline{\sigma_i} = \left\{k_e + \sum_{i=1}^{j}\frac{k_i s}{\left(s + \frac{1}{\tau_i}\right)}\right\}\bar{\varepsilon} \qquad (3.13)$$

The material parameters for the polymer can be obtained from fitting this stress-strain function to the experimental data from the particle compression tests.

At any time, *t*, during a particle compression test the loading force $P = nt$, where n is the load rate. The normalized stress is therefore $\sigma = \frac{nt}{\pi R^2}$, where R is the radius of the particle. So the Laplace transformation of the stress is:

$$\mathcal{L}(\sigma) = \mathcal{L}\left(\frac{nt}{\pi R^2}\right) = \frac{n}{\pi R^2}\cdot\frac{1}{s^2} = K\cdot\frac{1}{s^2} \qquad (3.14)$$

where $K = \frac{n}{\pi R^2}$, which is the normalized loading rate. If there is only one Maxwell-Weichaert branch, the stress-strain differential function simplifies to:

$$\bar{\sigma} = \overline{\sigma_e} + \overline{\sigma_v} = \left\{k_e + \frac{k_1 s}{\left(s + \frac{1}{\tau_1}\right)}\right\}\bar{\varepsilon} \qquad (3.15)$$

Applying the Laplace transformation to the stress:

$$K \cdot \frac{1}{s^2} = \left\{ k_e + \frac{k_1 s}{\left(s + \frac{1}{\tau_1} \right)} \right\} \bar{\varepsilon} \tag{3.16}$$

By reversing the Laplace transformation, the strain ε as a function of time t is:

$$\varepsilon = K \left\{ \frac{t}{k_e} - \frac{\tau_1 \cdot k_1}{{k_e}^2} \left(1 - e^{-\frac{k_e \cdot t}{\tau_1 (k_e + k_1)}} \right) \right\} \tag{3.17}$$

The Young's modulus, k_e , the modulus of the Maxwell branch, k_1, and the relaxation time, τ_1, can be determined by the curve fitting to the experimental data for subsequent use in the FEA models. The normalized stress-strain relationship for the 3.0 μm acrylic copolymer particles at the loading rate of 0.2 mN/s was imported into the software Origin 9.0, and then Equation 3.31 was written into the software to fit the imported data. Table 3.4 lists the materials properties used in this study, where the polymer properties were determined using the fitting process described above. It should be noted that Equation 3.26 refers to the uniaxial experimental data and no constitutional equations describing the stress-strain relationship of viscoelastic behaviour of spherical material have been published due the extremely extreme complicated mathematical issues of a sphere under large deformation. Whilst the normalised stress and strain of the spherical particle were obtained using Equation 3.1 and 3.2. Therefore it is believed that the viscoelastic property parameters obtained from curve fitting were not accurate enough in the modelling.

Table 3.4 Summary of the Materials Properties Used for FEA Models

	Density *(kg/m^3)*	***Young'smodulus*** *(GPa)*	***Poisson's ratio***
Silicon [139]	2329	170	0.28
Nickel [140]	8900	207	0.31
Gold [140]	19320	77.2	0.42
Diamond [141]	3430	1140	0.07
Polymer	1300	k_e=1.5GPa	Poisson's ratio $\nu = 0.33$
	Branch 1	k_1=0.68GPa	Relaxation time $\tau_1 = 300$s

3.5.2 Compression Test Modelling for Individual Particles

FEA including large deformation and friction level was used to simulate the compression behaviour of individual particles, as shown in Figure 3.34. Three models were built using the commercial FEA code COMSOL Multiphysics 4.4 to simulate the behaviour of both the uncoated 3.0 μm acrylic copolymer particles and 3.8 μm Ni/Au-MCPs. These were an uncoated particle model (Model I) with linear viscoelastic Polymer core properties, a Ni/Au coated particle model with elastic polymer core properties (Model II), and a Ni/Au coated particle model including viscoelastic core properties (Model III). The models used two-dimensional axisymmetric elements to greatly reduce the number of degrees of freedom in the model and therefore significantly reduce the analysis time. The complete mesh consists of 3041 triangular elements, and the number of degrees of freedom solved is 36221. The bottom face of the silicon has all of its nodes fixed in the vertical direction, while the load force is applied through the top surface of the diamond layer, thereby simulating the experimental setup. Although monocrystalline, both silicon and diamond were treated as being isotropic since their anisotropy was not expected to have any significant effects in this situation. The study was set as time dependent ranging from 0 to 500 s using the loading rate of 0.02 mN/s. The differences between the purely elastic model and the viscoelastic model were compared to gain a better understanding of the effect of viscoelasticity in the polymer core material on the particle behaviour. The uncoated particle model was used to verify the validity of the model, and the results used to improve the Ni/Au particle model to obtain better modelling results. As the polymer viscoelasticity makes it sensitive to the loading rate, an analysis of the particle fracture mechanism was conducted by analysing the variation in stress distribution within the nickel layer with loading rate.

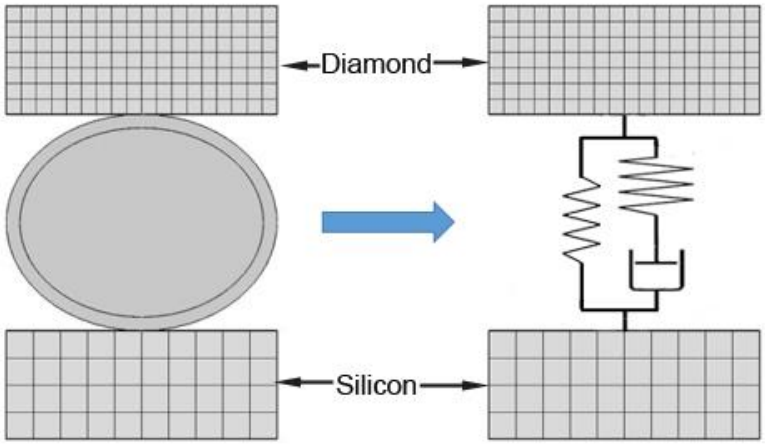

Figure 3.34 Schematic images of particle compression test with equivalent spring and damper model.

It was found that the calculation cannot reach the time of 500 s and stopped in the middle when reaching a very large deformation level. Figure 3.35 illustrates the predicted deformation and von Mises stresses for an uncoated particle at a load of 1 mN and loading rate of 0.02 mN/s. The results predict that for the uncoated particles the stress concentrates either side of the contact area, with substantially lower stresses occurring at the actual contact surfaces.

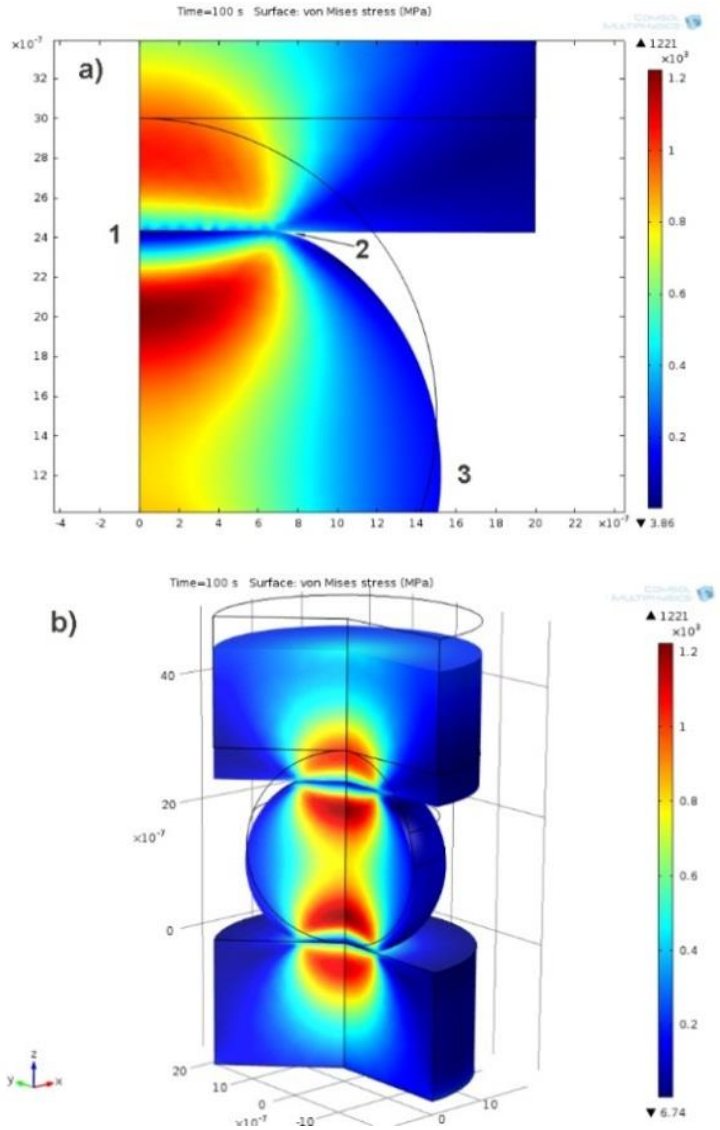

Figure 3.35 Combined deformation and von Mises stress plots for uncoated particles (FEA Model I) (a) cross-section through centre of contact area and (b) 3D plot.

Point 1 and 2 are at the centre and edge point of the contact area respectively, while Point 3 is on the equator of the particle. Figures 3.37, 3.38 and Figures 3.39, 3.40 show the difference in stress between a purely linear elastic model (Model II) and one considering the viscoelasticity of the polymer core (Model III) along the curve from Point 1 to Point 2, and then Point 3. From these images, it can be seen that around the contact area, the outer face of the nickel layer

endures the highest stress, while the stress at the inner face of the nickel is higher, except in the contact area. Meanwhile introducing viscoelasticity into the polymer properties has a significant effect on the whole structure, but especially on the stress at the interface between the nickel layer and polymer core. When including viscoelasticity in the model, the polymer core damped the deformation showing less stress level and redistributed the stress between the polymer core and inner face of nickel layer.

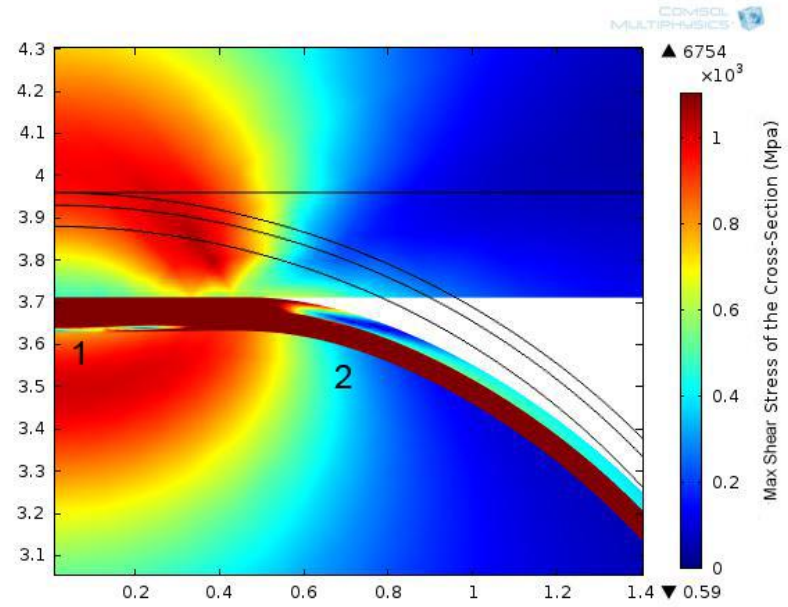

Figure 3.36 Maximum shear stress plot for a cross-section through a Ni/Au coated particle with viscoelasticity (Model III).

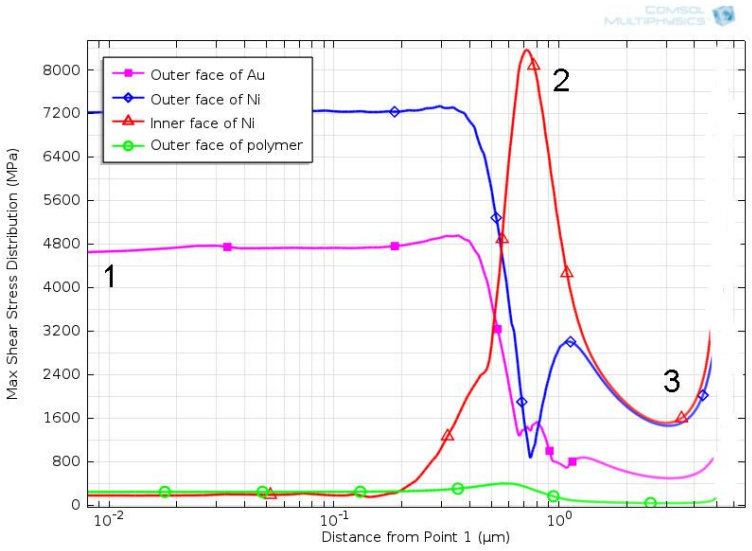

Figure 3.37 Maximum shear stress in the different layers of the Ni/Au coated polymer particle versus position along the curve from Point 1 for the purely elastic Model II.

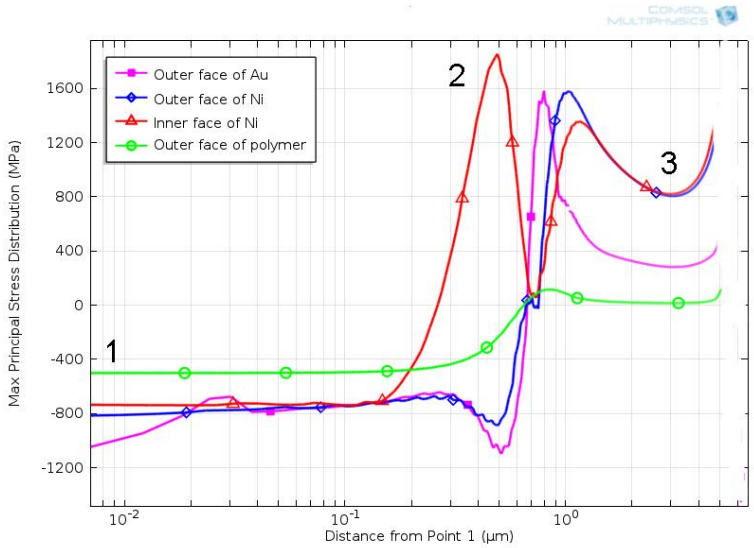

Figure 3.38 Maximum principal stress in the different layers of the Ni/Au coated polymer particle versus position along the curve from Point 1 for the purely elastic Model II.

Figure 3.39 and 3.40 illustrated the stress distribution of maximum shear stress and maximum principal stress for the viscoelastic Model III. It can be seen that the inner face of nickel layer at Point 2 is the stress concentrated location for both the maximum shear stress and maximum principal stress, which is believed to be the most vulnerable point under compression. Compared with the stress distribution for pure elastic model, the overall maximum shear stress decreased after considering the viscoelastic property of the polymer core except for the increasing shear stress of polymer core. In terms of the maximum principal stress, the stress of Point 2 decreased substantially from approximately 1,800 MPa to about 850 MPa, which proves that the viscoelastic property plays a significant role under compression.

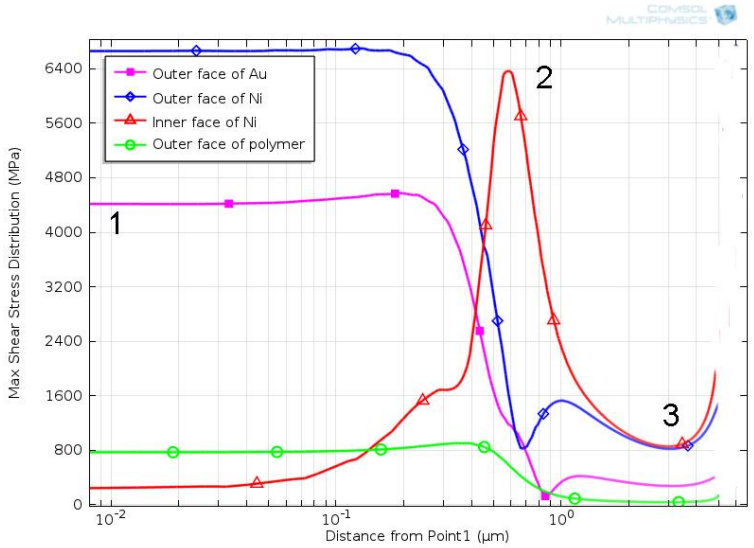

Figure 3.39 Maximum shear stresses in the different layers of the Ni/Au particle versus position along the curve from Point 1 for the viscoelastic Model III.

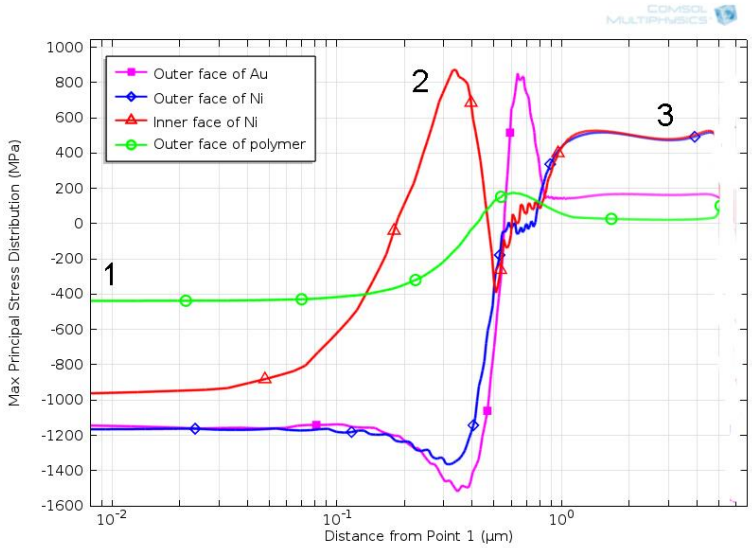

Figure 3.40 Maximum principal stresses in the different layers of the Ni/Au particle versus position along the curve from Point 1 for the viscoelastic Model III.

3.5.3 Analysis of Crack Initiation and Propagation Based on FEA Results

During the ACA bonding process, fracture of the metal coating strongly affects the mechanical and electrical properties of the resulting interconnections [142]. There three two different cracks modes that were observed in the compression experiments depending on the applied loading conditions i.e. cracks initiated in the region in contact with the substrate/diamond tip and propagated in longitudinal direction, and cracks initiated at the equator then propagated in latitudinal direction [143], which is consistent with our findings. The most likely fracture structure during compression was similar to our experimental finding as shown in Figure 3.26 and Figure 3.27. The maximum shear stress and maximum principal stress distribution of the Ni/Au coated particle under compression are illustrated in Figure 3.38 and 3.39 considering the viscoelastic characterisation of the polymer core.

It is apparent that the stress concentrates in a ring at the inner surface of the Ni layer near to the edge of the contact area between the particle and substrate or punch. This location is identified as Point 2 and is therefore the most vulnerable location for a crack to initiate. Unlike Point 1 and Point 3, which are fixed, Point 2 being near to the edge of the contact area moves toward Point 3 with increasing compression. During this process, the stress in the polymer also increases until Point 2 reaches its ultimate tensile strength when fracture will initiate at this location. As point 2 progresses gradually towards Point 3 as the particle flattens, the crack evolves in the radial direction. The metal layer in the model is effectively perfect, whilst initial defects have been observed to exist in the Ni/Au coated particle. So, in the latitudinal direction, the areas around these initial defects are the vulnerable locations, and in the longitudinal

direction Point 2 is the highest stress concentrated point. As a result, the crack is believed to initiate at the cross point between the contact corner and the longitudinal circle with initial defect, then propagate toward the initial defect quickly, which is consistent with the experimental data as shown in Figure 3.26 and 3.27 The second crack model, where the crack initiates at the middle part of the particle and also propagated in the longitudinal direction is believed to be related to the hoop stress of the metal coating layer. As discussed earlier, this second crack model is very likely to evolve into a "Y" structure crack with two latitudinal cracks when approaching the contact surface between the particle and diamond tip/silicon substrate. The third kind of crack which initiates in the equator of the particles and also propagates in the latitudinal direction is attributed to the shape changing from sphere to rectangular board due to the severe cracks at two adjacent sides. Further modelling is needed to established the influence of hoop stress and clarify the proposed mechanism for different fracture models.

Instead of a small deformation in linear elastic region which can be fully recovered after removing load, the particle endured a large deformation and plastic deformation of the metal coating layer can be clearly seen from the experimental results. The stresses plotted in this section are relatively very high (Maximum shear stress > 2 GPa). The main reason is that only elastic deformation of nickel and gold layers and viscoelasticity of polymer core are considered in the model. However plasticity of the nickel and gold are not added in the model as well as viscoplasticity of the polymer core. The stress level will reduce significantly when considering the plasticity of the materials. Overall, the deformation of individual particle under compression is very complicated combining various characteristics of the metal coating layers and polymer core. The modelling analysis in this section is at a very initial stage, and these initial models focused on the parameters derivation and model establishing process. The FEA results illustrated for the first time the distribution of shear stress and principal stress within each layers, and helped to better understand the experimental results achieved using in-situ nanomechanical system. In the next step, plasticity of metal coating layers, viscoplasticity of the polymer core, initial defects within the metal coating, and crack simulation etc. will be added subsequently, and consequently more meaningful results can be accomplished in the future.

3.6 Summary

The results from the mechanical characterisations tests on individual pure polymer particles and Ni/Au coated particles have been analysed and discussed in this chapter. This research

established the behaviour of the pure polymer particles and Ni/Au coated particles at different loading conditions and analysis of pure polymer results allowed estimation of the polymer viscoelastic properties. Meanwhile the novel in-situ nanomechanical compression tests used in this research for the first time enables the detailed study on the crack propagation and fracture pattern of the particles. The data were used to create the FEA models, and the FEA analysis contributes to a better understanding of the deformation behaviour of the particle under compression. The results have significant practical value for the industrial applications.

Significant findings include:

- The mechanical deformation of individual particles are strongly effected by different loading conditions, indicating that both the polymer particles and Ni/Au coated polymer particles are heavily rate-dependent materials. This is attributed to the viscoelastic characteristics of the polymer core.
- Both kind of particles show clear strain-rate hardening phenomenon. The strain-rate sensitivity index of the polymer ranges from 0.038 to 0.053, while that of the Ni/Au coated particles is in the range of 0.047 to 0.058.
- Two modulus, initial modulus and high-strain modulus, are defined to describe the mechanical deformation process of individual particle, and both moduli show clear relationship with the loading rates and strain rates. Strain-rate coefficient and sensitivity for the high-strain modulus are defined, which can be used to forecast the deformation behaviour of the particles at different loading conditions.
- The initial modulus of the Ni/Au coated particles are much higher than that of polymer particles due to the existence of harder metal coating layer. However the high-strain modulus of the Ni/Au coated particles ranges from 3.8 GPa to 4.5 GPa, which are even slightly lower than those of polymer particles ranging from 3.9 GPa to 4.9 GPa at different strain rates. The reason is supposed to be the crack of the metal coating layer bringing initial defects to the polymer core, thereby reducing the stiffness of whole particle. This is also confirmed by the subsequent in-situ compression experiments.
- No obvious cracks were observed during the first deformation process of the pure polymer particles until reaching a a large strain (around 50%). The cracks were found to initiate in the region in contact with silicon substrate/diamond tip surface, and then propagate rapidly in the longitudinal direction leading to the final fracture of the polymer particle. Due to viscoelastic behaviour of the polymer core, higher strain rates limits the time for the movement between molecular chains to dissipate the applied energy, thereby resulting in the severe cracks. In contrast, the polymer particle remain intact without observed cracks at the lowest strain rate of 0.00086 s^{-1} (4 nm/s).
- The deformation of Ni/Au coated particles is summarised into three steps: in the first

deformation region both the polymer core and metal coating can tolerate the strain and stress without cracks; the cracks initiate in the metal coating layer and then propagate in different directions at the second deformation step, where some corresponding initial defects are believed to be created in the polymer core; at the final step it is the failure of the polymer core that results in the crushing of the Ni/Au coated particles.

- There are three patterns of cracks observed in the experiments. The first is that the cracks initiate in the region in contact with the silicon substrate/diamond tip surface and propagate longitudinally. The second is that the cracks initiate in the midline circle of the Ni/Au coated particles and this is very likely to induce subsequent latitude cracks when approaching the contact surface forming the ultimate "Y" structure crack. The third kind of cracks initiate at the exact equator of the particle and propagate in the latitudinal direction. The probability of latitudinal cracks rise substantially with the increasing strain rate. Whilst the Ni/Au coated particles at the extreme low strain rate display small cracks and good integrity. The longitudinal cracks are believed to be less effective to the conductivity of the Ni/Au coated particles under compression, which however can be significantly impacted by the latitudinal cracks. Therefore higher applied deformation rates should be carefully controlled from the aspect of the academic study, while production efficiency is a compulsory parameter which must be considered in the industrial world.
- The experimental data was used to establish the viscoelastic model for the finite element analysis (FEA). The FEA study confirmed the importance of the viscoelastic characteristics of the polymer core by comparing the pure elastic model and viscoelastic model. The plotted stress distribution within the polymer particle and Ni/Au coated particles helps to explain the crack propagation patterns. The maximum shear stress and principal stress concentration area locates at the inner surface of the nickel layer around the region in contact with silicon substrate/diamond tip, which determines the initial crack combined with the place of initial defects on the metal coating layer. The cracks initiate in the middle of the particle is believed to be closely related to the hoop stress, and further modelling analysis is needed to better understand the latitudinal cracks.

Chapter 4

Electrophoretic Deposition of ACA Conductive Particles

4.1 Introduction

In electronic interconnections with anisotropic conductive adhesives (ACAs), large amount of particles must be used to ensure at least several particles can be captured during the bonding to enable the conductivity of the junction, which on the other hand increases the possibility of bridging. Meanwhile, following the increasing demand for high-density interconnections, ACAs are becoming more and more difficult to meet the challenge of fine or ultra-fine pitch packaging, because bridging and open circuits are much more likely to occur on this occasion. Electrophoretic deposition (EPD) technology has been developed over hundreds of years, and EPD is becoming increasing popular and attracting widespread interest recently due to its simplicity, the speed and purity of the resulting deposits, cost-effective setup process, and compatibility for a wide range of materials. However little work in literature was available on the electrophoretic deposition of micro-scale metal particles because of their higher density leading to severe sediment issue during deposition.

As discussed in chapter 3, compliant Ni/Au coated polymer particles have a relatively lower density due to the large volume percentage of the polymer core, hence providing an opportunity for a longer suspending time in adequate solvent for the electrophoretic deposition. Some initial attempts have shown that the Ni/Au coated polymer particles can be deposited electrophoretically onto the pads of an application-specific integrated circuit device (ASIC) such as flip-chip interconnections [144]. This selectively depositing method maintains the benefits of ACAs integration, and saves large number of excess particles in conventional ACAs packaging, increases the particles density on the pads without causing the short-circuiting, thereby making it possible for a fine or ultra-fine pitch flip-chip packaging, as shown in Figure 4.1.

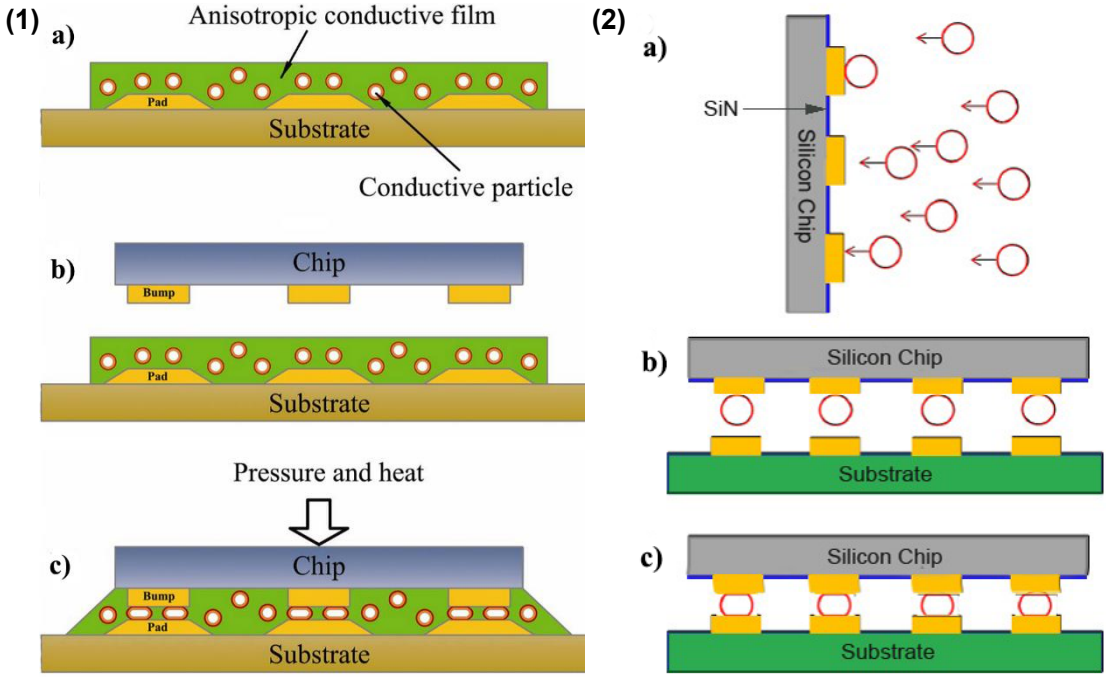

Figure 4.1 Schematic diagram of (1) conventional ACA bonding process: a) pre-bonding; b) alignment; c) final bonding [46], and (2) EPD process: a) particle being deposited onto bond pads of the device; b) flip-chip being aligned with the substrate and c) particles forming interconnection.

There are two steps during electrophoretic deposition process, one is the migration of charged particles under an electric field towards the oppositely charged electrode, and the other step is their subsequent deposition at the electrode surface. During the EPD process the deposition of the particles in the suspension is determined by the combination of physical and chemical properties, including the size and shape of the particles, their charge and suspension concentration, the liquid viscosity and the applied electric field strength. This chapter presents the chips, apparatus, deposition system, and experimental methodology for electrophoretic deposition of Ni/Au coated particles. The mechanism of the acid immersion charging method was systematically analysed, consequently novel effective harmless charging method was developed based on the better understanding of the zeta potential. Even though electrophoretic deposition has been developed and utilised since the 19th century, the mechanism of this deposition process is still a matter of debate [145]. In this chapter, research was performed to investigate the assembly mechanism of the electrophoretic deposition of Ni/Au coated particles using metal cations charging method. The results of zeta potential of the Ni/Au coated particles as a function of the pH value and salt concentration are presented, followed by the evaluation of electrophoretic deposition quality using different alternative metal cations charging approach. The silicon chips with electrophoretically deposited particles were used for the subsequent bonding process, and the results are presented in Chapter 6.

4.2 Materials and Apparatus

4.2.1 Materials

4.2.1.1 Particles

Two kinds of particles, Type I and Type III, are used in the experiments in this chapter, which are the Ni/Au coated polymer core particles of two diameters, i.e. 4.66 μm and 9.8 μm. The details of these particles are given in the materials section in Chapter 3.

4.2.1.1 Test Chips

The chips used in this project were dummy components without active circuitry, and the bump pattern and metal paths were designed for the subsequent measurement of electrical resistance once bonded forming interconnections. The materials involved in the interconnects include silicon, nickel, gold, aluminum, and titanium, as such three groups of these chips are considered based on the materials composition. For these three categories of chips, each group has its unique advantages which can be applied for different experiments. Two kinds of chips were used in the electrophoretic deposition experiment, and their materials, layout design, and special merits are illustrated in details in this section.

Two types of Si based chips were designed and fabricated with two different structures: daisy-chain structure and Kelvin structure as shown in Figure 4.2, which enables the subsequent mechanical and electrical test after bonding. The pad consists of a thin adhesion layer of Cr of approximately 12 nm thick, and a deposited layer of Au of 250 nm. The regions on the substrate surrounding the pads are covered with a 100 nm thick passivation layer of Si_3N_4, thus separating the conductive from the non-conductive regions which creates the application potential for selective electrophoretic deposition. The size of square pad ranges from 50 μm, 100 μm, 200 μm, to 300 μm, for the tests of the deposition preference of each deposition process. The pads are distributed along four sides of the chip, forming a daisy-chain structure when bonded to the matching substrate chip. The daisy-chain structure can increase the testing number of the interconnections to decrease the error deviation of the test of each individual interconnection. Therefore, the chips with daisy-chain structure can meet both the challenges of deposition preference limitation and the relative accurate test of resistance of interconnection. As shown in Figure 4.2 (d), another chip structure is the kelvin structure. This structure enables the four-point resistance testing which significantly increases the testing accuracy of the middle interconnection. Meanwhile, this structure can also help to calculate the resistance of the conductive patch, which can be used to correct the measurement of daisy chain chips.

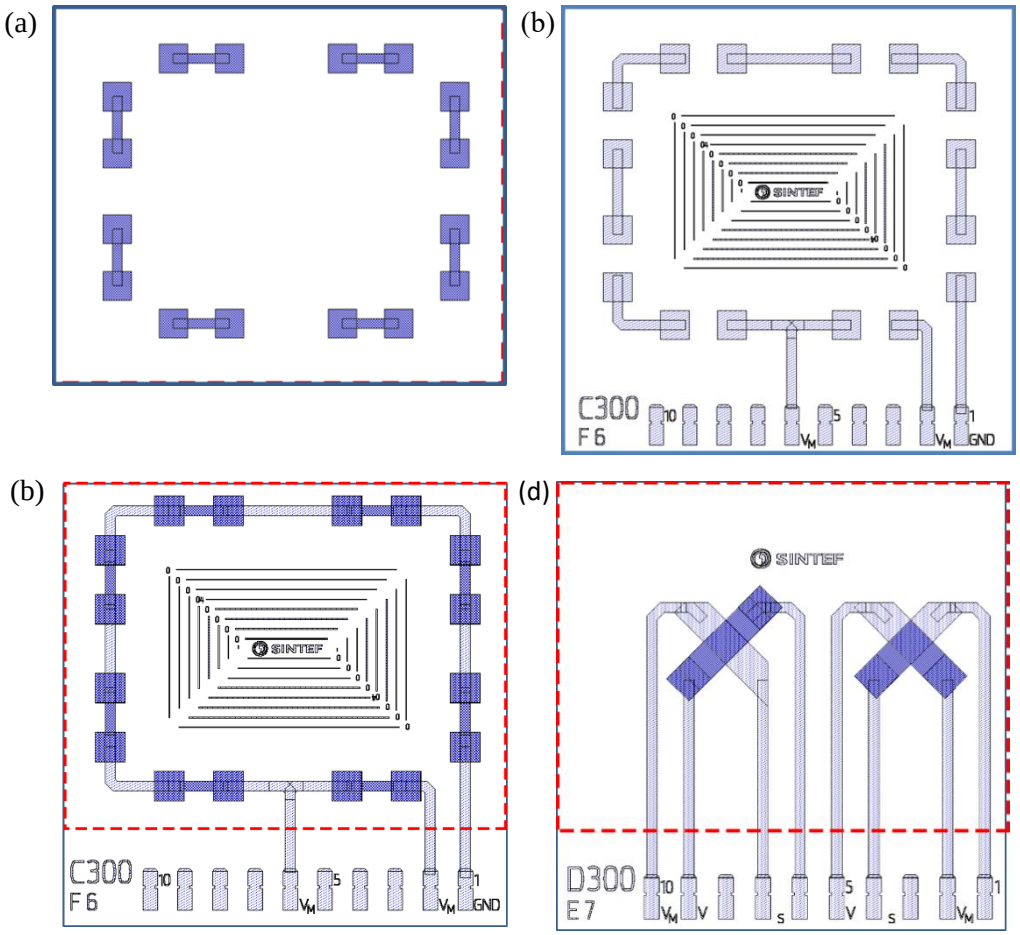

Figure 4.2 Schematic images showing the chip structures: Daisy chain structures (a) top chip (4.5 × 3.8 mm) with edge distributed square pads, (b) substrate chip (4.5 × 3.8 mm) with the testing circuitry, (c) the daisy chain interconnections formed after bonding top and substrate chip, (d) kelvin structure chips after bonding two part.

Ferromagnetic materials are not included in the chips described above; therefore the second group of chips were fabricated which can be used for both electrophoretic deposition and magnetic assembly processes. Besides the daisy-chain and Kelvin structures, a third structure is designed to test the limitation of various self-assembly methods, as shown in Figure 4.3. Instead of Cr/Au pads, the pads were coated with a 50 nm thick titanium adhesion layer by magnetron sputtering, followed by layers of nickel and gold with the thickness of 50 nm, 500 nm, and 50 nm respectively. The remaining area of the chip was coated with a 200 nm insulation layer of Si_3N_4 through inductively coupled plasma chemical vapor deposition (ICPCVD). The electrical conductivity of Si_3N_4 ranges from 10^8~10^{10} Ω·m, while for gold it is only 2.3×10^{-8} Ω·m, therefore they can also be used for electrophoretic deposition due to the significant difference of electrical resistance.

With the development of more sophisticated and minimized electronic devices, the demand for higher input/output (I/0) density has been continuously increasing. Some applications have already been utilized to meet this challenge, such as the flip chip ball grid array (FCBGA) [146]

and wafer level chip scale packages (WLCSP) [147], and the pitch between the pads is becoming smaller and smaller. Therefore the chips with different pad arrays were designed and fabricated. The bump pitch refers the distance between two adjacent bump centre, and the bump spacing is the gap from one bump to the adjacent one. With regard to this kind of chips, different diameters of the pad ranges from 10, 20, 30, 40 to 50 μm, and the pitches between the pads also vary from 15 to 90 μm. All these three kinds of chips with different structures were designed in the same wafer in order to ensure the consistency of the chip materials. Individual chip was separated through a following dicing process.

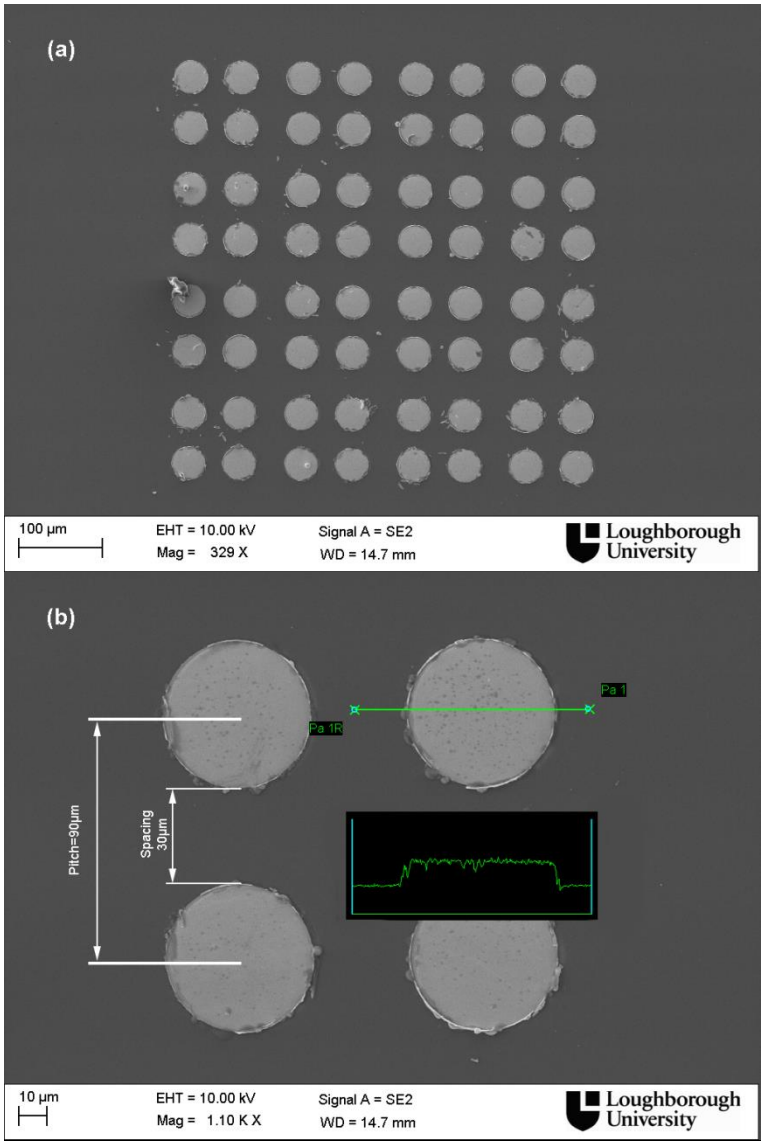

Figure 4.3 Pad array structure of chips, (a) 64 pads array with the diameter of 40 μm, (b) standoff of the pad compared with the substrate.

4.2.2 Apparatus

Zetasizer Nano ZS

The zeta potential of the samples was tested using Zetasizer Nano NS fabricated by Malvern Instrument Limited as shown in Figure 5.2. With the implementation of second-generated technique of phase analysis light scattering combined with the patented mixed-mode measurement (M3-PALS), this Zetasizer Nano system significantly simplifies the zeta potential test process and also improves the measurement accuracy. PALS is a variation of laser Doppler velocimetry (LDV), and LDV measures the particle mobility generated using the frequency shift of light caused by the particles moving in a classical electrophoresis cell. The mobility measured is then converted to zeta potential using established theories. PALS is much more sensitive technique that utilises the information contained in the phase of the scattered light to determine the frequency shift, and the measured phase shift is directly proportional to the change in position where the electrophoretic mobility is lower than the typical 10^{-8} m^2/sV found in aqueous media. M3 is a relatively new technique for measuring zeta potential, and it combines the best features of measurement at the stationary layer and the recently fast field reversal technique. The combination of M3 and PALS, M3-PALS, generates unprecedented accuracy and resolution for zeta potential measurement [Malvern website]. As shown in Figure 4.4, the model Zetasizer Nano ZS provides accurate measurement for the particle size ranging from 0.3 nm -10 microns, zeta potential ranging >+/_500 mV, as well as some parameters of the suspension i.e. the conductivity and viscosity. The zeta potential measurement system comprises of six main components as schematically shown in Figure 4.5.

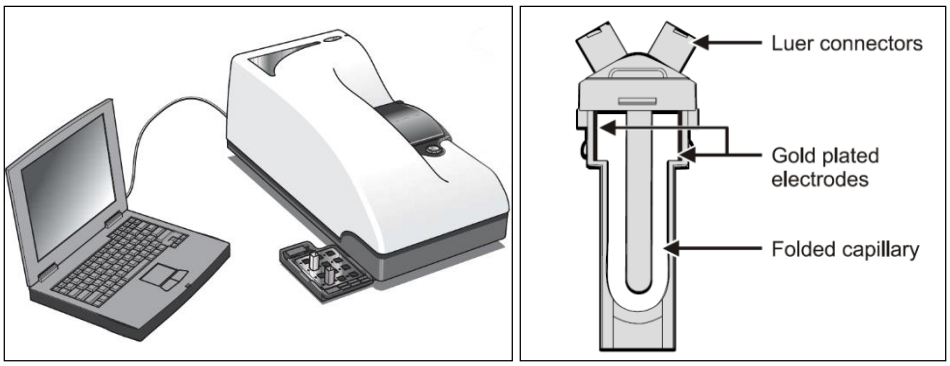

Figure 4.4 Zetasizer Nano ZS Malvern system (a) Zetasizer instrument and the connected computer with the installed Zetasizer software, (b) folded capillary cell for zeta potential measurement.

First a source light is created by a laser ① to illuminate the particles within the suspension. This light source is split into the incident and reference beam. The incident laser beam passes through the centre of the sample cell ② and the scattered light is detected at an angle of about

13° ③. Under an electric field applied in the cell, any particles moving through the measurement volume will cause the intensity of light, which can be detected to fluctuate with a frequency proportional to the particles speed. The information is collected by the digital signal processor ④ and then passed to the computer ⑤. The software in this Zetasizer Nano software produces a frequency spectrum, hence calculating electrophoretic mobility, and finally the zeta potential is provide based on the established theories coded in the software. The scattered light must be within a specific range so that can be successfully detected and measured, which is achieved by the attenuator ⑥ by adjusting the intensity of incident beam light and hence the intensity of the scattering. In order to correct any differences in the cell wall thickness and dispersant refraction, compensation optics ⑦ are installed to maintain the optimum alignment.

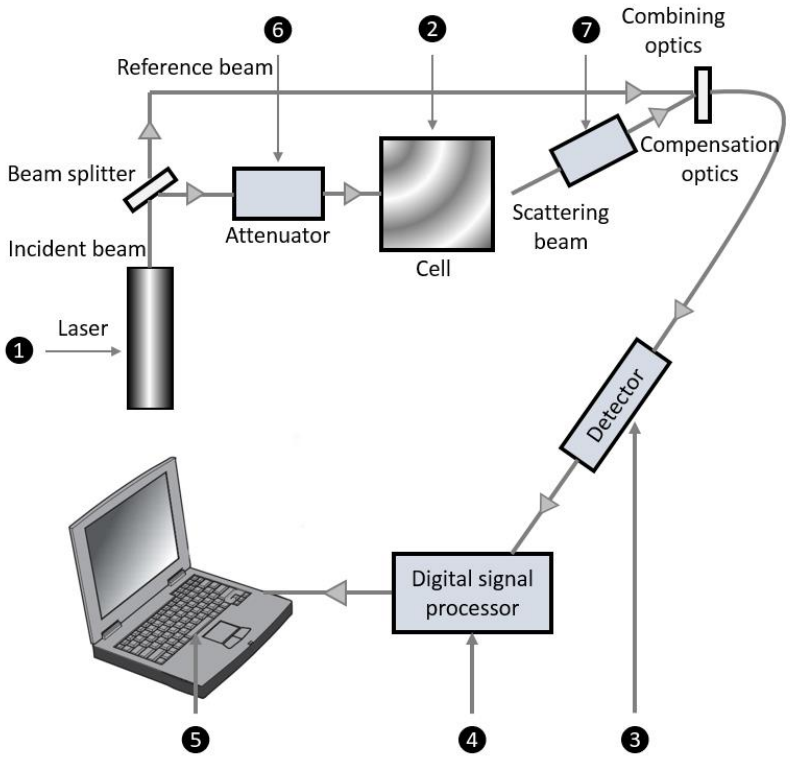

Figure 4.5 Optical configuration of the Zetasizer Nano series for zeta potential measurement.

4.3Experiment Methodology

4.3.1 Deposition system

Due to the small size of the chips, a specific system for electrophoretic deposition has been established as show in Figure 4.8. A vacuum pump was used to generate the vacuum

environment, which connects to the metal tube through a conical flask, thereby providing the attracting force for the tiny chip. Meanwhile, the metal connecting with the chip also established the current path between a DC power (PL330 fabricated by Thurlby Thandar Instrument) and chip. The conical flask is the extra safety device to protect the pump from any corruption damage if there is any possible leakage between the chip and metal tip. A feedback and inspect system was built with a multi meter and computer. An ampere meter (Model: MS8226T manufactured by Huayi Ltd.) was connected to this system in series, enabling an in situ current measurement. The computer was used to record the testing data of the ampere meter during the electrophoretic deposition process. A 50 ml Pyrex beaker (Fisher Scientific limited) was used to provide the suitable electrophoretic cell for the deposition of the particles. The anode was well polished aluminium with submerged dimensions of 25mm×20mm×1mm, which was connected by alligator clip. The cathode was the target chip. The circuit consisted of mutually parallel electrodes at a fixed separation distance of 14 mm, connected to a DC programmable power supply.

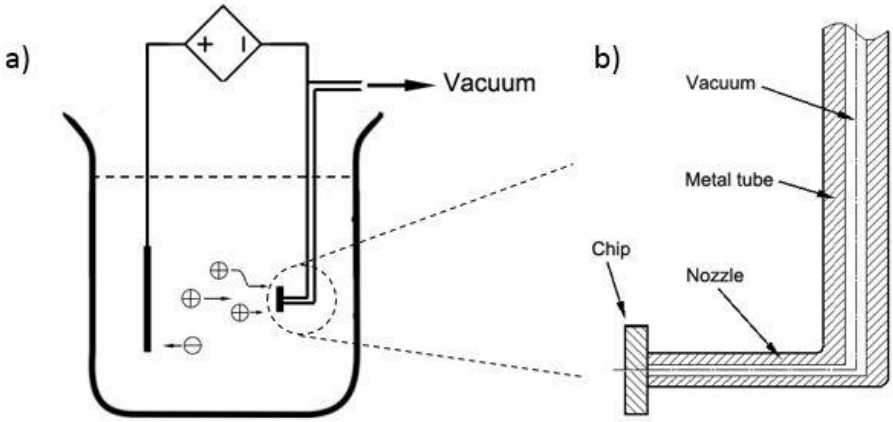

Figure 4.6 Schematic of the electrophoretic deposition system, and (b) detail of the vacuum tip which holds the chips while providing electrical connection.

4.3.2 Acid Charging Method

In order to perform the electrophoretic deposition, the particles should get charged in advance. Previous study has shown that Ni/Au particles cannot be deposited electrophorectically after immersed in the water solution, however can get charged after being immersed into the hydrochloric acid (HCl) solution and then successfully used in the electrophoretic deposition [148]. However the mechanism of this charging process is not clear and the effect of acid immersion on the particles has not been fully estimated.

The EPD process of the particles in this work was carried out using organic solvent isopropyl alcohol (IPA) to avoid the potential electrolysis. Although these particles (1.79 g/cm^3)

are significantly denser than water (1 g/cm^3) or IPA solvent (0.78 g/cm^3), because of their small size they can remain suspended in such solvents for approximately 25 minutes thereby allowing their processing and deposition sufficient time to take place. In this work 30 mg 9.8 μm Ni/Au coated particles were prepared to allow a rapid EPD process by being immersed into 40 ml HCl solution (32% wt%, Fisher Scientific Ltd.) for 30 minutes. Then the suspension was rinsed with deionized water for three times, and subsequently transferred into isopropyl alcohol (IPA) for the following electrophoretic deposition. The ultrasonic bath was used to agitate the suspension for 2 minutes before electrophoretic deposition.

A DC potential of 15 V was applied between the electrodes resulting in an electric field strength of 10.7 V/cm. The deposition time was ranged from 5 to 10 minutes. After the EPD process, the particles left in the suspension were recycled by employing a permanent magnet at the bottom of the beaker thus allowing the separate the particles that were attracted at the bottom from the suspension. The deposition results were observed using FEGSEM, and the effects of acid immersion on the particles were analysed along with the deposition efficiency.

4.3.3 Zeta Potential Study

Zeta potential is an essential parameter in EPD, which plays significantly effects on the suspension stability and particle mobility. It is usually of the order of a few tens of millivolts, and quantifies the charge developed at the interface between a solid surface and liquid medium [16]. Figure 4.7 illustrates the double electrical layers that are believed to form around a charged particle and identifies the zeta potential. In the first (Stern) layer there is a relatively high concentration of counter ions, while in the outer and more diffuse layer, a balance between the electrostatic force and random thermal motion determines the distribution of ions, and the potential decays gradually with the distance from the particle surface, until it reaches that of the bulk solution (which is conventionally taken to be zero). When the suspended particle is placed within an electric field it will move, and the zeta potential is defined as the potential at an imaginary “slipping plane” within which the particle and any of its surrounding ions move through the solution as a unit.

However zeta potential is very difficult to measure directly and it is usually calculated from the mobility of the particle within an electric field using the Henry equation [18]:

$$U_E = \frac{2\varepsilon Z \cdot f(\kappa a)}{3\eta} \tag{4.1}$$

where U_E is electrophoretic mobility, which can be directly measured by Zetamaster, Z is zeta potential, ε is dielectric constant, and η is the viscosity. The unit of κ, termed the Debye

length, is reciprocal length of κ^{-1} which is often taken as measurement of the "thickness" of the electrical double layer. The parameter "a" is the radius of the particle, therefore κa refers the ratio of the particle radius to electrical double layer thickness. $f(\kappa a)$ is 1.5, as referred to the Smoluchowski approximation, when the radius of the particles is larger than 0.2 microns dispersed in electrolytes containing more than 10^{-3} molar salt.

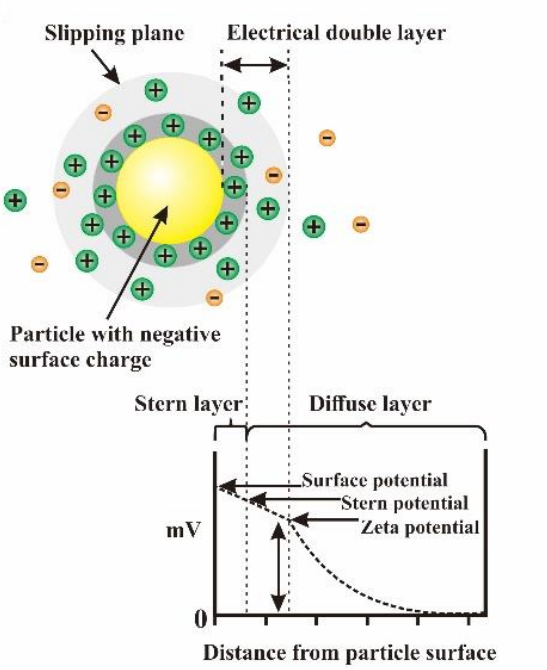

Figure 4.7 Schematic image showing the double layer distribution of ions surrounding a charged particle and the evolution of the electric potential from the surface potential to zero far from the particle.

Four groups of suspensions at different concentrations of the Ni^{2+} ions ranging from 10^{-5} mol/L, 10^{-4} mol/L, 10^{-3} mol/L, to 10^{-2} mol/L were prepared. For each group, 30 mg particles were well dispersed into 40 ml deionized water, and the only difference is the dissolved mess of $NiCl_2 \cdot 6H_2O$. The pH of each suspension was tested immediately after the preparation as well as the zeta potential of the particles in each suspension. Two group suspensions (10^{-4} mol/L and 10^{-2} mol/L) are chosen to study the influence of different pH on the zeta potential of the particles, and each group was divided into two separate 20 ml waiting for being added into HCl and NaOH solution respectively for the following zeta potential test. Electrophoretic depositions at different pH values were also carried out using suspensions with two different concentrations of Ni^{2+} ions (10^{-4} and 10^{-2} mol/L) under the same applied voltage of 20 V for 2 minutes in order to study the deposition quality as a function of pH.

4.3.4 Electrophoretic Deposition Process

Even 0.95 mg $NiCl_2 \cdot 6H_2O$ cannot be fully dissolved in 40 ml pure isopropyl alcohol (IPA), so that different mass of $NiCl_2 \cdot 6H_2O$ was dissolved in 1ml deionized water first, and then filled with 39 ml IPA forming the final suspension for electrophoretic deposition. Three groups of suspensions with the different concentrations of Ni^{2+} ions (10^{-4} mol/L, 10^{-3} mol/L and 10^{-2} mol/L) were prepared for the subsequent EPD process. Different parameters were applied to perform electrophoretic deposition experiments including different voltage ranging from 10V to 30V and deposition time 10s to 2 minutes, and the current was measured in Ampere Meter and recorded in the connected laptop. After the deposition, the chips were transferred into deionized water immediately and rinsed three times. The deposition morphology was observed by FEG-SEM, and the cross section was cut using Focused Ion Beam (FIB) along with the EDS analysis.

4.4 Results and Discussion

4.4.1 Mechanism of Acid Immersion

Electrophoretic deposition depends on the ability of the surface of the particles to accept and retain sufficient charge within the liquid in which they are dispersed. At first, no deposition was observed when the Ni/Au particles were immersed in DI water and then transferred to IPA solvent. Then after the Ni/Au particles' immersion in a hydrochloric acid solution and subsequent transfer to IPA, successful deposition onto the target pads were accomplished using electrophoretic techniques, as shown in Figure 4.13 and 4.14. The successful deposition proves that the acidic treatment is able to produce a positive net-charge for Ni/Au coated particles, enabling their subsequent deposition on the cathode chips. The mechanism of the acid immersion was initially studied. Figure 4.8 shows the acid immersion charging process of Ni/Au coated particles in HCl solution.

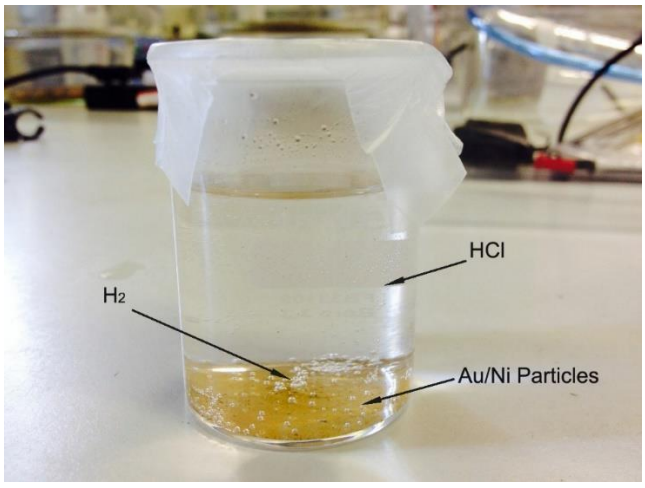

Figure 4.8 The chemical reaction of Ni/Au particles immersed into HCl solution.

The gold layer on the particles is very thin, but is sufficient to ensure good and stable conductivity. Under standard conditions (25°C, 1 molar solution and 1 atm pressure) the reduction potential for gold ions to gold is 1.498V, whilst that of nickel ions to nickel is -0.25V. The positive reduction potential for gold shows that it will not be affected by a HCl solution. However, as this gold layer is porous the nickel layer underneath can interact with a hydrochloric acid solution. It can be clearly seen from Figure 4.8 that the particles sedimented to the bottom of beaker where the reaction between Ni/Au coated particles and HCl occurred and air bubbles emerged. The produced gas was found to be exactly located around the surface of Ni/Au coated particles, so that it can be confirmed to be hydrogen. Therefore, the main chemical reaction occurred during the acid immersion charging is concluded as:

$$Ni + 2H^{+} \rightarrow Ni^{2+} + H_2 \uparrow \tag{4.2}$$

Gold coated particles will become negatively charged when immersed in aqueous suspension [12]. It is supposed to be the Ni^{2+} ions produced from acid etching that tend to be attracted to the negatively charged gold surface areas of the particle resulting in a net positive surface charge on the particles. The etching process of the metal coating layer is illustrated in Figure 4.9. The nickel layer starts to be etched when touching the HCl solution via the pin holes of the gold coating layer as shown in Figure 4.9 (b) and (c). There may be some nickel oxidation on the surface of nickel around the pin holes, which however will not hinder the etching due to the easily reaction between the nickel oxidation and HCl. It should be noted that excessive etching is very likely to increase the possibility of the delamination.

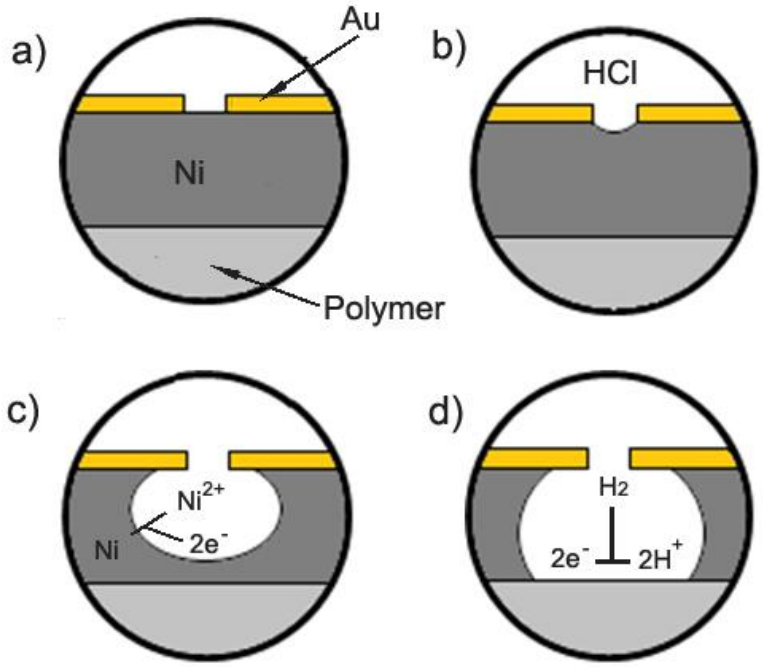

Figure 4.9 Illustration of the etching process of the Ni/Au particles immersed into the HCl.

As shown in Figure 4.10, it was clearly observed that the morphology of the particles were changed completely after the 30 minutes immersion in HCl solution. The pin holes developed into much bigger ones and severe delamination occurred on the surface of the particle, which will certainly reduce the conductivity of Ni/Au coated particles and decrease the ultimate reliability of the interconnection.

Temperature is a key parameter during the oxidation-reduction reaction, and heating transfer always exists in this process. The replacement reaction between Ni and H2 is exothermic, so that much heat was generated during the reaction process. As a consequence the temperature of the suspension was increased, thus in turn accelerating the reaction speed. The suspension temperature was measured to be approximately 40 ℃ during the reaction process. Without the proper consideration of temperature, experiments on individual study on the influence of immersion time is not accurate. In this acid immersion charging method, the comprehensive analysis of both the temperature and immersion time determines the ultimate charge of the Ni/Au particles obtained. More importantly, it can have a significant influence on the electric resistance and reliability of the interconnection.

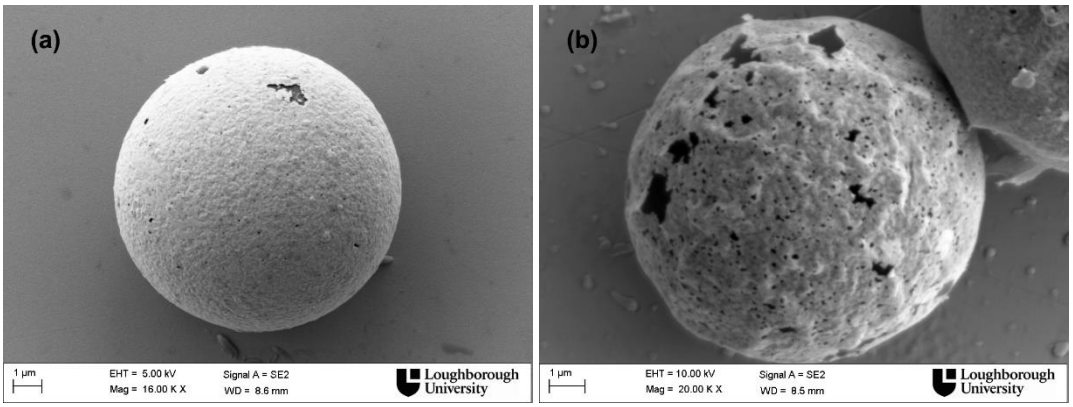

Figure 4.10 FEGSEM images of the Ni/Au coated particles showing the effect of hydrochloric acid immersion on the metal layer. The particles (a) before immersion and (b) following immersed in the 32 wt% HCl for 30 minutes.

4.4.2 Results of EPD using Acid Charging Method

The electric field strength and deposition time are the two main parameters that impacting the quality of electrophoretic deposition. Figure 4.11 shows typical particles distributions achieved after deposition for 5 and 10 minutes. From the results, it is clear that low applied potential and shorter deposition time resulted in a fairly low density of deposited particles, however higher applied potential and longer deposition time although increasing the particle density tend to result increasingly in multilayer deposition.

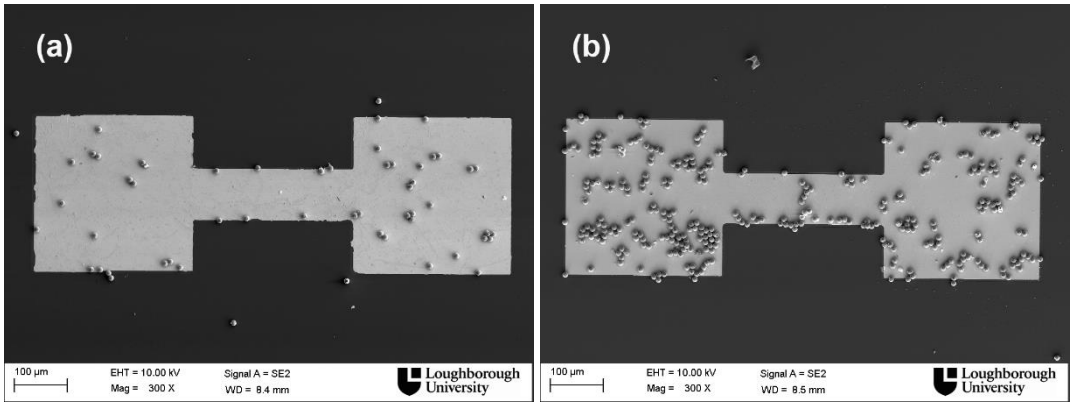

Figure 4.11 FEGSEM images of particles deposited directly on to the pad for (a) 5 minutes and (b) 10 minutes.

As shown in Figure 4.12, even after 10 minutes of deposition several particles had begun to create an area of three-layer deposition, where the top particle (third layer) is connected with only one particle in the second layer. It is believed that such multiple layers will lead to problems during the flip-chip bonding process, because the strong connections formed between the particles and to the chip will prevent them compressing down into a single layer and this may significantly impact the conductivity and reliability of the interconnections formed. In order to understand whether it is possible to achieve dense and uniform, but single layer, deposition, will require further detailed investigations of the effects of all of the critical process parameters such as the viscosity of the suspension, applied potential, zeta potential of the particles etc.

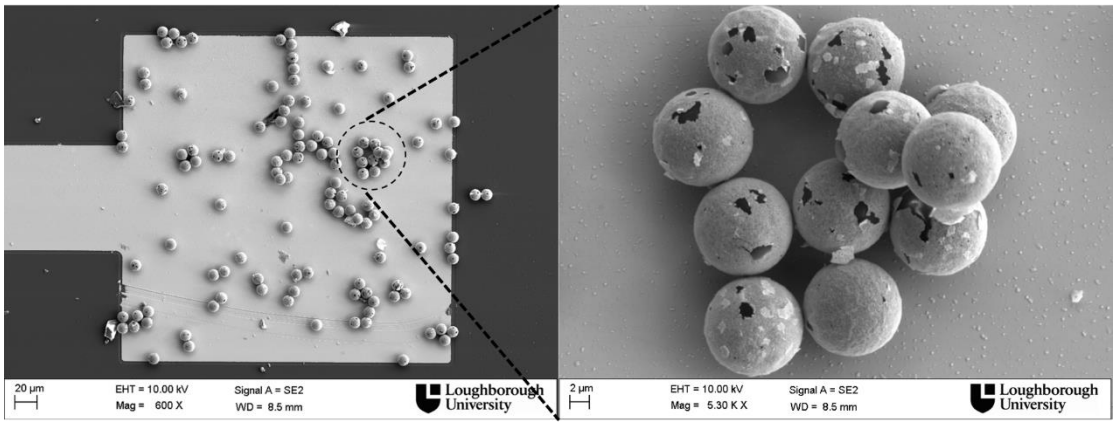

Figure 4.12 SEM images of a multilayer cluster of the particles after electrophoretic deposition using 15V for 10 minutes.

4.4.3 Results of Zeta Potential Study

4.4.3.1 Zeta potential: Salt concentration effect

Nickel chloride solution is directly used to charge the Ni/Au coated particles. To investigate the

influence of the different $NiCl_2$ concentrations on the zeta potential of the Ni/Au coated particles, four groups of samples with the same particle solids loading as low as 0.044 vol% and 0.1 wt% were prepared and the results are shown in Figure 4.13, and the positive zeta potential at all concentrations suggests the particles get positive charged after immersing into $NiCl_2$ solution. The conductivity of the suspension plays an important role in EPD process and will be changed in different salt concentrations or pH values. If the conductivity of suspension is too high, the particle motion will be correspondingly very slow. In contrast, the stability of suspension along with zeta potential will be lost if the suspension is too resistive [93]. However this data is usually missing in the figure plot of zeta potential study.

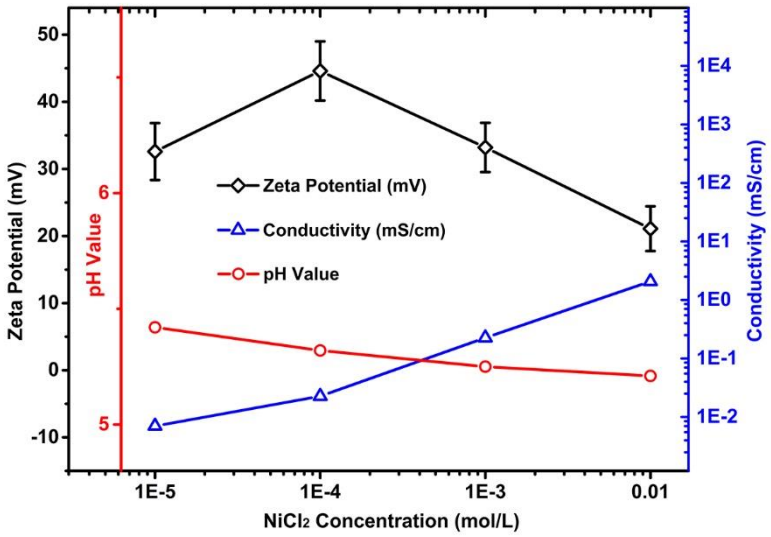

Figure 4.13 Zeta potential of Ni/Au coated polymer core particles at different $NiCl_2$ concentrations.

In this work, the data on the conductivity of the suspension is monitored and plotted in Fig. 4.1.3 alongside the salt concentration and the pH values. With the increasing $NiCl_2$ concentration from 10^{-5} mol/L to 10^{-2} mol/L, the pH values of the suspensions decreases slightly from 5.42 to 5.21, while the conductivity of the suspension increases significantly from 0.00700 mS/cm, 0.0270 mS/cm, 0.226 mS/cm, to 2.07 mS/cm. As a consequence, the zeta potential of the particles increases from 32.6mV in 10^{-5} mol/L to 44.6mV in 10^{-4} mol/L, and then decrease gradually to 21.1mV in 10^{-2} mol/L. The results illustrate that the zeta potential of the Ni/Au coated particles is very sensitive to Ni^{2+} ion concentration. A relatively very low concentration of Ni^{2+} ions can contribute to a high zeta potential. The subsequent increases of salt concentration will compress the thickness of double electrical layer outside the particle surface, which consequently leads to a decreasing zeta potential and lower mobility of the particle. Some

literatures suggested that the reduction of the double layer thickness due to higher ionic conductivity can also decrease the electrostatic repulsion between the particle, hence resulting in particles agglomerate and poor deposition quality [149] . However, the highest zeta potential does not mean a final green electrophoretic deposition quality. The deposition experiments show that the adhesion force between the electrophoretic deposited particles and pad surface has a close relationship with the Ni^{2+} concentration, and low concentration of Ni^{2+} ions is likely to lead a poor adhesion strength, thus resulting in a potential threat to the final reliability of the interconnection.

4.4.3.2 Zeta potential: pH effect

Conductivity of suspensions suppresses the influence of pH and decreases the zeta potential when it's very high. Two groups concentration of Ni^{2+} ions solutions are chosen to study the surface charge of the Ni/Au coated particles as a function of pH, and the zeta potential results are plotted in Figure 4.14 for 10^{-4} mol/L and 10^{-2} mol/L respectively. The conductivity can be different at the same pH value if mixing HCl and NaOH, therefore for each group of suspension it was divided into two separate parts during the pH varying process. Point 1, 2, 3, and 4 are tested without adding any HCl or NaOH into the suspension. Point 1 and 3 are the first testing points, and Point 2 and 4 are tested later when finishing the zeta potential tests for the acid region. Overall, it is clear to notice that higher conductivity of the suspension suppresses the influence of pH variation on the zeta potential through the comparison between these two groups. At the lower concentration of Ni^{2+} ions (10^{-4} mol/L), the total fluctuation of the zeta potential from pH 2 to 10 is 63.92 mV (62.5~-1.42). While the zeta potential at 10^{-2} mol/L concentration fluctuates only 12.2 mV (28.9 mV to 16.7 mV), which is only one fifth of that at 10^{-4} mol/L. For both groups the conductivity remains at a relatively low level and increases dramatically when the pH is lower than 2.5. Consequently, the zeta potential of the particles significantly dropped due to the reduction of double layer resulting from the increasing conductivity of the suspension.

It was found that the conductivity of the suspension decreased for both groups after the testing in acid region, especially for 10^{-4} mol/L concentration suspension. From Point 1 to Point 2, the conductivity decreases approximate 30% from 0.0500 mS/cm to 0.0375 mS/cm, as a result the zeta potential decreases nearly 50% from 42.7 mV to 23.1mV. As a comparison, the zeta potential of the particles at higher $NiCl_2$ concentration (10^{-2} mol/L) increases from 22.8 mV to 28.6 mV when the conductivity decreases from 2.07 to 2.02. This may be attributed to the variation of Ni^{2+} concentration caused by the hydrolysis process of Ni^{2+} ions, which decreases the concentration of Ni^{2+} ions and the suspension conductivity. The decreasing concentration of Ni^{2+} ions reduces the zeta potential for the particles at lower concentration (10^{-2} mol/L), whilst it contributes to an increasing zeta potential of the particles at higher

concentration of Ni^{2+} ions (10^{-4} mol/L) due to the less influence of the high salt conductivity.

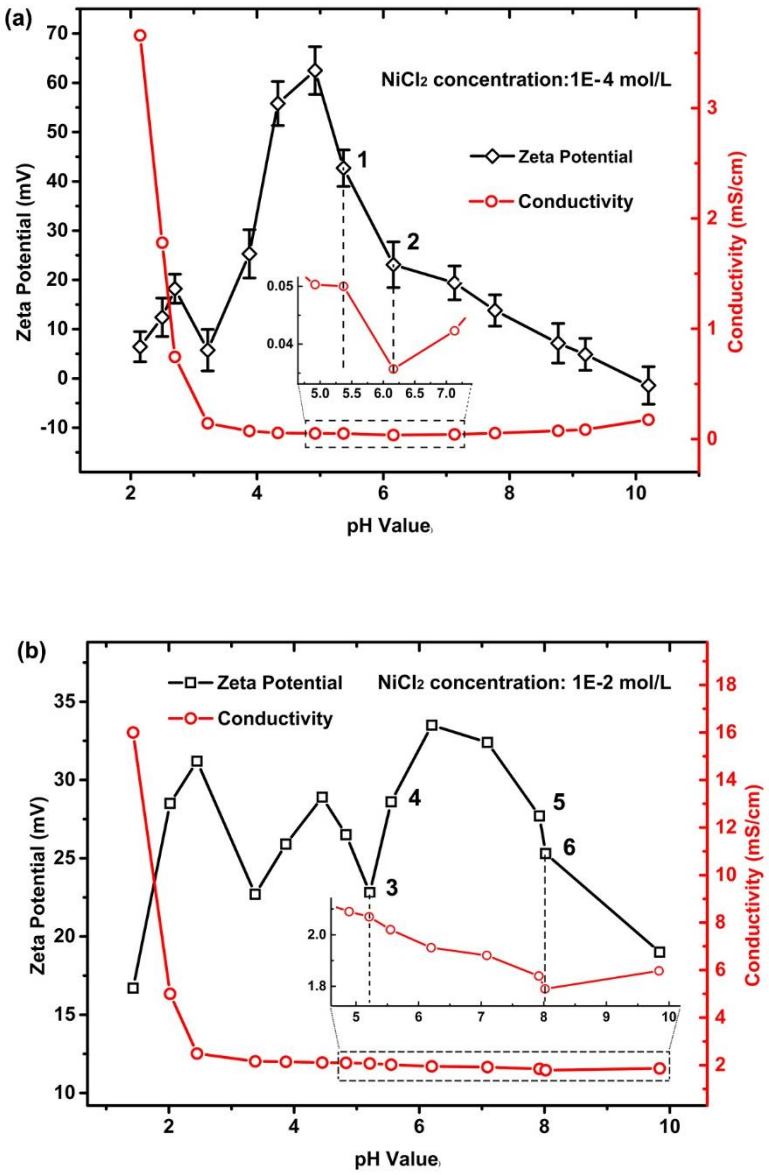

Figure 4.14 Zeta potential of the Ni/Au coated particles as a function of pH in (a) 10^{-4} mol/L and (b) 10^{-2} mol/L Ni^{2+} ions suspension.

Zeta potential change in acid region

After adding HCl into the suspension, the zeta potential of both groups of particles increases and reaches the highest point 62.5 mV and 28.9 mV at pH 4.92 and 4.45 respectively. This is attributed to the adsorption of the H^+ onto the particle surface, thereby enhancing the electrostatic repulsion force. However a sharp decrease of the zeta potential occurs when pH continues decreasing to around 3.5, which is also reported in [72, 92, 149]. J. Ma et. al [149] suggested that it is due to the increasing conductivity causing the reduction of double layer thickness. However in this work the conductivity of the suspension increases at a very limited

level in the pH range (5~3.5) as shown in Figure 4.14, and it dramatically increases until pH is lower than 2.5 as discussed. Therefore it is believed there must be some factors other than the conductivity which dominates this decreasing zeta potential when pH decreases from 5 to 3.5. Moreover, the zeta potential increases again following the decreasing pH from approximate 3.5 to 2.5 for both groups of samples. The mechanism these changes of zeta potential with the decreases of pH value from 5 to 2.5 remains unclear, but possibly relates the etching reaction between H^+ and nickel through the porous gold layer creating a larger metal surface and higher Ni^{2+} concentration, as well as the coupling impact of increasing concentration of Ni^{2+}, $NiCl^+$, and Cl^- [150].

Zeta potential change in alkaline region

As reported by J. Ji et. al, insoluble $Ni(OH)_{2(S)}$ is expected to form and increase with the increasing pH while the amount of $NiOH^+$, $Ni(OH)_{2(aq)}$, $Ni(OH)_3^-$ and $Ni(OH)_4^{2-}$ decreases when the concentration of $NiCl_2$ changes from 10^{-6} to 10^{-1} mol/L [150]. In this work, when adding NaOH solution into the suspension (from Point 2), the conductivity starts to increase immediately for the suspension at 10^{-4} mol/L $NiCl_2$ concentration as shown in Figure 4.4 (a), which indicates that most free Ni^{2+} ions were consumed quickly and the OH^- ions plays the dominated role in leading to a consecutively decreases of zeta potential to -1.42 mV at pH 10.2. However for the suspension at 10^{-2} mol/L $NiCl_2$, the conductivity continues decreasing when adding NaOH solution (from Point 4) until reaching Point 6. From Point 5 to 6, owing to the aggressively processed reaction forming $Ni(OH)_{2(S)}$, there is a sharp drop for the conductivity and the pH value remains at a narrow range (7.92~8.02) even continuously adding NaOH solution into the suspension. At the end of the reaction, lots of white flocculent solids ($Ni(OH)_{2(S)}$) appears surrounding the particles, and this surrounding distribution is believed to be caused by the increasing Ni^{2+} ions concentration toward the stern layer of the particles surface. The zeta potential of particles increases to the highest point 33.5 mV at pH 6.2, then decreases to 19 mV when pH reaches 9.84. The formation of insoluble $Ni(OH)_{2(S)}$ consumes large amount of free Ni^{2+} ions, and causes the decreasing conductivity. It was found that the IPA is a promising solvent for the charged particles, because the zeta potential can sustain almost the same when the particles get positively charged in hydrochloric acid solution and then transformed into the IPA solvent [151, 152].

4.3.4 Results of EPD using $NiCl_2/CuCl_2$ Charging Method

4.3.4.1 Effect of suspension pH on Deposition Quality of EPD

The quality of electrophoretic deposition heavily depends on the suspension condition, and a well-dispersed stable suspension is supposed to be the first priority for EPD. The principle to

achieve a green deposition for EPD is to find a systematic approach to making the suspension where the particles have a high zeta potential while keeping the ionic conductivity of the suspension at a relatively low level. Both zeta potential and ionic conductivity are determined by the $NiCl_2$ concentration and pH value. Table 1 shows the results of Ni/Au coated particles deposition at various pH under a constant applied voltage of 20 V for 2 minutes. It can be seen that the deposition results were consistent with the zeta potential and conductivity measurements shown in Figure 4.14. Uniform depositions can only be achieved using the suspensions with high zeta potential and appropriate conductivity. Many gas bubbles were found on the chips surface when the pH is lower than 2, especially for 10^{-2} mol/L concentration of Ni^{2+} ions, which leaded to the non-uniform deposition of Ni/Au coated particles. The reason is contributed to the substantially increasing conductivity of suspension due to the high concentration of H^+ ions, which were reduced to hydrogen when touching the cathode chip. When the suspension was in the alkaline regime (>8), no deposition was achieved because of $Ni(OH)_{2(S)}$ formed around the particles outside, even though the zeta potential measured remain positive as shown in Figure 4.14.

Table 4.1 Electrophoretic deposition quality at various pH

Suspension pH	EPD quality of particles
<2	Non-uniform
2.9	Uniform
3.5	Uniform
5.3	Uniform
>8	No deposition

Based on the proposed theory in Section 4.4.5, the electroplated materials along with the deposited particles are electroplated solid nickel using $NiCl_2$ charging method. During the pH variation experiments, three different surface morphologies of the electroplated nickel were observed, i.e nanorod structure and solid plate, using suspensions at different pH values, as shown in Figure 4.15. It is clear that the deposition morphology of electroplated nickel was slowly transferred from nanorod structure to solid plate using the same suspension at 10^{-4} mol/L concentration of Ni^{2+} ions but with the decreasing pH ranging from 5.3, 3.5, to 2.0, as shown in Figure 4.15 (b), (c), and (d). Similar nanorod structure of electroplated nickel was also observed during EPD on daisy-chain chips using suspensions without adjusting the pH at the 10^{-3} mol/L concentration of Ni^{2+} ions as shown in Figure 4.15 (a).

It should be noted that the concentration of Ni^{2+} ions in suspension was also decreased with the decreasing pH due to its consumption during EPD process. Whilst the surface morphology is an index of the crystalline state of electroplated materials, which can be affected by a variety of electroplating parameters including ions content and concentration, pH,

temperature, current density etc. [153, 154]. The surface morphology of electroplated nickel will significantly affect the adhesion strength of the electrophoretically deposited Ni/Au coated particles as well as the conductivity and reliability of the interconnection. Therefore, further experiment needs to be performed to understand the dominating parameters that can lead to different morphology evolution along with the effects on the finalised interconnection.

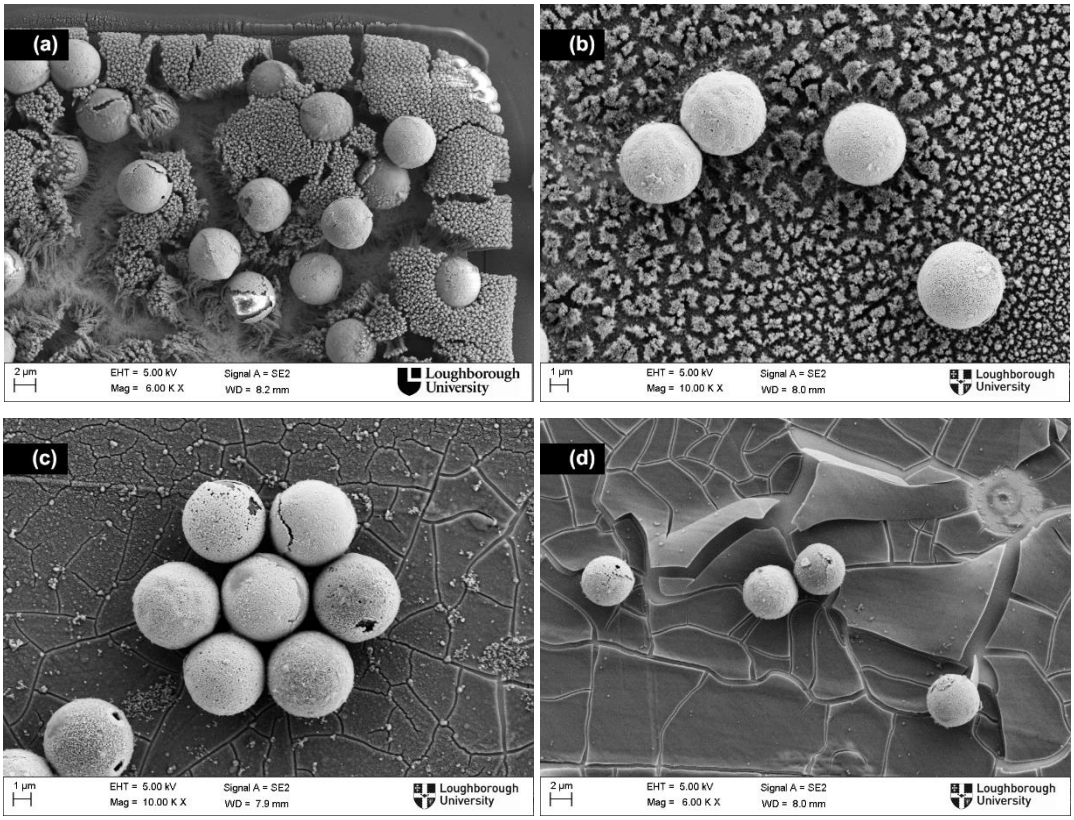

Figure 4.15 Different morphologies of electroplated nickel using suspensions at different pH and concentrations of Ni^{2+} ions (a) 10-3 mol/L Ni2+ ions at pH 5.2, (b) (c) and (d) using the same suspension at 10-4 mol/L concentration of Ni2+ ions with decreasing pH from 5.3, 3.5, to 2.0.

4.4.4.2 EPD on fine and ultra-fine pitch pads

The positively charged particles were successfully deposited onto the pad surfaces, as shown in Figure 4.16. Meanwhile it is clear that EPD of Ni/Au coated particles is a highly selective process and nearly no particles were found other than on the pad surfaces. This selective deposition saves large numbers of particles, which can also significantly reduce the probability of short circuits between adjacent pads thus enabling the ultra-fine pitch deposition. As shown in Figure 4.16 (a), (b), (c), and (d), selective deposition without any short circuits was readily achieved for the pads with diameters of 50 µm, 40 µm, and 30 µm. all the pads were covered with deposited particles, which proves that this method works very well at this scale. However the difficulty of achieving a high density of deposited particles without bridges increases dramatically for the finer pads.

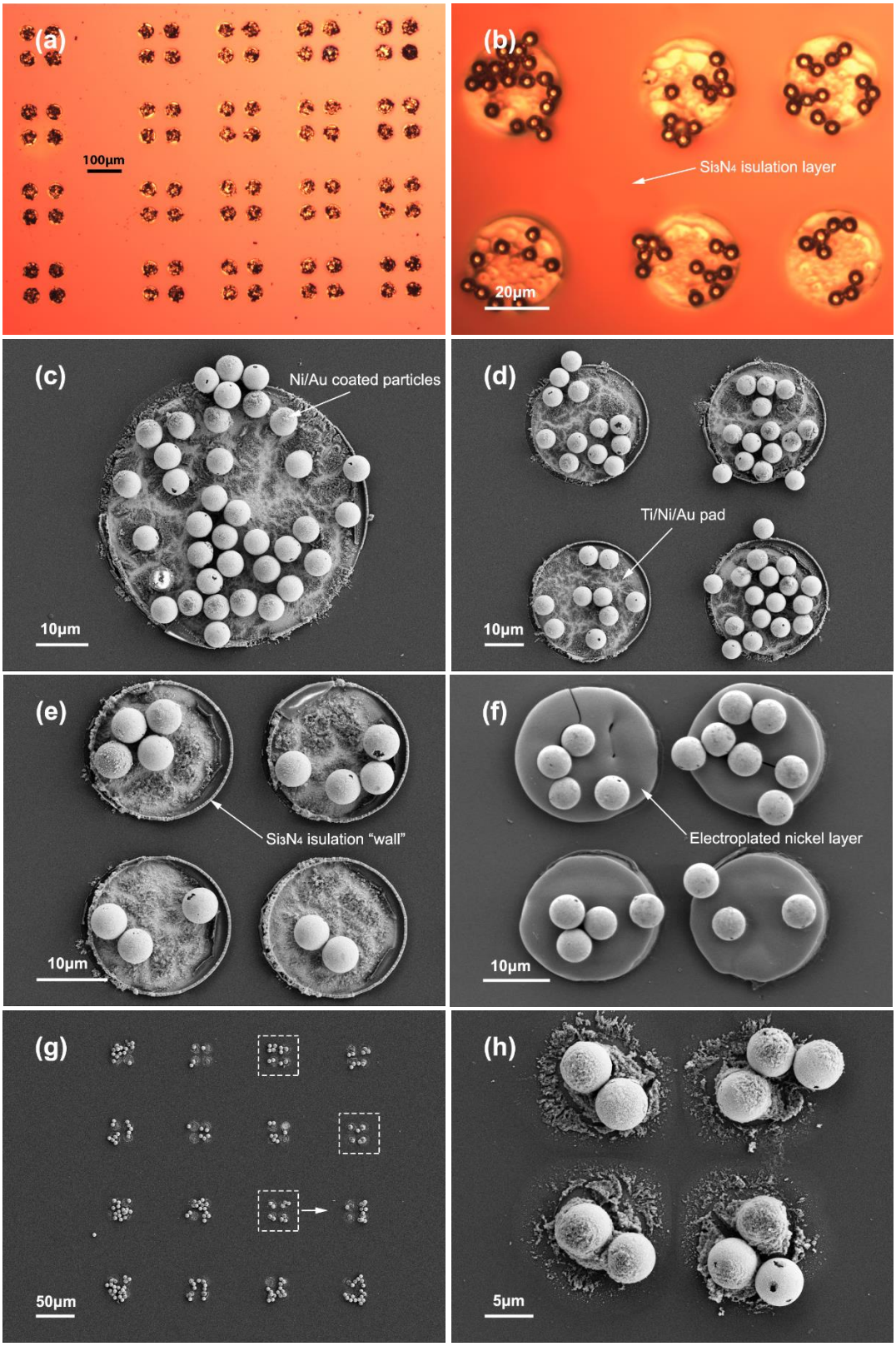

Figure 4.16 Examples of electrophoretic deposition of Ni/Au coated particles onto the pad array silicon chip (a) and (c) 50 μm in diameter with around 30 μm gap, (b) and (d) 30 μm in diameter with around 20 μm gap, (e) and (f) 20 μm in diameter with around 5 μm gap, (g) and (h) 10 μm in diameter with around 5 μm gap.

The gaps between the pads with diameters of 20 and 10 μm are only around 5 μm, which is just over the particle diameter, and the risk of shorts forming can be expected to rise dramatically for gaps less than twice the diameter [11]. However, with precise control and optimization of the applied voltage, a good deposition result was accomplished for the 20 μm diameter pads as shown in Figure 4.16 (e) and (f). The Si_3N_4 insulation wall left around the pad edge as shown in Figure 4.16 (e) was not manufactured on purpose, however can be exploited to stop the movement of particles in subsequent underfilling process. Unsurprisingly the electrophoretic deposition of Ni/Au coated particles yielded unsatisfactory bridging results for the 10 μm diameter pads, because this diameter is only approximately two times the diameter of the particles, so bridging is very likely to occur even if there are only three particles deposited onto each pad as shown in Figure 4.16 (g). Still three good depositions were achieved using the pad with the diameter of 10 μm as highlighted using the white dashed line in Figure 4.16 (g), and one was shown in Figure 4.16 (h). Meanwhile electrophoretic deposition quality keeps to be very uniform using the daisy-chain or kelvin structure chips (the minimum diameter of the pad is 50 μm). However it should be noted that sometimes the distribution of the deposited particles was non-uniform and the particles were more likely concentrated on the "edge" of the pad array. The reason is believed to be closely related with the electric field distribution during the EPD process, and further experiment needs to be carried out to study the mechanism of "edge" distribution so as to avoid this phenomenon.

4.3.5 Assembly Mechanism Study

Several theories, such as the charged particles accumulation by Hamaker and Verwey [155], electrochemical particle coagulation [156], and the latest double layer distortion and thinning [80], have been published to explain assembly mechanism during the electrophoretic deposition process, and some of which are even contradict to each other. For instance, no charge transfer happens on deposition during EPD process according to the reference [79], and this is also satisfied with Sarkar and Nich's theory [80], where particle/electrode reactions are not involved in EPD. While in Troelstra's experiment, the ceramic particles did not lose charge after being deposited and can be striped when reversing the applied electric field [81], which also provide strong evidence to support this theory. However Grillon et al. [157] suggested the charged particles moves to the opposite electrode and precipitate through charge neutralization. This theory illustrates the deposition of monolayer particles but cannot explain the formation of multilayer coating since most deposited colloidal or ceramic particles are nonconductive. However, the particle deposition quality by EPD is usually unaccpetable due to the poor adhesion force between the deposited material and substrate, as such the upper deposited layer can be easily washed off [108]. Therefore, additional step of processes is necessary, for instance,

sintering for ceramics [158] or a subsequent electroplating for deposited nanotubes [71].

No previous studies have been carried out to study the electrophoretic deposition of microscale metal particles using metal cation charging method, and our findings provide another explanation for the assembly mechanism of the electrophoretic deposition. In this work it was found that electrophoretic deposition and electroplating process can occur simultaneously during EPD process. The assembly mechanism is illustrated in Figure 4.17, where the positively charged Ni/Au particles are driven to the cathode under the external electric field and then adhered onto the pad surface by the electroplated solid nickel. There are three main steps:

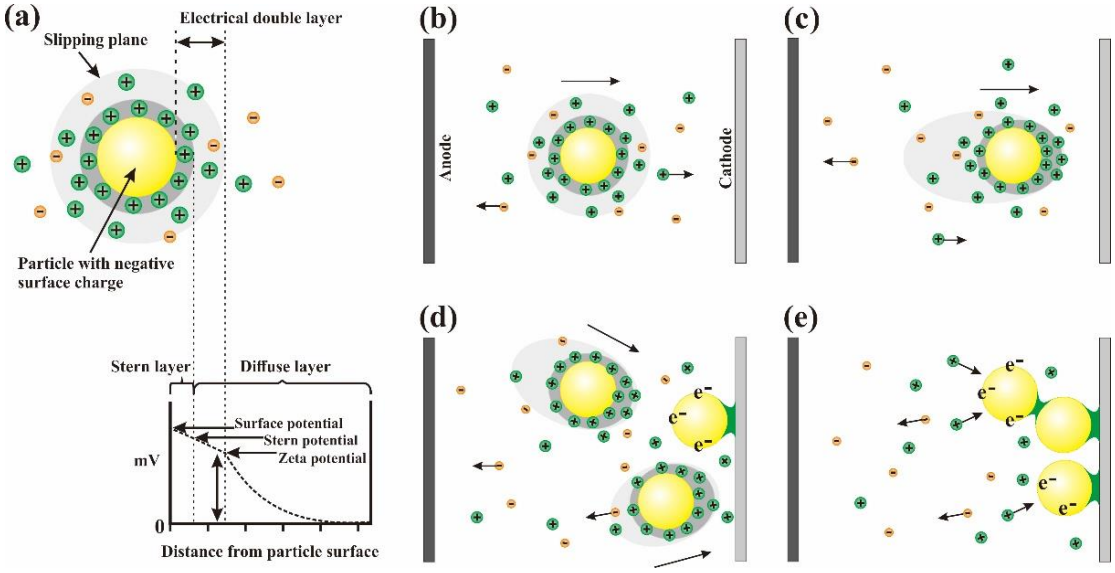

Figure 4.17 . Schematic image showing the mechanism of the electrophoretic deposition: (a) the electrical double layer distribution of the Ni/Au coated polymer core particle, (b) the initial state of the charged particle in the suspension at the moment of applying voltage, (c) double layer distortion and the starting movement of the particle toward cathode under applied electric field, (d) electroplated solid nickel adheres the particle onto the cathode, (e) multiplayer electrophoretic deposition due to continuously electroplating process.

i) As shown in Figure 4.17 (a) and (b), the charged particle is surrounded by the electrical double layer, where the concentration of Ni^{2+} increases toward the surface of the particle. Under the applied electric field, the double layer experiences a distortion process [80] as illustrated in Figure 4.17 (c) and becomes thinner ahead with a higher aggregation of Ni^{2+} ions.

ii) The Ni^{2+} ions are neutralized once in contact with the cathode, and the higher concentration of Ni^{2+} in the particle head area results in a relatively thicker electroplating layer which adheres the particle onto the cathode surface as shown in Figure 4.17(d) leading to a solid and strong connection between the particle and pad surface.

iii) Because of the solid connection, the electrons can be transferred to the metal coated

particle surface from the pad. The deposited particle behaves as cathode and enables the subsequent electroplating process and electrophoretic deposition of multiplayer particles as shown in Figure 4.17 (e).

The Ni/Au coated particles were charged using different concentration of $NiCl_2$ solution, and subsequent studies including the adhesion force between the deposited particle and pad surface, cross section of the deposition using FIB, electroplated materials study using TEM, provides strong support for this theory.

As shown in Figure 4.18, the positively charged particles are selectively deposited onto the target pads by EPD, and the electroplated nickel layer is obvious proving that the electrophoretic deposition and electroplating process occur simultaneously. For the group I with 10^{-4} mol/L concentration of Ni^{2+} ions, an almost monolayer of particles deposition was achieved at the applied voltage of 10V for 2 minutes as shown in Figure 4.18 (a). As shown in Figure 4.18 (b), there is an obvious electroplated nickel layer on top of the electrophoretically deposited particle. The thickness of the electroplated nickel can be an indicator of the deposited time of each particle, for instance the particles with relative smooth surface suggests that it was deposited within a short time. It is believed that the electroplated nickel connected the particle to the pad surface contributing to a solid connection between the particle and cathode pad, consequently the metal coated particles behaves as the cathode which enables the subsequent electrophoretic and electroplating process. Meanwhile the following experiments also prove that the electroplated materials act as a natural symbol showing the distribution of the electric field around the pad area. After two minutes deposition at voltage 20V and 30V, multilayer aggregated particles were deposited on the pad surface for Group II and Group III particle suspensions at different concentration of Ni^{2+} ions as shown in Figure 4.18 (c) (10^{-3} mol/L) and Figure 4.18 (e) (10^{-2} mol/L) respectively. As shown in Figure 4.18 (d) and Figure 4.18 (f), the electroplated nickel covers most area of the particle surface and even buries some particles inside, and these results also prove that the electrophoretic deposition can also proceed on the surface of the electroplated nickel, which verifies the proposed theory as illustrated in Figure 4.17. Whilst the morphology of the electroplated nickel changes from needle structure (Figure 4.18 (b)) to solid block at higher concentration of Ni^{2+} ions as shown in Figure 4.18 (d) and (f), and the structure of the electroplated nickel is found to be more sensitive to concentration of Ni^{2+} ions instead of the applied voltage or deposition time. However thicker electroplated nickel layer induces higher residue stress, which accordingly leads to the severe crack and its propagation during the drying process as shown in Figure 4.18 (e). It is believed that by adding some buffer electrolytes into the suspension, a solid “concrete” configuration mixing the electroplated material and Ni/Au coated particles can be formed with optimized control of electrophoretic deposition parameters, which can expand the potential application of this structure.

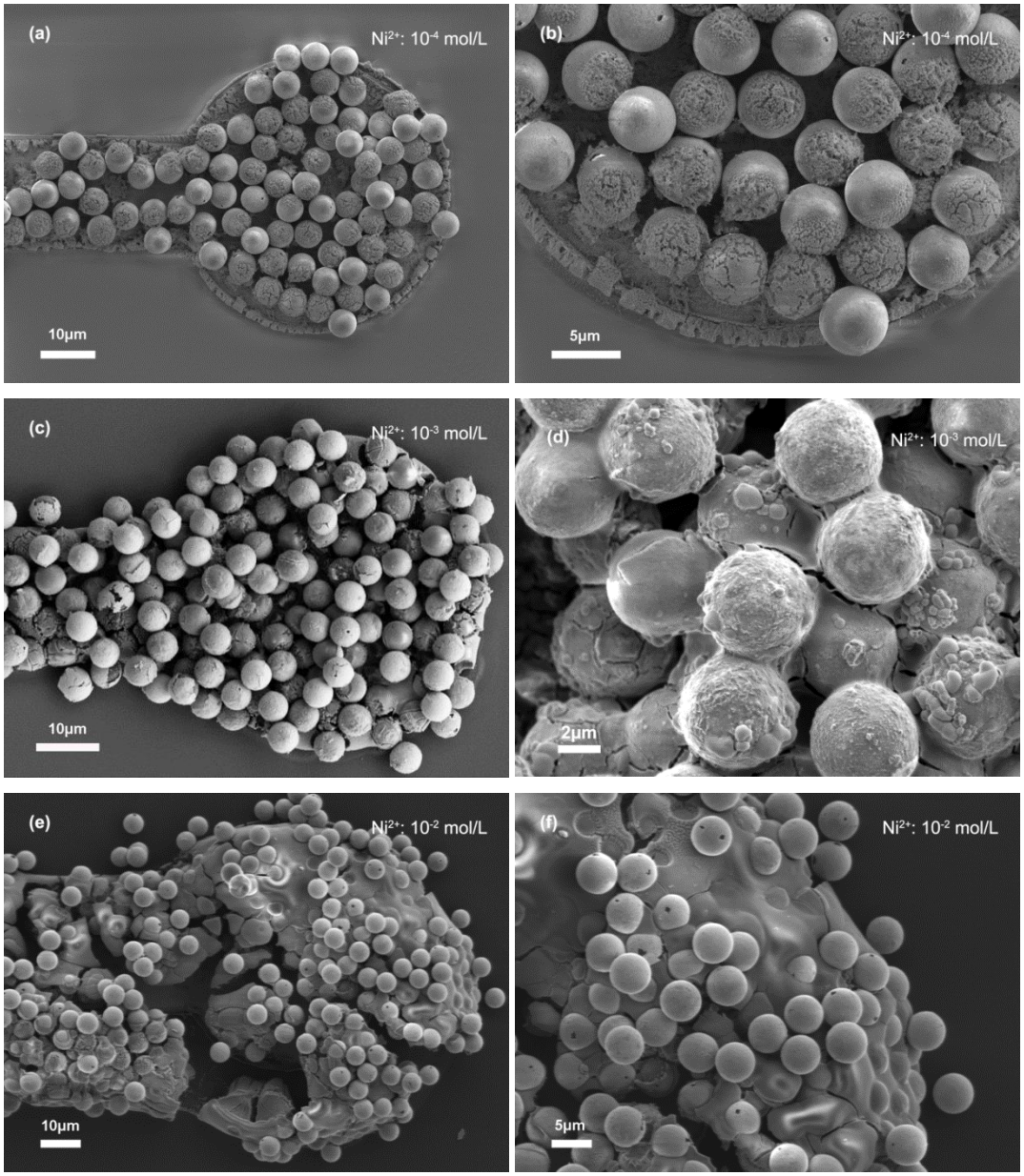

Figure 4.18 FEGSEM images of the electrophoretically deposited 5 μm Ni/Au coated polymer particles on Ti/Ni/Au pad surface with 50 μm in diameter: (a) (b) monolayer of the deposited particles using the group 1 particle suspension at the concentration of 10^{-4} mol/L Ni^{2+} ions, and needle structure of the electroplated nickel on the surface of the deposited particle; (c) (d) multilayer deposited particles on the pad surface using the group 2 particle suspension at the concentrations of 10^{-3} mol/L Ni^{2+} ions, and the thick electroplated nickel covering most the surface of the particles; (e) (f) "concrete" structure mixing the electrophoretically deposited particles and electroplated nickel using the particle suspension at the concentration of 10^{-2} mol/L Ni^{2+} ions, and severe crack formed during the drying process.

In order to validate the proposed theory, another chloride salt $CuCl_2$ solution is also used to charge the Ni/Au coated polymer core particles. The Ni/Au coated particles were positively charged at the concentration of 10^{-3} mol/L Cu^{2+} ions, and successfully deposited onto the target

as shown in Figure 4.19. Compared with the $NiCl_2$ solution charging method, the charging process using $CuCl_2$ solution is much more complicated. First, the replacement reaction between the nickel layer of the particle and copper cation has to be considered in the solution. The porous gold layer on the particle enables the direct contact between the inside nickel coating layer and copper cation, and the replacement reaction results in a strong etching effect on the nickel layer. Second, the electroplated dotted Cu formed on the surface of the Ni/Au coated particle. It was found that these electroplated Cu was formed during the electrophoretic deposition process instead of the charging process, and the particles have already been covered with a layer of dotted Cu on the surface even before reaching the cathode pad under the applied electric field as shown in Figure 4.19 (a). As Cu is not active as Ni from Hofmeister series, it is easier to be reduced to solid copper from Cu^{2+} compared with Ni^{2+}. Consequently the Cu^{2+} ions are more easily to be electroplated which is supposed to be the reason of electroplated dotted Cu. After two minutes deposition at 10 V, several layers of dotted Cu decorated particles were deposited onto the pad surface as shown in Figure 4.19 (b). The subsequent FIB cross section studies also proves that there is a much stronger connection between the electrophoretically deposited particles using Cu^{2+} ions charging method than Ni^{2+} ions.

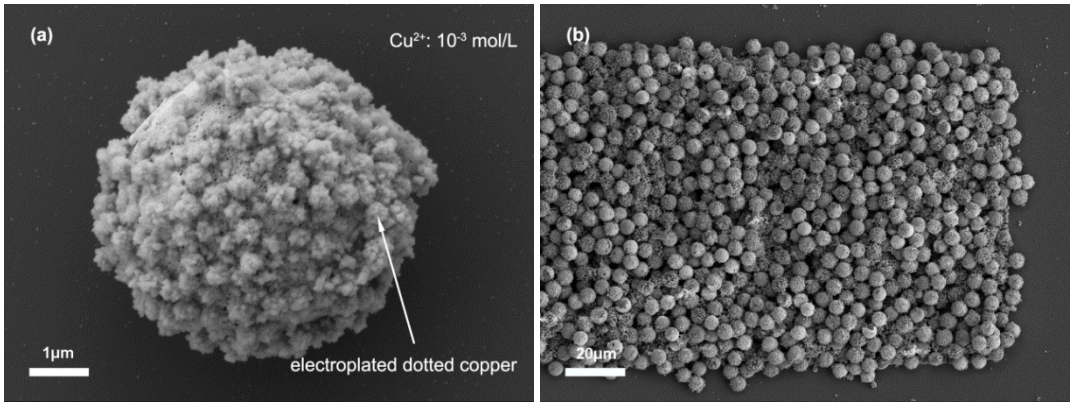

Figure 4.19 The morphology of (a) Ni/Au coated particle which is electroplated with dotted Cu on the particle surface and (b) electrophoretic deposition of the positively charged particles using CuCl2 solution.

In order to investigate the structure of the deposited material, cross sections were obtained using Focused Ion Beam (FIB). Before the FIB cutting, a 1.5 μm layer of platinum was deposited on the top surface to protect the initial deposition morphology as shown in Figure 4.20 (a) (b) and (d) and Figure 4.21 (a) (c). It can be clearly seen that the electrophoretically deposited Ni/Au coated particles and electroplating materials mix together forming the "concrete" structure, which proves that these two processes occur simultaneously. A strong eutectic joint is formed between the metal layer of the deposited particle and electroplated material as shown in Figure 4.20 (b) and (d), so that the adhesion force is relatively strong

compared with the conventional electrophoretic deposition of colloidal or ceramic particles. Moreover, this joint also established an electric connection bridge which enables the following deposition and electroplating process. The charged particles can consecutively be deposited on the surface of the bottom layer particle or the electroplated material, as well as the electroplating process continuously proceeds on the bottom layer surface providing better conductivity of the metal layer of the particles. Therefore, these two processes promote each other to some extent, and contribute to the final "concrete" structure.

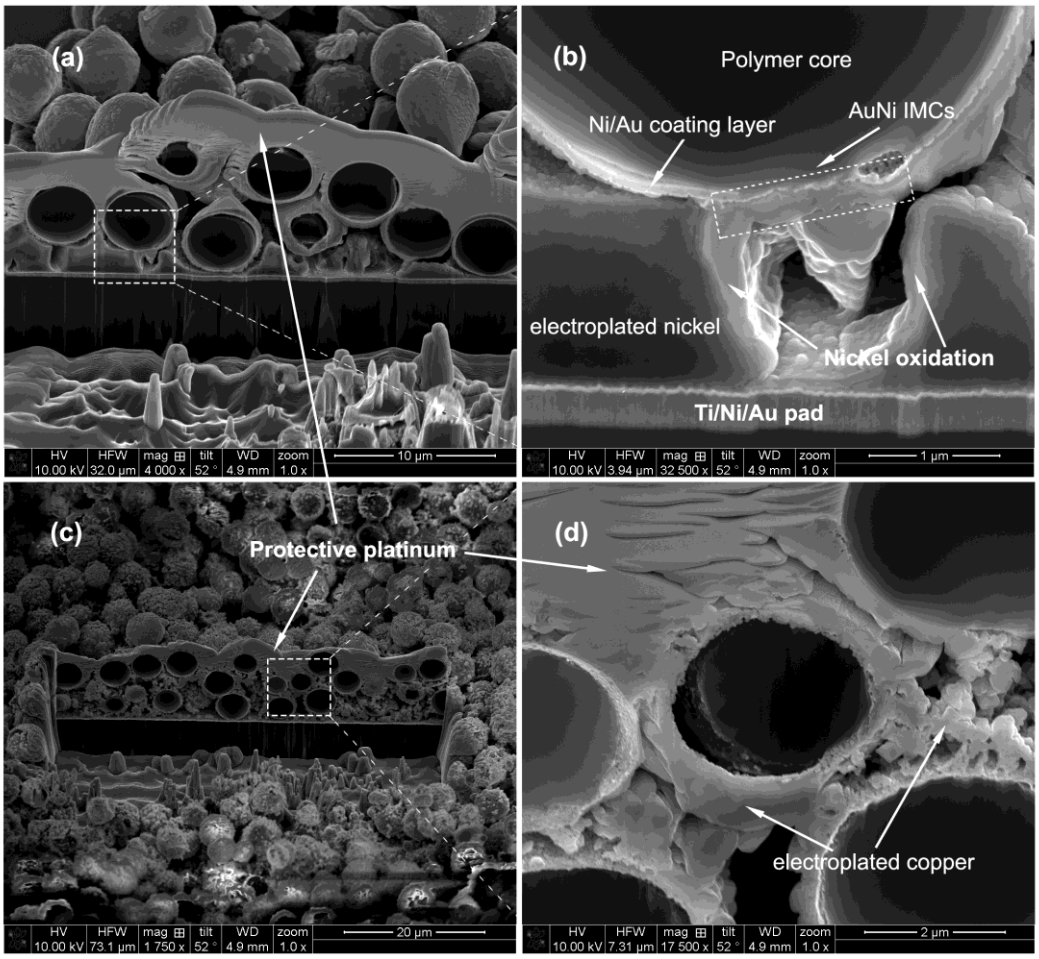

Figure 4.20 Cross section images of the concrete structure charged by (a) and (b) NiCl2 solution with the concentration of 10-3 mol/L, and (c) and (d) CuCl2 solution with the concentration of 10-3 mol/L.

The assembly mechanism is closely related to the charging cations Ni^{2+} or Cu^{2+}, which exist in the deposition cell and concentrate in the electrical double layer around the particles. Under applied electric field, both the cations and positively charged particles move to the opposite cathode surface. Once reaching the cathode, the cations acquire electrons and are reduced to the solid nickel or copper which adhere the particle onto the cathode surface. In other words, the electroplated materials provide the assembly medium for the electrophoretic

deposition of the particles, and the solid joint provides strong evidence that the electroplated materials contribute to the main assembly reason in terms of these metal coated particles with cation charging method. However, the influences of other forces cannot be neglected and eliminated such as van der Walls, electrostatic and capillary forces. Fresh nickel can be easily oxidized, and the nickel oxidation is clearly observed in Figure 4.20 (b). This oxidation is supposed to be formed after removing the chip out of the deposition cell. Further test is needed to study influence of this oxidation to the conductivity of whole structure, and silver chloride will be used to charge the particles to avoid the potential decreasing conductivity due to the metal oxidation afterwards.

As shown in Figure 4.18 (e), due to the high concentration of Ni^{2+} (10^{-2} mol/L) and high applied voltage (30V), a “concrete-like” structure with multilayers and electroplated materials was formed, and some particles were even totally buried. After the FIB cutting, the inner morphology is displayed in Figure 4.23. Large quantity of the electroplated materials can be observed, and the EDS analysis confirmed that nickel is the dominated material. The existence of other elements were induced by the subsequent processes instead of the electroplating process such as “O” is due to the oxidation of nickel, “Pt” is the deposited protective materials before FIB cutting, “Cl” is due to the suspension residue even after rinsing process in DI water, and “Ga” is introduced by the electron scanning beam etc. Furthermore, the phenomenon that Ni/Au particles were buried in the electroplated nickel and massive electroplated nickel was growing on top of the particles which also validates the proposed theory on the assembly mechanism of electrophoretic deposition.

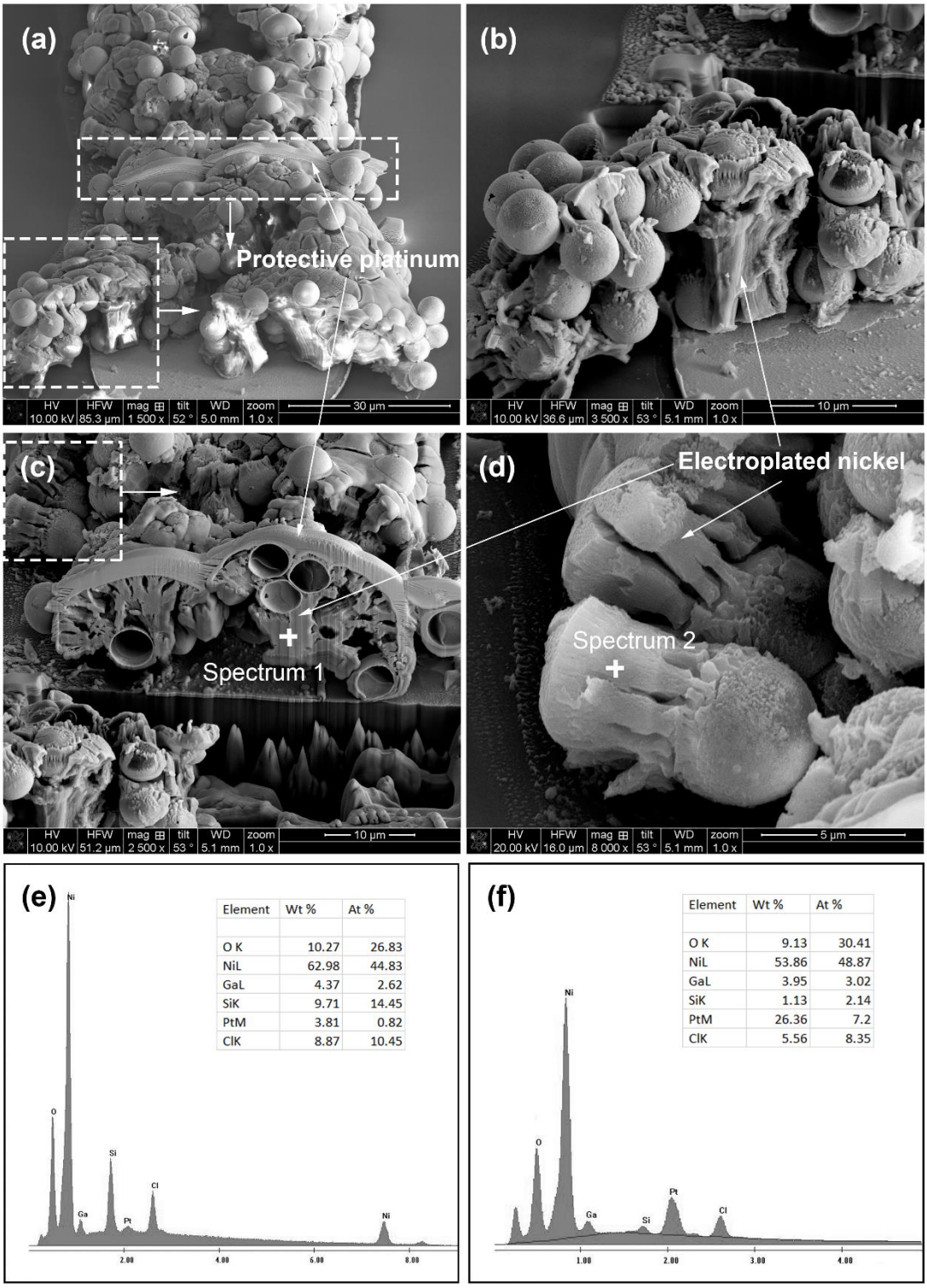

Figure 4.21 Cross section images of the concrete structure charged by NiCl2 solution with the concentration of 10-2 mol/L and the Energy dispersive Spectroscopy (EDS) analysis of the electroplated material.

4.5 Summary

Ni/Au coated polymer particles charged using acid immersion method were successfully electrophoretically deposited onto the pads on a test chip using a modified system which allows simplified processing of small chips. The etching process of metal coating layer within the acid is believed to impact the conductivity and reliability of the interconnection, and the charging mechanism analysis suggests that it is the Ni^{2+} ions obtained from the etching nickel layer that are adsorbed onto the particle surface thereby resulting in the positive charge of Ni/Au coated particles. The Ni/Au coated polymer core particles were positively charged using $NiCl_2$ and $CuCl_2$ solution, and the subsequent electrophoretic deposition of the charged particles was successfully carried out to enable a highly robust deposition on the target pads with an ultra-fine pitch, which proves that this novel process can be a promising alternative for the future flip-chip interconnection. Furthermore, the influences of the conductivity and pH on the zeta potential of Ni/Au coated particles were systematically studied in this chapter. The results show that the conductivity of the suspension presented a strong effect on the zeta potential and can also act as a sign to reveal the mechanism of the impact of pH during its variation. Higher conductivity not only resulted in a lower zeta potential but also contributes more complexity to the impact of pH. Most importantly, the concentration of the $NiCl_2$ and $CuCl_2$ determines the conductivity of the deposition suspension, and consequently results in different deposition morphology. Therefore we proposed a new theory to explain the assembly mechanism of the electrophoretic deposition which can better reflect the deposition process. The subsequent FIB cross cutting analysis also provides strong evidence to support this theory, i.e. the electrophoretic deposition and electroplating process occurs simultaneously and the electroplated material creates the adhesion medium for the electrophoretic deposition. There are a wide of potential applications for such “concrete-like” structure produced in this work such as increasing adhesion strength for the electrophoretically deposited materials i.e. carbon nanotubes or ceramic particles, increasing electroplating speed of copper pillar bump by mixing the particles into the solder.

Chapter 5

Magnetic Assembly of ACA Conductive Particles

5.1 Introduction

As one of the intrinsic features of nature, magnetism has a strong application potential in many areas. Some microspheres and nanoparticles display the magnetic properties so that they can be detected and controlled by magnetic field. Magnetic assembly has already been successfully utilized in the biomedicine areas for many years benefitting its particular advantage of controlling magnetic medicines to targeted positions. Nowadays, there is an increasing interest in the application of magnetism in the field of self-assembly. One of the advantages of the magnetic assembly is its programmable process resulting in a tunable and reversible deposition morphology. For example, a high-resolution magnetic printing is achieved by modulating the magnetic ink through the precise control of external magnetic field [113]. Meanwhile magnetic assembly is not limited to magnetic materials. Le He et al. accomplished the magnetic assembly of nonmagnetic particles on the nonmagnetic templates [106], where the nanoscale particles were highly preferred deposited onto the ultra-fine pitch (approximately 10 μm) pads. Magnetic assembly has been regarded as a promising approach to achieve the self-assembly process benefiting its many advantages such as simple, tunable, low cost, and high efficiency [99, 109, 110]. There is a wide application potential of magnetic assembly within the area of electric packaging where high accuracy and high cost are needed. However no previous study has been found at the moment.

This chapter presents the research on the magnetic assembly of Ni/Au coated polymer core particles. The results show that the Ni/Au coated polymer core particle displays promising magnetic properties because of the ferromagnetic nickel layer, which provides a novel alternative to control the particles and deposit them onto target pads. The apparatus, assembly system, and experimental methodologies for magnetic assembly of Ni/Au coated particles are presented in this chapter. The magnetic characterisation of Ni/Au particles was systematically studied as well as the Ti/Ni/Au pad. In this chapter, two different methodologies with/without the external magnetic field were used to achieve the final assembly of the particles on the target pad. As a consequence, the results showed that a highly preferred deposition morphology was achieved for both methodologies, where only particles were deposited onto the pad surface. A subsequent thermocompression bonding was conducted afterwards to achieve the final interconnection (Chapter 6).

5.2 Material and Apparatus

5.2.1 Materials

5.2.1.1 Particles

The particles used in the magnetic assembly are Particle Type III, which is comprised of a polymer core with the diameter of 9.8 μm, and the coated nickel and gold layer with the thickness of 100 nm and 50 nm, respectively. The details of this kind of particles are given in the materials section in Chapter 3.

5.2.1.2 Test Chips

Among the materials used in the chips, silicon and gold are diamagnetic, and titanium is paramagnetic, but only nickel is a ferromagnetic material, which can be easily magnetized under magnetic field and remain the magnetized property after removed from the external magnetic field. This kind of ferromagnetic material, nickel, exists in both the bump of certain chips and Ni/Au coated particles, thereby enabling the magnetic assembly process. Besides the second group of chips with Ti/Ni/Au pads that has been introduced in Chapter 4, another group of chips was also used here for magnetic assembly process.

This kind of silicon chips were utilised for the initial trials of magnetic assembly. The pads are comprised of electroless nickel, and uniformly distributed on the silicon chip. The other materials in the chip are the aluminium path and silicon substrate. Aluminium and silicon are non-magnetic substance which means that they are negligibly affected by magnetic field, thus nickel is the only material which can remain magnetized, which makes this chip an ideal option for the magnetic assembly trials. Figure 5.1 shows that the layout of the silicon chip and the Ni/Au particles used in this experiment.

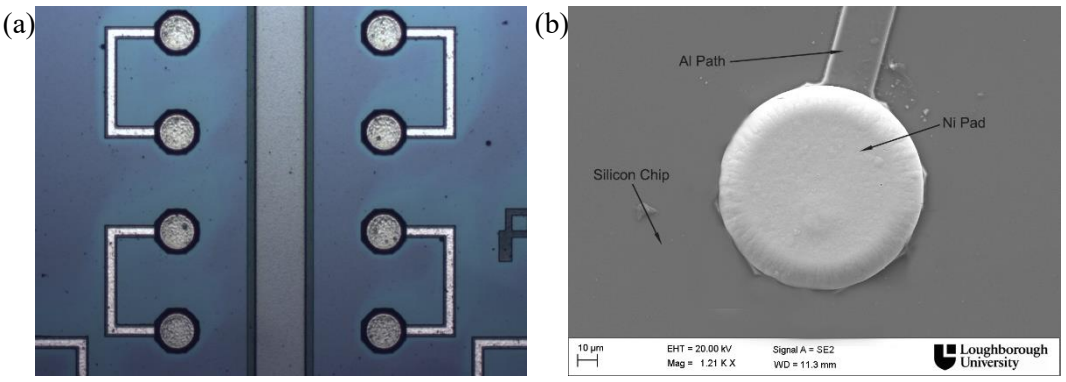

Figure 5.1 Layout of the chip for magnetic deposition: a) microscope image of the pad distribution in the chip, b) field emission gun scanning electron microscope image of the 9.8μm Ni/Au particle used in magnetic assembly on the nickel pad

.

5.2.2 Apparatus

Magnetic assembly requires specialized devices due to its difficulty to precisely control the magnetic field. There are many different kinds of potential magnets, i.e. different kinds of permanent magnets using different materials such as ceramic, alnico, samarium cobalt neodymium iron boron and so on. It is relatively easy to test the magnetic properties of the particles or chip using the permanent magnets for the initial trials. However it is extremely difficult to modify the magnetic field using permanent magnets. Thus solenoids electromagnets were utilised in this work to build the magnetic assembly system. A relatively uniform magnetic field can be established and it is much easier to control the strength of the magnetic field by simply changing the applied current. The diameter of beaker used in the experiment is 49mm, so the electromagnet P75/50 is used in this experiment. Both sides of the electromagnets are shown in Figure 5.2 (a). There is a mounting hole in the middle of the back side, which enables its possibility to be fixed to the whole system providing an easy way to control the position of magnet. On the front side, the round metal area in the middle of right one is the working area. The diameter of the working area of the electromagnet is 50 mm which ensures a sufficient area to build a relatively uniform magnetic field within the beaker area. Figure 5.2 (b) illustrates the cross section of the electromagnet, which is make by winding the copper wires into multiple loops around the centre stainless steel cylinder core. The magnetic field is created by applying the external current, and is also dramatically intensified by stainless steel core, which results in the establishment of a strong and controllable magnetic field.

(a)  (b) 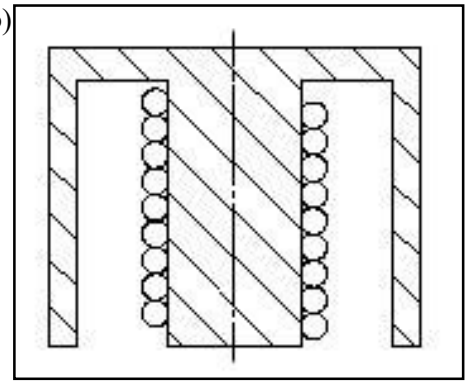

Figure 5.2 the electromagnet used in the experiment: (a) microscope images of both sides of the electromagnet (left one shows the back side, while right the front side), (b) schematic image showing the cross section of the electromagnet.

There are two different kinds of magnetic field, namely static magnetic field and time-varying magnetic field. Static magnetic field does not change in density of direction over time, hence has a frequency of 0 Hz. In contrast, time-varying magnet field reverses its direction at a regular frequency usually by applying an alternating current (AC). The strength of the static

magnetic flux density is defied in Tesla (T) or Gauss (G) (1 Tesla = 10,000 Gauss). The strength level of the natural geomagnetic field varies from approximate 30 to 70 μT (1 μT is 10^{-6} T), while much stronger magnetic field can be generated in the area of industry and medical equipment, for example it can reach 1.5 to 3 T for Medical Resonance Imaging (MRI) devices. In this work, a Gaussmeter WT-10A is used to measure static magnetic field intensity as shown in Figure 5.3, and it has a high sensitivity of 0.1 mT with two optional ranges between 0~200mT and 0~2000mT. The magnetic field detect sensor is located in the concave of the metal bar as shown in Figure 5.3 (a), and the sensor should directly face the target to enable an accurate result during the measurement as illustrated in Figure 5.3 (b).

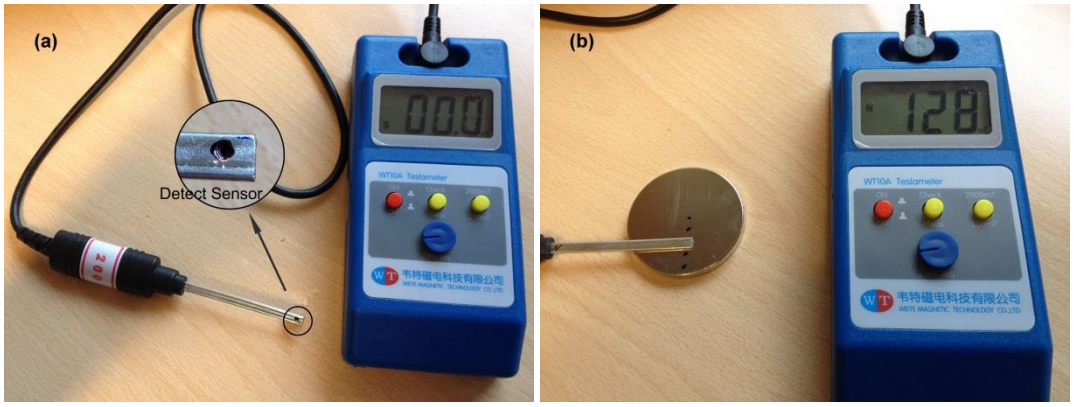

Figure 5.3 The Gaussmeter used in the experiment: a) detect sensor, b) measure method.

The Vibrating Sample Magnetometer (VSM) is a commonly used instrument to characterize the magnetic properties of materials as a function of magnetic field, temperature, and time. A uniform magnetic field is created through a pair of opposite electromagnets when applying the direct current. The sample being tested is suspended in the centre using carbon fiber due to its advantage of extremely rigid and light, and the sample can generate its own magnetic field within this uniform magnetic field. A VSM operates by vibrating the sample up and down in this controlled uniform magnetic field. The time dependence of the induced current resulting from the vibration of the sample is picked up by the detect sense coils, and the output signal is collected and analysed by the connected computer, which generates the final magnet moments of the sample forming the *M-H* hysteresis loops. In this project, magnetic properties measurements were carried out using a Model 7400 Vibrating Sample Magnetometer (VSM) produced by Lake Shore Crytronics.

Figure 5.4 Microscope image of the Lake Shore Crytronics Model 7400 Vibrating Sample Magnetometer (VSM) (http://www.lakeshore.com/products/Vibrating-Sample-Magnetometer/7400-Series-VSM/Pages/Overview.aspx).

A WDN-280 Single Yoke Double-tuned Air Gap Alterable Electromagnet fabricated by the British General Magnetic Changchun Co. Ltd was used to magnetize the silicon chips and particles as shown in Figure 5.5.

Figure 5.5 The WDN-280 Single Yoke Double-tuned Air Gap Alterable Electromagnet.

The magnetic field created by a pair of electromagnets is in the horizontal direction parallel to the ground. The centre area of magnetic field, 30×30×30 mm^3, is considered to be uniform with a uniform degree of $\frac{\Delta H}{H} = 0.02$. The pole diameter of the two electromagnets is 280 mm, and the diameter of working pole face is 150 mm. At the highest working power 12.0 KW, the maximum magnetic field can reach 2.6 T when the air gap between two electromagnets is 15 mm.

An inverted digital Axio Observer microscope provided by Zeiss UK is used to study the magnetic assembly process as shown in Figure 5.6. This microscope system is fast, flexible, economic and efficient, and the dedicated software modules provide reliable and reproducible analysis such as the analysis of grain sizes and phases, size and distribution of the graphite particles, measurement of the thickness of geometric properties. Experiments will be carried out to deposit Ni/Au particles onto the facing-bottom chip in a transparent beaker under the control of magnetic field. The most important advantage of this microscope is that this inverted microscope system enables the observation from the bottom of the beaker so that the movement trajectory of particles during the deposition process, and the results can be recorded by the connect computer for subsequent analysis.

Figure 5.6 the inverted digital Axio Observer Microscope.

5.3 Experiment Methodology

5.3.1 Magnetic Assembly Mechanism Study

Some theoretical analysis has been carried out to study the dipole-dipole interactions forces between the magnetic particles and the dipole-field parking force under external magnetic field, and these two kinds of fundamental forces contributed to various magnetic assembly applications using a variety of particles and substrates. Some simulation results also proves that the particles tend to form chain structure when the magnetic dipole-dipole interaction is attractive with the angle between two particles and the external field $0 \leq \alpha < 54.09°$ [111]. There are two main methods to control the movement and trajectory of the particles, which are the current of the electromagnet and viscosity of the solvent. The magnetic intensity gradient provides the initial moving force for the particles, while the viscosity strongly impacts the velocity and trajectory. It is easy to control the magnetic field by simply changing the current to each electromagnet. However due to the small size of the particles and the organic liquid deposition environment, it is difficult to observe the interactions between the particles within the exchange of external magnetic field. In order to better understand the movement of the particles under magnetic field, specific system with an inverted digital microscope is set up as shown in Figure 5.7.

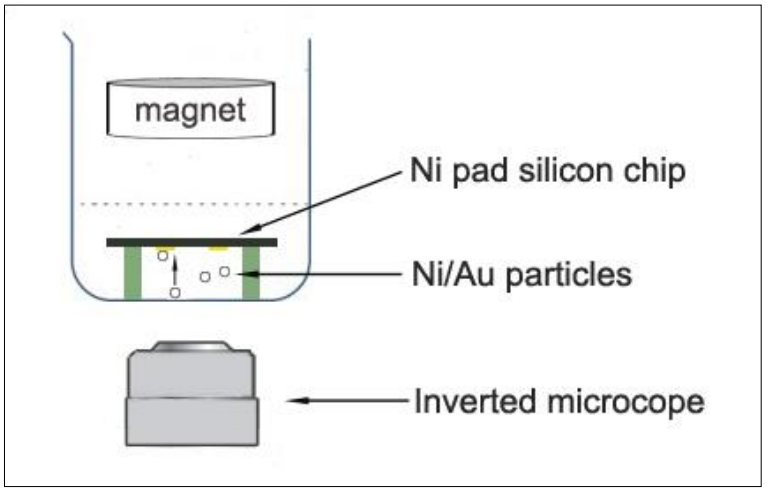

Figure 5.7 Schematic diagram showing the inverted experiment system for the video recorded process study of magnetic assembly.

A small amount of Ni/Au coated polymer particles with 9.8 μm in diameter were dispersed in an organic solvent propan-2-ol (isopropyl alchol (IPA)), IN a 50 ml Pyrex beaker with a dameter of 39 mm. The density of the particle, at around 1.79 g/cm^3, is significantly higher than that of IPA (0.79 g/cm^3), so most of the particles sediment to the bottom 25 minutes later. A silicon chip with nickel pads (Chip I) was placed facing downwards, supported by two thin

slices of glasses with the thickness of 0.5mm leaving an empty area for the magnetic assembly process. Finally a permanent reached the chip from the topside and the magnetic field was controlled by changing the distance between the chip and magnet. The new Axio Observer microscope provided by Zeiss UK enables a relatively long focus distance, which provides the possibility of observing the movement of the particle within the suspension under the external magnetic field. The results were recorded in a video which is saved in the connected computer for the further analysis. In the near future, the permanent magnet can be changed to a current controlled electromagnet, and this system will contribute a much better understanding of the interactions between the magnetic particles under different exchange of magnetic fields.

5.3.2 Magnetic Assembly I with External Magnetic Field

Microscale particles have been used to fulfill the packaging of smart cards and screen for nearly two decades, and there are many different kinds of particles such as pure silver particles, metal particles with a thin layer of polymer outside, nickel coated polymer particles, and nickel gold coated polymer particles. But still only two available mediums, anisotropic conductive adhesives (ACAs) and anisotropic conductive film (ACF), are commercially used for the electric packaging. Theoretically there are still many properties of the particles which have not been fully developed and can be further utilised for the future applications. Magnetic assembly technology takes advantage of the ferromagnetic property of the nickel layer of the Ni/Au particles and directly onto the targeting pad without any harm of the metal layer. The basic concept of the magnetic assembly process is that even if not permanently magnetised, when placed in a magnetic field ferromagnets will become magnetised and will therefore be attracted to each other. By suspending the particles in a nonmagnetic liquid in proximity to the chip it was therefore expected that the particles would be attracted to the nickel bumps, but this attraction would be weak and therefore the overall magnetic field should encourage movement of the particles towards the chip thereby increasing the probability of the bumps “capturing” the particles.

In order to obtain a uniform deposition over the area of the chip, a uniform magnetic field in *x*-*y* plane is needed to ensure the particles remain dispersed uniformly in the solvent whilst they move towards the chip. Meanwhile, there must be a magnetic gradient in the *z* direction to provide the motive force toward to the chip for the Ni/Au particles under magnetic field. There are several methods to create a uniform magnetic field. For volumes of a few cubic millimeters, a permanent magnetic with a focusing pole piece is possible. However for larger volumes, superconducting magnets are ideal such as the spectrometer used in magnetic resonance imaging (MRI). For the experiment in the lab, MRI is not available considering its large size and high price, therefore for the initial trials without a significant high demand for homogeneity, a system with two electromagnets was set up as shown in Figure 5.8.

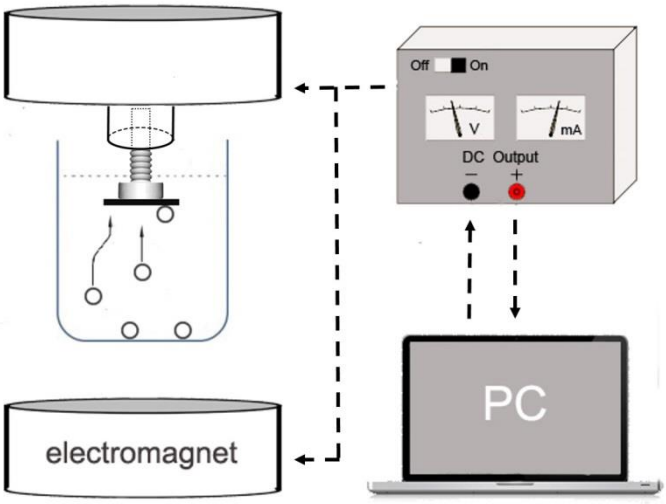

Figure 5.8 Schematic images showing the system of magnetic deposition with external magnetic field.

Figure 5.8: Schematic images showing the system of magnetic deposition with external magnetic field. In this system, the DC current in the electromagnets is controlled by the computer so that the magnetic field versus time can be controlled. The two magnets are supplied with the same, but opposite direction current. Consequently a relatively uniform magnetic field is established by facing the working areas of these two electromagnets. One side of a special polymer holding device is attached to the working area of top electromagnet, and the other adjustable side provides the surface for the back side of the chip, leading to a facing down chip for the assembly process. The positions of the electromagnets, beaker, and the holing device can all be adjusted, thus create the optimized situation for the magnetic assembly process. The Ni/Au particles were dispersed in the organic propan-2-ol (isopropyl alcohol (IPA)) in a 50 ml Pyrex beaker, and after 15 minutes ultrasonic bath, the particles were dispersed uniformly in the solvent.

5.3.3 Magnetic Assembly II with Pre-magnetized Particles and Chips

Without the external magnetic field, the magnetic dipole-field parking force between the Ni/Au coated particles and nickel pads chip is not strong enough to overcome the gravity and viscosity resistance and drive the particles onto the top chip. The magnetic assembly process II is relatively simple, where the chip was placed at the bottom of the beaker facing upward, so the gravity of the particles contributes to the assembly as a comparison. However both the particles and pads must be pre-magnetised so that the particles can move toward the target pad. Both the Ni/Au coated particles and Ti/Ni/Au bumped silicon chips were tested using a Lake Shore Cryotronics model 7400 Vibrating Sample Magnetometer (VSM). The obtained hysteresis loop

reveals the detailed magnetic properties of the specimen, which provides reference data for the magnetizing process. This magnetic assembly process is illustrated in Figure 5.9.

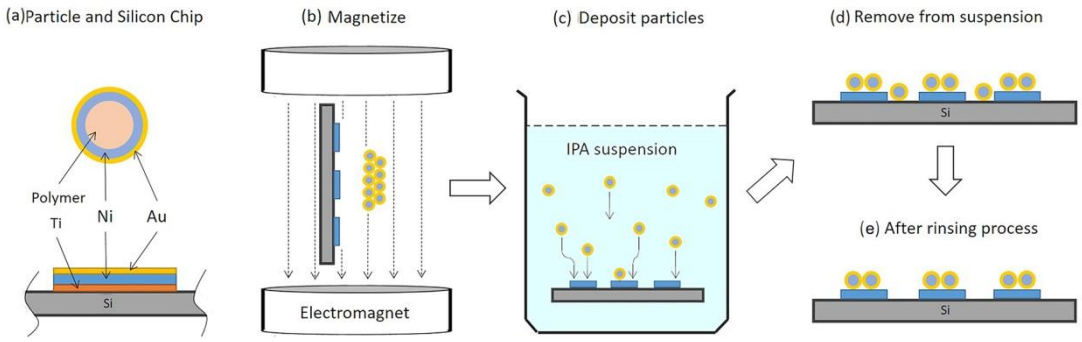

Figure 5.9 Schematic diagram of the (a) Ni/Au coated polymer core particle and Ti/Ni/Au pad, and the magnetic deposition process (b) magnetize the chips and particles, (c) transfer the chips and particles into IPA solution, (d) remove the chips and particles from the suspension, (e) the final assembly structure after rising process.

A WDN-280 Single Yoke Double-tuned Air Gap Alterable Electromagnet fabricated by the British General Magnetic Changchun Co. Ltd was used to magnetize the silicon chips and particles. At the supplied voltage of 20A, a magnetic field of 5 kOe can be obtained, and both the particles and silicon chips were put into a magnetic field for 2 minutes to complete the magnetizing process. Two different orientations were adopted for magnetizing the silicon chips, where the chip was either parallel or perpendicular to the direction of the magnetic field. Following magnetization the chips and an excess of particles were transferred into isopropyl alcohol (IPA). The density of the particles, at around 1.79 g/cm^3, is significantly higher than that of IPA (0.79 g/cm^3), but due to their small size their sedimentation rate is low allowing sufficient time for deposition to take place. Finally the chips were removed from the IPA after two minute and then gently rinsed with deionized water to remove any loose particles on the passivation area on the chip surface. The particles on the magnetized pads were supposed to be remained in place during rinsing because of the magnetic attraction between them and the pads.

5.4 Results and Discussion

5.4.1 Forces Analysis of Ni/Au Coated particle

There are several forces acting on the particle: the gravity of the particle, buoyance force in the medium, magnetic induced force, and the hydrodynamic resistance during movement. The particle can suspend in the isopropyl alcohol (IPA) for about half an hour which means that gravity and buoyance force can be neglected in the calculation. In the completely uniform

magnetic field, there is only torque for the Ni/Au particles, but no translation action. A magnetic field gradient is required to produce the motive force for the particles. For the magnetic force acting on Ni/Au particle:

$$\boldsymbol{F_m} = \left(\boldsymbol{m}\cdot\nabla\right)\boldsymbol{B} \tag{5.1}$$

where $\boldsymbol{F_m}$ is the total force of the particle, $\boldsymbol{m}$ is the magnetic moment which can calculated from $\boldsymbol{m} = V_m\boldsymbol{M}$ (V_m is the volume of the particle and $\boldsymbol{M}$ is its volumetric magnetization**),** and $\boldsymbol{B}$ is the magnetic induction. $\boldsymbol{M}$ is given by $\boldsymbol{M} = \Delta\chi\boldsymbol{H}$, where $\Delta\chi = \chi_m - \chi_s$ is the effective susceptibility of the particle relative to the deposition solvent.

The particles are suspended in isopropyl alcohol (IPA), and the overall response of the particles plus IPA is approximately $\boldsymbol{B} = \mu_0\boldsymbol{H}$. As shown in Figure 5.9, the magnetic field is relatively uniform in x-y plane while there is a magnetic field gradient in z direction and the magnetostatic field energy density is higher as approaching to the terminate electromagnets. So the magnetic induced force of the particle is

$$F_m = V_m\cdot\Delta\chi\cdot\Delta\left(\frac{B^2}{2\mu_0}\right) \tag{5.2}$$

The hydrodynamic resistance force acting on the particles is given by

$$F_h = 6\pi\eta R_m\Delta v\,, \tag{5.3}$$

where η is the viscosity of the IPA, R_m is the radius of the Ni/Au particle, and $\Delta v = v_m - v_i$ is the difference in velocities of the particle and the IPA solvent [159]. Apparently when hydrodynamic force will increase with the increase of velocity of the particle, and when reaching the stable status, $F_m = F_h$, which leads to the velocity of the particle

$$\Delta v = \frac{R_m^2\Delta\chi}{9\mu_0\eta}\nabla\left(B^2\right) \tag{5.4}$$

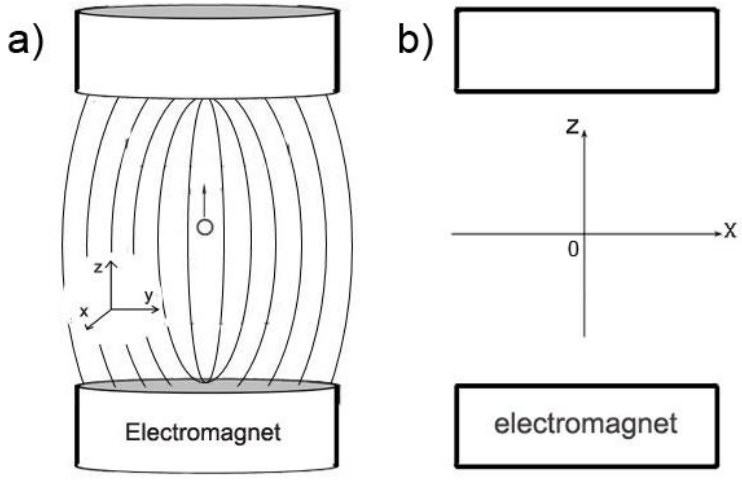

Figure 5.10 Schematic diagram showing (a) the magnetic induction lines distribution (b)

coordinate system within the cross section of the magnetic deposition system.

The magnetic field intensity both from *x* direction and *z* direction were measured and the results are shown in Figure 5.11 and Figure 5.12. The results illustrate that the established magnetic field meets the requirement of magnetic assembly, which is relatively uniform in *x*-*y* plane to ensure the equal deposition possibility for each pad, while the magnetic gradient in z direction creates the initial motive force for the Ni/Au particles.

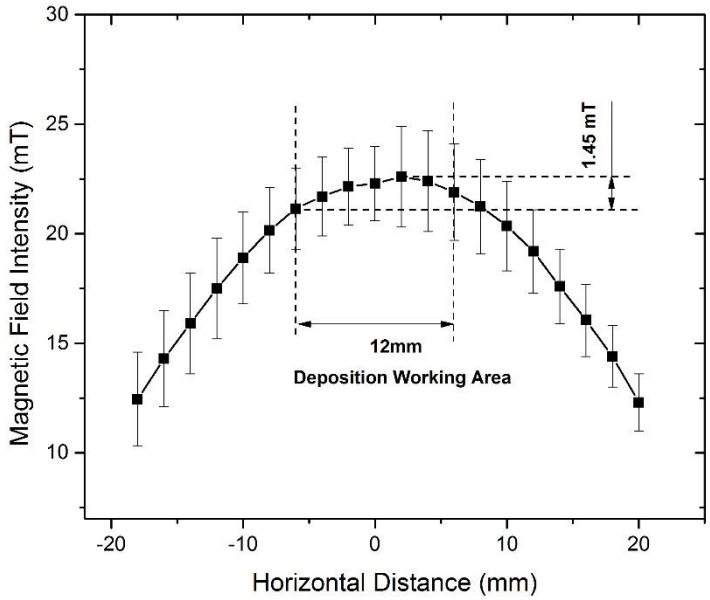

Figure 5.11 The magnetic field intensity distribution in the horizontal plane (z=0, -18<x<18).

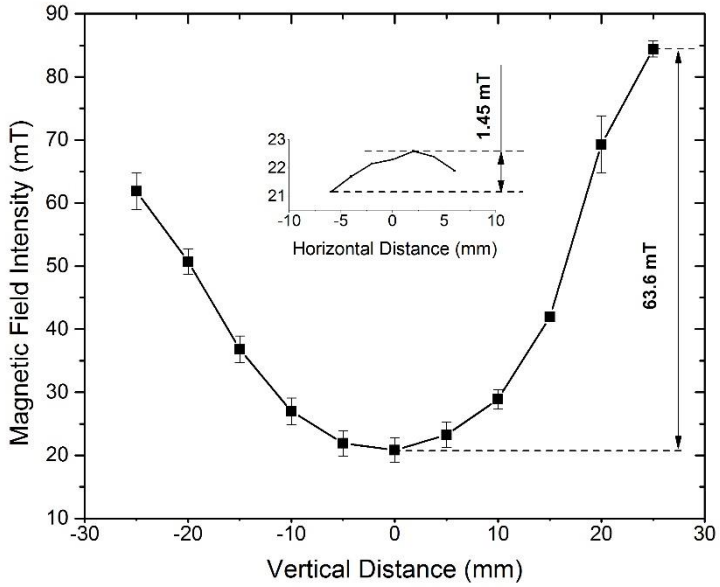

Figure 5.12 The magnetic field intensity distribution at the vertical level (x=0, -50<z<50).

The size of the chips used in the experiments includes 4.5×3.5 mm (with Ti/Ni/Au pad) and 8×8 mm (with Ni pad), and thus the working area of the magnetic field in the horizontal plane is defined as 12 mm, which is one and half times larger than the chip size. In the horizontal working area, the fluctuation of the magnetic field intensity in 1.45 mT as shown in Figure 5.13, and the calculated gradient ranges from 0.025 T/m to 0.275 T/m. Compared with the fluctuation in the horizontal plane within the working area, there is a big fluctuation of magnetic field (63.6 mT) and the gradient in the z direction ranges from 0.55 T/m to 5.56 T/m. These results prove that the magnetic field is relatively uniform in the x-y plane, while there is a significant magnetic field gradient in the z direction. According to the minimum energy principle, the magnetic particles tend to move to the strongest magnetic field area to reduce the magnetostatic energy, which is the area around z=0 in the horizontal plane and the area near the electromagnets in the vertical plane. The relatively uniform magnetic field and the relatively low gradient in the x-y plane restrain the particles' movement horizontally which ensures the particles remain uniformly distributed over the overall chip area, while the big gradient in the z direction creates the motive force on the Ni/Au particles to move them towards the chip area which has stronger magnetic field.

The relationship between the magnetic field intensity, H, at the centre of the working volume was found to increase linearly with the applied voltage, i.e. H = 0.93 mT/V as shown in Figure 5.13. This linear relationship can be used to calculate the intensity so as to specifically design different magnetic field by applying different modulated external voltage.

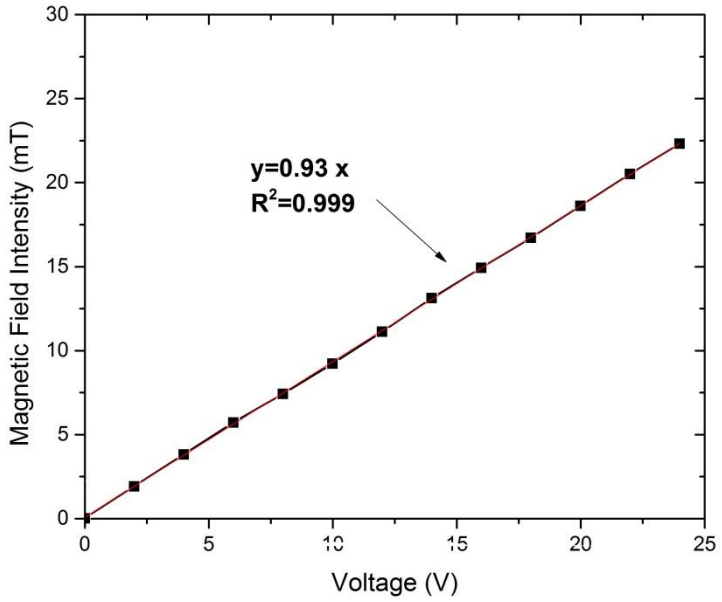

Figure 5.13 The relationship between magnetic field intensity of the middle point (x=0,y=0,z=0) and applied voltage.

.

5.4.2 Results of Magnetic Assembly I

Using the microscope it could be seen that the thin layer of nickel on the particles produced enough magnetic moment for the electromagnet to attract them despite only comprising 2 % of the volume of the particles. For this test the particles were initially allowed to sediment out of suspension so that they were dispersed randomly on the bottom of the beaker; however once the magnetic field was applied they were attracted together quickly and formed different length particle chains aligned with the magnetic field direction, as shown in Figure 5.14. At this moment the applied magnetic field was at a low level, and all the particles still landed on the bottom of the beaker. Following the decreasing distance between the permanent magnet and the chip, the particles started to move upwards due to the increasing magnetic field.

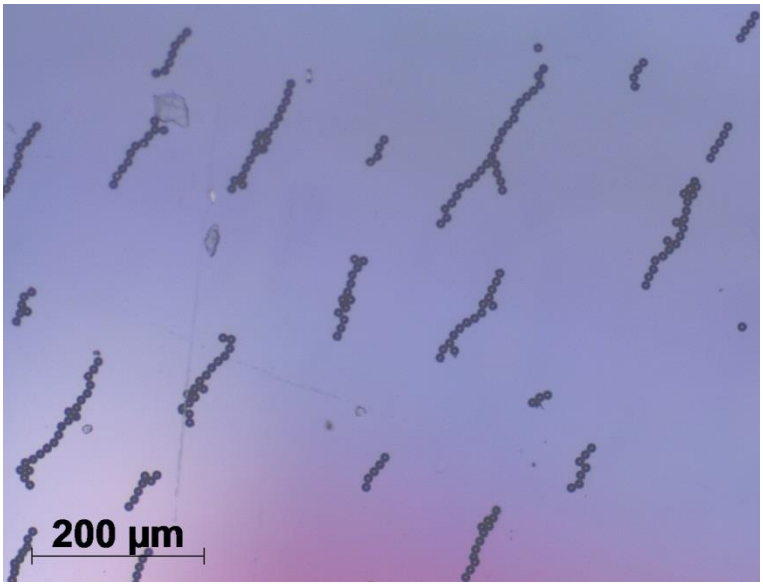

Figure 5.14 Inverted digital microscope image of the Ni/Au particles sedimented on the bottom of the beaker.

These results also illustrate that the basic units during the magnetic deposition are not individual particles, but particle chains of varying length. In the external magnetic field, these particle chains move slowly toward the nickel pads. The chip before deposition is depicted in Figure 5.15 (a) while Figure 5.15 (b) shows that by the end of the deposition, only one end of the particle chain was attached to the surface of the bump, while most of the particles remain part of the chains aligned in the magnetic field direction. Benefiting the transparent beaker and IPA solvent, all these images were taken within the IPA suspension by the invented microscope, and the whole magnetic assembly process was also recorded as a video. Consequently, magnetic dipole-dipole interactions between the Ni/Au coated particles were directed observed forming the chain-like structure, which testified the theoretical study. Meanwhile, the interactions

between the Ni/Au coated particles and nickel pad were also recorded in the video. Therefore an in situ study system using inverted microscope significantly helps to better understand the magnetic assembly process, and each procedure during the assembly process can be studied in detail by analysing the recorded video. Furthermore due to the advantage of tunable and reversible magnetic assembly process, different magnetic fields can be applied within this system in order to study the interactions between the magnetic particles and nickel pads, which helps to design and build an optimized magnetic assembly in the subsequent experiment.

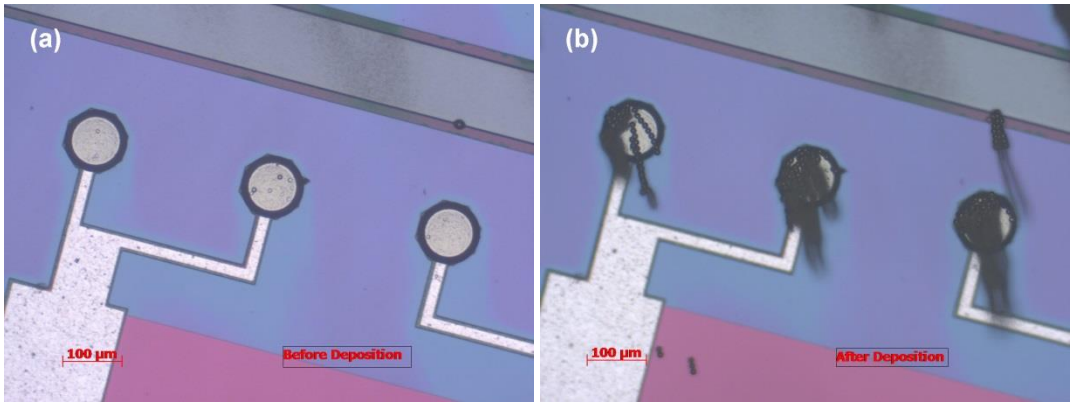

Figure 5.15 Microscope images showing the magnetic deposition results in the solvent IPA: (a) the Ni pad silicon chip before deposition, (b) the Ni/Au particles deposited onto the pads.

From the magnetic assembly mechanism study using the in situ inverted microscope system, it is clearly that the Ni/Au coated particles can be deposited onto the target pad within the IPA suspension under the external magnetic field. Therefore the magnetic assembly process I was carried out. In the first experiments when the particles were successfully deposited onto the bumps, the current supply to the electromagnet was then shut off, and the silicon chip was then slowly removed from the IPA. As shown in Figure 4.18, it was found that most of the particles had moved to surround the nickel bumps and only a few particles remained on the bump surface. Compared to the initial deposition in the solvent shown in Figure 5.16, it is clear that many of the particles which were on the bump while in the solvent were washed off during the process of removal from the solvent. Further experimentation confirmed that surface tension forces in the solvent overcame the weak attachment between the deposited particles and magnetized bump.

The first method tested to keep the particles on the top surface of the magnetized bumps was keeping the chip exactly parallel to the x-y plane when extracting it from the solvent, in order to reduce the possibility of a washing off effect. However this did not improve the results significantly because the solvent remaining attached to the surface of the chip forms a droplet as a result of surface tension and this flow sweeps the particles off the bumps.

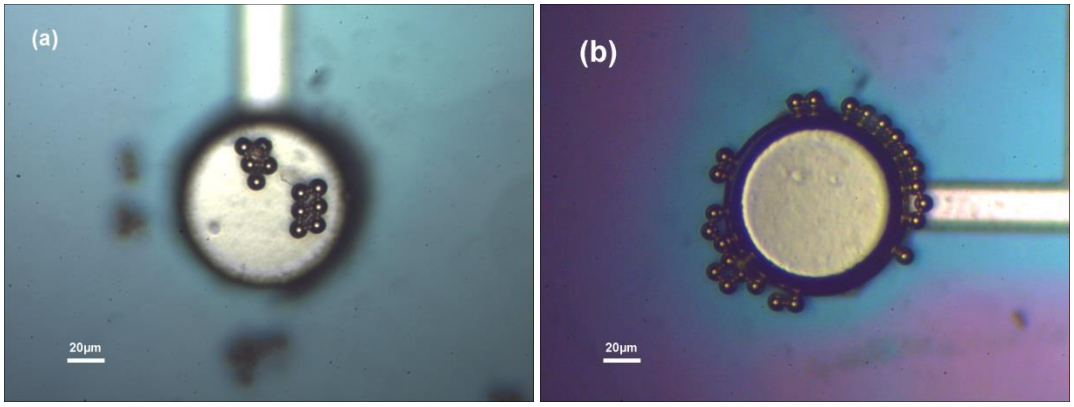

Figure 5.16 Microscope images of the magnetic deposition when moving out the chips from the IPA solvent without external magnetic field.

The next method tested was to increase the magnetic field intensity whilst removing the chip from the solvent and maintaining this strong magnetic field until the solvent had completely dried. As shown in Figure 5.17, this method leads to a much better deposition quality and many particles remaining on the bump surface. However the particles tended to form a ring around the edge of the bump, as can be seen in Figure 5.16, with no particles in the central area of the pad. This is believed to be because the magnetic field gradient will be highest at the edges of the bumps when removing the applied magnetic field. Based on the in situ observation shown in Figure 5.17 (b), many particles chains with loads of particles were deposited onto the pad surface. Compared with the final deposition morphology as shown in 5.16, it is clearly that most particles were washed off when extracting the chip out of the solvent. Therefore the unfixed assembly between the particles and pad surface also brings the issue that how to maintain enough particles on proper area of the pad surface. More potential improvements to the process, including improved control over the distribution and magnitude of the magnetic field throughout the entire particle deposition and drying process and bump and particle surface modifications are currently undergoing evaluation to understand how they affect the deposition quality.

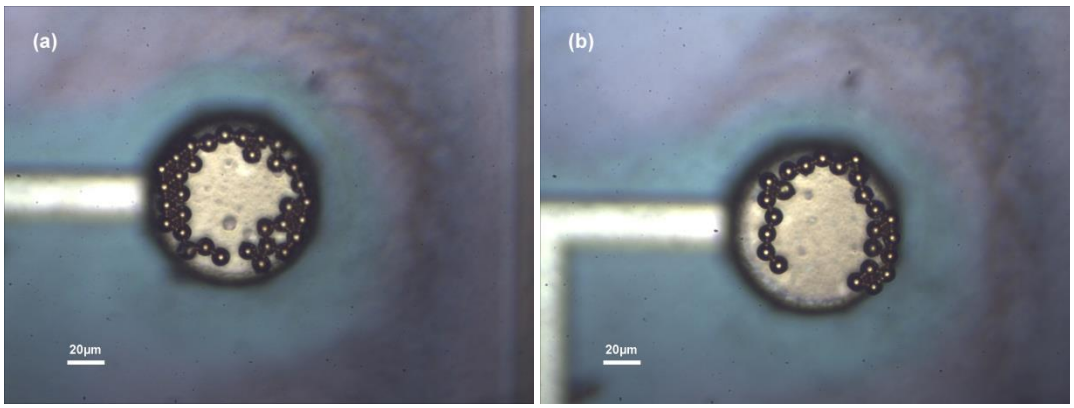

Figure 5.17 Microscope images the magnetic deposition when moving out the chips from the IPA solvent with extra strong magnetic field.

5.4.3 Results of Magnetic Assembly II

5.4.3.1 Magnetic Properties of the Silicon Chip (Chip III) and particles

Among the element silicon, titanium, gold, and nickel in the silicon chips and particles, silicon and gold are diamagnetic, titanium is paramagnetic, but only nickel is a ferromagnetic material and can retain magnetized property after removed from the magnetic field. The magnetic properties of the silicon chips and particles are shown in Figure 5.17 and the non-zero values of y_1, y_2 and y_3 show that both the silicon chips and Ni/Au coated particles were successfully magnetized.

The Hysteresis loops of the chips and particles reveal lots of useful information such as the saturation induction, retentivity, coercive force, permeability, and reluctance. In this experiment, saturation point and retentivity are the most important parameters, which determine the required external magnetic field during magnetising process and the success ability of subsequent magnetic assembly. As shown in Figure 5.18 (a), for silicon chips the magnetic field reaches a saturation point above which there is a decreasing trend in the magnetic moment. The reason for this is that the effect of the diamagnetic materials becomes stronger with the increasing magnetic field. However for the particles the influence of the very thin gold layer is negligible and as shown in Figure 5.18 (b) the magnetic hysteresis loop for the particles fits perfectly to that of a standard ferromagnetic material.

Therefore, the diamagnetic material silicon is supposed to be the main reason which causes the decreasing magnetic moment after saturation point for the silicon chip. The saturation magnetic fields for the silicon chips and Ni/Au coated particles are both around 5 kOe, which means that the magnetic field adopted in the magnetizing process is sufficient to magnetize them. The actual residual magnetism may be lower than the retentivity if the external magnetic field does not reach the saturation level during the magnetising process. The results illustrate that the magnetic properties of the silicon chips are significantly affected by the chip orientation during the magnetizing process, and the remanent moment of the chip magnetized in the parallel orientation (45.47E-6 emu) is double that in vertical orientation (28.31E-6 emu). The retentivity and saturation of the particles are 4.72 emu/g and 8.41 emu/g receptivity.

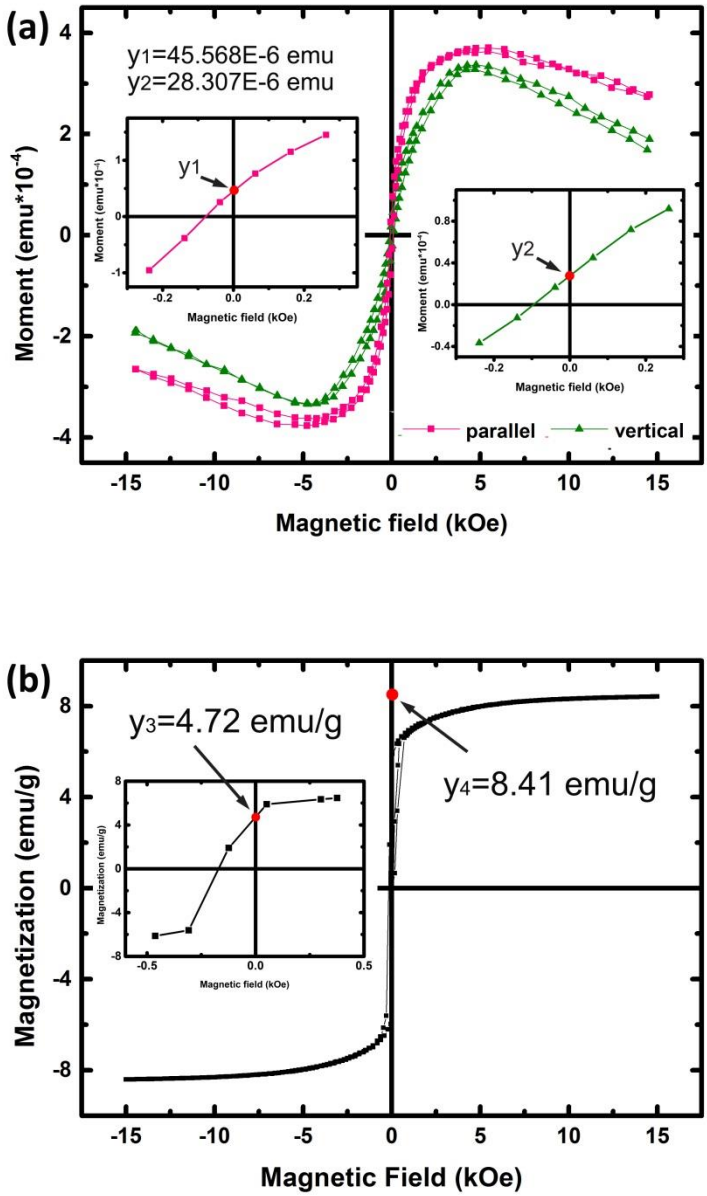

Figure 5.18 Magnetic hysteresis loops for (a) the silicon chips comparing the parallel and vertical magnetizing process, and (b) Ni/Au coated polymer particles.

5.4.3.2 Results of the Magnetic Assembly Process II

A current of 20A was applied to the WDN-280 Single Yoke Double-tuned Air Gap Alterable Electromagnet, which created a 5 kOe magnetic field. The intensity of this magnetizing field is the same with the measured saturation magnetic field for silicon chips and particles, in order to ensure the retentivity measured using VSM. Two different orientations of the chips during the magnetizing process were tested with the chip surface, which are perpendicular to the magnetic induction lines and parallel to the magnetic induction lines. For the first perpendicular magnetizing process, almost no particles were left after the rinsing process, while a good

deposition density was achieved using the parallel magnetizing process. As presented in Figure 5.19, the rinsing process slightly removed the loose particles on the on the Si_3N_4 layer, while most particles on the Ti/Ni/Au pads still remained on the pad surface. The results proved that the magnetic attraction force between the magnetized particles and Ni pads is sufficient to retain the particles during the rising process.

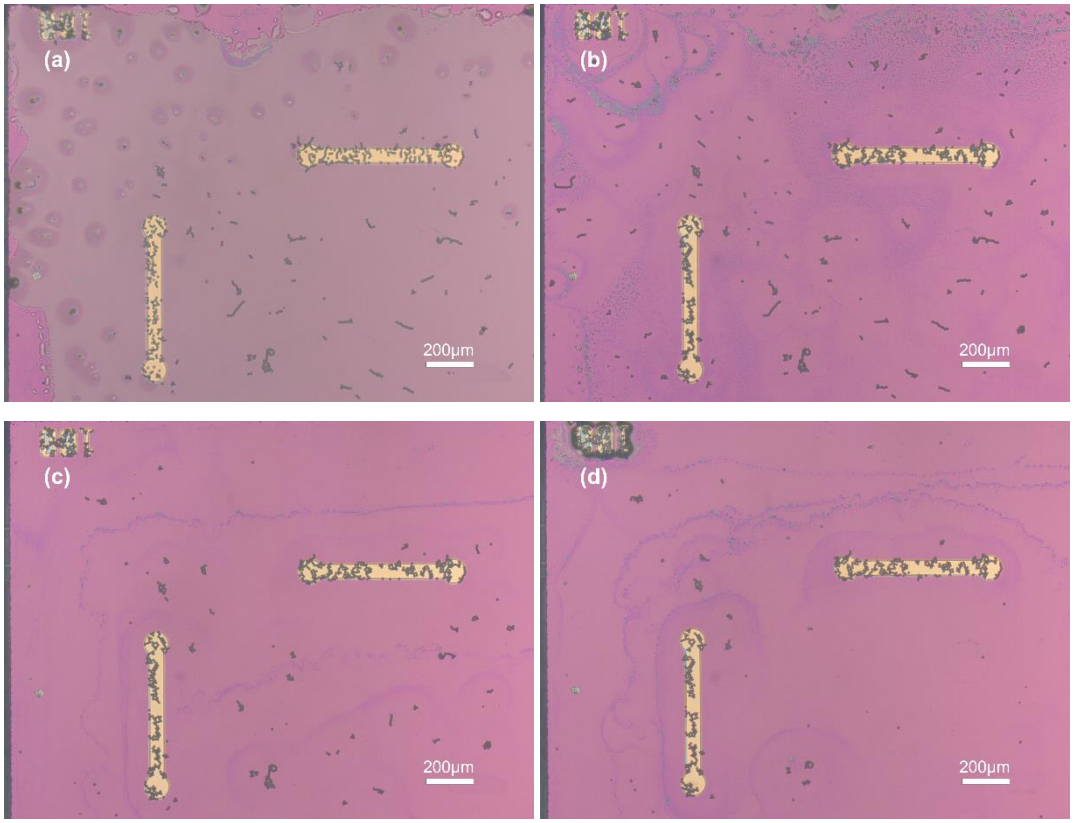

Figure 5.19 Microscope images showing the rinsing process.

For four different sizes of pads, including 50, 100, 200, and 300 μm, the magnetized particles were successfully assembled on the pad surface in the end using the silicon chips magnetized in the parallel direction with the magnetic field, and the deposition results are shown in Figure 5.20. This proved that the magnetic force between the particles and chips is strong enough to draw the particles onto the pad and remain there after rinsing. However, with the silicon chips perpendicularly magnetized, the magnetic depositions resulted in no particles remaining after rinsing. This is attributed to the lower remanent moment compared to the parallel magnetisation (Figure 5.20 (a)), as well as the effect of the different magnetization direction within the metal pad. Further experiment will be carried out to systematically study the influence of magnetising angle to the final magnetic assembly quality.

Compared with traditional flip-chip packaging with ACAs, the particle density of around 3000 particles/mm^2, on the pads is very high, without increasing the probability of short-circuits because of their selective deposition. It was observed that most particles were initially randomly

dispersed on the pad, but an aggregation had occurred during the subsequent evaporation of the rinsing water, leading to surface tension driven movement. The magnetic dipole-dipole interaction between the magnetized particles is regarded to be another contribution to this aggregation process. Furthermore, the magnetized particles tend to form a dense monolayer, which also decreases the possibility of multiple layers forming. The occasional multilayers observed will however not impact significantly on the reliability of the interconnection as any multilayer particles are very likely to be compressed down to a monolayer during assembly due to the tunable contact between the particles and pad contributed by the static magnetic attraction force.

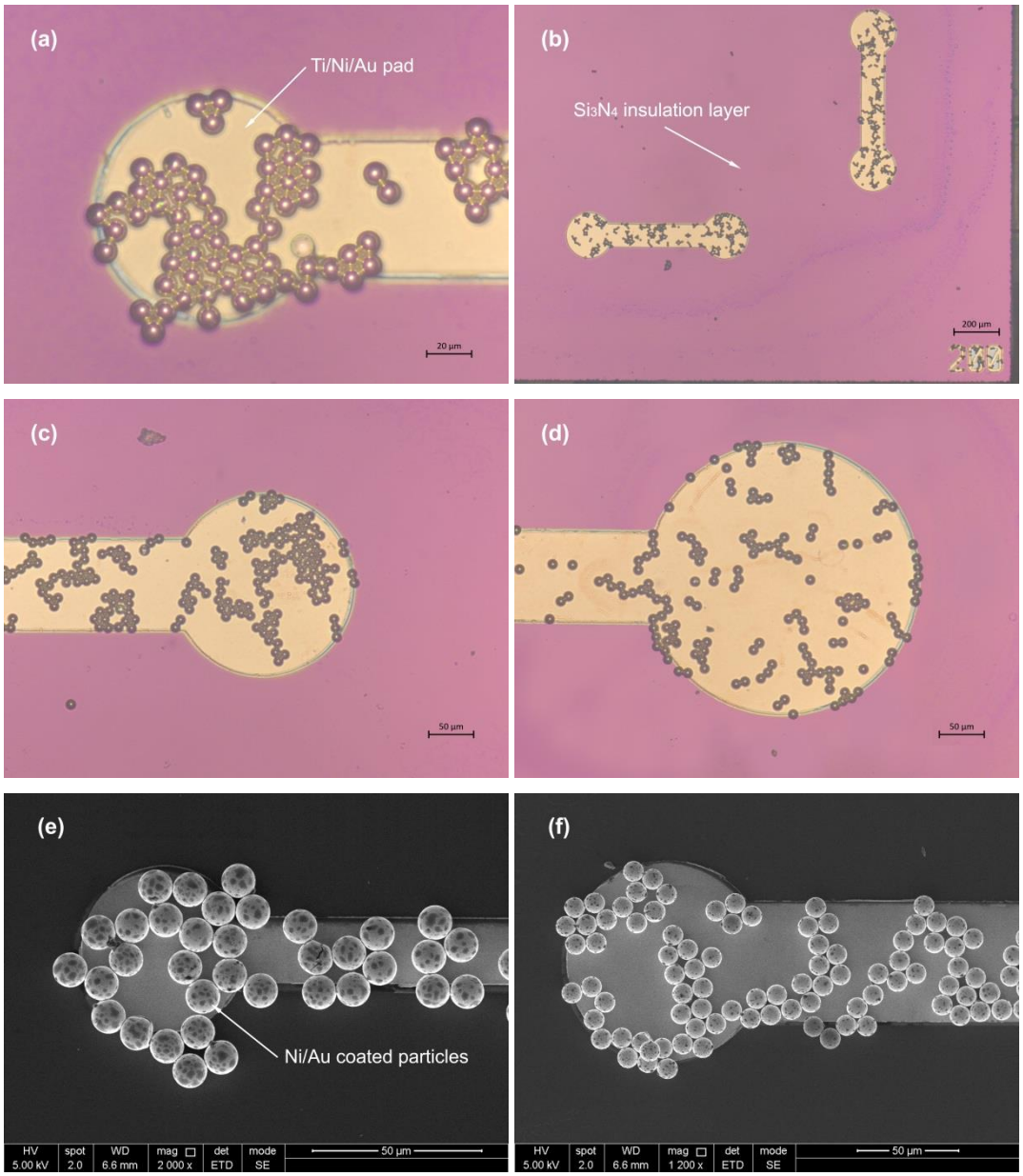

Figure 5.20 Microscopic and SEM images showing the magnetic deposition results for Ni/Au coated polymer particles onto the Ti/Ni/Au pad0.s with diameters of a) 100 µm, b) 200 µm, c) 50 µm, and d) 100 µm.

Most importantly, the particles were distributed over the whole area of the pad, instead of forming a ring around the edge of the pad as shown in Figure 5.17. One possible reason for this better distribution is that the nickel layer in the pad is 500nm which is much thinner than that in Chip I which were 20μm, so that the magnetic field gradient does not significantly concentrate around the edges. During the final bonding process using different kinds of underfilling, the particles on the edge area of the pads are very likely to be squeezed off the pad while the randomly distributed particles are believed to be more possible to survive.

Furthermore only limited multilayer deposition was observed, even though the magnetically deposited particles tend to aggregate together. As discussed earlier it is believed that during the electrophoretic deposition process, when the particles contact the chip pads that Ni^{2+} ions on the particle surface gain electrons and are reduced into elemental nickel which bonds the particle to the metal pad preventing further movement. However, magnetic deposition relies on the static magnetic attraction force between pad and particles, and the particles can still move in relation to each other. For instance it has been observed that the particles are initially randomly dispersed on the pads whilst in the solvent, but when removed from the solvent and dried they aggregate together under the combination of solvent flow due to evaporation and surface tension. This type of behaviour for small particles has been reported previously, e.g. by Liu et al. [160]. The magnetic attraction between the particles will also contribute to this process of aggregation as shown in Figure 5.21. Although some multilayer formation was observed with the new MD process, it is thought this will not seriously affect the final bonding process as the multilayer is very likely to readily compress down to a mono-layer as the particles are not fixed in place.

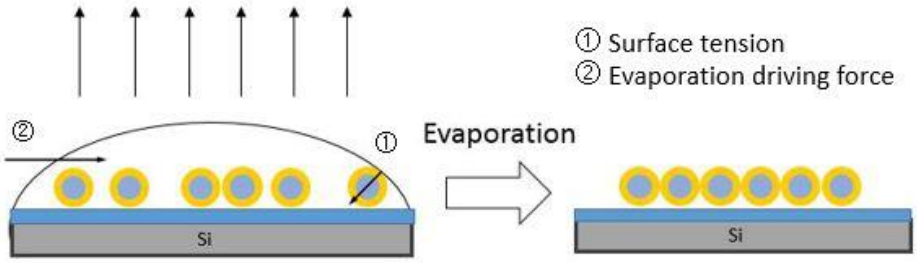

Figure 5.21 Schematic of the aggregating process for the deposited particles during solvent evaporation.

5.4.4 Comparisons between ACA, EPD, and MA

Flip-chip packaging processes using ACAs have been used for more than two decades [9, 10] with few fundamental advances in the technology and the issue of controlling the concentration

of particles to achieve a balance between conductivity and probability of short-circuits has remained a substantial issue [161-163]. There is a demand for methods to achieve ultra-high density interconnections at low cost. The methods described here offer the potential to extend the use of ACA particles in such applications by both allowing finer pitches and reducing material cost, due to reduced particle usage. Electrophoretic deposition (EPD) of the charged particles can achieve fine-pitch interconnections, however the current acid immersion charging method damages the conducting nickel layer resulting in a risk of poor reliability of the interconnections. A charging method that does not damage the particles and optimized control of the parameters, such as the electric field applied, deposition time and viscosity of the suspension, are required to achieve a good electrophoretic deposition quality for typical ACA type conductor particles. Table 5.1 provides a summary of the advantages and disadvantages of these three interconnection methods which utilise metal coated polymer particles.

Table 5.1 Comparison of the different flip-chip packaging method using mono-sized Ni/Au coated polymer particles.

	Process cost and complexity	**Ultra-fine pitch capability**	**Particle Cost**	**Conductivity of particle**
ACA	Low	No	High	Good
EPD	High	Yes	Low	Reduced
MA	Low	Yes	Low	Good

As shown in Table 5.1, the novel MD process provides a promising approach, with its specific advantages of lost cost, simplicity, fine-pitch potential and good conductivity. However this method is not suitable for all devices as the deposition requires the device bond pads to have specific magnetic properties, as do the conductor particles. Where it is feasible to establish magnetic attraction between the particles and the component or substrate pads MD can be used, which decreases the possibility of multiple layer formation, however it also introduces the requirement for a rinsing process to remove particles from the passivation area which must be carefully controlled as an aggressive process may also disturb the particles deposited onto the metal pads.

5.5 Summary

It has been shown in this study that magnetically guided deposition of Ni/Au coated polymer core particles can successfully be used to attach them to Ni bumps on a semiconductor device. For the simple magnetic deposition system built field measurement results showed that the

magnetic field intensity is relatively even throughout the working area, while a strong gradient in the z direction provides the motive force for the particles. The Ni/Au particles initially form chains aligned with the field and were initially deposited onto the nickel bump as these chains. Subsequent solvent removal and drying with the continued application of a sufficient magnetic field strength to retain the particles on the bumps result in a sufficient particle density on the bumps, with few particles on the rest of the chip surface, although the particles were clustered in a ring around the perimeter of the bump surface. This work has demonstrated the feasibility of magnetic deposition as an alternative method for selectively depositing conductor particles in applications where the bond pads or bumps are ferromagnetic, however further work is required to improve the uniformity of particle distribution over the bump surface and to evaluate the achievable uniformity of particle density over larger areas

A magnetic assembly process was demonstrated in this work with the advantages including simplicity, low cost, and ultra-fine pitch suitable for high density wafer level flip-chip interconnects as well as the wearable electronics and flexible displays. The magnetic properties of the silicon chips and Ni/Au coated polymer particles were studied, and both were successfully magnetized under a sufficient magnetic field followed by a successful selective deposition of the particles onto the pad. This indicates a sufficient magnetostatic interaction force between the magnetized particles and pads enables a high density deposition of particles. The deposited particles can meet the high conductivity requirement but reduce the short circuits probability, which is the potential application for finer pitch Flip-chip interconnects.

Chapter 6

Experiments on Assembly Process and Results Discussion

6.1 Introduction

Previous results in Chapter 4 and 5 have demonstrated that the Ni/Au coated particles can be selectively deposited onto the target pads. However final interconnection needs to be accomplished to testify the applicable capability of these methods. This chapter is committed to investigating the proper assembly process for the chips with pre-deposited particles on the pads and studying the conductivity performance of the achieved interconnection after bonding.

Traditional anisotropic conductive adhesives (ACAs) or anisotropic conductive films (ACFs) are comprised of the conductive fillers dispersed in adhesive matrix, and the curing of the polymer matrix during thermocompression helps to hold the two components together and maintain the pressure contact between the component surfaces and conductive particles. In this project, the conductive particles are separated from the adhesives and deposited directly onto the target pads using electrophoretic deposition or magnetic deposition techniques. The direct assembly of the chips without underfill is suitable for the chips that thermo-insulation is required in the *z*-direction. However a separate underfilling step is more likely to be implemented to improve long term reliability of the interconnection, which is similar with the underfilling process for packaging using isotropic conductive adhesive (ICA). The purpose of this study was to explore the proper underfilling methods so as to build a reliable and applicable approach for the EPD and MA of Ni/Au-MCPs. Two kinds of adhesives with two different bonding processes were performed, and subsequent tests were carried out to measure the conductivity of achieved interconnection. The materials and apparatus used were presented, followed by the experimental procedures for assembly process and measurement of the electrical conductive of the interconnection. Finally the results of assembly processes were analysed and electrical performance was discussed.

The bonding experiments were conducted at Norwegian University of Science and Technology. The first assembly trial was performed with the cooperation with Dr. Helge Kristiansen and Miss Giang Nghiem, and second bonding trails were carried out by themselves using the chips with pre-deposited particles prepared in Loughborough University.

6.2 Materials and Apparatus

6.2.1 Materials

6.2.1.1 Particles and Chips

The particles used are Type II Ni/Au-MCPs with a 4.78 μm polymer core coated with nickel and gold with the thickness of 50 and 30 nm, respectively. The detailed information on this kind of particles is illustrated in Chapter 3. The chips used in these experiments include pad array structure, daisy-chain and Kelvin structures. The chips were prepared in pairs including the top chip and substrate chip, and Ni/Au-MCPs were already deposited onto the pad surface of the top chips using electrophoretic deposition. The detailed information on the structure and materials of the chips is illustrated in Chapter 4. Following on the successful deposition, thermocompression bonding can be employed to fulfill the final bonding between these two silicon chips e.g. daisy-chain structure chips, as shown in Figure 6.1. There are not alignment marks on the chips; however the four corners can be used to align the chips directly during bonding. The top chip is smaller than the substrate chip, so that the testing pads at the bottom of the substrate will not be covered after bonding, which provide the possibility of further electrical conductivity test. Meanwhile transparent glasses were also utilised to act as substrates, thereby enabling the study on the influence of adhesives on the particles distribution during the underfilling process.

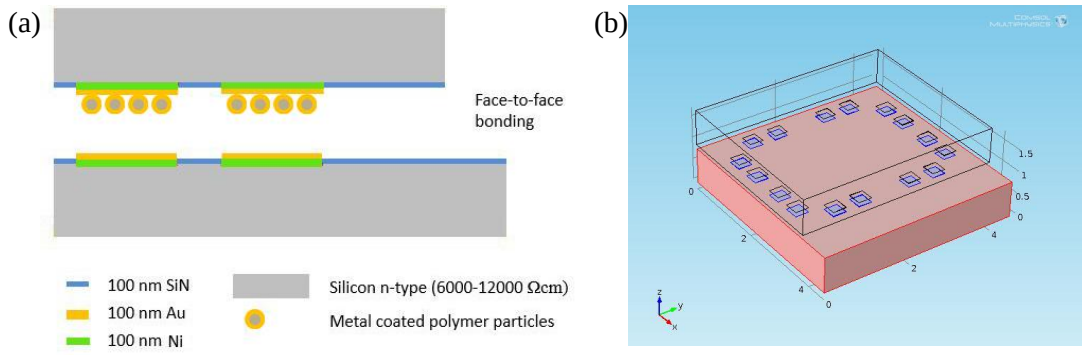

Figure 6.1 Illustration of daisy chips packaging：a) cross section of the chip, b) overview of the chips after bonding

6.2.1.2 Adhesives

The characterisation of adhesive matrix plays the dominating role in the reliability of interconnection, and it is commonly classified as thermoplastic or thermosetting depending on whether the molecular structures are linear or cross-linked after the assembly process [164].

The principal advantage of thermoplastic adhesives is that the interconnection can be disassembled for repair operations. However the thermoplastic adhesives are rigid materials below the glass transition temperature (*Tg*), and the assembly temperature must exceed the *Tg* to achieve good adhesion. In contrast, thermosetting adhesives can be cured using different techniques i.e. heat, UV light, and added catalyst. Once cured, the formed three-dimensional cross-lined structure transformed the adhesives into rigid solid, and the process is irreversible. The ability of maintain strength at high temperature and deformation is the principle advantages of thermosetting adhesives [8, 165].

Two kinds of adhesives used as underfill materials in these experiments are both thermosetting materials. The first is Adhesive I (Araldite Instant in 24ml Syringe), and this is a strong, long lasting solvent-free adhesive which is water resistance and can be painted or sanded. It can be cured in 90 seconds at room temperature after mixing the epoxy and harder, thus leaving little time for the assembly process of chips with pre-deposited particles. The curing room temperature simplifies the bonding process by eliminating the increasing temperature process. However the adhesive is relatively very viscous, which may affect the final bonding quality. The temperature resistance of this kind of adhesive lies in the range of -30℃ to 65℃.

The second kind of adhesive used in the bonding experiment is Adhesive II (Araldite PY 302-2$^{\#}$). Adhesive II is suitable for the formulation of solvent-free, easy-to-apply coatings. Compared with Adhesive I, this kind of adhesive is a clear liquid with markedly lower viscosity. At room temperature, the curing time for Adhesive II is 480 to 580 minutes, and the curing time reduces by half with the curing temperature increasing every additional 20 ℃, i.e. 80 min at 60 ℃, 40 min at 80 ℃, 5-8 min at 120 ℃. This kind of low viscous adhesive allows enough time for the alignment of the chips during bonding, and it is also believed to has less effect on the pre-deposited particles under compression.

6.2.2 Apparatus

The diameter size of the pads of daisy-chain and Kelvin chips ranges from 50 μm, 100 μm, 200 μm, to 300 μm, while the pad arrays chips include pads with the diameter from 10 μm to 50 μm. Therefore, specialized bonding machine is required due to the fine placement tolerance and applied time/temperature demand. The bonding machine used in the experiment is multi-purpose Die Bonder (Fineplacer Pico Ma), as shown in Figure 6.2. The placement accuracy of this multi-purpose Die Bonder is 5 μm, and the minimize and maximum component size ranges from 0.125 mm × 0.125 mm to 40 mm × 40 mm. The highest temperature is able to reach 400 ℃, with the maximum force to 700 N. This bonding machine can be used in a wide range of areas such as the thermocompression bonding, thermosonic bonding, ultrasonic bonding, UV curing and mechanical assembly. Specific applications include flip-chip bonding, precise die

attach, laser diode bonding, wafer level packaging (W2W, C2W) and components requiring a novel bonding approach.

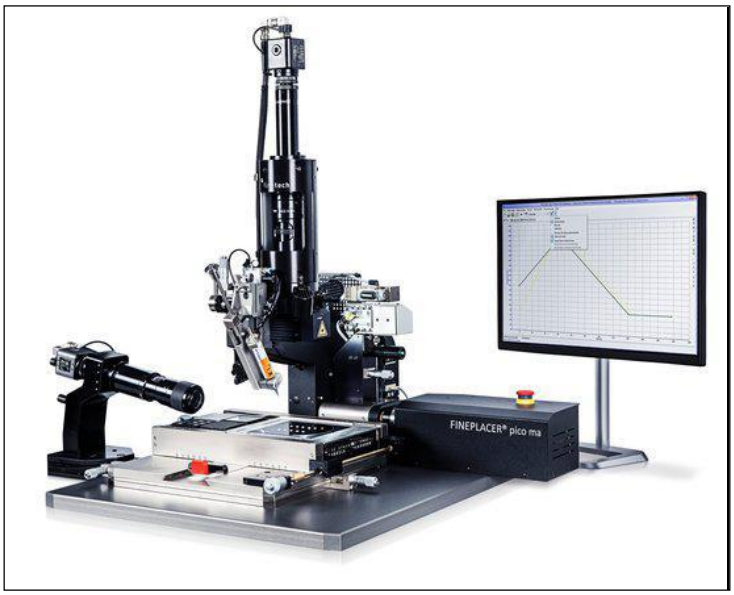

Figure 6.2 Multi-purpose Die Bonder Fineplacer Pico Ma fabricated by Finetech Ltd (http://www.finetechusa.com/bonders/products/fineplacerr-pico-ma.html).

In order to measure the electric resistance of bonding interconnection, a Keithley Model 580 Micro-Ohmmeter was used in these experiments. This Ohmmeter is designed for low-ohms measurement with the measurement ranging from 200 mΩ to 200 kΩ with a minimum resolution of 10 μΩ. The width of measuring pads is around 75 μm, which is far beyond the testing scale of this Ohmmeter. Hence, a wafer A-Zoom analytical probing microscope system fabricated by Qioptiq Ltd. is connected to the micro-Ohmmeter. The diameter of the wafer probe tip is approximately 20 μm, thus allowing it to touch the measuring pad directly with the assistance of the attached microscope in the wafer probe.

6.3 Methodologies

In order to evaluate the feasibility of electrophoretic deposition of Ni/Au coated particles as a novel flip-chip method, the assembly process and the subsequent reliability test are necessary, which helps to better understand and establish a systematic evaluation of the method. The assembly processes determines the product quality of electronic devices and their fatigue life, while the reliability experiments generates a comprehensive analysis, which in turn helps to modify the assembly process.

6.3.1 Assembly process

ACAs/ACF assembly process requires the application of pressure during the curing of adhesives. The curing process of adhesives needs extra energy to activate the chemical reaction and the commonly used standard methods include heat, ultraviolet (UV) radiation, and added catalyst. A variety of parameters can affect the bonding quality of the interconnection during the assembly process, such as curing/bonding temperature and time, temperature ramp rate, alignment accuracy, pressure value, distribution and pressure application rate, bump height and uniformity, board planarity [3, 11, 46]. Among them, the bonding temperature is a very sensitive parameter especially nowadays multi-reflow and high temperature are trying to be avoided in the 3D stacking packaging [166, 167] and the increasing wearable electronics market due to the temperature tolerance of the organic flexible substrates [18]. Thermocompression is typically utilised for ACA/ACF assembly process because of its relatively low temperature and easy setup. As discussed in Chapter 3, the loading conditions significantly impact on the crack propagation and fracture model which are closely related to the conductivity of the conductive spheres. Unfortunately, the bonding machines used in the experiments cannot provide programmed loading condition and it is controlled manually here.

An underfilling process for the flip-chip has already been proved to be able improve the reliability of the interconnection and enhance the fatigue life of the product [168]. The typical assembly processes for ACAs and ICA are shown in Figure 6.3.

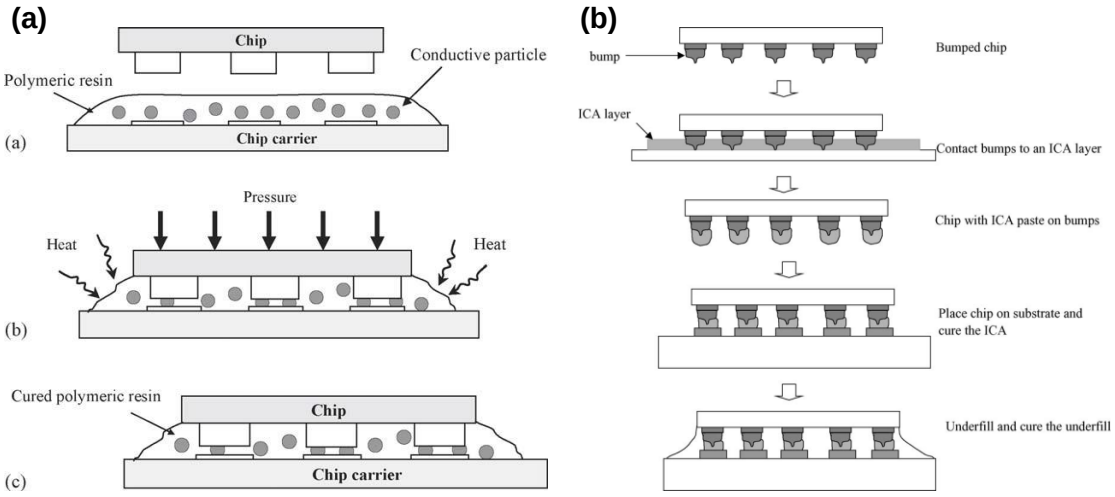

Figure 6.3 A typical flip-chip bonding process using (a) anisotropic conductive adhesives (ACAs) and (b) isotropic conductive adhesives (ICAs) [8].

The assembly process has been detailed reviewed in Chapter 2, which consists of pre-assembly, component placement, thermocompression bonding, and cooling as shown in Figure 6.3 (a). It is worth noticing the adhesives matrix with conductive fillers inside are printed simultaneously in the pre-assembly process. In contrast, due to the isotropic conductivity of

ICA, a separate underfilling process needs to be carried out after the curing of the ICA interconnection as shown in Figure 6.3 (b) [8, 169].

With regard to the assembly process for the chips with pre-deposited ACA particles, the underfilling process also needs to be an individual process, which is similar to the assembly process of ICA. As shown in Figure 6.4 (a), most of current underfill encapsulants are performed by dispensing the adhesives on one or two edges of an assembled flip-chip package. The process utilises surface tension force to drive the adhesives into the gap between the chip and substrate via capillary action. However compared with the relatively large ICA bump size (>50 μm) usually forming by stencil printing process or stud transfer method, the gap between the chip and substrate in the bonding experiment is less than 5 μm, which is supposed to be very difficult to proceed the conventional underfilling process. The compression flow underfilling process was invented and utilised nowadays by dispensing the adhesives in advance and fulfilling the curing process simultaneously for the solder/ICA and underfill [169, 170], as shown in Figure 6.4 (b). The underfilling encapsulant is required to meet a variety of challenges such as the good adhesion ability, low coefficient of thermal expansion (CTE), and good temperature compatibility.

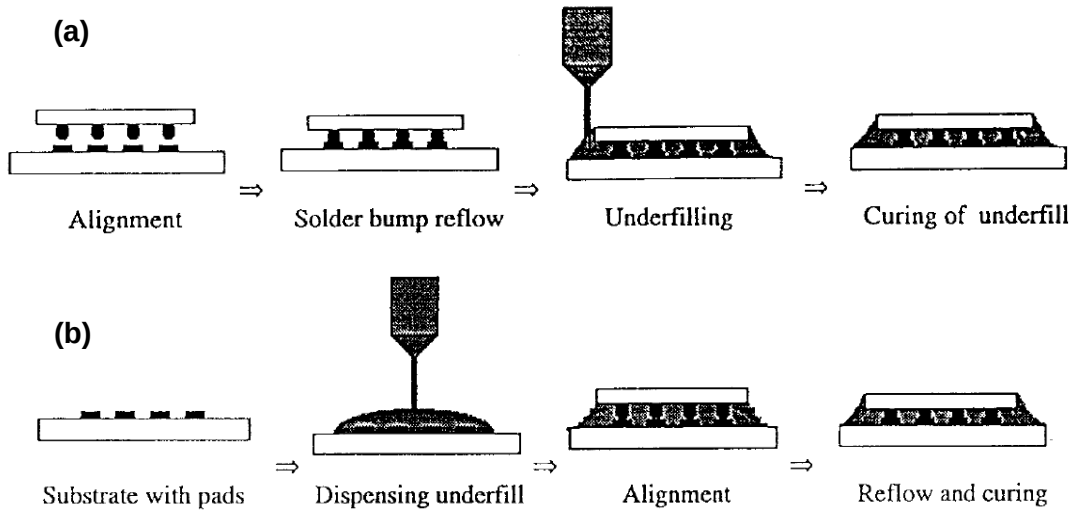

Figure 6.4 Schematic images showing the (a) conventional underfilling process and (b) compression flow underfilling process [169].

In the assembly process of the chips with pre-deposited particles, the compression flow underfilling process was employed in the experiments as shown in Figure 6.5. The mixed adhesive was dispensed in the centre of the substrate chip, while the top chip with deposited particles were attracted by the vacuum tip from the backside. In terms of the bonding trials using Adhesive I, a load force ranging from 10 N to 20 N was applied for 5 minutes so as to ensure the complete cure of the adhesive. During the bonding process, the adhesives was compressed and filled the gap between the chips. A glass substrate instead of chip was also

used to study the influence of the adhesive flowing on the deposited particles, and the bonding results were systematically analysed subsequently.

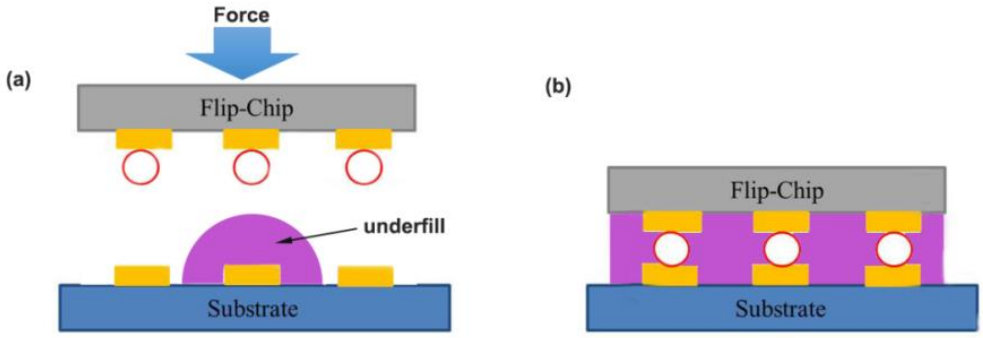

Figure 6.5 Schematic image of (a) bonding process and (b) interconnection after bonding with underfill.

In terms of the assembly process using Adhesive II, thermocompression was employed due to its curing conditions. Compared with the flux bonding or local reflow bonding, thermocompression bonding are more widely utilised in the fine-pitch electronic devices because of its relatively low bonding temperature, easy setup, and cost-effective advantages. Load force, temperature, and tacking time (time needed to soft and flow the adhesive), and bonding time (final cure time) are important parameters during thermocompression bonding [43, 171]. Figure 6.6 illustrates the temperature profile used for the thermocompression bonding experiments. The chips were placed onto the stage with idle temperature of 80 ℃, and the ramp temperature increasing speed is 3 ℃/s. The bonding temperature was carried out at a temperature range of 160-190 ℃ with bonding time of 40 s, which is believed to be enough to cure the Adhesive II. A load force was applied at a range from 1 to15 N. After the elapse of main bonding time, the assembled chips were cooled while maintaining the loading pressure.

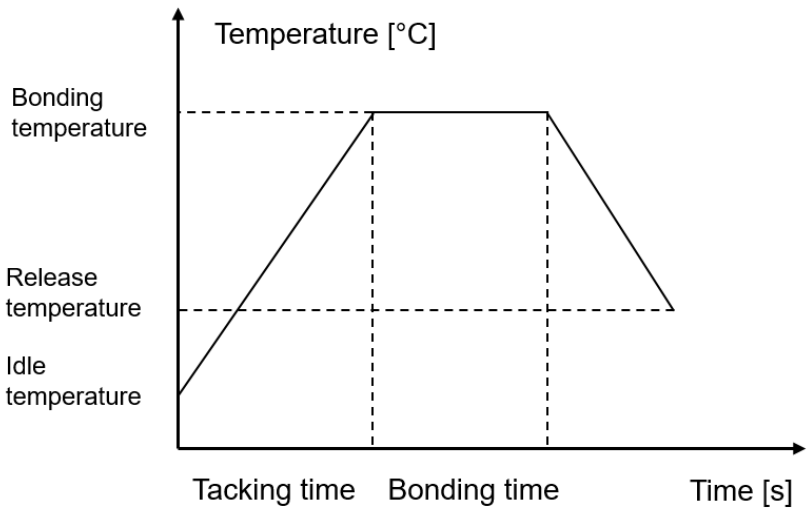

Figure 6.6 Schematic image of the bonding temperature profile.

6.3.2 Electric Conductivity Test

The electrical resistance level of the measuring wires from both the micro-Ohmmeter and wafer probe may impact on the measurement accuracy of the interconnection. Therefore, four-point testing method was utilised to measure the contact resistance of the achieved interconnections using Kelvin structure chips. For daisy-chain chips, only two-point probe testing method can be carried out. As shown in Figure 6.7 (a), a wafer A-Zoom analytical probing microscope is connected to a four-point probe tester to enable the four-point testing due to the small size dimension of the pads on the substrate. Two Figure 6.4 (b) depicts the image from the eyepiece of optical microscope, where it is clearly to see that the four probes touched four different testing pads. The resistance of interconnection and conductive path was also measured using two-point testing method separately.

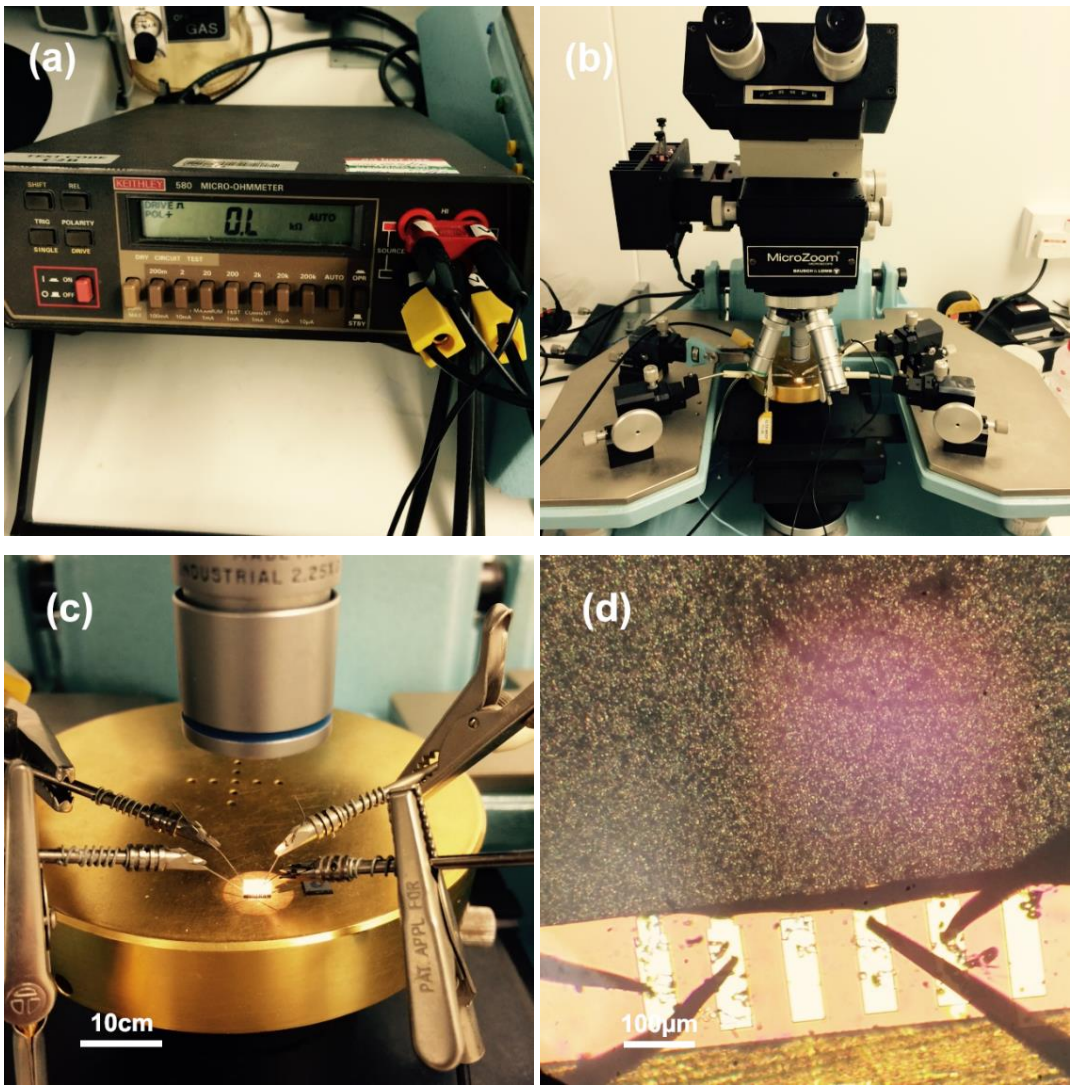

Figure 6.7 Microscope images showing the four-point probe testing process for the bonded chips.

6.4 Results and Discussion

6.4.1 Force Analysis within Bonding Process

There are three kinds of forces contributing to the final bonding results, which are the applied load force, adhesive pushing force during the compression, and the connection strength between the deposited particles and pad as shown in Figure 6.8.

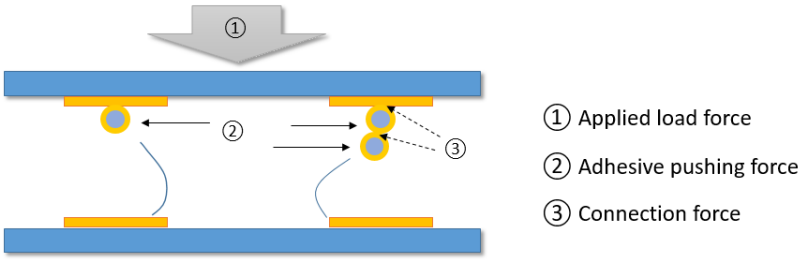

Figure 6.8 Schematic image showing the force analysis during the bonding process.

Applied load force is the motivation parameter in the bonding process, which plays significant influence on the subsequent forces to achieve the final interconnection. The maximum loading force mainly determines the final morphology of bonding structure. More importantly, as presented in Chapter 3, the applied load methods are closely related with the crack propagation and fracture patterns of Ni/Au coated particles that strongly impacts on the conductivity of the conductive particles. The flip-chip bonder used in the experiment cannot provide programmed approach to control the loading condition. Therefore, the load force was applied at a relatively slow speed in the bonding experiments.

Adhesive pushing force depends much on the viscosity of the adhesive. The mechanism underneath the adhesive pushing force is supposed to be a comprehensive forces combination including the surface tension and interaction electromagnetic forces within the surfaces of adhesives, chip substrate, and Ni/Au coated particles. In the first group of bonding trials, the adhesive is very viscous, which can be cured at room temperature for only 90s. Thus it is very likely to create a strong adhesive pushing force within the bonding process leading to the movement of deposited particles on the pad surface.

Based on the proposed theory in Chapter 4, the connection strength between the deposited particles and pad surface is contributed to the elemental nickel reduced from the Ni^{2+} during the electrophoretic deposition. The concentration of Ni^{2+} ions within the suspension plays the predominant role in the connection as well as the different deposited morphologies of electroplated nickel resulting from different deposition parameters. Compared with the relatively strong connection force resulting from EPD, the static magnetic force between the magnetised Ni/Au coated particles and Ti/Ni/Au pad is very poor since the particles by

magnetic deposition can be easily washed off through the rinsing process. That is also the reason that only the chips prepared by EPD were used in the assembly experiments. The adhesive pushing force and connection force contradict with each other, which determines the ultimate particles positions after bonding.

6.4.2 Bonding Results using Glass Substrate

The utilisation of glass substrate enables the direction observation of the final bonding morphology via the optical microscope, and the bonding results using glass substrates were shown in Figure 6.9. Most particles survived during the bonding process, which indicates that connection strength between the deposited particles and pad is normally stronger than the adhesive pushing force. With regard to the bonding using Adhesive I, it can be clearly seen that the pushing effect of the adhesive was more apparent due to the high viscosity, as shown in Figure 6.9 (a)-(f). Large percentage of particles were pushed away from the pad surface using Adhesives I. As a comparison, most particles still remained on the pad after bonding using Adhesives II, as shown in Figure 6.9 (g) and (h). In terms of the daisy-chain chips or kelvin structure chips, the influence of pushed-away particles is not obvious. However this pushing phenomenon is very likely to induce open circuits (no particles left on the pad after bonding) and the bringing issue for the chips with fine pitch and ultra-fine pitch pad array.

Multilayer particles were supposed to lead to co-planarity issue after bonding, which affect the conductivity of the interconnection. However no multilayer issue was observed after bonding even though at the areas where multilayer particles were deposited. This is attributed to two possible reasons. The first is that multilayer particles endured much higher adhesive pushing force under bonding, which are much likely to be pushed off during the compression. Whilst, the connection strength between the deposited particles and pad can be neglected compared with the load force, and thus the survived multilayer particles after adhesive pushing can still be easily compressed into monolayer in the end.

Co-planarity issue occurred in half of the bonding chips using glass substrate, while it is not apparent in the other two bonded chips. The co-planarity of the bonding tip is supposed to be the main reason, and the multilayer particles were supposed to create little influence on the final co-planarity problem. During the underfilling process, voids should be avoided because of many potential damages including increasing inhomogeneity within the interconnection, stress raising around the voids, possible metal oxidation, and possibility of moisture absorption [8]. No voids were observed in the Kelvin and daisy-chain structure chips; however voids were formed in the all the pad array chips, and most of which were distributed around the pad array area as shown in Figure 6.9 (f). The reason is supposed to be that the pad array area generates complicated underfilling channels around the pads under compression, which significantly increases the flow capability of the adhesives.

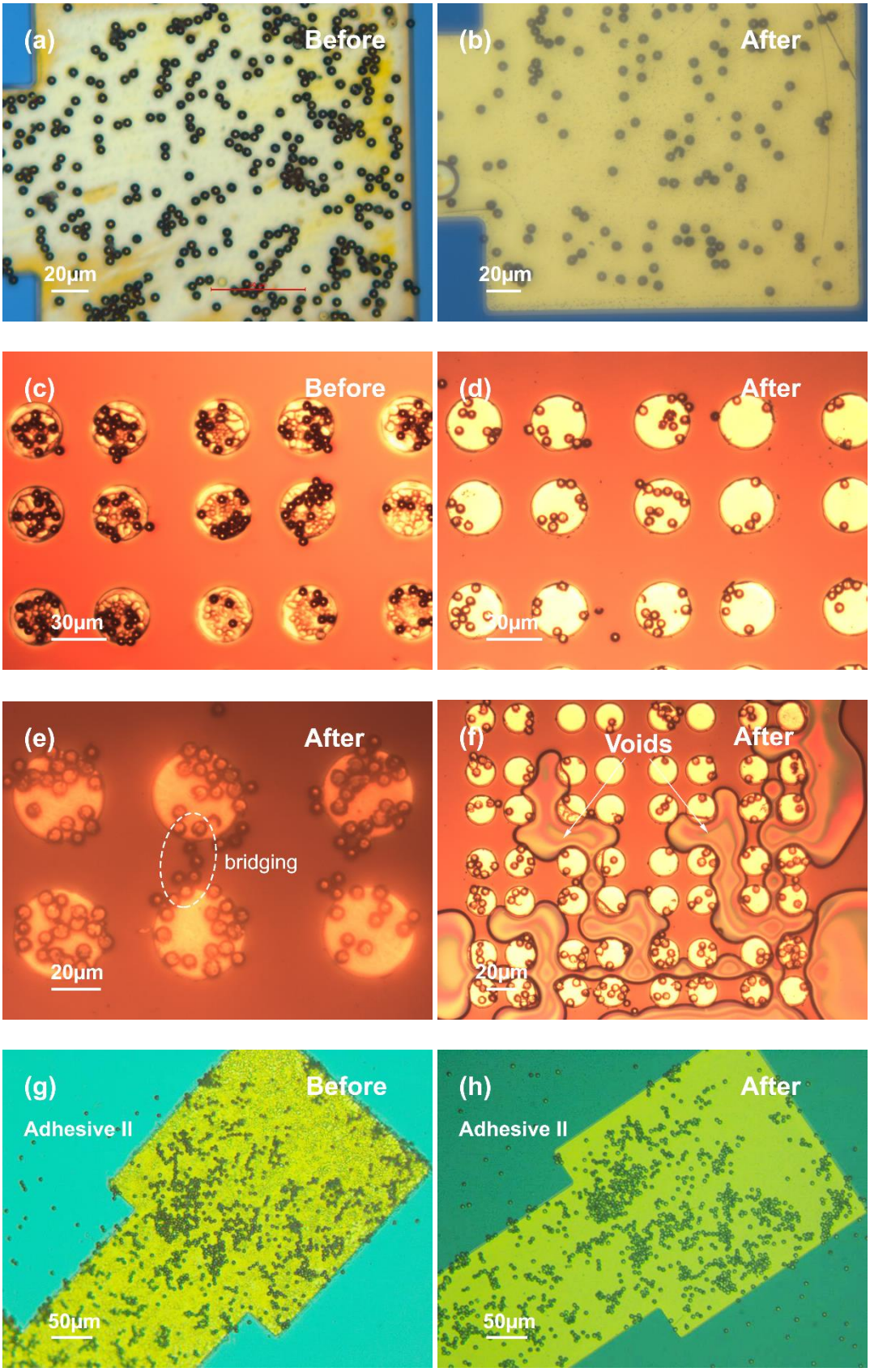

Figure 6.9 Optical images showing the comparisons before and after bonding using glass substrates: (a)-(f) using Adhesive I, and (g) and (h) using Adhesive II.

6.4.3 Results of Electric Resistance Measurement

Both Kelvin structure chips and daisy-chain chips were used for assembly experiments, thus allowing for the further electric resistance measurement. The alignment of top and substrate chips before the application of load force is shown in Figure 6.10, where the electrical path after bonding were also clearly illustrated. Kelvin structure enables the four-point probe measurement, which can eliminate the resistance of conductive path and contact resistance between the probe and testing pad.

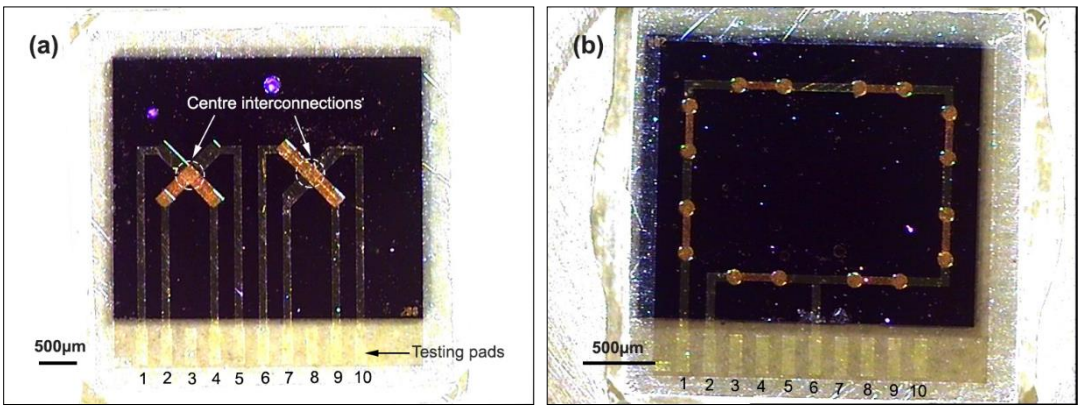

Figure 6.10 The alignment of top and substrate chips with (a) Kelvin structure and (b) daisy-chain structure before the application of load force.

As shown in Figure 10, there are ten testing pads on each kind of chips, thus enabling the measurement of different interconnections. However the overall results of assembly process for chips were bad, and only several good conductive interconnections were established. For kelvin structure chips, only all the good connection quality of three interconnections can ensure the successful four-point probe measurement. The results indicated that only two four-point probe measurements were carried out successfully, showing the resistance of centre interconnections with 22.04 Ω and 19.9 Ω. While the several two-interconnection resistance were measured, for example by touching the two probes at testing pad 1 and 2, or pad 4 and 5. The two-interconnection resistance ranged from 50.7 Ω, 55.4 Ω, to 65.1 Ω, and it should be noted that it also included the resistance of measuring probes and conductive path.

With regard to daisy chain structure chips, all the full-chain interconnections were open circuit (resistance between testing pad 1 and 2) both for the chips using Adhesive I and II, even though the second group bonding trails using Adhesive II was supposed to be better. First the total number of bonded chips is very limited, and the optimized parameters during bonding has not been settled to achive a good quality bonding. More importantly, it is attributed to the underfilling methods used for the assembly process, and the pushing effect resulted in severe movement of deposited particles thereby leading to the ultimate open circuits. The co-planarity

issue is also very likely to result in not enough deformation or completely fracture of Ni/Au coated particles, thus leading to the open circuit of the full-chain interconnections.

6.5 Future work

6.5.1 Alternative Underfilling Process

The experimental results above suggest that both underfilling process are not able to establish a good interconnection quality and all the long daisy-chain interconnections were open circuits. Conventional underfilling process is supposed to be very time-consuming due to the extremely small gap within two chips. Further experiment needs to be conducted to investigate the failure of utilisation of compression flow underfilling process. Alternative underfilling process is still compulsory to improve the assembly process of the chips with pre-deposited particles on the pad. Figure 6.9 illustrates the assembly process of double-layered ACF, which is comprised of ACF and nonconductive film (NCF) layer [47]. This kind of double-layered ACF is able to reduce the mobility of conductive fillers under compression thus achieving an ultra-fine interconnection with a decreasing possibility of bridging between adjacent pads. Based on the analysis of double-layered ACF, alternative underfilling processes will be performed by pasting/spinning a thin layer of adhesive on the substrate chip, or directly using a thin adhesive film as shown in Figure 6.11.

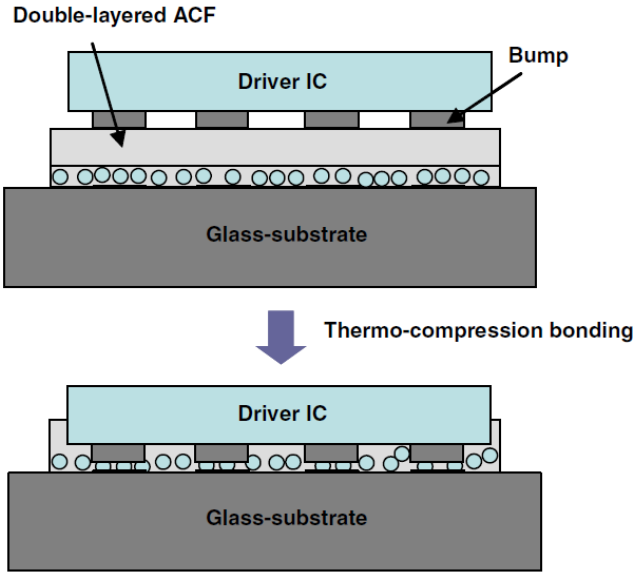

Figure 6.11 Schematic images of COG bonding process using developed double-layered ACF [47].

These two underfilling processes are supposed to be able enhance the efficiency and reliability of assembly process. The main purpose is to reduce the flow of adhesives under compression thus alleviating the pushing effect on the deposited particles. The first approach is to paste or spin a thin layer of adhesive on the substrate chip as shown in Figure 6.12 (a), while the second method is to apply a thin adhesive film directly. The essential parameter is the thickness of applied adhesive. Too thick adhesives may result in the over-filled underfilling and corresponding contamination of other components. While too thin layer is very likely to induce voids after bonding. Subsequent analysis including the glass substrate trials and electric resistance measurement will also be performed to evaluate different underfilling processes. Shear test will be conducted to study the adhesion force of underfill, and cross-section of the boned chips will be observed from SEM to study the contact morphology between the particles and pads and evaluate the bonding quality.

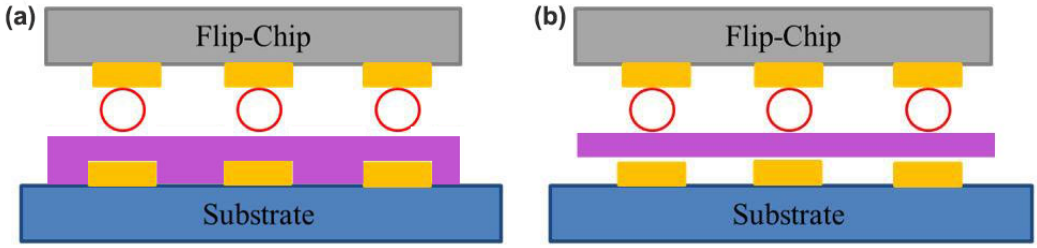

Figure 6.12 Three different methods to accomplish underfill process (a) in vacuum environment after bonding b) with a film of underfill c) paste underfill on the side of substrate.

6.5.2 Reliability Test

The electrical conductivity of the interconnection is one of the most significant parameters for the electronic devices, and a series of reliability experiments are compulsory to evaluate the interconnection quality. The well-connected daisy-chain structure chips will be will be wire bonded to a data acquisition system enabling the in situ monitoring of their constant electric resistance during reliability experiments. After the assembly process, the testing pads are still exposed, so that they can be wired bonded to the designed PCB board to perform the further reliability experiments. Figure 6.11 illustrates the main part of the in situ monitoring system, which consists of PCB board, connector, and main board. The bonded daisy chip can be fixed to the square area of the PCB board, and then wired bonded to the gold fingers. The PCB will be inserted to the connector in the main board, establishing the full chain to test the resistance of the chip. It is worth noticing that the electrical conductive paths in PCB boards in the

experiments are all coated with a layer of gold in order to gain the best conductivity and avoid oxidation or corruption during the thermal cycling experiments. This system will be placed into the environmental chamber, and the signals can be linked to the data logger outside the chamber. In term of the thermal cycling experiment, temperature range of -40 ℃ to +125 ℃ will be applied at a rate of 5℃/minute using temperature cycling chamber. Instead of stopping the experiment and taking the samples out of the chamber to measure the resistance, the system can in situ record the electric resistance of the interconnections during the thermal cycling, which is significantly helpful to better understand the effect of temperature and other parameters, moisture for example in high temperature high humidity experiments.

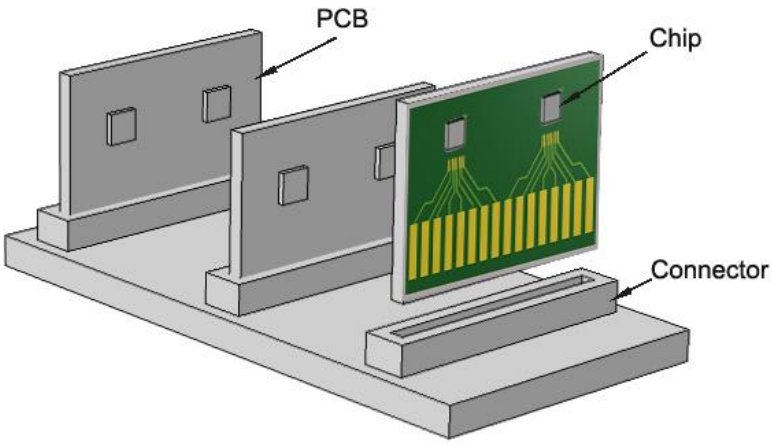

Figure 6.13 Schematic of the system for the in situ electric resistance measurement of daisy chip.

6.6 Summary

In this chapter, the chips with pre-deposited Ni/Au coated particles were successfully bonded using the compression flow underfilling process with two different kinds of adhesives. Conventional underfilling process is very difficult due to the extremely thin gap between two chip (< 5μm), therefore compression flow underfilling method was employed to achieve the assembly process. This set of assembly trails have generated a better understanding of the effects of different parameters on the ultimate electric resistance. The results have been analysed and summarised below.

- The properties of adhesives are the predominant parameters in the assembly process. High viscous adhesives are more likely to induce strong adhesive pushing effect under compression, which can result in open circuits when all the particles on the pad were

pushed off and bridging issue due to concentration of pushed-off particles within two adjacent pads. Voids are also easily induced at the pad array area because of the flow difficulty to fill the complicated underfilling channels.

- The connection strength between the particles and pad is supposed to be relatively strong based on the proposed theory in Chapter 4. However multilayer particles issue has not been observed in the bonding trials using glass substrate, which suggested that the connection strength between the deposited particles and pad was very small compared with the loading force. Thus multilayer particles can be easily compressed in to monolayer.
- Co-planarity issue exist in half percentage of the bonding chips, which contributes to the open circuits of full-chain interconnection after bonding.
- Successful interconnection from the results of electric resistance measurements proves that the method of electrophoretically deposited Ni/Au coated particles for fine or ultra-fine pitch interconnection is applicable. The open circuits of full-chain interconnection suggested that further experiments are needed to optimize the underfilling process. Alternative underfilling methods were designed by spinning/pasting a thin layer of adhesives on the substrate or directly utilizing a thin film.
- In situ monitoring system was designed for the subsequent reliability test, which enables a consecutive electric resistance measurement during thermal cycling or high temperature high humidity experiments.

Chapter 7

Conclusions and Future Work

The research presented in this thesis has advanced the fundamental understanding of the mechanical characterisation of micro-sized Ni/Au coated polymer particles and its application in fine or ultra-fine pitch interconnections. The conclusions for this work and a number of avenues for future work are summarised in this chapter.

7.1 Thesis Conclusions

The conclusions from the research work presented in this thesis are grouped into two parts in this section: the mechanical properties of the individual polymer particles and Ni/Au coated polymer core particles, the novel assembly methods of Ni/Au coated particles in the area of fine or ultra-fine pitch flip-chip interconnections.

7.1.1 Experiment on Mechanical Characterisations of Individual Particles

The viscoelastic behaviour of individual polymer particles and Ni/Au coated particles has been studied in this research. The deformation process of individual Ni/Au coated particles has been investigated using the in-situ nanomechanical system, which enables a consecutive direct observation under compression. The significance of viscoelastic characteristics of the polymer core and stress distribution within each metal coating layers have been analysed on the basis of finite element analysis using COMSOL Multiphysics. The most significant conclusions from these studies are listed in the following sections.

Viscoelastic properties

- Both the pure polymer particles and Ni/Au coated particles display clear strain-rate hardening phenomenon. The strain-rate sensitivity index of the polymer ranges from 0.038 to 0.053, while that of the Ni/Au coated particles is in the range of 0.047 to 0.058. Two modulus, initial modulus and high-strain modulus, are defined to describe the mechanical deformation process of individual particle, and both moduli show clear relationship with the loading rates and strain rates. Strain-rate coefficient and sensitivity for the high-strain modulus are defined, which can be used to forecast the

deformation behaviour of the particles at different loading conditions.

- The initial modulus of the Ni/Au coated particles are much higher than that of polymer particles due to the strengthening effect of harder metal coating layer. However the high-strain modulus of the Ni/Au coated particles ranges from 3.8 GPa to 4.5 GPa, which are even lower than those of polymer particles ranging from 3.9 GPa to 4.9 GPa at each different strain rate. The reason is attributed to be the crack of the metal coating layer bringing initial defects to the polymer core, thereby reducing the stiffness of whole particle.

Deformation Process

- The typical deformation process of pure polymer particles has been identified in two stages. In this first stage, the polymer particles endures a smooth deformation area without obvious cracks. When the deformation reaches a large strain level (around 50%), cracks start to initiate in the region in contact with silicon substrate/diamond tip surface, and then propagate rapidly in the longitudinal direction leading to the final fracture of the polymer particle.
- The deformation of Ni/Au coated particles is summarised into three steps. In the first deformation region both the polymer core and metal coating can tolerate the strain and stress without cracks at a small strain level (< around 17%). The cracks initiate in the metal coating layer and then propagate in different directions at the second deformation step, where some corresponding initial defects are created in the polymer core by the crack of metal coating layer. At the third step, the strengthening effect of metal coating completely vanishes, and the particles endures a large deformation area without fluctuation of stress-strain relationship until the crushing of polymer core resulting in the final failure of the Ni/Au coated particle.

Crack Propagation and Fracture Patterns

- Three crack propagation and fracture patterns of Ni/Au coated particles under compression are summarised based on the in-situ observation system. The first is that the crack initiates at the contact corner and propagates longitudinally, which is consistent with the FEA analysis because the maximum shear stress and principal stress concentration point locates at the inner surface of the nickel layer around the region in contact with substrates/diamond tip then propagates in the longitudinal direction. The second is that the crack initiates in the middle of the Ni/Au coated particles and this kind of crack is very likely to induce subsequent latitude cracks after approaching the contact surface forming the ultimate “Y” structure crack. The reason is believed to due

to the friction force between contact surface between particle and substrate/diamond locks the contacted metal coating part, so the crack separates into "Y" structure after approaching the contact area. The third kind of crack initiates at the exact equator of the particle and propagates in the latitudinal direction. The reason is believed to because severe crack and delamination occurs at higher strain rate, consequently it equals to compress a square metal board leading to this equator crack.

- Due to the viscoelastic properties of the particles, the crack propagate and fracture patterns are closely related with the applied strain rate. The probability of latitudinal cracks rise substantially from 0% to 100% with the increasing strain rate from 0.00083 s^{-1}(4 nm/s) to 0.83 s^{-1} (4000 nm/s). While at the lowest strain rate 0.00083 s^{-1}(4 nm/s), both the pure polymer particles and the polymer core of Ni/Au coated particles stay intact without fracture, and the Ni/Au coated particles displays small cracks and good integrity. The longitudinal cracks are supposed to be less effective to the conductivity of the Ni/Au-MCPs under compression, which however will be significantly impacted by the latitudinal cracks. Therefore higher applied deformation rates should be avoided from the aspect of the academic study, while production efficiency is the compulsory parameter which also should be considered in the industrial world.
- The strong relationship between the crack/fracture patterns and strain rate is attributed to the stress distribution and energy transfer during the compression process. Higher strain rates limits the time for the relative movement between molecular chains to dissipate the applied energy, so large percentage of energy is released by breaking the molecular chains of polymer or accelerating the movement of dislocation within the metal coating layer leading severe crack propagation and fracture. Whilst, the stress level within the particles is higher at high strain rate, which also contributes to the cracks. The modelling analysis suggests that the highest von Mises stress concentrates at the inner surface of the nickel layer around contact corner, which determines the initial crack position combined with the place of initial defects on the metal coating layer. The cracks initiates in the middle of the particle is believed to be closely related with the hoop stress.

7.1.2 Experiment on Novel Assembly of Ni/Au Coated Particles

The properties of Ni/Au coated particles have been further analysed and utilised. Consequently, electrophoretic deposition and magnetic deposition of Ni/Au coated particles have been established and a fine or ultra-fine pitch deposition has been accomplished. The assembly

process has also been performed subsequently. The most important conclusions from the experiment are listed below.

Electrophoretic Deposition

- Systematic analysis of the mechanism of zeta potential proves that Ni^{2+} ions obtained from the nickel layer etching are absorbed onto the metal coating surface thus resulting in the positive charge of Ni/Au coated particle. Further harmless and efficient charging method have been developed by directly adding $NiCl_2$ or $CuCl_2$ into the suspension. The zeta potential of Ni/Au coated particles are significantly affected by the concentration of charging addictive and pH variation. A green deposition on the target pads with ultra-fine pith can be achieved after optimization of the different parameters including the applied voltage, deposition time, concentration of Ni^{2+} ions, and pH value.
- A new theory has been proposed to explain the assembly mechanism of electrophoretic deposition of Ni/Au coated particles using metal cations charging method, as shown in Figure 4.17. The charged particle is surrounded by the electrical double layer, where the concentration of Ni^{2+} increases toward the surface of the particle as shown in Figure 4.17 (a) and (b). Under the applied electric field, the double layer experiences a distortion process as illustrated in Figure 4.17 (c) and becomes thinner ahead with a higher aggregation of Ni^{2+} ions. The Ni^{2+} ions are neutralized once touching the cathode, and the higher concentration of Ni^{2+} in the particle head area results in a relatively thicker electroplating layer which adheres the particle onto the cathode surface as shown in Figure 4.17 (d) leading to a solid and strong connection between the particle and pad surface. Because of the solid connection, the electrons can be transferred to the metal coated particle surface from the pad. The deposited particle behaves as cathode and enables the subsequent electroplating process and electrophoretic deposition of multiplayer particles as shown in Figure 4.17 (e).
- A variety of deposition morphologies mixing the electroplated nickel/copper and electrophoretically deposited particles have been achieved, which strongly supports the proposed theory. The results have proved that electrophoretic deposition and electroplating process occurs simultaneously and the electroplated material creates the adhesion medium for the electrophoretic deposition. The “concrete” structure produced in this work can be utilised in a wide range of potential areas such as increasing adhesion strength for the electrophoretically deposited materials i.e. carbon nanotubes or ceramic particles, or increasing electroplating speed of copper pillar bump by mixing the particles into the solder.

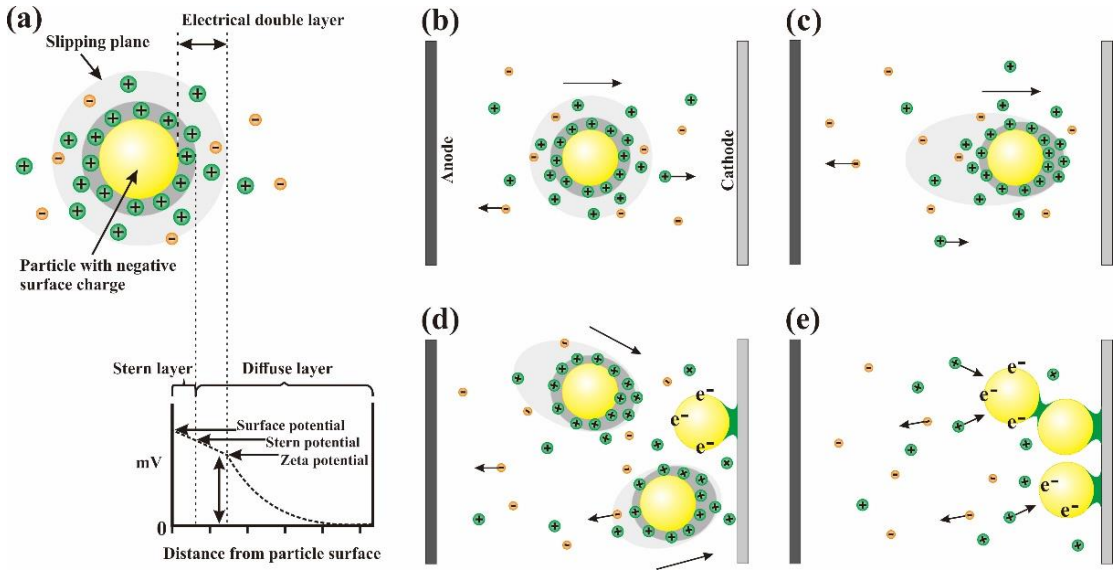

Figure 4.17: The proposed assembly mechanism of electrophoretic deposition of Ni/Au coated particles using metal cations charging method

Magnetic Deposition

- The magnetic properties of Ni/Au coated particles and chips with Ti/Ni/Au pads have been systematically studied in the work, and the results shows that both can be successfully magnetised under external magnetic field. Magnetic deposition process has been demonstrated, and this indicates a sufficient magnetostatic interaction force between the magnetized particles and pads enables a high density deposition of particles. The magnetising angle between the chip and external magnetic field has a significantly influence on the magnetic deposition quality.
- A magnetic deposition system has been established to deposit the Ni/Au coated particles onto the nickel bump surface under the control of external magnetic field. The Ni/Au particles initially form chains aligning with the magnetic field, and then land on the pad surface after polling out of the solvent. The adhesion force between the particles and pad is an essential parameter, which is relatively low using the magnetic deposition system without pre-magnetising the particles and pads.

Assembly Process

- Successful conductive interconnections have been fulfilled by the assembly process of the chips with pre-deposited particles, which illustrates the applicable capability of the electrophoretic deposition of Ni/Au coated particles for fine or ultra-fine pitch interconnection. However the high percentage of open circuits indicates that the underfilling process needs to be further developed to increase the final assembly quality.

- The properties of adhesives are the predominant parameters in the assembly process. High viscous adhesives are more likely to induce strong adhesive pushing effect under compression, which can result in open circuits when all the particles on the pad were pushed off and bridging issue due to concentration of pushed-off particles within two adjacent pads. Voids are also easily induced at the pad array area because of the flow difficulty to fill the complicated underfilling channels.
- Multilayered particles has not lead to the co-planarity issue after bonding, because the connection force between the particles and pad is neglectable compared with the load force and multilayer issue has not been observed after assembly process. However the co-planarity issues still exists which can contribute to the open circuit problem.

7.2 Future Work

The research carried out in this thesis has given rise to a number of ideas for future work on the characterisation of individual Ni/Au coated particle and its self-assembly process for fine or ultra-fine flip-chip interconnection:

- The viscoelastic property of the polymer core determines that the particles will be very sensitive to the temperature. Meanwhile the temperature is also increased during the thermocompression bonding process in the real industrial world. Therefore, the mechanical behaviours of the pure polymer particles and Ni/Au coated particles under the increasing temperature are of interest, particularly to check the possible difference in the crack propagation and fracture patterns of Ni/Au coated particles under high temperature.
- The electrical conductivity of Ni/Au coated particles is the essential parameter under compression, which dominates the quality and reliability of final interconnection. Further experiment can be performed by adding the electric resistance of individual particles into the in-situ nanomechanical system, so that the influence of cracks or fractures on the electrical conductivity under compression or increasing temperature can be studied directly.
- Due to the extremely small size of the particles, experimental measurement of the stress distribution of each composition of Ni/Au coated particle is very difficult. Efforts can be spent on the further modelling study on the deformation process of individual particles. Such a study might include the stress distribution simulation, crack initialisation and propagation modelling, and electric resistance simulation during the deformation process at room and increasing temperature. The modelling results can significantly help to better understand the experimental results.

- The results in the assembly chapter show that good conductivity can be achieved even the particles are covered with the electroplated nickel after electrophoretic deposition even though The oxidation of electroplated nickel layer during EPD may lead to potential increase of electric resistance. However interest is located in the exact electric resistance different between the electroplated materials covered particles and normal ones. Therefore, further individual compression experiment can be utilised to study the mechanical deformation behaviours and electrical conductivity of individual Ni/Au coated particle covered by the different electroplated materials after electrophoretic deposition process, which can also help to investigate the choice of alternative charging addictives, AgCl for example.
- The morphology of electroplated nickel during the EPD process of Ni/Au coated particles is significantly affected by a variety of parameters such as the concentration of Ni^{2+} ions, pH values, and applied voltage. Further experiment can be carried out to find the most suitable morphology of electroplated nickel in order to achieve the best adhesion strength between the particles and pad and best conductivity after compression. In-situ shear test can be conducted to study the exact adhesion strength.
- The poor adhesion strength of electrophoretically deposited carbon nanotube or graphene has always been a problem. Further research can be organised to study the influence of metal ions charging approach for carbon nanotube/graphene in order to increase its adhesion strength.
- The solder materials, usually copper and tin, are electroplated onto the pad surface with the other areas covered by the photoresist in the fabrication of micro-C4 or copper pillar bumps. Due to the limited solder volume, full intermetallic compound (IMC) joint is very likely to form after bonding, which results in a fragile interconnection. Experimental trials can be conducted by adding certain amount of Ni/Au coated or silver coated polymer core particles in to the electroplating unit. The Sn/Ag/Cu IMC or other related IMC formed between the solder and metal coating layer of particles are supposed to be able lock the particles within solder. More importantly, the viscoelastic characterisation of polymer core can absorb large amount of energy during deformation, which is supposed to be able to increase the toughness of the interconnection and slowing the crack propagation speed.
- Magnetic deposition process has a lot of advantages such as simple, low cost, and efficient. However the adhesion force resulting from magnetostatic attraction is not strong enough. Additional research can be performed to apply a layer of sticky materials only on the target pad surface, resulting in a more promising magnetic deposition process using Ni/Au coated particles. Meanwhile, trials can be carried out

to study the magnetic deposition of non-magnetic solder materials onto non-magnetic pads using magnetic medium, which will dramatically extend the potential application in electronic packaging area.

- More work is required to explore different underfilling processes and optimise different parameters during the bonding. A series of reliability experiments are needed to establish a comprehensive evaluation about each novel self-assembly methods of Ni/Au coated particles for fine or ultra-fine pitch flip-chip interconnections.

References

1. D.P. Seraphim and I. Feinberg, *Electronic packaging evolution in IBM.* IBM Journal of Research and Development, 1981. **25**(5): pp. 617-630.
2. I. Szendiuch, *Development in electronic packaging moving to 3D system configuration.* Radioengineering, 2011. **20**(1): pp. 214-220.
3. J. Liu, Y. Wang, J. Morris, and H. Kristiansen, *Ontology for the anisotropic conductive adhesive interconnect technology for electronics packaging applications*. in Proc. IEEE High Density Microsystem Design and Packaging and Component Failure Analysis, Shanghai, China, June 27-30, 2005, pp. 1-17.
4. M. Gerber, C. Beddingfield, S. O'Connor, M. Yoo, M. Lee, D. Kang, S. Park, C. Zwenger, R. Darveaux, and R. Lanzone, *Next generation fine pitch Cu Pillar technology—Enabling next generation silicon nodes*, in Proc. IEEE Electronic Components and Technology Conference (ECTC), Lake Buena Visata, Florida, USA, May 31-June 03, 2011, pp. 612-618.
5. Y. Zhang, L. Li, Z. Lu, A. Jantsch, M. Gao, H. Pan, and F. Han, *A survey of memory architecture for 3D chip multi-processors.* Microprocessors and Microsystems, 2014. **38**(5): pp. 415-430.
6. K. DeHaven and J. Dietz. *Controlled collapse chip connection (C4)-an enabling technology*. in *Electronic Components and Technology Conference, 1994. Proceedings., 44th*. 1994. IEEE.
7. J. Maria, B. Dang, S. Wright, C. Tsang, P. Andry, R. Polastre, Y. Liu, L. Wiggins, and J. Knickerbocker. *3D Chip stacking with 50 μm pitch lead-free micro-c4 interconnections,* in Proc. IEEE Electronic Components and Technology Conference (ECTC), Lake Buena Visata, Florida, USA, May 31-June 03, 2011, pp. 268-273.
8. M.J. Yim and K.W. Paik, *Recent advances on anisotropic conductive adhesives (ACAs) for flat panel displays and semiconductor packaging application,* International journal of adhesion and adhesives, 2006. **26**(5): pp. 304-313.
9. K. Gilleo, *Assembly with conductive adhesives.* Soldering & Surface Mount Technology, 1995. **7**(1): pp. 12-17.
10. H. Nishida, K. Sakamoto, H. Ogawa, and H. Ogawa, *Micropitch connection*

using anisotropic conductive materials for driver IC attachment to a liquid crystal display, IBM journal of research and development, 1998. **42**(3.4): pp. 517-526.

11. D. Williams, D. Whalley, O. Boyle, and A. Ogunjimi, *Anisotropic conducting adhesives for electronic interconnection.* Soldering & Surface Mount Technology, 1993. **5**(2): pp. 4-8.
12. P. Clot, J.-F. Zeberli, J.-M. Chenuz, F. Ferrando, and D. Styblo, *Flip-chip on flex for 3D packaging*. in *Electronics Manufacturing Technology Symposium,* in Proc. IEEE 24th International Electronics Manufacturing Technology Syposium, Austin, TX, USA October 18-19, 1999, pp. 36-41.
13. Q. Tan, S.C. Beddingfield, and D.G. Mitchell, *Fine pitch bumping with improved device standoff and bump volume*, 2002, Google Patents.
14. S. Park, H. Bang, H. Bang, and J. You, *Thermo-mechanical analysis of TSV and solder interconnects for different Cu pillar bump types,* Microelectronic Engineering, 2012. **99**(0): pp. 38-42.
15. G.-T. Lim, B.-J. Kim, K. Lee, J. Kim, Y.-C. Joo, and Y.-B. Park, *Temperature effect on intermetallic compound growth kinetics of Cu pillar/Sn bumps.* Journal of electronic materials, 2009. **38**(11): pp. 2228-2233.
16. M.-H. Chan, Y.-C. Liao, C.-T. Lin, K.-W. Chuang, H.-N. Huang, C.-T. Yeh, W.-T. Tseng, and J.-Y. Lai. *Thermal cycling effect on intermetallic formation with various surface finish of micro bump interconnect for 3D package*. in Proc. IEEE Electronic Components and Technology Conference (ECTC), Las Vegas, NV, USA, May 28-31, 2013, pp. 2163-2167.
17. J.-e. Luan, Y. Jin, K.-Y. Goh, Y. Ma, G. Hu, Y. Huang, and X. Baraton. *Challenges for extra large embedded wafer level ball grid array development*. in Proc. IEEE 11th Electronics Packaging Technology Conference (EPTC), Singapore, December 09-11, 2009, pp. 202-207.
18. M. Stoppa and A. Chiolerio, *Wearable electronics and smart textiles: a critical review.* Sensors, 2014. **14**(7): pp. 11957-11992.
19. B. Bober, A. Bochenek, B. Olszewska-Mateja, and Z. Żaluk. *Current trends in flip-chip bonding technique for multichip modules–especially micro-jet printing*, in Proc. 24th International Conference IMAPS-Poland, Warsaw, Poland, 2000, pp. 47-61.
20. J. Liu, A. Tolvgard, J. Malmodin, and Z. Lai, *A reliable and environmentally*

friendly packaging technology-flip-chip joining using anisotropically conductive adhesive, Components and Packaging Technologies, 1999. **22**(2): pp. 186-190.

21. R. Windemuth and T. Ishikawa. *New flipchip technology*, in Proc. IEEE Microelectronics and Packaging Conference (EMP), Rimini, Italy, June 16-18, pp.1-6.
22. P.A. Totta, *History of Flip Chip and Area Array Technology*, in *Area Array Interconnection Handbook*. 2001, Springer. pp. 1-35.
23. N.-C. Lee, *Reflow soldering processes and troubleshooting: SMT, BGA, CSP, and flip chip technologies,* PhD Thesis, Oxford, U.K. Elsevier, 2001.
24. J. Hwang, J. Kim, W. Kwon, U. Kang, T. Cho, and S. Kang. *Fine pitch chip interconnection technology for 3D integration*. in *Electronic Components and Technology Conference (ECTC), 2010 Proceedings 60th*. 2010. IEEE.
25. Y. Orii, *Ultra fine pitch flip chip interconnection for 3D integration*, in Proc. 5th Internatiaonl Microsystems Packaging Assembly and Circuits Technology Conference (IMPACT), Taipei, Taiwan, China, October 20-22, 2010, pp. 1-24.
26. F. Dai, D. Yu, W. Yin, N. Zhao, L. Wan, H. Yu, S. Wang, and J. Sun. *Newly developed in-situ formation of SnAg and SnAgCu solder on copper pillar bump*, in Proc. 13th Electronics Packaging Technology Conference (EPTC), Singapore, December 07-09, 2011, pp. 175-179.
27. W.-M. Ki, M.-S. Kang, S. Yoo, and C.-W. Lee, *Fabrication and bonding process of fine pitch Cu pillar bump on thin Si chip for 3D stacking IC*, in IEEE 2011 3D Systems Integration Conference (3DIC), Osaka, Japan, 2012, January 31-February 2, pp. 1-4.
28. B. de Brugiere, F. Marion, M. Fendler, V. Mandrillon, A. Hazotte, M. Volpert, and H. Ribot, *A 10μm pitch interconnection technology using micro tube insertion into Al-Cu for 3D applications*, in Proc. 61st Electronic Components and Technology Conference (ECTC), Lake Buena Vista, FL, USA, 2011, May 31-June 03, pp. 1400-1406.
29. B.G. de Brugiere, F. Marion, M. Fendler, V. Mandrillon, A. Hazotte, M. Volpert, and H. Ribot, *Micro tube insertion into indium, copper and other materials for 3D applications*, in Proc. 60th Electronic Components and Technology Conference (ECTC), Las Vegas, NV, USA, June 01-June 04, 2010, pp. 1757-1762.

30. J. Liu, *ACA bonding technology for low cost electronics packaging applications–current status and remaining challenges,* Soldering & Surface Mount Technology, 2001. **13**(3): pp. 39-57.
31. D.D. Chang, P.A. Crawford, J.A. Fulton, R. McBride, M.B. Schmidt, R.E. Sinitski, and C. Wong, *An overview and evaluation of anisotropically conductive adhesive films for fine pitch electronic assembly.* Components, Hybrids, and Manufacturing Technology, IEEE Transactions, 1993. **16**(8): pp. 828-835.
32. G. Dou, D.C. Whalley, and C. Liu. *Electrical conductive characteristics of ACA bonding: a review of the literature, current challenges and future prospects*, in IEEE 6th High Density Microsystem Design and Packaging and Component Failure Analysis, Shanghai, China, July 3-3, 2004, pp. 264-276.
33. Y. Li, K.-S. Moon, and C. Wong, *Monolayer-protected silver nano-particle-based anisotropic conductive adhesives: Enhancement of electrical and thermal properties,* Journal of electronic materials, 2005. **34**(12): pp. 1573-1578.
34. C. Goh, H. Yu, S. Yong, S. Mhaisalkar, F. Boey, and P. Teo, *The effect of annealing on the morphologies and conductivities of sub-micrometer sized nickel particles used for electrically conductive adhesive,* Thin Solid Films, 2006. **504**(1): pp. 416-420.
35. P. Savolainen and J. Kivilahti, *A solder alloy filled Z-axis conductive epoxy adhesive,* The Journal of Adhesion, 1995. **49**(3-4): pp. 187-196.
36. P. Savolainen and J. Kivilahti, *Electrical properties of solder filled anisotropically conductive adhesives,* Journal of Electronics Manufacturing, 1995. **5**(01): pp. 19-26.
37. J. Liu, *Conductive Adhesive for Electronics Packaging, 1999*. 1999, Electrochemical Publications Ltd., Port Erin, Isle of Man, British Isles.
38. D. Whalley, L. Chen, and J. Liu, *Modelling of the anisotropic adhesive assembly process*. in *Proc. 4th IEEE International Symposium on Electronic Packaging Technology, Beijing*, China, 2001, pp. 319-324.
39. K.F. Harsh, V.M. Bright, and Y. Lee, *Solder self-assembly for three-dimensional microelectromechanical systems,* Sensors and Actuators A: Physical, 1999. **77**(3): pp. 237-244.
40. C. Wu, J. Liu, and N. Yeung, *The effects of bump height on the reliability of ACF in flip-chip.* Soldering & Surface Mount Technology, 2001. **13**(1): pp25-

30.

41. S. Tan, Y. Chan, Y. Chiu, and C. Tan, *Thermal stability performance of anisotropic conductive film at different bonding temperatures,* Microelectronics Reliability, 2004. **44**(3): pp. 495-503.
42. Y. Chiu, Y. Chan, and S. Lui, *Study of short-circuiting between adjacent joints under electric field effects in fine pitch anisotropic conductive adhesive interconnects,* Microelectronics Reliability, 2002. **42**(12): ppp. 1945-1951.
43. X. Chen, J. Zhang, C. Jiao, and Y. Liu, *Effects of different bonding parameters on the electrical performance and peeling strengths of ACF interconnection.* Microelectronics Reliability, 2006. **46**(5): pp. 774-785.
44. Y. Wu, M. Alam, Y. Chan, and B. Wu, *Dynamic strength of anisotropic conductive joints in flip chip on glass and flip chip on flex packages,* Microelectronics Reliability, 2004. **44**(2): pp. 295-302.
45. M.-J. Yim and K.-W. Paik. *Design and understanding of anisotropic conductive films (ACFs) for LCD packaging*, in Proc. IEEE 1st Polymeric Electronics Packaging, Norrkoping, Sweden, October 30-30, 1997, pp. 233-242.
46. G. Dou, D.C. Whalley, and C. Liu, *The effect of co-planarity variation on anisotropic conductive adhesive assemblies*, in Proc. IEEE 56th Electronic Components and Technology Conference (ECTC), San Diego, CA, USA, May 30-June 02, 2006, pp. 932-938.
47. M.J. Yim, J. Hwang, and K.W. Paik, *Anisotropic conductive films (ACFs) for ultra-fine pitch Chip-On-Glass (COG) applications,* International journal of adhesion and adhesives, 2007. **27**(1): pp. 77-84.
48. Y. Lin and J. Zhong, *A review of the influencing factors on anisotropic conductive adhesives joining technology in electrical applications,* Journal of Materials Science, 2008. **43**(9): pp. 3072-3093.
49. D.C. Whalley, S.H. Mannan, and D.J. Williams, *Anisotropic conducting adhesives for electronic assembly.* Assembly Automation, 1997. **17**(1): pp. 66-74.
50. M. Rizvi, Y. Chan, C. Bailey, H. Lu, and A. Sharif, *The effect of curing on the performance of ACF bonded chip-on-flex assemblies after thermal ageing,* Soldering & Surface Mount Technology, 2005. **17**(2): pp. 40-48.
51. C. Yin, M. Alam, Y. Chan, C. Bailey, and H. Lu, *The effect of reflow process on the contact resistance and reliability of anisotropic conductive film*

interconnection for flip chip on flex applications. Microelectronics Reliability, 2003. **43**(4): pp. 625-633.

52. J. Liu, *Reliability aspects of electronics packaging technology using anisotropic conductive adhesives.* Journal of Shanghai University (English Edition), 2007. **11**(1): pp. 1-16.
53. M.J. Yim, Y.-D. Jeon, and K.-W. Paik, *Reduced thermal strain in flip chip assembly on organic substrate using low CTE anisotropic conductive film,* IEEE Transactions on, Electronics Packaging Manufacturing, 2000. **23**(3): pp. 171-176.
54. S.-C. Kim and Y.-H. Kim, *Review paper: flip chip bonding with anisotropic conductive film (ACF) and nonconductive adhesive (NCA),* Current Applied Physics, 2013. **13**: pp. S14-S25.
55. N. Yeung, Y. Chan, and C. Tan, *Effect of bonding force on the conducting particle with different sizes,* Journal of Electronic Packaging(Transactions of the ASME), 2003. **125**(4): pp. 624-629.
56. W.-S. Kwon, S.-J. Ham, and K.-W. Paik, *Deformation mechanism and its effect on electrical conductivity of ACF flip chip package under thermal cycling condition: An experimental study,* Microelectronics Reliability, 2006. **46**(2): pp. 589-599.
57. W.-S. Kwon and K.-W. Paik, *Experimental analysis of mechanical and electrical characteristics of metal-coated conductive spheres for anisotropic conductive adhesives (ACAs) interconnection,* IEEE Transactions on Components and Packaging Technologies,, 2006. **29**(3): pp. 528-534.
58. M. Grzelczak, J. Vermant, E.M. Furst, and L.M. Liz-Marzán, *Directed self-assembly of nanoparticles,* ACS nano, 2010. **4**(7): pp. 3591-3605.
59. A. Winkleman, B.D. Gates, L.S. McCarty, and G.M. Whitesides, *Directed self-assembly of spherical particles on patterned electrodes by an applied electric field,* Advanced Materials, 2005. **17**(12): pp. 1507-1511.
60. G.M. Whitesides and M. Boncheva, *Beyond molecules: Self-assembly of mesoscopic and macroscopic components,* in Proceedings of the National Academy of Sciences, 2002. **99**(8): pp. 4769-4774.
61. G.M. Whitesides and B. Grzybowski, *Self-assembly at all scales,* Science, 2002. **295**(5564): pp. 2418-2421.
62. N.V. Shestopalov, G. Henkelman, and G.J. Rodin, *Guided self-assembly of*

electrostatic binary monolayers via isothermal-isobaric control, The Journal of Chemical Physics, 2011. **135**(15): pp. 154501.

63. X. Ang, F. Li, W. Tan, Z. Chen, C.C. Wong, and J. Wei, *Self-assembled monolayers for reduced temperature direct metal thermocompression bonding,* Applied Physics Letters, 2007. **91**(6): pp. 061913.
64. J. Lyklema, H. Van Leeuwen, and M. Minor, *DLVO-theory, a dynamic re-interpretation,* Advances in colloid and interface science, 1999. **83**(1): pp. 33-69.
65. H. Xu, D. Chen, S. Wang, Y. Zhou, J. Sun, W. Zhang, and X. Zhang, *Macromolecular self-assembly and nanotechnology in China,* Philosophical Transactions of the Royal Society of London A: Mathematical, Physical and Engineering Sciences, 2013. **371**(2000): pp. 20120305.
66. Y. Xia, Y. Yin, Y. Lu, and J. McLellan, *Template-assisted self-assembly of spherical colloids into complex and controllable structures,* Advanced Functional Materials, 2003. **13**(12): pp. 907-918.
67. J. Vermant and M. Solomon, *Flow-induced structure in colloidal suspensions,* Journal of Physics: Condensed Matter, 2005. **17**(4): pp. R187.
68. F. Reincke, S.G. Hickey, W.K. Kegel, and D. Vanmaekelbergh, *Spontaneous assembly of a monolayer of charged gold nanocrystals at the water/oil interface,* Angewandte Chemie International Edition, 2004. **43**(4): pp. 458-462.
69. A. Böker, J. He, T. Emrick, and T.P. Russell, *Self-assembly of nanoparticles at interfaces.* Soft Matter, 2007. **3**(10): pp. 1231-1248.
70. S. Put, J. Vleugels, G. Anné, and O. Van der Biest, *Functionally graded ceramic and ceramic–metal composites shaped by electrophoretic deposition,* Colloids and Surfaces A: Physicochemical and Engineering Aspects, 2003. **222**(1): pp. 223-232.
71. W.Y. Sung, S.M. Lee, W.J. Kim, J.G. Ok, H.Y. Lee, and Y.H. Kim, *New approach to enhance adhesions between carbon nanotube emitters and substrate by the combination of electrophoresis and successive electroplating,* Diamond and Related Materials, 2008. **17**(6): pp. 1003-1007.
72. A.R. Boccaccini, J. Cho, J.A. Roether, B.J. Thomas, E.J. Minay, and M.S. Shaffer, *Electrophoretic deposition of carbon nanotubes.* Carbon, 2006. **44**(15): pp. 3149-3160.
73. K. Tada and M. Onoda, *Nanostructured conjugated polymer films by*

electrophoretic deposition, Advanced Functional Materials, 2002. **12**(6-7): pp. 420-424.

74. S.J. Limmer and G. Cao, *Sol–gel electrophoretic deposition for the growth of oxide nanorods,* Advanced Materials, 2003. **15**(5): pp. 427-431.
75. O.O. Van der Biest and L.J. Vandeperre, *Electrophoretic deposition of materials,* Annual Review of Materials Science, 1999. **29**(1): pp. 327-352.
76. S. Put, J. Vleugels, and O. Van der Biest, *Functionally graded WC–Co materials produced by electrophoretic deposition.* Scripta materialia, 2001. **45**(10): pp. 1139-1145.
77. P. Sarkar, S. Datta, and P.S. Nicholson, *Functionally graded ceramic/ceramic and metal/ceramic composites by electrophoretic deposition.* Composites Part B: Engineering, 1997. **28**(1–2): pp. 49-56.
78. S. Put, J. Vleugels, G. Anné, and O. Van der Biest, *Functionally graded ceramic and ceramic–metal composites shaped by electrophoretic deposition.* Colloids and Surfaces A: Physicochemical and Engineering Aspects, 2003. **222**(1–3): pp. 223-232.
79. S. Heavens, *Electrophoretic deposition as a processing route for ceramics,* Noyes Publications, Advanced Ceramic Processing and Technology., 1990. **1**: pp. 255-283.
80. P. Sarkar and P.S. Nicholson, *Electrophoretic deposition (EPD): mechanisms, kinetics, and application to ceramics.* Journal of the American Ceramic Society, 1996. **79**(8): pp. 1987-2002.
81. S. Troelstra, *Applying coatings by electrophoresis.* Philips Tech. Review, 1951. **12**: pp. 1950-51.
82. M. Ammam, *Electrophoretic deposition under modulated electric fields: a review,* RSC Advances, 2012. **2**(20): pp. 7633-7646.
83. M. Cheverton, P. Singh, L.S. Smith, K.P. Chan, J.A. Brewer, and V. Venkataramani, *Ceramic-Polymer Additive Manufacturing System for Ultrasound Transducers.*
84. S. Novak, U. Maver, Š. Peternel, P. Venturini, M. Bele, and M. Gaberščček, *Electrophoretic deposition as a tool for separation of protein inclusion bodies from host bacteria in suspension.* Colloids and Surfaces A: Physicochemical and Engineering Aspects, 2009. **340**(1): pp. 155-160.
85. J. Wang and M. Kuwabara, *Moldless micropatterning of BaTiO3 nanoparticles*

via electrophoretic deposition: A simple and feasible method. Journal of electroceramics, 2010. **24**(2): pp. 104-109.

86. H. Zhang, X. Zhang, D. Zhang, X. Sun, H. Lin, C. Wang, and Y. Ma, *One-step electrophoretic deposition of reduced graphene oxide and Ni (OH) 2 composite films for controlled syntheses supercapacitor electrodes,* The Journal of Physical Chemistry B, 2012. **117**(6): pp. 1616-1627.
87. M.N. Naim, M. Iijima, K. Sasaki, M. Kuwata, H. Kamiya, and I.W. Lenggoro, *Electrical-driven disaggregation of the two-dimensional assembly of colloidal polymer particles under pulse DC charging,* Advanced Powder Technology, 2010. **21**(5): pp. 534-541.
88. B. Ferrari and R. Moreno, *The conductivity of aqueous Al 2 O 3 slips for electrophoretic deposition,* Materials letters, 1996. **28**(4): pp. 353-355.
89. N. Sato, M. Kawachi, K. Noto, N. Yoshimoto, and M. Yoshizawa, *Effect of particle size reduction on crack formation in electrophoretically deposited YBCO films,* Physica C: Superconductivity, 2001. **357**: pp. 1019-1022.
90. E. Traversa, G. Oskam, G. Hunter, R. Penn, and N. Subcommittee, *Nanostructured Metal Oxides: Processing and Applications*, Electrochemical Society, 2006. **12**(6-7): pp. 420-424.
91. S. Salgın, U. Salgın, and S. Bahadır, *Zeta potentials and isoelectric points of biomolecules: the effects of ion types and ionic strengths,* Int. J. Electrochem. Sci, 2012. **7**: pp. 12404-12414.
92. R. Powers, *The Electrophoretic Forming of Beta-Alumina Ceramic,* Journal of The Electrochemical Society, 1975. **122**(4): pp. 490-500.
93. L. Besra and M. Liu, *A review on fundamentals and applications of electrophoretic deposition (EPD),* Progress in Materials Science, 2007. **52**(1): pp. 1-61.
94. A.H. Morrish, *The physical principles of magnetism,* The Physical Principles of Magnetism, by Allan H. Morrish, pp. 696. ISBN 0-7803-6029-X. Wiley-VCH, January 2001, **1**.
95. R. Molday, S. Yen, and A. Rembaum, *Application of magnetic microspheres in labelling and separation of cells,* Letters to Nature, 1977. **268**: pp. 437-438.
96. P.A. Zimmerman, J.M. Thomson, H. Fujioka, W.E. Collins, and M. Zborowski, *Diagnosis of malaria by magnetic deposition microscopy,* The American journal of tropical medicine and hygiene, 2006. **74**(4): pp. 568.

97. Q.A. Pankhurst, J. Connolly, S. Jones, and J. Dobson, *Applications of magnetic nanoparticles in biomedicine.* Journal of physics D: Applied physics, 2003. **36**(13): pp. R167.

98. K. Mosbach and U. Schröder, *Preparation and application of magnetic polymers for targeting of drugs,* FEBS letters, 1979. **102**(1): pp. 112-116.

99. S. Karl, M. David, L. Moore, B.T. Grimberg, P. Michon, I. Mueller, M. Zborowski, and P.A. Zimmerman, *Enhanced detection of gametocytes by magnetic deposition microscopy predicts higher potential for Plasmodium falciparum transmission.* Malar J, 2008. **7**: pp. 66.

100. Y. Xie, P. Zeng, R.A. Siegel, T.S. Wiedmann, B.E. Hammer, and P.W. Longest, *Magnetic deposition of aerosols composed of aggregated superparamagnetic nanoparticles,* Pharmaceutical research, 2010. **27**(5): pp. 855-865.

101. T. Schenkel, M. Malve, M. Reik, M. Markl, B. Jung, and H. Oertel, *MRI-based CFD analysis of flow in a human left ventricle: methodology and application to a healthy heart.* Annals of biomedical engineering, 2009. **37**(3): pp. 503-515.

102. P. Nath, J. Strelnik, A. Vasanji, L.R. Moore, P.S. Williams, M. Zborowski, S. Roy, and A.J. Fleischman, *Development of multistage magnetic deposition microscopy.* Analytical chemistry, 2008. **81**(1): pp. 43-49.

103. R.M. Erb, H.S. Son, B. Samanta, V.M. Rotello, and B.B. Yellen, *Magnetic assembly of colloidal superstructures with multipole symmetry,* Nature, 2009. **457**(7232): pp. 999-1002.

104. L. He, Y. Hu, X. Han, Y. Lu, Z. Lu, and Y. Yin, *Assembly and photonic properties of superparamagnetic colloids in complex magnetic fields,* Langmuir, 2011. **27**(22): pp. 13444-13450.

105. L. He, Y. Hu, H. Kim, J. Ge, S. Kwon, and Y. Yin, *Magnetic assembly of nonmagnetic particles into photonic crystal structures,* Nano letters, 2010. **10**(11): pp. 4708-4714.

106. L. He, M. Wang, Q. Zhang, Y. Lu, and Y. Yin, *Magnetic Assembly and Patterning of General Nanoscale Materials through Nonmagnetic Templates,* Nano letters, 2012. **13**(1): pp. 264-271.

107. M. Sastry, A. Kumar, S. Datar, C.V. Dharmadhikari, and K.N. Ganesh, *DNA-mediated electrostatic assembly of gold nanoparticles into linear arrays by a simple drop-coating procedure,* Applied Physics Letters, 2001. **78**(19): pp. 2943-2945.

108. N.V. Dziomkina, M.A. Hempenius, and G.J. Vancso, *Symmetry control of polymer colloidal monolayers and crystals by electrophoretic deposition on patterned surfaces,* Advanced Materials, 2005. **17**(2): pp. 237-240.
109. D. Zerrouki, J. Baudry, D. Pine, PP. Chaikin, and J. Bibette, *Chiral colloidal clusters,* Nature, 2008. **455**(7211): pp. 380-382.
110. K.H. Li and B.B. Yellen, *Magnetically tunable self-assembly of colloidal rings,* Applied Physics Letters, 2010. **97**(8): pp. 083105.
111. L. He, M. Wang, J. Ge, and Y. Yin, *Magnetic assembly route to colloidal responsive photonic nanostructures,* Accounts of chemical research, 2012. **45**(9): pp. 1431-1440.
112. J. Ge, S. Kwon, and Y. Yin, *Niche applications of magnetically responsive photonic structures,* Journal of Materials Chemistry, 2010. **20**(28): pp. 5777-5784.
113. T. Ahn, S. Oh, X. Hu, J.W. Lee, C.W. Park, H.M. Yang, C. Kim, and J.D. Kim, *Controlled Self-Assembly for High-Resolution Magnetic Printing,* Small, 2014. **10**(6): pp. 1081-1085.
114. W. Rattanasakulthong, P. Sirisangsawang, S. Pinitsoontorn, and C. Sirisathitkul, *Dependence of hysteresis loops on thickness of thin nickel films prepared by RF sputtering,* Advanced Materials Research, 2011. **335**: pp1443-1447.
115. P. Weiss and R. Forrer, *Magnetization and magnetocaloric phenomena of nickel.* Ann de Physique, 1926. **10**(5).
116. K. Raj, B. Moskowitz, and R. Casciari, *Advances in ferrofluid technology,* Journal of magnetism and magnetic materials, 1995. **149**(1): pp. 174-180.
117. S.-H. Lee, T.-W. Kim, K.-L. Suk, and K.-W. Paik, *Nanofiber Anisotropic Conductive Films (ACF) for Ultra-Fine-Pitch Chip-on-Glass (COG) Interconnections,* Journal of Electronic Materials, 2015. **44**(11): pp. 4628-4636.
118. L. Jia, X. Sheng, Z. Xiong, Z. Wang, and H. Ding, *Particle on Bump (POB) technique for ultra-fine pitch chip on glass (COG) applications by conductive particles and adhesives,* Microelectronics Reliability, 2014. **54**(4): pp. 825-832.
119. J. Ugelstad, A. Berge, T. Ellingsen, R. Schmid, T.-N. Nilsen, P. Mørk, P. Stenstad, E. Hornes, and Ø. Olsvik, *Preparation and application of new monosized polymer particles,* Progress in Polymer Science, 1992. **17**(1): pp. 87-161.
120. J. He, Z. Zhang, and H. Kristiansen, *Compression properties of individual*

micron-sized acrylic particles, Materials Letters, 2009. **63**(20): pp. 1696-1698.

121. Z. Zhang, H. Kristiansen, and J. Liu, *A method for determining elastic properties of micron-sized polymer particles by using flat punch test,* Computational materials science, 2007. **39**(2): pp. 305-314.
122. J. Perez, *Physcis and Mechanics of Amorphous Polymers,* Book, 1998.
123. M. Jerabek, Z. Major, and R. Lang, *Uniaxial compression testing of polymeric materials,* Polymer testing, 2010. **29**(3): pp. 302-309.
124. B. Steels, F. Leermakers, and C. Haynes, *Analysis of compression of polymer mushrooms using self-consistent field theory,* Journal of Chromatography B: Biomedical Sciences and Applications, 2000. **743**(1): pp. 31-40.
125. R.D. Egholm, S.F. Christensen, and P. Szabo, *Stress–strain behavior in uniaxial compression of polymer gel beads.* Journal of applied polymer science, 2006. **102**(3): pp. 3037-3047.
126. S.F. Lee, *Viscoelastic behaviour of poly (methyl methacrylate) and polystyrene*, PhD Thesis, Loughborough University, 2002.
127. M. Stout and PP. Follansbee, *Strain rate sensitivity, strain hardening, and yield behavior of 304L stainless steel,* Journal of Engineering Materials and Technology, 1986. **108**(4): pp. 344-353.
128. R. Vasin, F. Enikeev, and M. Mazurski, *Method to determine the strain-rate sensitivity of a superplastic material from the initial slopes of its stress–strain curves,* Journal of materials science, 1998. **33**(4): pp. 1099-1103.
129. A. Smolej, B. SkAzA, and M. FAzArinc, *Determination of the strain-rate sensitivity and the activation energy of deformation in the superplastic aluminium alloy Al-Mg-Mn-Sc Določevanje indeksa občutljivosti na preoblikovalno hitrost in aktivacijske energije za deformacijo superplastične aluminijeve,* Original Scientific Papers–Izvirni znanstveni članki Determination of the strain-rate sensitivity and the activation energy of deformation in the superplastic aluminium alloy Al-Mg-Mn-Sc, 2009. **56**(4): pp. 389-399.
130. J. Chen, L. Lu, and K. Lu, *Hardness and strain rate sensitivity of nanocrystalline Cu,* Scripta Materialia, 2006. **54**(11): pp. 1913-1918.
131. Y. Wang and E. Ma, *Strain hardening, strain rate sensitivity, and ductility of nanostructured metals,* Materials Science and Engineering: A, 2004. **375**: pp. 46-52.
132. J. May, H. Höppel, and M. Göken, *Strain rate sensitivity of ultrafine-grained*

aluminium processed by severe plastic deformation, Scripta Materialia, 2005. **53**(2): pp. 189-194.

133. S. Roy, S. Furukawa, and M. Mehregany, *Determination of Young's modulus and residual stress of electroless nickel using test structures fabricated in a new surface micromachining process,* Microsystem technologies, 1995. **2**(1): pp. 92-96.

134. A. Mathur and J. Erlebacher, *Size dependence of effective Young's modulus of nanoporous gold,* Applied Physics Letters, 2007. **90**(6): pp. 1910.

135. S. Wang, M.J. Yaszemski, J.A. Gruetzmacher, and L. Lu, *Photo-crosslinked poly (ε-caprolactone fumarate) networks: roles of crystallinity and crosslinking density in determining mechanical properties,* Polymer, 2008. **49**(26): pp. 5692-5699.

136. J. He, Z. Zhang, H. Kristiansen, K. Redford, G. Fonnum, and G. Modahl, *Crosslinking effect on the deformation and fracture of monodisperse polystyrene-co-divinylbenzene particles,* eXPRESS Polym Lett, 2013. **7**(4): pp. 365-374.

137. R. Schwaiger, B. Moser, M. Dao, N. Chollacoop, and S. Suresh, *Some critical experiments on the strain-rate sensitivity of nanocrystalline nickel,* Acta materialia, 2003. **51**(17): pp. 5159-5172.

138. D. Roylance, *Engineering viscoelasticity.* Department of Materials Science and Engineering–Massachusetts Institute of Technology, Cambridge MA, 2001. **2139**: pp. 1-37.

139. K. Lee, N. Yeung, and Y. Chan, *Modelling the effect of voids in anisotropic conductive adhesive joints,* Soldering & Surface Mount Technology, 2005. **17**(1): pp. 4-12.

140. K. Chiang, C. Chang, and C. Lin, *Process modeling and thermal/mechanical behavior of ACA/ACF type flip-chip packages,* Transactions on American Society of Mechanical Engineers Journal of Electronic Packaging , 2001. **123**(4): pp. 331-337.

141. J.A. Knapp, D.M. Follstaedt, S.M. Myers, J.C. Barbour, and T.A. Friedmann, *Finite-element modeling of nanoindentation,* Journal of Applied Physics, 1999. **85**(3): pp. 1460-1474.

142. G. Dou, D.C. Whalley, and C. Liu, *Mechanical characterization of individual Ni/ Au coated microsize polymer particles,* Applied Physics Letters, 2008. **92**:

pp. 104108.

143. J. He, S. Nagao, H. Kristiansen, and Z. Zhang, *Loading rate effects on the fracture of Ni/Au nano-coated acrylic particles,* Express Polymer Letters, 2012. **6**: pp. 198-203.

144. M.W. Sugden, C. Liu, D. Hutt, D. Whalley, and H. Kristiansen, *Metal-coated mono-sized polymer core particles for fine pitch flip-chip interconnects*, in Proc. IEEE 62th Electronic Components and Technology Conference (ECTC), San Diego, CA, USA, May 29-June 01, 2012, pp. 218-224.

145. I. Zhitomirsky, *Cathodic electrodeposition of ceramic and organoceramic materials. Fundamental aspects,* Advances in Colloid and Interface Science, 2002. **97**(1–3): pp. 279-317.

146. C.-T. Peng, C.-M. Liu, J.-C. Lin, H.-C. Cheng, and K.-N. Chiang, *Reliability analysis and design for the fine-pitch flip chip BGA packaging,* IEEE Transactions on Components and Packaging Technologies, 2004. **27**(4): pp. 684-693.

147. P. Garrou, *Wafer level chip scale packaging (WL-CSP): an overview,* IEEE Transactions on Advanced Packaging, 2000. **23**(2): pp. 198-205.

148. M.W. Sugden, D.A. Hutt, D.C. Whalley, and C. Liu, *A novel flip-chip interconnection process for integrated circuits,* Circuit World, 2012. **38**(4): pp. 214-218.

149. J. Ma and W. Cheng, *Deposition and packing study of sub-micron PZT ceramics using electrophoretic deposition,* Materials Letters, 2002. **56**(5): pp. 721-727.

150. J. Ji and W.C. Cooper, *Nickel speciation in aqueous chloride solutions,* Electrochimica Acta, 1996. **41**(9): pp. 1549-1560.

151. M.W. Sugden, C. Liu, D.A. Hutt, D.C. Whalley, and H. Kristiansen, *Electrophoretic Deposition of Mono-Sized Polymer Core Micro-Spheres for Use in Flip-Chip Interconnections,* 2013.

152. M.W. Sugden, C. Liu, D.A. Hutt, D. Whalley, and H. Kristiansen, *Effect of Surface Metallisation Layers on the Electrophoretic Deposition of Metal Coated Polymer Micro-Spheres,* 2013.

153. L. Zhu, O. Younes, N. Ashkenasy, Y. Shacham-Diamand, and E. Gileadi, *STM/AFM studies of the evolution of morphology of electroplated Ni/W alloys,* Applied surface science, 2002. **200**(1): pp. 1-14.

154. J. Kim, J. Yu, J. Lee, and T. Lee, *The effects of electroplating parameters on the*

composition and morphology of Sn-Ag solder, Journal of electronic materials, 2004. **33**(12): pp. 1459-1464.

155. H. Hamaker and E. Verwey, *Part II.—(C) Colloid stability. The role of the forces between the particles in electrodeposition and other phenomena,* Transactions of the Faraday Society, 1940. **35**: pp. 180-185.
156. D. De and P.S. Nicholson, *Role of ionic depletion in deposition during electrophoretic deposition,* Journal of the American Ceramic Society, 1999. **82**(11): pp. 3031-3036.
157. F. Grillon, D. Fayeulle, and M. Jeandin, *Quantitative image analysis of electrophoretic coatings,* Journal of materials science letters, 1992. **11**(5): pp. 272-275.
158. C. Kaya, A.R. Boccaccini, and K.K. Chawla, *Electrophoretic Deposition Forming of Nickel-Coated-Carbon-Fiber-Reinforced Borosilicate-Glass-Matrix Composites,* Journal of the American Ceramic Society, 2000. **83**(8): pp. 1885-1888.
159. M. Zborowski, *Physics of magnetic cell sorting*, in *Scientific and clinical applications of magnetic carriers,* 1997, Springer. pp. 205-231.
160. S. Liu, T. Zhu, R. Hu, and Z. Liu, *Evaporation-induced self-assembly of gold nanoparticles into a highly organized two-dimensional array,* Phys. Chem. Chem. Phys., 2002. **4**(24): pp. 6059-6062.
161. S. Lahokallio, K. Saarinen-Pulli, and L. Frisk, *Effects of different test profiles of temperature cycling tests on the reliability of RFID tags,* Microelectronics Reliability, 2015. **55**(1): pp. 93-100.
162. J.-H. Kuang, C.-M. Hsu, and A.-D. Lin, *A Study on the Conductivity Variation of Au Coated Conductive Particles in ACF Packaging Process,* Journal of Nanomaterials, 2014.
163. S.H. Mannan, D.J. Williams, and D.C. Whalley, *Some optimum processing properties for anisotropic conductive adhesives for flip chip interconnection,* Journal of Materials Science: Materials in Electronics, 1997. **8**(4): pp. 223-231.
164. G. Rabilloud, *Adhesives in electronics.* Handbook of Adhesives and Sealants, 2005. **1**: ppp. 349-483.
165. J.J. Licari and D.W. Swanson, *Adhesives technology for electronic applications: materials, processing, reliability*, Book, 2011.
166. C.-T. Ko and K.-N. Chen, *Reliability of key technologies in 3D integration.*

Microelectronics Reliability, 2013. **53**(1): ppp. 7-16.

167. C.-T. Ko and K.-N. Chen, *Low temperature bonding technology for 3D integration,* Microelectronics reliability, 2012. **52**(2): ppp. 302-311.
168. W.H. Leong, *Developing an underfill process for dense flip chip applications*. in *Electronics Manufacturing Technology Symposium,* in Proc. IEEE 19TH International Electronics Manufacturing Technology Symposium, October 14-16, Austin, Texas, USA, 1996, pp. 10-17.
169. C. Wong, S.H. Shi, and G. Jefferson, *High performance no-flow underfills for low-cost flip-chip applications: material characterization,* IEEE Transactions on Components, Packaging, and Manufacturing Technology, Part A, 1998. **21**(3): pp. 450-458.
170. C. Wong and D. Baldwin, *No-flow underfill for flip-chip packages.* US patent disclosure, 1996.
171. Y. Chan and D. Luk, *Effects of bonding parameters on the reliability performance of anisotropic conductive adhesive interconnects for flip-chip-on-flex packages assembly II. Different bonding pressure,* Microelectronics Reliability, 2002. **42**(8): pp. 1195-1204.